

11-2011

Extending Integral Concepts to Curved Bridge Systems

Saeed Eghtedar Doust

University of Nebraska-Lincoln, sedoust@gmail.com

Follow this and additional works at: <http://digitalcommons.unl.edu/civilengdiss>



Part of the [Civil Engineering Commons](#), and the [Structural Engineering Commons](#)

Eghtedar Doust, Saeed, "Extending Integral Concepts to Curved Bridge Systems" (2011). *Civil Engineering Theses, Dissertations, and Student Research*. 41.

<http://digitalcommons.unl.edu/civilengdiss/41>

This Article is brought to you for free and open access by the Civil Engineering at DigitalCommons@University of Nebraska - Lincoln. It has been accepted for inclusion in Civil Engineering Theses, Dissertations, and Student Research by an authorized administrator of DigitalCommons@University of Nebraska - Lincoln.

EXTENDING INTEGRAL CONCEPTS TO CURVED BRIDGE SYSTEMS

by

Saeed Eghtedar Doust

A DISSERTATION

Presented to the Faculty of

The Graduate College at the University of Nebraska

In Partial Fulfillment of Requirements

For the Degree of Doctor of Philosophy

Major: Interdepartmental Area of Engineering

(Civil Engineering)

Under the Supervision of Professors Elizabeth G. Jones and Atorod Azizinamini

Lincoln, Nebraska

November, 2011

EXTENDING INTEGRAL CONCEPTS TO CURVED BRIDGE SYSTEMS

Saeed Eghtedar Doust, Ph.D.

University of Nebraska, 2011

Advisors: Elizabeth Jones and Atorod Azizinamini

The behavior of integral abutment systems and the extension of their application to curved bridges are investigated. First, the stresses in the elements of a typical integral abutment are studied by conducting nonlinear finite element analysis using the software package Abaqus. The results are design recommendations for the details of such abutments. The effect of integral abutments on the responses of bridges is also investigated. Steel and concrete bridge systems are studied separately.

The studied steel bridge systems are composed of composite I-girder superstructures and integral abutments supported on steel H-piles. A series of finite element studies for different bridge lengths and radii are conducted and the effects of several load cases on the bridges are studied. In these bridges, the stresses in the abutment piles are of critical importance from the design standpoint. The results show that horizontal curvature mitigates these stresses. The bridge movement is also studied and a procedure to find the end displacements of curved bridges is presented. Pile orientation is another significant design factor that is studied elaborately. The results indicate that, for straight bridges, the strong-axis pile bending yields lower levels of stress. A method for finding the optimum pile orientation in curved integral bridges is developed. The effect of different bearing types is also investigated. This investigation reveals the superior structural performance of elastomeric bearings compared to other bearing types.

The concrete bridge systems that are studied consist of voided slab superstructures, integral abutments and concrete drilled shafts. A matrix of finite element studies is performed for different lengths and curvatures. Similar to steel I-girder bridges, it is concluded that horizontal curvature mitigates the internal forces of the abutment elements. The orientation of the concrete shafts is also examined which again shows the advantage of strong-axis orientation. Integral abutment bridges can have flexible piers integrally connected to the superstructure to eliminate all the bridge bearings. The effect of such integral piers on the internal forces of integral abutments is also examined. In these flexible piers, moment magnification can be of crucial significance. It is shown that choosing the integral abutment system reduces the magnification effects in the slender pier columns compared to jointed bridge systems.

© Copyright by

Saeed E. Doust

(2011)

Dedication

To
My wife Golboo
and
My daughter Taraneh

Acknowledgement

The present dissertation was conducted in the National Bridge Research Organization under the supervision of Professor Atorod Azizinamini. I am really thankful of him for his guidance, advice and help throughout the course of my doctoral studies.

I would like to express my sincere thanks to Professor Andrezj Nowak for his valuable considerations during the past years. His attention has meant a lot to me. I am extremely appreciative of his continual kindness.

I am deeply grateful of Professor Mehrdad Negahban for his valuable guidance and friendship. He gave me confidence in the most difficult days that I had.

I wish to thank Professor Elizabeth Jones, the Graduate Chair of the department for her sincere helps and guidance. I also thank Professor Fred Choobineh who served on my committee and evaluated my studies. And I appreciate the friendship and assistance of Dr. Aaron Yakel during the past years. I will never forget his precious helps.

I want to offer my special thanks to my beloved wife, Golboo, for her priceless patience, understanding and support. If she was not helping me, I was not able to accomplish this work. I owe her a life. And I apologize my daughter, Taraneh, for those times that I was tired and couldn't play with her. I promise to spend more time for her from now on.

At the end, I would like to thank my parents for spending their lives on my growth and progress.

Table of Contents

Table of Contents	v
List of Figures.....	xi
List of Tables.....	xix
Chapter 1 Introduction, Background and Objectives	1
1.1 Introduction	1
1.2 Background.....	6
1.3 Literature Review	7
1.3.1 Straight IA Bridges	8
1.3.2 Curved Bridges	10
A) Analysis.....	14
B) Elastic lateral torsional buckling capacity	15
C) Cross-Frame Spacing	16
D) Effect of Cross Frames.....	16
E) Flange Local Buckling of Curved Girders.....	17
1.3.3 Curved IA Bridges.....	17
1.4 Scope	19
1.5 Objectives of the study	20
Chapter 2 Mechanistic Study of Curved IAB	23
2.1 Introduction	23
2.2 Analysis of a Curved Girder.....	24
2.3 Analysis of an I-Girder under Torsion	27
2.4 Analysis of Two-girder Bridges	32
2.5 Analysis of Multi-girder Bridges.....	37
2.6 Cross Frame Spacing.....	41
Chapter 3 Detailed Study of Connections in an Integral Abutment	43
3.1 Introduction	43
3.2 Abutment Configuration.....	44
3.3 Steel Material Modeling	45
3.3.1 Tension Test.....	48
3.3.2 Validity of Constant Volume Assumption	52

3.3.3	Elastic Rebound of Cross Section.....	54
3.3.4	Proposing a New Model for Steel Material	56
3.3.5	Curve Fitting.....	57
3.3.6	A Sample Model: Grade 50 Steel	61
3.4	Concrete Material Modeling.....	61
3.4.1	Concrete Response under Compression	62
3.4.2	Concrete Compression Response Models	63
A)	Hognestad Model	64
B)	Polynomial Model.....	65
C)	Carreira and Chu Model.....	65
D)	Comparison of Different Models	66
3.4.3	Concrete Response under Tension.....	67
3.4.4	Concrete Tension Response Models.....	68
3.4.5	Concrete Response Modeling in Abaqus.....	72
3.4.6	Employed Concrete Models	77
3.5	Elements	79
3.5.1	C3D8(R)	79
3.5.2	C3D4.....	81
3.5.3	C3D10M	81
3.5.4	T3D2.....	81
3.6	Stress Functions Definition	81
3.7	Finite Element Modeling.....	85
3.8	Moment Capacity of the Superstructure.....	98
3.9	Results of Analysis.....	101
3.9.1	Girder Stresses.....	101
A)	Effect of Girder Stiffener	102
B)	Effect of Girder End Shear Studs.....	103
C)	Ultimate Loading	104
3.9.2	Abutment Wall Stresses At Girder Embedment Zone.....	108
A)	Effect of Girder Stiffener on Wall Stresses	109
B)	Effect of Girder End Shear Studs.....	110
3.9.3	Abutment Wall Stresses At Pile Embedment Zone	112
A)	Effect of Pile Stiffener	113
3.9.4	Pile Stresses	114
A)	Effect of Pile Stiffener	115
Chapter 4	Effect of Curvature on Steel IA Bridges.....	117
4.1	Introduction	117
4.2	Bridge Configuration.....	118
4.2.1	Superstructure	118
4.2.2	Abutments.....	120
4.2.3	Piers	121
4.3	Finite Element Modeling.....	123

4.3.1	Material Properties.....	123
4.3.2	Loading.....	124
A)	Dead Load (DC).....	124
B)	Wearing Surface Load (DW).....	124
C)	Earth Pressure (EH).....	125
D)	Live Load (LL).....	126
E)	Braking Force (BR).....	127
F)	Centrifugal Force (CE).....	128
G)	Wind Load (WS).....	129
H)	Uniform Temperature Changes (TU).....	133
I)	Temperature Gradient (TG).....	133
J)	Shrinkage (SH).....	134
4.3.3	Load Combinations.....	138
4.3.4	Soil-Structure Interaction.....	140
A)	Soil-Abutment interaction.....	141
B)	Soil-Pile Interaction.....	143
B1)	Lateral Load-Deflection in Soft Clay.....	144
B2)	Lateral Load-Deflection in Sand.....	147
4.3.5	Elements.....	152
A)	Beam Element.....	153
B)	Shell Element.....	153
C)	Nonlinear Link Element.....	154
D)	Nonlinear Support Element.....	157
4.3.6	Finite Element Models.....	158
4.4	Results of FE Analysis.....	159
4.4.1	Effects of Length and Curvature on Load Responses.....	161
A)	Bending Moment of Abutment Piles.....	163
A1)	Contraction.....	164
A2)	Expansion.....	166
A3)	Live Load.....	168
A4)	Wind Load.....	170
A5)	Dead Load.....	172
A6)	Concrete Shrinkage.....	174
A7)	Horizontal Earth Pressure.....	176
A8)	Centrifugal Force.....	178
A9)	Weight of Wearing Surface.....	179
A10)	Braking Force.....	181
A11)	Positive Temperature Gradient.....	183
A12)	Negative Temperature Gradient.....	185

A13) Combination of the Loads	186
B) Shear Force of Abutment Piles	188
4.4.2 Bridge Movement	189
A) Factors Affecting Bridge Displacement.....	192
B) Bridge Shortening Due to Contraction	196
C) Bridge Shortening Due to Shrinkage	198
D) Total Bridge Shortening.....	199
E) Effect of Bridge Width on the Displacement Direction.....	201
E1) Effect of Width on Contraction End Displacement	201
E2) Effect of width on Shrinkage End Displacement	202
E3) Effect of width on Total End Displacement	202
F) Direction of Displacement	204
G) Bridge End Displacement	207
H) Step by Step Procedure	211
I) Example	212
4.4.3 Pile Orientation.....	214
A) Analysis of Modeled Bridges with Weak and Strong Orientation for Abutment Piles.....	217
B) The Procedure to Find the Optimal Pile Orientation	228
4.4.4 Effect of Bearing Type and Orientation	228
A) Effect of Bearing Type on Abutment Pile Moments	230
B) Effect of Bearing Type on Pier Columns Moments.....	231
C) Bearing Orientation.....	234
Chapter 5 Effect of Curvature on Concrete IA Bridges.....	237
5.1 Introduction	237
5.2 Bridge Configuration.....	238
5.2.1 Superstructure	238
5.2.2 Abutments.....	239
5.2.3 Piers	240
5.3 Finite Element Modeling.....	242
5.3.1 Material Properties.....	242
5.3.2 Loading	242
A) Dead Load (DC).....	243
B) Wearing Surface Load (DW)	243
C) Earth Pressure (EH)	244
D) Live Load (LL)	244
E) Braking Force (BR).....	246
F) Centrifugal Force (CE)	246
G) Uniform Temperature Changes.....	247
H) Temperature Gradient	248
I) Shrinkage	248
5.3.3 Soil-Structure Interaction.....	250

A)	Soil-Abutment Interaction	250
B)	Soil-Pile Interaction	251
B1)	Lateral Load-Deflection in Soft Clay	251
B2)	Lateral Load-Deflection in Sand.....	254
5.3.4	Elements	257
A)	Beam Element.....	258
B)	Shell Element.....	258
C)	Nonlinear Link Element.....	258
D)	Nonlinear Support Element.....	260
5.3.5	Finite Element Models.....	261
5.4	Results of FE Analysis	262
5.4.1	Effect of Length and curvature on Load Responses.....	263
A)	Bending Moment of Abutment Piles	263
A1)	Contraction.....	263
A2)	Expansion.....	264
A3)	Live Load	265
A4)	Dead Load	266
A5)	Concrete Shrinkage.....	267
A6)	Horizontal Earth Pressure (EH).....	268
A7)	Centrifugal Force	271
A8)	Weight of Wearing Surface	272
A9)	Braking Force	273
A10)	Positive Temperature Gradient	274
A11)	Negative Temperature Gradient	275
A12)	Combination of the Loads	276
B)	Shear Forces of Abutment Piles.....	277
5.4.2	Pile Orientation.....	277
5.4.3	Bearing-Isolated Pier vs. Flexible Integral Pier.....	284
5.4.4	Mitigation of Moment Magnification.....	285
Chapter 6	Concluding Remarks and Future Research	291
6.1	Connections of Integral Abutments.....	291
6.2	Steel I-girder IA Bridges	292
6.2.1	Effects of Bridge length and curvature on load responses	293
6.2.2	Bridge Movement	295
6.2.3	Pile Orientation.....	297
6.2.4	Effect of Bearing Type	297
6.3	Concrete IA Bridges	299

6.3.1	Effects of Bridge Length and Curvature on Load Responses.....	299
6.3.2	Pile Orientation.....	301
6.3.3	Bearing-Isolated Piers versus Integral Piers.....	302
6.3.4	Mitigation of Moment Magnification Factor.....	302
6.4	Recommendations for Future Research.....	303

References 305

Appendix A Effect of Bridge Length and Curvature on Shear Force of Abutment Piles 317

A1	Contraction	317
A2	Expansion	319
A3	Live Load.....	321
A4	Wind Load	323
A5	Dead Load	325
A6	Concrete Shrinkage	327
A7	Horizontal Earth Pressure.....	329
A8	Centrifugal Force.....	331
A9	Weight of Wearing Surface	332
A10	Braking Force	334
A11	Positive Temperature Gradient.....	336
A12	Negative Temperature Gradient	337
A13	Combination of the Loads	339

Appendix B MATLAB Moment-curvature Program.....342-351

List of Figures

Figure 1.1-1	A Typical a) Integral Abutment b) Semi-Integral Abutment.....	4
Figure 2.2-1	Plan View of a Curved Girder Under Gravity Loads in z Direction.....	24
Figure 2.3-1	Effect of Torsional Moment Applied to a Cantilever I-Girder (Boresi et al.).....	28
Figure 2.4-1	Plan View of the Two-Girder Bridge.....	33
Figure 2.4-2	Flange Forces of the Girders.....	33
Figure 2.4-3	Equilibrium of a Segment of the Girder Flange.....	34
Figure 2.4-4	3D View of the Two-Girder Bridge.....	35
Figure 2.5-1	Cross Section of the Multi-Girder Curved Bridge.....	37
Figure 3.2-1	General Configuration of an Integral Abutment.....	45
Figure 3.3-1	Strain-Stress Curves (Tension Test # 1)	49
Figure 3.3-2	Strain-Stress Curves (Tension Test # 2)	50
Figure 3.3-3	Strain-Stress Curves (Tension Test # 3)	50
Figure 3.3-4	Strain-Stress Curves (Tension Test # 4)	51
Figure 3.3-5	Designation of the Key Points on the Strain-Stress Curves.....	56
Figure 3.3-6	Scheme of Fitted Curve Between Points C and D	59
Figure 3.3-7	Fitted Curve Between Points C and D	60
Figure 3.3-8	Material Model for Grade 50 Steel	61
Figure 3.4-1	Strain-Stress Curves of Concrete Specimens of Different Strength	63
Figure 3.4-2	Hognestad Model for Strain-Stress of Concrete in Compression	64
Figure 3.4-3	Strain-Stress Curves of Concrete in Compression in Different Models	67
Figure 3.4-4	Strain-Stress Curves of Concrete in Tension in Different Models	68
Figure 3.4-5	Schematic Strain-Stress Curve of Concrete in Tension	69
Figure 3.4-6	Strain-Stress Curves of Concrete in Tension and Compression	73
Figure 3.4-7	Biaxial Failure Surface of Concrete.....	75

Figure 3.4-8	Definition of Compressive Inelastic strain Used for Definition of Compression Hardening Data (Abaqus Documentation).....	76
Figure 3.4-9	Definition of Tensile Cracking Strain used for Definition of Tension Stiffening Data	77
Figure 3.4-10	Total and Inelastic Strain vs. Stress for 4 ksi Concrete in Compression ...	78
Figure 3.4-11	Total and Cracking Strain vs. Stress for 4 ksi Concrete in Tension	79
Figure 3.5-1	C3D8 Brick Element.....	80
Figure 3.5-2	C3D10M Tetrahedron Element.....	81
Figure 3.7-1	General Configuration of the Integral Abutment Model.....	86
Figure 3.7-2	Girder Element of the Connection	87
Figure 3.7-3	Embedded End of the Girder.....	88
Figure 3.7-4	Highlighted Position of the Girder Element.....	89
Figure 3.7-5	Concrete Wall of the Abutment	90
Figure 3.7-6	Highlighted Position of the Abutment Wall.....	91
Figure 3.7-7	Highlighted Position of the Deck Slab.....	92
Figure 3.7-8	Haunch Element of the Connection	92
Figure 3.7-9	Highlighted Position of the Haunch.....	93
Figure 3.7-10	H- Pile Element of the Connection	94
Figure 3.7-11	Highlighted Position of the H-Piles	95
Figure 3.7-12	Highlighted Rebars of the Deck Slab.....	96
Figure 3.7-13	Highlighted Rebars of the Abutment Wall	97
Figure 3.7-14	Shear Studs Attached to the Girder Bottom Flange	97
Figure 3.8-1	Superstructure Section at the Vicinity of Abutment Wall (Section A-A)	99
Figure 3.8-2	Moment–Curvature of the Superstructure at Section A-A.....	99
Figure 3.8-3	Stress Distribution in the Superstructure at the Vicinity of Abutment Wall Corresponding to Maximum Moment Capacity.....	100
Figure 3.9-1	Mises Stresses of Girder without any Stiffener or End Shear Stud	102
Figure 3.9-2	Mises Stresses of Girder with Stiffener without End Shear Stud	103
Figure 3.9-3	Mises Stresses of Girder with End Shear Stud without Stiffener	104
Figure 3.9-4	Mises Stresses of Half of the Girder	105
Figure 3.9-5	Mises Stresses of Concrete Deck	106
Figure 3.9-6	Mises Stresses of Girder’s End Corresponding to Mid-span Plastification.....	107

Figure 3.9-7	Mises Stresses of Abutment Wall Supporting an Unstiffened Girder	108
Figure 3.9-8	Mises Stresses of Abutment Wall Supporting a Stiffened Girder.....	109
Figure 3.9-9	Mises Stresses of Abutment Wall - Girder without End Shear Studs.....	111
Figure 3.9-10	Mises Stresses of Abutment Wall - Girder with End Shear Studs.....	111
Figure 3.9-11	Mises Stresses of the Concrete Wall Around the Piles	112
Figure 3.9-12	Stiffened Pile at the Wall Lower Face Section	113
Figure 3.9-13	Mises Stresses of the Concrete Wall Around the Piles with Stiffener.....	114
Figure 3.9-14	Mises Stresses of Abutment Piles	115
Figure 3.9-15	Mises Stresses of Abutment Piles with Stiffener	116
Figure 4.1-1	A Curved Steel I-girder Bridge Similar to the Studied Bridges	118
Figure 4.2-1	Cross Section of the Composite Steel Superstructure.....	119
Figure 4.2-2	Steel I-Girder Dimensions	120
Figure 4.2-3	Abutment Integral Details.....	121
Figure 4.2-4	Pier Configuration.....	122
Figure 4.2-5	Springs Modeling the Bearings of the Piers.....	123
Figure 4.3-1	Wearing Surface of the Modeled Steel Bridges.....	125
Figure 4.3-2	Positioning of the Live Load.....	127
Figure 4.3-3	Positive Temperature Gradient in the Superstructure Section	134
Figure 4.3-4	Annual Average Ambient Relative Humidity in Percent.....	136
Figure 4.3-5	Relationship of Wall Movement vs. Soil Pressure.....	142
Figure 4.3-6	Force-Displacement Curves of the Abutment Backfill Springs.....	143
Figure 4.3-7	Force-Displacement Curves of the Springs of Piles of Abutments in Soft Clay	146
Figure 4.3-8	Force-Displacement Curves of the Springs of Piles of Piers in Soft Clay	147
Figure 4.3-9	Initial Modulus of Subgrade Reaction	148
Figure 4.3-10	Values of Coefficients C_1 , C_2 and C_3 as a Function of Angle of Friction	150
Figure 4.3-11	Force-Displacement Curves of the Springs of Piles of Piers in Sand.....	151
Figure 4.3-12	Force-Displacement Curves of the Springs of Piles of Abutments in Sand.....	152
Figure 4.3-13	Modeling of the Bearings.....	156
Figure 4.3-14	Typical Finite Element Models of the Studied Bridges.....	159

Figure 4.4-1	Maximum Moment in Abutment Piles Due to Contraction	165
Figure 4.4-2	Normalized Moment in Abutment Piles Due to Contraction.....	166
Figure 4.4-3	Maximum Moment in Abutment Piles Due to Expansion	167
Figure 4.4-4	Normalized Moment in Abutment Piles Due to Expansion.....	168
Figure 4.4-5	Maximum Moment in Abutment Piles Due to Live Load	169
Figure 4.4-6	Normalized Moment in Abutment Piles Due to Live Load	170
Figure 4.4-7	Maximum Moment in Abutment Piles Due to Wind Load.....	171
Figure 4.4-8	Normalized Moment in Abutment Piles Due to Wind Load.....	172
Figure 4.4-9	Maximum Moment in Abutment Piles Due to Dead Load	173
Figure 4.4-10	Normalized Moment in Abutment Piles Due to Dead Load	174
Figure 4.4-11	Maximum Moment in Abutment Piles Due to Concrete Shrinkage	175
Figure 4.4-12	Normalized Moment in Abutment Piles Due to Concrete Shrinkage	176
Figure 4.4-13	Maximum Moment in Abutment Piles Due to Horizontal Earth Pressure	177
Figure 4.4-14	Normalized Moment in Abutment Piles Due to Horizontal Earth Pressure	178
Figure 4.4-15	Maximum Moment in Abutment Piles Due to Centrifugal Force.....	179
Figure 4.4-16	Maximum Moment in Abutment Piles Due to Weight of wearing Surface	180
Figure 4.4-17	Normalized Moment in Abutment Piles Due to Weight of Wearing Surface	181
Figure 4.4-18	Maximum Moment in Abutment Piles Due to Braking Force.....	182
Figure 4.4-19	Normalized Moment in Abutment Piles Due to Braking Force.....	183
Figure 4.4-20	Maximum Moment in Abutment Piles Due to Positive Temperature Gradient.....	184
Figure 4.4-21	Normalized Moment in Abutment Piles Due to Positive Temperature Gradient.....	184
Figure 4.4-22	Maximum Moment in Abutment Piles Due to Negative Temperature Gradient.....	185
Figure 4.4-23	Normalized Moment in Abutment Piles Due to Negative Temperature Gradient.....	186
Figure 4.4-24	Maximum Moment in Abutment Piles in Load Combinations Envelope..	187
Figure 4.4-25	Normalized Moment in Abutment Piles in Load Combinations Envelope.....	188
Figure 4.4-26	Directions of End Displacements in A Curved Bridge	193

Figure 4.4-27	Bridge End Movement- a) Pure Translation -b) Rotation.....	194
Figure 4.4-28	Modification Factor for Bridge Shortening Due to Contraction.....	197
Figure 4.4-29	Modification Factor for Bridge Shortening Due to Shrinkage.....	199
Figure 4.4-30	Modification Factor for Bridge Shortening Applied to Total Shortening	200
Figure 4.4-31	Direction of End Displacement Due to Contraction	201
Figure 4.4-32	Angles α_{in} and α_{out} in Total Displacement.....	203
Figure 4.4-33	Values $\alpha/90^\circ$ versus W/Lc	204
Figure 4.4-34	Modified Displacement Directions versus L/R.....	207
Figure 4.4-35	Deformed Bridge General Configuration.....	208
Figure 4.4-36	Deformed Bridge Simplified Configuration	209
Figure 4.4-37	Critical Load Combination Type	215
Figure 4.4-38	Critical Load Combination Type	223
Figure 4.4-39	Direction of Pile Displacement	224
Figure 4.4-40	Average Displacement Directions of Abutment Piles Top Node	225
Figure 4.4-41	Design Displacement Directions of Abutment Piles Top Node	226
Figure 4.4-42	Bending Moment of Abutment Piles with Different Bearing Types	230
Figure 4.4-43	Longitudinal Bending Moment of Pier Columns with Different Bearing Types	232
Figure 4.4-44	Transverse Bending Moment of Pier Columns with Different Bearing Types.....	234
Figure 4.4-45	Guided Bearing Orientation in Jointed Bridges	235
Figure 4.4-46	Guided Bearing Orientation in Bridges with Restraint Superstructure for a Trial Point	236
Figure 5.1-1	A Concrete Curved Integral Bridge Similar to the Studied Bridges.....	238
Figure 5.2-1	Cross Section of the Superstructure of the Modeled Bridges	239
Figure 5.2-2	A Typical Integral Connection for Voids Slab Bridges.....	240
Figure 5.2-3	Integral Connection of Piers and Superstructure	241
Figure 5.2-4	Bearing-Isolated Connection of Piers and Superstructure	241
Figure 5.3-1	Wearing Surface of the Modeled Bridges.....	244
Figure 5.3-2	Positioning of the Live Load (distances in inch)	245
Figure 5.3-3	Force-Displacement Curves of the Abutment Backfill Springs.....	251
Figure 5.3-4	Force-Displacement Curves of the Springs of Piles of Abutments in Soft Clay	253

Figure 5.3-5	Force-Displacement Curves of the Springs of Piles of Piers in Soft Clay	254
Figure 5.3-6	Force-Displacement Curves of the Springs of Piles of Piers in Sand	256
Figure 5.3-7	Force-Displacement Curves of the Springs of Piles of Abutments in Sand	257
Figure 5.3-8	Modeling of the Elastomeric Bearings	260
Figure 5.3-9	A Typical Finite Element Model of the Studied Bridges	262
Figure 5.4-1	Maximum Moment of Abutment Piles Due to Contraction	264
Figure 5.4-2	Maximum Moment of Abutment Piles Due to Expansion	265
Figure 5.4-3	Maximum Moment of Abutment Piles Due to Live Load	266
Figure 5.4-4	Maximum Moment of Abutment Piles Due to Dead Load	267
Figure 5.4-5	Maximum Moment of Abutment Piles Due to Concrete Shrinkage	268
Figure 5.4-6	Maximum Moment of Abutment Piles Due to Horizontal Earth Pressure	269
Figure 5.4-7	Plan View of Deformed Shape of the Bridge with R=200' under EH	270
Figure 5.4-8	Plan View of Deformed Shape of the Bridge with R=600' under EH	270
Figure 5.4-9	Plan View of Deformed Shape of the Bridge with R=1000' under EH	271
Figure 5.4-10	Maximum Moment of Abutment Piles Due to Centrifugal Force	272
Figure 5.4-11	Maximum Moment of Abutment Piles Due to Weight of Wearing Surface	273
Figure 5.4-12	Maximum Moment of Abutment Piles Due to Braking Force	274
Figure 5.4-13	Maximum Moment of Abutment Piles Due to Positive Temperature Gradient	275
Figure 5.4-14	Maximum Moment of Abutment Piles Due to Negative Temperature Gradient	276
Figure 5.4-15	Envelope of Moment of Abutment Piles in Different Load Combinations	277
Figure 5.4-16	PCACOL Design Sheet for Strong-Axis Orientation (1 of 2)	280
Figure 5.4-17	PCACOL Design Sheet for Strong-Axis Orientation (2 of 2)	281
Figure 5.4-18	PCACOL Design Sheet for Weak-Axis Orientation (1 of 2)	282
Figure 5.4-19	PCACOL Design Sheet for Weak-Axis Orientation (2 of 2)	283
Figure 5.4-20	Envelope of Moment of Abutment Piles in Different Load Combinations in Bridges with Integral Piers vs. Bridges with Elastomeric Isolated Piers	285
Figure 5.4-21	$P\Delta$ Effect in Non-Sway Mode	288

Figure 5.4-22	$P\Delta$ Effect in Sway Mode	288
Figure 5.4-23	$P\Delta$ Effect in a Jointed Abutment Bridge with Flexible Piers	289
Figure 5.4-24	$P\Delta$ Effect in an Integral Abutment Bridge with Flexible Piers	290
Figure A-1.	Maximum Shear Force in Abutment Piles Due to Contraction	318
Figure A-2.	Normalized Shear Force in Abutment Piles Due to Contraction	319
Figure A-3.	Maximum Shear Force in Abutment Piles Due to Expansion	320
Figure A-4.	Normalized Shear Force in Abutment Piles Due to Expansion	321
Figure A-5.	Maximum Shear Force in Abutment Piles Due to Live Load.....	322
Figure A-6.	Normalized Shear Force in Abutment Piles Due to Live Load	323
Figure A-7.	Maximum Shear Force in Abutment Piles Due to Wind Load	324
Figure A-8.	Normalized Shear Force in Abutment Piles Due to Wind Load.....	325
Figure A-9.	Maximum Shear Force in Abutment Piles Due to Dead Load.....	326
Figure A-10.	Normalized Shear Force in Abutment Piles Due to Dead Load	327
Figure A-11.	Maximum Shear Force in Abutment Piles Due to Concrete Shrinkage.....	328
Figure A-12.	Normalized Shear Force in Abutment Piles Due to Concrete Shrinkage ..	329
Figure A-13.	Maximum Shear Force in Abutment Piles Due to Earth Pressure	330
Figure A-14.	Normalized Shear Force in Abutment Piles Due to Earth Pressure.....	331
Figure A-15.	Maximum Shear Force in Abutment Piles Due to Centrifugal Force	332
Figure A-16.	Maximum Shear Force in Abutment Piles Due to Weight of Wearing Surface	333
Figure A-17.	Normalized Shear Force in Abutment Piles Due to Weight of Wearing Surface	334
Figure A-18.	Maximum Shear Force in Abutment Piles Due to Braking Force	335
Figure A-19.	Normalized Shear Force in Abutment Piles Due to Braking Force	335
Figure A-20.	Maximum Shear Force in Abutment Piles Due to Positive Temperature Gradient.....	336
Figure A-21.	Normalized Shear Force in Abutment Piles Due to Positive Temperature Gradient	337
Figure A-22.	Maximum Shear Force in Abutment Piles Due to Negative Temperature Gradient	338
Figure A-23.	Normalized Shear Force in Abutment Piles Due to Negative Temperature Gradient	339
Figure A-24.	Envelope of Maximum Shear Force in Abutment Piles in Different Load Combinations	340

Figure A-25. Envelope of Normalized Shear Force in Abutment Piles in Different Load Combinations

List of Tables

Table 1.1-1	Different Types of Jointless Bridges.....	3
Table 2.5-1	C Factor for Different Number of Girders	40
Table 4.3-1	Multilane Presence Factors	126
Table 4.3-2	C Factor for Different Radii.....	129
Table 4.3-3	Base Wind Pressure, P_B Corresponding to $V_B = 100 \text{ mph}$	130
Table 4.3-4	Values of V_o and Z_o for Various Upstream Conditions	131
Table 4.3-5	Base Wind Pressure, P_B for Various Angles of Attack.....	131
Table 4.3-6	Wind Pressure, P_D for Various Angles of Attack.....	133
Table 4.3-7	Proposed API p-y Curve for Soft Clay	144
Table 4.4-1	Normalized Weight Factors for Bending Moment of Abutment Piles	163
Table 4.4-2	Direction of Total Displacement (Results of FE Analyses) (W=60'-8")...	202
Table 4.4-3	Angles and Modified Angles of Total Displacement Direction.....	206
Table 4.4-4	Ratios of Abutment Pile Stresses (Weak Axis Orientation to Strong Axis Orientation).....	219
Table 4.4-5	Critical Load Combination Category for Abutment Pile Stresses	222
Table 4.4-6	Ratio of Piles Weak-axis Orientation Stress to Optimized Stress	227
Table 4.4-7	Ratio of Piles Strong-axis Orientation Stress to Optimized Stress	227
Table 4.4-8	Different Bearing Types and the Associated DOF's.....	229
Table 5.3-1	C Factor for Different Radii	247
Table 5.4-1	Internal Forces of Shafts with Different Orientations.....	278

Chapter 1

Introduction, Background and Objectives

1.1 Introduction

Bridges have been built since thousands of years ago by human beings. From prehistoric times to the Renaissance bridges had two main characteristics: The main construction materials were stone and natural cement and the spans were less than 100 feet. Despite the limitations that the architects and engineers of those times had, long bridges up to a total length of 1000 feet can be found among ancient bridges. After the Renaissance, modern bridges came into existence in the seventeen and eighteen century. The greatest differences of these modern bridges and the old ones were the material and span length. The material changed to iron (or steel) and later concrete. The span length gradually increased up to 3000 feet in the early twentieth century. So, the engineers were in charge of designing longer and longer bridges.

This trend in building bridges caused new approaches to appear in bridge industry. To accommodate the movements of long bridges, the designers adopted new techniques in

their designs. Moveable expansion joints and bearings were among those techniques. These devices have been used in bridges for more than 200 years. But, their performance has affected the long term performance of new bridges. Expansion joints have different designs which all of them have some sort of dysfunction. Even though they have high quality in the first months or years of service, after a longer time, most of them have problems such as leakage and poor ride quality due to wear or fracture. Bearings also have shown their intrinsic problems. In most bearing types, elastomeric layers are used. These elastomers lose their original properties in time. Ozone can damage the elastomer, even if there is no load or movement applied to the elastomer. That's why most of bearings should be replaced after some years.

The deficiencies of expansion joints and bearings drew the bridge designers to some new concepts of bridge design in the past years. Elimination of joints and bearings was the new target. This led to the introduction of a new type of structural system known as *Integral bridges*. These bridges are composed of:

- Abutments at the two ends
- Approach slabs that rest on abutments and their backfill
- Intermediate piers
- And finally a “*jointless*” superstructures built integral to the abutments

Note that there are no joints from the end to end of approach slabs. This bridge system is an ideal one which has no bearings and no joints. But, based on the needs, some other structural systems have also developed. First is an integral bridge that has rigid piers with movable and/or fixed bearings. In this type of bridges, all expansion joints and also the

abutment bearings are eliminated. But, piers still have bearings. If the durability of the pier bearings is guaranteed, these bridges can survive for a long time without any major deterioration. The second system has integral piers, but it has bearings in the abutments. In these bridges, the piers are flexible to be able to accommodate the movements, and the abutments are rigid, so they are isolated from the superstructure. A third system is a jointless bridge that has bearings both in the abutments and piers. Those jointless structural systems that have bearings in the abutments are called *semi-integral*. Table 1.1-1 shows different types of jointless bridges.

Bridge Type	Joint	Bearing over Piers	Bearing in Abutments
Integral with Flexible Piers	No	No	No
Integral with Rigid Piers	No	Yes	No
Semi-integral with Flexible Piers	No	No	Yes
Semi-integral with Rigid Piers	No	Yes	Yes

Table 1.1-1. Different Types of Jointless Bridges

As described before, integral bridges do not have joints whether they have bearings or not. Therefore, a better name for these bridges is “Jointless”. These two terms have been used interchangeably in the literature and also in the present study. The integral bridges with no bearing in the abutments are sometimes called “integral Abutment Bridges”. Figure 1.1-1 illustrates typical integral and semi-integral abutment details.

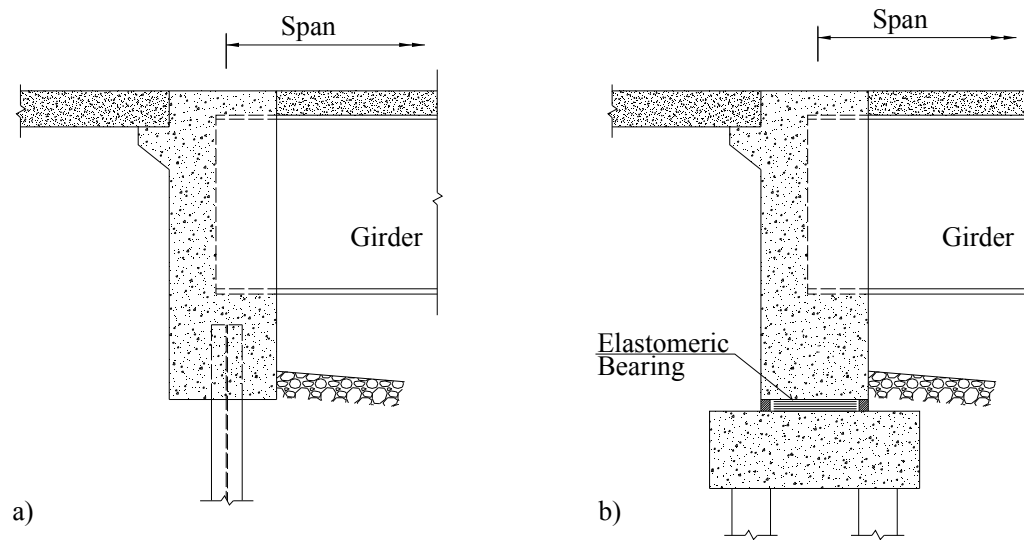


Figure 1.1-1. A Typical a) Integral Abutment b) Semi-Integral Abutment

Integral bridges have several advantages compared to jointed ones. The main advantages include:

- Lower initial and maintenance cost
- Longer service life
- No water leakage from superstructure down to substructure
- Improved riding quality
- Easier and faster construction
- Easier inspection
- More resistant to pavement growth/pressure phenomenon
- Reduced number of bearings (except for semi-integral with rigid piers)
- Easier embankment compaction

- No need to cofferdams for abutment excavation and pile driving
- Small excavation for abutments
- No need to battered piles for flexible abutments or piers
- Increased factor of safety for buoyancy
- Simple formwork for abutments and piers pile caps
- Fewer joints (just two joints at the ends of approach slabs)
- Broader construction tolerance
- Reduced removal of existing substructure (new configuration to straddle old foundations)
- Simple beam seat details
- Elimination of bearing anchor bars
- Broader end to intermediate span ratio
- No risk of superstructure falling during major earthquakes and eliminating seat width requirements in seismic design
- More distribution for live load
- Simpler Design (if the bending stiffness of abutment piles is ignored)

In the present study, both types of integral abutment bridges, with flexible and rigid piers, are studied. The abbreviations used for these bridges depending on the context are IA for “integral abutment” and IAB for “integral abutment bridges”.

1.2 Background

The first integral abutment bridge in the United States was built in 1938. Since then building integral bridges has spread throughout the country. Construction of integral bridges has also been adopted in Europe, Australia, New Zealand, Japan, South Korea and some other countries.

In the first decades, integral bridge systems were used for bridges with concrete superstructure. These bridges had a length between 50 to 100 feet. It was not until early 1960's that this concept was adopted for steel girder bridges. After that, several steel bridges with a skew angle less than 30 degrees and lengths not more than 300 feet were constructed using this method. Jointless steel bridges of length less than 300 feet have had an excellent performance in some states like North Dakota, South Dakota and Tennessee. Such bridges with concrete superstructures have been constructed and served with lengths of less than 800 feet in other states like California, Kansas and Colorado.

In 1987, eleven states of the US reported construction of jointless integral bridges with lengths of about 300 feet. Among those states, Tennessee and Missouri implemented the approach to longer bridges. Missouri reported concrete and steel integral bridges with the length of 500 and 600 feet, respectively. Tennessee DOT is leading the way in construction of long integral bridges. They have constructed a prestressed concrete integral abutment bridge with a length of 1175 feet.

The same tendency is seen in other countries. In Europe, European Commission is spreading the integral bridge concept among bridge designers. In the UK, integral and semi-integral bridge systems are recommended for relatively short bridges with less than

30 degrees skew angle. In Canada, integral construction is encouraged among designers where each province has its own provisions for these bridges. Ontario recommends jointless technique for bridges shorter than 328 feet.

The above mentioned trend shows that making use of integral bridges will become standard among the bridge designers and responsible agencies like DOT's in the near future. But, the use of this type of bridges becomes even more popular when comprehensive design guides are available and if their enhanced long term performance and durability is more proven. On the other hand, as thousand of existing bridges are jointed and during years are deteriorated, converting them into jointless integral bridges appears to be a reasonable solution if the design provisions and details of such bridges are documented. That will ensure the designers and owners of their decision and there will be more justification for adoption of such methodology.

1.3 Literature Review

To have a detailed study on curved integral abutment bridges, three different subjects should be considered: curved bridges, integral bridges and curved integral bridges. This is attributed to the fact that the problems associated with a curved jointed bridge or a straight integral bridge may be inherited by a curved integral bridge. Therefore, the literature review on curved integral abutment bridges is carried out in three steps. First, the previous research on integral abutment straight bridges is reviewed. These studies mainly include the investigations on thermal response and examination of the available field monitoring data related to integral bridges. Then, the studies that have been conducted on curved bridges are examined. This part presents a summary of decades of

research on the behavior of curved I- and box-girder bridges, their design requirements and the approaches to evaluate their strength. And then, the previous studies on curve integral abutment bridges are briefly summarized.

1.3.1 Straight IA Bridges

Straight integral bridges have been the subject of several studies. National Steel Bridge Alliance of American Iron and Steel Institute has published a report on integral abutments for steel bridges (American Iron and Steel Institute, Tennessee, Dept. of Transportation, Structures Division, & National Steel Bridge Alliance, 1996). This report authored by Wasserman and Walker was one of the first ones discussing the details and basic design requirements of steel integral bridges. As an almost old report, it has been a conservative guideline for designing integral bridges. The report discusses the practices of design agencies, the geometrical and construction limitations of jointless bridges and also provides an elementary example for design of piles.

Arsoy et al. have prepared a report for Virginia Transportation Research Council that presents the results of their works in a literature review, field trip and a finite element analysis related to integral bridges (Arsoy et al., 1999). They have concluded that the important factors regarding the integral bridges are the settlement of the approach fills, loads on the abutment piles, abutment displacement characteristics, the earth pressure distribution, the effects of secondary loads and the soil-structure interaction. They have discussed the techniques of reducing the approach fills settlements and have made some recommendations to enhance the performance of these bridges.

Fennema et al. have studied the response of an integral abutment bridge through analysis and field monitoring (Fennema, Laman, & Linzell, 2005). Their research verified that the inclusion of multi-linear soil springs resulted from p-y curves is a valid method of soil-pile interaction analysis. It is also shown that superstructure thermal movement is accommodated through rotation of the abutment about its base rather than pure longitudinal translation of the wall. They have also indicated that soil pressures are between active and at-rest pressure values. Also, it is demonstrated that the maximum soil pressure is at a point approximately 1/3 of the abutment height below the road surface.

Pugasap et al. have studied long-term response of integral abutment bridges (Pugasap, Kim, & Laman, 2009). They have continuously monitored three Pennsylvania integral abutment bridges for about two years and shown that the bridge movement progresses year to year and the long term response is significant with respect to static predictions. In this study, seasonal cyclic ambient temperature and equivalent temperature derived from time-dependent strains using the age-adjusted effective modulus have been employed. To model the hysteretic behavior of soil-pile and soil-abutment interaction and the abutment-to-backwall connection, the elastoplastic p-y curves, classical earth pressure theories and moment-rotation relationships with parallel unloading path were used. In their study, the predicted earth pressures have been similar to the measured pressures. They have shown that the ratios of long-term to short-term abutment displacements vary from 1.5 to 2.3 which indicate the importance of considering the long-term response of integral abutment bridges.

In 2009, Vermont Agency of Transportation published a guideline on design of integral abutment bridges (VTrans, 2009). The guideline discusses general design and location features, loads, structural analysis methods, the needed guideline to design concrete and steel elements of such bridges, foundation, abutments and pier requirements and several other subjects. The format of presenting the subjects is in accordance to AASHTO LRFD. But the problem with this report is the comprehensiveness of the discussed problems. It seems that this guideline follows the previous codes and reports and leaves several problems about jointless bridges unanswered.

There are also several other studies on the behavior of integral abutment straight bridges. Although, there is not an all-inclusive design guide for straight integral bridges, but it seems there is enough research, tests and data available to be compiled for composition of a design guide.

1.3.2 Curved Bridges

In geometrical design of roads, tendency to use smooth transitions forces the designers to employ curved paths and inevitably demand for curved bridges in their designs. The use of curved bridges has increased drastically over the past 30 years so that these bridges constitute about one-third of all bridges being built today (Linzell, Leon, & Zureick, 2004).

Until 1960s there was not a major research project on understanding the behavior of curved bridges. The need for curved bridges, because of their advantages to chord bridges, led to development of the specifications for these bridges. The first official attempt was creation of the Consortium of University Research Teams (CURT) project in

1969 which was funded by 25 states under the direction of the Federal Highway Administration (FHWA). The consortium collected all existing data on curved bridges, conducted analytical and experimental research and developed analysis and design methods for curved bridges (Linzell, Hall, & White, 2004). But, all the results were based on the available information and techniques of those days.

The research on curved bridges continues in 1970s leading to publication of the first AASHTO design guide in 1980 when AASHTO issued the Guide Specifications for Horizontally Curved Bridges (American Association of State Highway and Transportation Officials, 1980). The guide was incomplete and conservative on the presented provisions. The reason for the conservative approach was the uncertainties on the response of curved bridges during construction and service. Therefore, more research was required to enhance the available recommendations. AASTHO revised the guide several times after first publication through the interim revisions and published a second edition of the specifications in 1993 (American Association of State Highway and Transportation Officials, 1993).

In 1992, another project was started by FHWA to study curved steel bridges. The project called Curved Steel Bridge Research Project (CSBRP) was conducted by Zureick et al. (Zureick et al., 1994). The project had several aspects ranging from reviewing existing research to providing new design recommendations. Another goal was to study curved bridges from constructability point of view. One of the major steps in the project was to conduct an experimental research on a large scale curved bridge. The main difference of the experiments in this project and the previous ones was the size of the test specimens and providing more realistic boundary conditions in the laboratory. The test

bridge in this project was a single span three-girder bridge with the mean span of 90 feet and mean radius of 200 feet. So, the span was a representative of the existing bridge spans and the radius was the lower bound for the real curved bridges. Based on the results of that experiment, Zureick et al. presented the state-of-the-art analysis methods for horizontally curved steel I-girder bridges (Zureick & Naqib, 1999). Also the capabilities of analysis tools to predict the behavior of girders during erection and the significance of erection sequence on the initial stresses of the girders were discussed by Linzell et al. (Linzell, Leon et al., 2004). Based on this research project, several other problems have been studied by the involved researchers like the research conducted by White et al (White, 2001).

In 1993, National Cooperative Highway Research Program (NCHRP) started a new project, NCHRP 12-38, conducted by Hall et al. to offer improved specifications compared to previous research. The results of this study were published in NCHRP report 424 (Hall et al., 1999). It includes an overview of curved bridge research, the US curved bridge design practice, a summary of Load Factor Design specifications by Hall and Yoo (Hall, National Research Council (U.S.), Transportation Research Board, National Cooperative Highway Research Program, & Bridge Software Development International, Ltd, 1998). The outcome of this project is reflected in AASHTO through the Guide Specifications for Horizontally Curved Bridges published in 2003 (American Association of State Highway and Transportation Officials, Subcommittee on Bridges and Structures, 2003).

Another project on curved bridges was the joint project of AISI and FHWA in 1999 to develop unified equations for curved and straight I-girder bridges for the LRFD code.

The results of this great project are presented by White et al. (White, 2001). This document includes a review of the curved I-girder strength equations and the required modifications to the AASHTO LRFD 2001. All of these efforts resulted in valuable outcomes in less than a decade (White et al., 2008).

One more great research project by NCHRP is the project 12-52 which revised the 2003 AASHTO Guide Specifications and provided valuable design examples for both I- and Box-girder curved steel bridges. These example are prepared by Kulicki et al. (J. M. Kulicki, National Cooperative Highway Research Program, & Modjeski and Masters, 2005a; J. M. Kulicki, National Cooperative Highway Research Program, & Modjeski and Masters, 2005b).

The research on uniting the design equations for straight and curved bridges was continued by White et al. and the most updated strength equations was first reflected in the AASHTO LRFD published in 2007 (American Association of State Highway and Transportation Officials, 2007).

In addition to these national bridge research projects, several other projects have been conducted by different researchers. For example, Bell and Linzell have studied the effects of different erection procedures on the deformations and stresses of a horizontally curved I-girder bridge. In this study that was on a three-span bridge, despite the large radius of the curvature of the bridge, the original erection scheme resulted in large deformations yielding a misaligned geometry. Their study shows the important effect of pair girder erection, lateral bracing and temporary shoring during construction (Bell & Linzell, 2007).

In addition to the general studies on curved bridge behavior, several researchers have studied more specific subjects in this field (J. M. Kulicki, National Cooperative Highway Research Program., American Association of State Highway and Transportation Officials, & United States, Federal Highway Administration, 2006). In the following subsections, some of these studies are summarized.

[In other countries, other than the US, it seems that Japan is one of the only countries which have published their own design guides for curved bridges. Japan Road Association has published the Guidelines for the Design of Horizontally Curved Girder Bridges.]

A) Analysis

There can be several different levels of analysis for curved girder bridges including hand calculations like V-Load method, 1D line girder analysis, 2D planar analysis and finally 3D analysis. 1D line girder analysis is any analysis method which extracts a girder out of the rest of structure and analyzes that girder individually. Employing such a method for curved bridges may result in huge approximations. 2D planar analyses methods have several varieties. Any analysis that includes just superstructure elements and incorporates the effects of substructures by means of boundary conditions lies in this group. Cross frames and diaphragms may or may not be modeled in a planar analysis. The components may be modeled using only frame elements. Plate or shell elements also may be used in such an analysis. On the other hand, a 3D finite element analysis includes all the components of super- and substructure. In 3D analyses, there can be different levels of refinement. Truss, frame, plate, shell or solid elements may be employed based on the needed accuracy. Some elements may be replaced by the boundary conditions in

the analysis. In this case, the results are valid provided that correct boundary conditions are chosen. Any analysis method for curved bridges that does not include the depth of the girders can't be considered as a full 3D analysis. Any 3D space frame analysis is not a full 3D analysis because of inability to account for the effect of deck slab or girder web in the third dimension.

Evaluation of the different analysis levels capabilities was a valuable outcome of the NCHRP Project 12-38. The evaluated analysis levels include 1D line girder analysis, 2D planar grid analysis and 3D finite element analysis that are compared through examples by Hall et al. (Hall et al., 1999). They have shown that there is a close correlation for dead load results among all three levels of analysis. For live load, the results of 2D and 3D analyses are fairly correlated, but 1D analysis results are noticeably different. The reason for the discrepancy may be attributed to the load distribution factors.

Nevling et al. have also examined the accuracy of different levels of analysis for curved I-girder bridges. In their study, a field test on a three-span bridge has been performed to evaluate different methods results. It is concluded that 2D grillage models and 3D finite element models predict girder vertical bending moments more accurately than a line girder analysis. Also, it is resulted that the girder vertical bending moment distributions of a 3D analysis are not significantly more accurate than those of a 2D analysis (Nevling, Linzell, & Laman, 2006).

B) Elastic lateral torsional buckling capacity

As the curved bridges have an intrinsic imperfection, the usual bifurcation type lateral torsional buckling moment may not be seen in such bridges. An eigenvalue analysis

yields buckling moments for the girders of these bridges. Davidson performed several analyses on hypothetical curved bridges which resulted in a fitted equation for such problems (J. S. Davidson, 1996).

C) Cross-Frame Spacing

Several finite element analyses conducted by Davidson et al. (J. S. Davidson, Keller, & Yoo, 1996) on a series of hypothetical curved bridges has ended in an equation for the spacing of the cross frames as follows:

$$S = L \left[-\ln \left(\frac{1.965 \frac{f_w}{f_b} R b_f}{L^2} \right) \right]^{-1.52} \quad \text{Eq. 1.1}$$

In which S is the cross frame spacing, L is span length of girder, f_w is the warping stress in the girder, f_b is the bending stress in the girder, R is the radius of curvature and b_f is the width of the compression flange of the girder.

D) Effect of Cross Frames

Addition of lateral bracing to the flanges of I-girders makes them to act like a box girder. One of the main structural roles of the cross frames in curved I-girder bridges is to increase the stiffness of the superstructure and so to reduce the deflection of the bridge. The other important effect of cross frames is the reduction of the girder bending and warping stresses.

E) Flange Local Buckling of Curved Girders

Eq. 1.2 was proposed by Davidson and Yoo which was the result of a number of analyses on curved I-girder bridges to limit the width to thickness ratio of the compression flange (J. S. Davidson & Yoo, 1996).

$$\left(\frac{b}{t}\right)_{curved} \leq \left(\frac{b}{t}\right)_{curved} \sqrt{\alpha} \quad \text{Eq. 1.2}$$

Where

$$\alpha = 1.05 - \frac{S^2}{4Rb_f} \leq 1.0 \quad \text{Eq. 1.3}$$

1.3.3 Curved IA Bridges

In the section on curved bridges, it was states that the trend to have optimum transitions in design of roads and highways urges the employment of curved paths and roads. These optimized geometrical designs necessitate construction of curved bridges. On the other hand, the request for elimination of joints directs the bridge designers to a solution called “*Curved Integral Abutment Bridges*”. Regarding their superior performance, this type of bridges is getting more and more popularity among the designers and also bridge owners. But, as there is not enough information on the structural behavior of these bridges, some DOT’s have restricted the application of curved IA bridges.

A limited number of investigations have been carried out on curved integral abutment bridges. Among them is a dissertation by Thanasattayawibul that is done in the University of Maryland, College Park in 2006 (Thanasattayawibul, 2006). In this

dissertation, several finite element analyses have been performed on curved steel I-girder IA bridges. The effects of dead, live and temperature loads have been considered. In this research, the main studied subjects have been the abutment pile stresses and the bridge lateral displacements.

Another study on curved integral abutment bridges is a master's thesis by Kalayci from the University of Massachusetts Amherst (Kalayci, 2010). In this thesis, the Stockbridge Bridge in Vermont is used as a baseline model which based on that five other models have been generated with the same length and different degrees of curvature. The effects of dead and temperature loading on the models have been studied. The weak-axis bending is chosen for the abutment piles. Reducing the restraint against bridge movement is stated as the reason for such a pile orientation. The finite element models have been studied for bridge displacements and pile and superstructure moments. In the modeling process it is tried to use simplified models which could have been resulted in errors in the responses. Again, it is stated that based on NCHRP Report 563, these simplified analysis methods cannot be considered full 3-D finite element analyses.

In the above-mention studies, there are some major problems. One of the problems is the practicality of the presented results. In some cases, just the “*relative*” values of the some important results, such as pile stresses or displacements, are given. Some of the results are absolutely weird. Several problems of great practical significance have not been investigated. For example, longer spans, like the spans close to 200 feet, have not been studied. The effects of several loads other than dead, live and temperature have not been considered. These loads include earth pressure, centrifugal force, braking force, wind load and concrete shrinkage. Based on the design codes, the internal forces should

be studied in load combinations. In the previous studies, the internal forces in those load combinations have not been studied. A mechanistic solution for the displacements of the curved integral abutment bridges has not been presented. The optimum orientation of the piles has not been discussed. Also other problems such as the effects of different types of bridge bearings or pier-to-superstructure connections have not been investigated.

1.4 Scope

In the present dissertation two different types of jointless bridges are studied:

- i- Integral abutment steel I-girder bridges with rigid piers
- ii- Integral abutment concrete bridges with flexible piers

The studied steel IA bridges have bearing over the intermediate piers and the studied concrete IA bridges do not have any type of bearings.

The other point to mention on the scope of this study is the radius of curvature of the bridges. In highway design manuals, the radius of curvature of roads is determined as a function of design speed, superelevation and coefficient of friction using the following equation:

$$R_{min} = \frac{V^2}{15(e + f)} \quad \text{Eq. 1.4}$$

In which R_{min} is the minimum radius of curvature in feet, V is the design speed in mile per hour, e is the superelevation and f is the side friction coefficient. This equation comes from equating the centrifugal force $\frac{mV^2}{R}$ and the summation of friction force and tangential component of weight on a slope. The constant 15 comes from the different

units used in the equation. Plugging a velocity of 25 mph, a superelevation of %6 and a side friction coefficient of 0.15, yields a radius of about 200 feet. If the design speed is changed to 30 mile per hour, the minimum radius increases to about 300 feet. These tight radii are in agreement with the radius chosen for the great experimental research of CSBRP project of FHWA which was the base of the works of leading researchers of this area in the US. Another research was conducted by Disantiago et al. who also chose a radius of 191 feet for their investigation (DeSantiago, Mohammadi, & Albaijat, 2005).

In the present study, as it is assumed that steel bridges practically cannot have radii less than 300 feet, the minimum radius of curvature used for studied steel bridges is 300 feet. And since the concrete bridges are assumed to have cast-in-place slab type superstructures in which the radius of 200 feet or even smaller is possible, a minimum radius of 200 feet is chosen for the studied concrete bridges. In each case, larger radii up to infinity which correspond to straight bridges are also studied.

1.5 Objectives of the study

The objective of the present study is to comprehend the behavior of curved integral abutment bridges. Because of existing uncertainty on the response of such structures, transportation agencies have limited their application. The conservative approach of the bridge designers and owners comes from inadequate past research on these bridges. As horizontal curvature induces a large amount of complexity in the response of curved bridges, lack of knowledge about their complicated behaviour has urged the bridge design code providers to adopt such conservatism. For example, Burke M. P., the author of several references on interal bridges, limits the curvature of such bridges to 5 degrees

(Burke, 2009). Also, Maruri and Petro set a limitation of 10 degrees on the curvature of steel and concrete bridges (Maruri and Petro, 2005). Arockiasamy et al. have limited the application of curved integral bridges to those bridges that have an angle subtended by a 30 meter arc-length greater than 5 degrees (Arockiasamy & Sivakumar, 2005). This means that the radius of such bridge should be larger than 1100 feet. One of the main targets of the present study is to check the validity of such limitations.

In this dissertation, curved integral steel I-girder and also concrete slab bridges are studied. The effect of bridge horizontal curvature and bridge length are investigated. The effect of different loads applied to an integral bridge is examined. These loads include gravity loads, lateral loads either longitudinal or transverse, temperature effects, concrete shrinkage and earth pressure.

Different opinions can be found in the literature about pile orientation in integral bridges. As the maximum pile stress is a limiting factor for the length of the integral bridges, optimum orientation for the pile is of critical importance. Although in several reports at least a section is devoted to pile orientation, the existing opinions are not based on a scientific reasoning. Those opinions are mainly based on a sense to make the integral bridges more flexible which is deeply discussed in present study.

Bridge end displacement is a major concern for bridge designers. This end displacement is of great significance from bridge structural design and pavement design standpoints. A sophisticated study is conducted on this problem in the case of steel bridges. The factors affecting the bridge movement are discussed. The effect of different participating causes such as bridge width are also included. It is tried to present a step by step procedure to calculate the curved bridge movement.

The other problem that is studied is the effect of bearing devices on the response of curved integral bridges. It is observed that due to lack of correct understanding of the response of curved integral bridges, wrong types of bearing devices are used in these bridges. The improper selection of the type of bearing devices creates overwhelming internal forces in the structure. In this study, the bearing devices are categorized based on the available degrees of freedom, and then their effects on bridge structural behavior are investigated.

Chapter 2

Mechanistic Study of Curved IAB

2.1 Introduction

The response of curved bridges to horizontal and gravity load is different than that of straight bridges. This difference is because of torsional actions due to the curvature of the longitudinal axis of the bridge. If the torsional forces are replaced by equivalent forces on equivalent straight girders, an approximate solution can be obtained. The equivalent forces are developed from equilibrium and are a function of bridge radius, spacing between the girders and the spacing between the cross frames. The following subsections explain the method of analysis. First a curved girder under gravity loads is analyzed to have a better understanding of the internal forces developed in such an element. The main outcome of this analysis is the torsional moment created in curved girders due to gravity loads. Then, the problem of torsional response of an I-girder is analyzed, which is divided into Saint-Venant's torsion and warping torsion. Next, the bridge systems with horizontal curvature are studied. For this purpose, first a two-girder bridge unit is analyzed, and then

a multi-girder system is studied. At the end, a method to calculate the spacing of the cross frames is presented.

2.2 Analysis of a Curved Girder

A curved girder with a horizontal radius of curvature of R is considered. The girder is assumed to have a fixed support at one end and a free support at the other end. This assumption for the boundary conditions does not hurt the generality of the problem. Also, it is assumed that the girder is under the uniform gravity load of w . The length of the girder is L and the angle subtended by the girder is Θ . The origin of the coordinate axes is located at the fixed end of the girder. Figure 2.2-1 shows the general picture of the assumed girders.

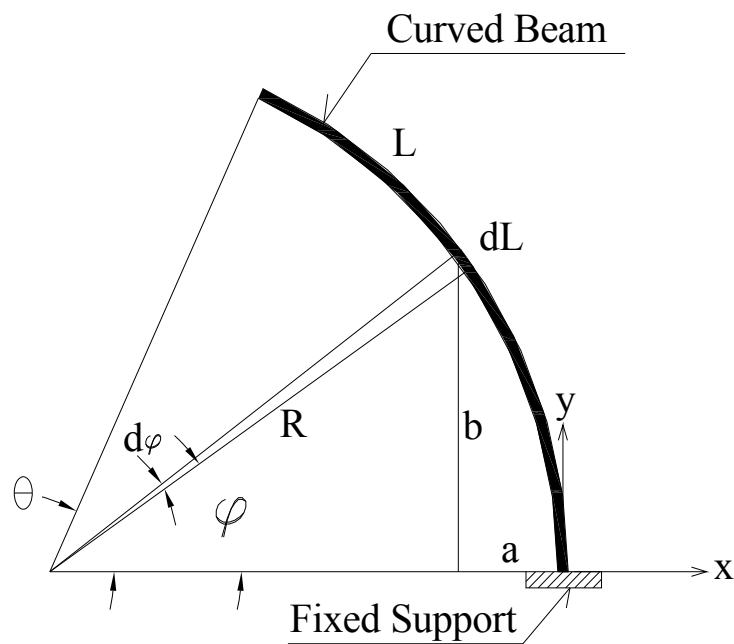


Figure 2.2-1. Plan View of a Curved Girder Under Gravity Loads in z Direction

To find the support reactions, the equilibrium equations about the axes x , y and z are written:

$$R_x = R_y = 0 \quad \text{Eq. 2.1}$$

$$R_z = wL \quad \text{Eq. 2.2}$$

$$M_x = \int_0^L d_{Mx} \quad \text{Eq. 2.3}$$

$$M_y = \int_0^L d_{My} \quad \text{Eq. 2.4}$$

$$M_z = 0 \quad \text{Eq. 2.5}$$

As can be observed there is no reaction forces in the x and y directions, also no moment about z direction and the reaction along z direction is nothing other than the applied vertical load, which in this case is the weight of the girder. In order to calculate the moment reaction about x and y directions, an infinitesimal element of the girder with the length of dl and location coordinates of (a, b) is considered. The position of the element in the polar coordinates can be written as:

$$a = -R(1 - \cos \varphi) \quad \text{Eq. 2.6}$$

$$b = R \sin \varphi \quad \text{Eq. 2.7}$$

The integrals are calculated as follows:

$$\begin{aligned} M_x &= \int_0^L d_{Mx} = \int_0^L (b)(w \, dl) = \int_0^\Theta (R \sin \varphi)(wR d\varphi) = R^2 w \int_0^\Theta \sin \varphi \, d\varphi \\ &= R^2 w (1 - \cos \Theta) \end{aligned} \quad \text{Eq. 2.8}$$

$$\begin{aligned}
 M_y &= \int_0^L d_{My} = \int_0^L (a)(w \, dl) = \int_0^\Theta R (1 - \cos \varphi)(wR d\varphi) \\
 &= R^2 w \int_0^\Theta (1 - \cos \varphi) d\varphi = R^2 w (\Theta - \sin \Theta)
 \end{aligned}
 \tag{Eq. 2.9}$$

Hence

$$M_x = R^2 w (1 - \cos \Theta) \tag{Eq. 2.10}$$

$$M_y = R^2 w (\Theta - \sin \Theta) \tag{Eq. 2.11}$$

The moment M_x is the bending moment of the curved girder at the support and the moment M_y is the torsional moment developed in the cross section of the girder at support. The noticeable fact is creation of torsional moment due to just gravity load, such as self weight, which is unheard in the case of straight girders. To verify the above equations, the values of M_x and M_y are evaluated for a special case of $R = \infty$ which is a straight girder:

$$\begin{aligned}
 \lim_{R \rightarrow \infty} M_x &= w \cdot \lim_{R \rightarrow \infty} R^2 (1 - \cos \Theta) = w \cdot \lim_{\Theta \rightarrow 0} \frac{L^2}{\Theta^2} (1 - \cos \Theta) = \\
 &= wL^2 \cdot \lim_{\Theta \rightarrow 0} \frac{(1 - \cos \Theta)}{\Theta^2} = wL^2 \cdot \lim_{\Theta \rightarrow 0} \frac{\sin \Theta}{2\Theta} = wL^2 \cdot \lim_{\Theta \rightarrow 0} \frac{\cos \Theta}{2} = \frac{wL^2}{2}
 \end{aligned}
 \tag{Eq. 2.12}$$

$$\begin{aligned}
 \lim_{R \rightarrow \infty} M_y &= w \cdot \lim_{R \rightarrow \infty} R^2 (\Theta - \sin \Theta) = w \cdot \lim_{\Theta \rightarrow 0} \frac{L^2}{\Theta^2} (\Theta - \sin \Theta) \\
 &= wL^2 \cdot \lim_{\Theta \rightarrow 0} \frac{(\Theta - \sin \Theta)}{\Theta^2} = wL^2 \cdot \lim_{\Theta \rightarrow 0} \frac{1 - \cos \Theta}{2\Theta} \\
 &= wL^2 \cdot \lim_{\Theta \rightarrow 0} \frac{\sin \Theta}{2} = 0
 \end{aligned}
 \tag{Eq. 2.13}$$

In the above calculations, the third and forth limits are evaluated using the L'Hopital's rule. The conclusions from this special case are in compliance with the common understanding of the behavior of straight girders. But, the major result of this part of

study is for curved girders; development of torsional moment in the girder due to gravity loads in the absence of any external lateral or torsional loads.

2.3 Analysis of an I-Girder under Torsion

When a section is under torsional moment, the response of the section can be divided into Saint-Venant's torsion and warping torsion. The participation of each of these two types of response depends on the stiffness of each of them. In an I-section, as the Saint-Venant stiffness is less than the warping stiffness, the role of section warping becomes important. When the end of an I-girder is restrained by a rigid support like an integral abutment, warping is prevented in that end of the girder. Therefore, torsion of a girder with such boundary conditions results in longitudinal stresses in the girder. In this section, the analysis of a one-end restrained I-girder under torsion is presented according to the formulations given by Borelli et al. (Borelli & Schmidt, 2003).

Consider an I-girder connected to the abutment wall at one end such as the I-girder shown in Figure 2.3-1. If the girder undergoes a torsional moment, balance of the section of the girder adjacent to the wall develops horizontal shear forces in the flanges. As the flanges are restrained at the end, the shear forces produce longitudinal stresses like a cantilever beam. As the distance of the section to the wall increases, the torsion is resisted partly by these shear forces and partly by Saint-Venant shear stresses in the section. At sections far away from the abutment, the warping shear forces in the flanges become smaller and smaller and the torsion is resisted mainly by Saint-Venant shear stresses.

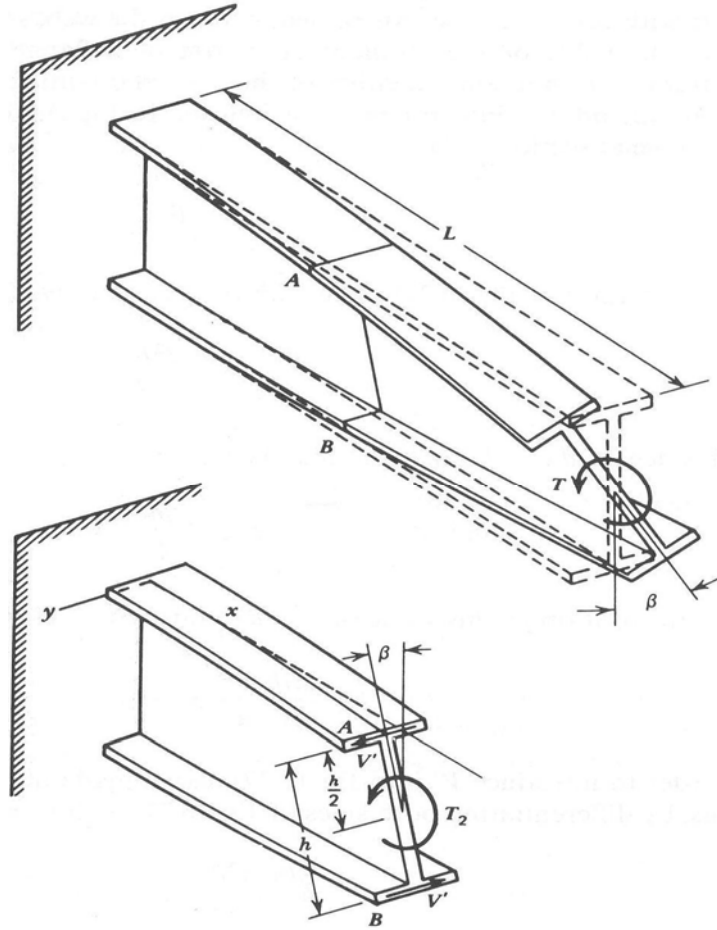


Figure 2.3-1. Effect of Torsional Moment Applied to a Cantilever I-Girder (Boresi et al.)

If the torsional moment of the section is T , part of that which develops warping shear forces in the flanges is T_w that is equal to:

$$T_w = V'h \quad \text{Eq. 2.14}$$

The other part of T is T_s which is the Saint-Venant torsion of the section.

$$T_s = JG\theta \quad \text{Eq. 2.15}$$

In the above equations, the parameters h , the distance of the flange centroids, J , the torsional constant and G , the shear modulus of elasticity are known. The flange horizontal

shearing force V' and the angle of twist per unit length θ are unknown. The angle θ is equal to $\frac{d\beta}{dx}$, where the coordinate axes x and y are defined in Figure 2.3-1. To find these two unknowns, the first equation that can be written is static equilibrium of the section:

$$T_w + T_s = T \quad \text{Eq. 2.16}$$

Or

$$V'h + JG\theta = T \quad \text{Eq. 2.17}$$

The other equation can be found from bending of the flange of girder:

$$\frac{EI}{2} \frac{d^2 y}{dx^2} = -M_f \quad \text{Eq. 2.18}$$

in which M_f is the lateral bending moment of the flange, E is the modulus of elasticity and I is the moment of inertia of the section with respect to the vertical axis z , so that $\frac{I}{2}$ is approximately equal to the moment of inertia of the flange about z axis. The above equation does not have any of the unknowns of the problem, V' and θ . The following geometric relation is used to introduce θ into Eq. 2.18:

$$y = \frac{h}{2} \beta \quad \text{Eq. 2.19}$$

Which related the lateral deflection of the flange y and the angle of torsion β . Two differentiations yields:

$$\frac{d^2 y}{dx^2} = \frac{h}{2} \frac{d^2 \beta}{dx^2} \quad \text{Eq. 2.20}$$

And as $\frac{d\beta}{dx} = \theta$, the following equation is obtained:

$$\frac{d_y^2}{d_{x^2}} = \frac{h}{2} \frac{d_\theta}{d_x} \quad \text{Eq. 2.21}$$

Substitution of Eq. 2.21 into Eq. 2.18 gives:

$$\frac{Elh}{4} \frac{d_\theta}{d_x} = -M_f \quad \text{Eq. 2.22}$$

On the other hand, $\frac{d_{M_f}}{d_x} = V'$. So,

$$\frac{Elh}{4} \frac{d_\theta^2}{d_{x^2}} = -V' \quad \text{Eq. 2.23}$$

Substituting V' from Eq. 2.23 into Eq. 2.17 gives:

$$-\frac{Elh^2}{4GJ} \frac{d_\theta^2}{d_{x^2}} + \theta = \frac{T}{GJ} \quad \text{Eq. 2.24}$$

If the parameter α is defined as:

$$\alpha = \frac{h}{2} \sqrt{\frac{EI}{GJ}} \quad \text{Eq. 2.25}$$

Then the Eq. 2.24 may be written as

$$-\alpha^2 \frac{d_\theta^2}{d_{x^2}} + \theta = \frac{T}{GJ} \quad \text{Eq. 2.26}$$

The solution for the above second order ordinary differential equation is as follows:

$$\theta = Ae^{x/\alpha} + Be^{-x/\alpha} + \frac{T}{GJ} \quad \text{Eq. 2.27}$$

To find the values of A and B boundary conditions of the problem should be defined. The boundary conditions are as follows:

$$\theta = \frac{d\beta}{dx} = 0 \quad \text{at} \quad x = 0 \quad \text{Eq. 2.28}$$

$$\frac{d\theta}{dx} = 0 \quad \text{at} \quad x = L \quad \text{Eq. 2.29}$$

Finding the values of A and B results in the following values for θ and β :

$$\theta = \frac{T}{GJ} \left(1 - \frac{\cosh\left(\frac{L-x}{\alpha}\right)}{\cosh\left(\frac{L}{\alpha}\right)} \right) \quad \text{Eq. 2.30}$$

$$\beta = \int_0^L \theta \, dx = \frac{T}{GJ} \left(L - \alpha \tanh \frac{L}{\alpha} \right) \quad \text{Eq. 2.31}$$

Substituting Eq. 2.30 into Eq. 2.15 yields the moment T_s at any section.

$$T_s = T \left(1 - \frac{\cosh\left(\frac{L-x}{\alpha}\right)}{\cosh\left(\frac{L}{\alpha}\right)} \right) \quad \text{Eq. 2.32}$$

The maximum torsional shear is calculated as:

$$\tau_{max} = \frac{2T_s h_{max}}{J} \quad \text{Eq. 2.33}$$

And the lateral bending moment of the flange is calculated as:

$$M_f = -\frac{T}{h} \alpha \frac{\sinh\left(\frac{L-x}{\alpha}\right)}{\cosh\left(\frac{L}{\alpha}\right)} \quad \text{Eq. 2.34}$$

So, the maximum lateral bending moment of the flange is equal to:

$$M_f = \frac{T}{h} \alpha \tanh \frac{L}{\alpha} \quad \text{Eq. 2.35}$$

As the length of the girders are relatively large, the value of $\tanh \frac{L}{\alpha}$ is approximately equal to unity and the following values are obtained for β and M_f :

$$\beta = \frac{T(L - \alpha)}{GJ} \quad \text{Eq. 2.36}$$

$$M_f = \frac{T}{h} \alpha \quad \text{Eq. 2.37}$$

Using the above equations, an approximate method for analyzing a one-end restrained I-girder can be derived. In this method, it can be approximately assumed that in a length of α from the abutment, the torsion is carried by the shear forces in flanges that are equal to:

$$V = \frac{T}{h} \quad \text{Eq. 2.38}$$

This shear force bends the flanges laterally so that the maximum normal stress can be obtained from Eq. 2.37 as:

$$\sigma = \frac{M_f C}{I} = \frac{T}{h} \alpha \frac{\frac{1}{2} b}{\frac{1}{12} t b^3} = \frac{6T\alpha}{h t b^2} \quad \text{Eq. 2.39}$$

In the remaining length of the girder away from abutment, it can be assumed that the whole torsion is carried by the Saint-Venant torsion of the girder and so classical torsion equations can be implemented to find the resulted shear stress.

2.4 Analysis of Two-girder Bridges

A method known as V-Load method which is based on static equilibrium is used to analyze a curved bridge with two girders (Fiechtl, 1987). If the spacing between the girders are assumed to be D , the angle of curvature of the bridge to be φ , the radius and

arc length of the outer girder to be R_1 and L_1 and the radius and arc length of the inner girder to be R_2 and L_2 , then the vertical forces on the girders can be obtained using the static equilibrium. Figure 2.4-1 shows a plan view of the considered bridge.

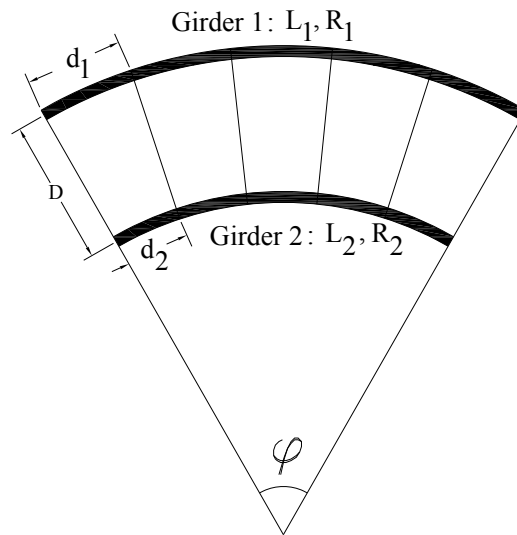


Figure 2.4-1. Plan View of the Two-Girder Bridge

If it is assumed that the bending moment in each girder is just resisted by the compression and tension of the top and bottom flanges and if the depth of the outer and inner girders are h_1 and h_2 respectively, then the flange forces due to moments M_1 and M_2 will be M_1/h_1 and M_2/h_2 . Figure 2.4-2 shows the flange forces of the girders resulted from equilibrium.

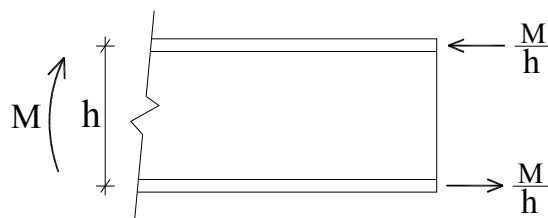


Figure 2.4-2. Flange Forces of the Girders

On the other hand, as the girders are curved, the horizontal forces of the flanges will not be in equilibrium. If a segment of the outer girder which has a diaphragm in its center is considered, as shown in Figure 2.4-3, because of curvature of the girder a horizontal force along the line of the diaphragm is needed to guarantee equilibrium. This force is similar and in the opposite direction for the top and bottom flanges. This force is calculated by setting the summation of the forces in the diaphragm line equal to zero. If the subtended angle of the neighboring diaphragms is θ , the horizontal force of the diaphragm will be:

$$H_1 = \frac{M_1 \theta}{h_1} \quad \text{Eq. 2.40}$$

Knowing that for the outer girder $\theta = d_1/R_1$ where d_1 is its diaphragm spacing and substituting into Eq. 2.40 results in:

$$H_1 = \frac{M_1 d_1}{h_1 R_1} \quad \text{Eq. 2.41}$$

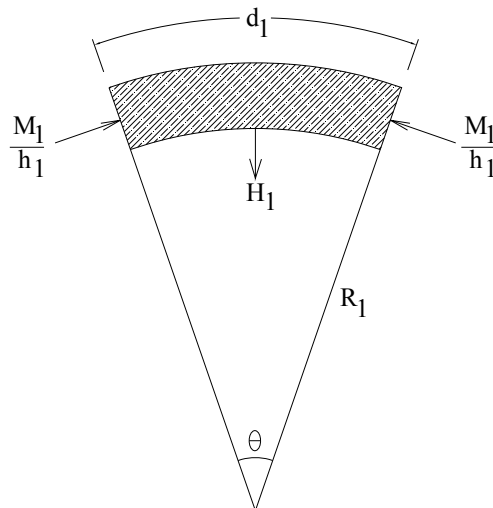


Figure 2.4-3. Equilibrium of a Segment of the Girder Flange

The corresponding force of the diaphragm for the inner girder H_2 is calculated in the same way as the method used for outer girder, with this difference that H_2 is in the opposite direction.

$$H_2 = \frac{M_2 d_2}{h_2 R_2} \quad \text{Eq. 2.42}$$

Figure 2.4-4 illustrates a three dimensional picture of the forces acting on the two-girder bridge.

As can be seen, the moment equilibrium of the diaphragm necessitates existence of the vertical shear forces that can be calculated from the following equation:

$$V = (H_1 + H_2) \frac{h}{D} \quad \text{Eq. 2.43}$$

in which h is the equal depth of the inner and outer girders.

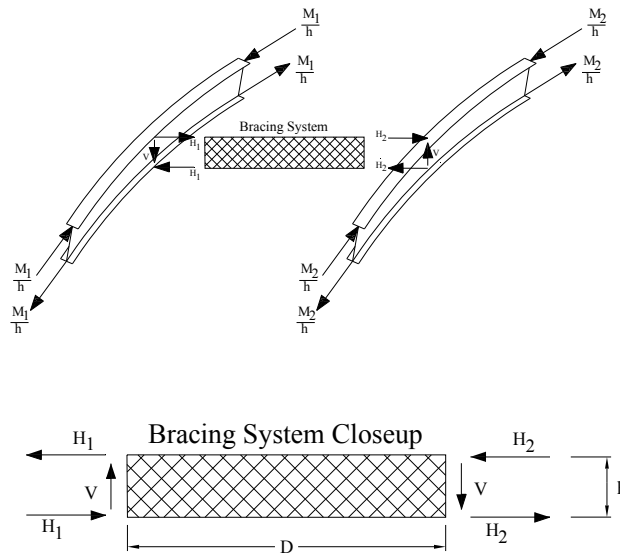


Figure 2.4-4. 3D View of the Two-Girder Bridge

Substituting for H_1 and H_2 from the previous equations leads to:

$$V = \frac{M_1 \frac{d_1}{R_1} + M_2 \frac{d_2}{R_2}}{D} \quad \text{Eq. 2.44}$$

Since

$$\frac{d_1}{R_1} = \frac{d_2}{R_2} = \frac{d}{R} \quad \text{Eq. 2.45}$$

The vertical reaction of the diaphragm will be:

$$V = \left(\frac{M_1 + M_2}{D} \right) \frac{d}{R} \quad \text{Eq. 2.46}$$

These vertical loads which are applied to the girders in the opposite directions are the effect of curvature on the bridge girders.

The bending moments M_1 and M_2 are the final moments produced in the girders of the bridge due to effects of applied loads and curvature. In this analysis, these two sources of producing moments are tried to be separated. If the moments due to applied loads are shown by subscript L and the moments due to curvature are shown by subscript C, then it can be written that:

$$M_1 = M_{1L} + M_{1C} \quad \text{Eq. 2.47}$$

$$M_2 = M_{2L} + M_{2C} \quad \text{Eq. 2.48}$$

To calculate the moments due to curvature, first it should be assumed that the moments in the girders are just due to applied loads. Then, the shear forces of the diaphragms can be calculated from Eq. 2.40. Then, the equivalent straight girder should be analyzed under application of the shear forces so that the moment due to curvature is obtained. The sum of the moments of applied load and curvature is the moment of the

girder. This method can be used iteratively so that more exact evaluations of the effect of curvature can be reached.

2.5 Analysis of Multi-girder Bridges

As shown in the previous section, in curved two-girder bridges the moment and shear force of the outer girder increases (compared to equivalent straight bridge) due to the effect of curvature while the forces of the inner girder decreases. The same approach as two girder bridges is used to analyze multi-girder bridges in horizontal curvature.

A bridge with N_g girders, girder spacing of s_g and girder depth of h is considered. Figure 2.5-1 illustrates a cross section of such a bridge. Equilibrium of the diaphragms leads to a relation between horizontal flange forces and vertical shears that the diaphragms apply to the girders:

$$\sum_{i=1}^{N_g} H_i = \sum_{i=1}^{N_g-1} V'_i \left(\frac{s_g}{h} \right) \quad \text{Eq. 2.49}$$

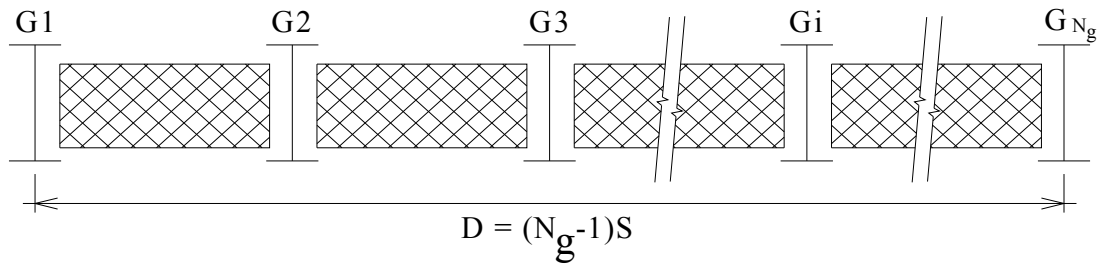


Figure 2.5-1. Cross Section of the Multi-Girder Curved Bridge

in which V'_i is the shear in the i -th diaphragm and H_i is the applied force to the flange of the i th girder. On the other hand, the horizontal force that is applied to each flange is a function of the bending moment of the girder M_i :

$$H_i = \frac{M_i d}{hR} \quad \text{Eq. 2.50}$$

where d is the cross frame spacing on the girder and R is the radius of curvature of the girder. Substitution of the Eq. 2.50 into Eq. 2.49 yields:

$$\sum_{i=1}^{N_g} M_i \frac{d}{RS_g} = \sum_{i=1}^{N_g-1} V'_i \quad \text{Eq. 2.51}$$

Considering the free body diagram of the bridge leads to a relation between the shear in j th diaphragm V'_j and the vertical forces applied to the girders 1 to j :

$$V'_j = \sum_{i=1}^j V_i \quad \text{Eq. 2.52}$$

in which V_i is the vertical force applied to the i th girder. Now, if a linear distribution is assumed for the vertical forces applied to the girders, then the force applied to the girder i can be written as a function of the force applied to the outer girder, V :

$$V_i = V \left(1 - \frac{2(i-1)}{N_g-1} \right) \quad \text{Eq. 2.53}$$

From the last two equations, it can be concluded that:

$$V'_j = \sum_{i=1}^j V \left(1 - \frac{2(i-1)}{N_g-1} \right) \quad \text{Eq. 2.54}$$

And from Eq. 2.51 it is resulted that:

$$\alpha V = \sum_{i=1}^{N_g} M_i \frac{d}{RS_g} \quad \text{Eq. 2.55}$$

in which

$$\alpha = \sum_{j=1}^{N_g-1} \sum_{i=1}^j \left(1 - \frac{2(i-1)}{N_g-1}\right) \quad \text{Eq. 2.56}$$

In other words

$$V = \frac{\sum_{i=1}^{N_g} M_i}{\alpha RS_g/d} \quad \text{Eq. 2.57}$$

This equation is similar to the equation derived for two girder bridges with a single difference which is α . Expansion of the obtained expression for α clarifies what this coefficient is.

$$\alpha = \frac{1}{2}N_g^2 - \frac{1}{6}N_g(2N_g - 1) \quad \text{Eq. 2.58}$$

If a new coefficient C is defined as $c = \alpha/(N_g - 1)$, then the vertical load on the outer girder will be

$$V = \frac{\sum_{i=1}^{N_g} M_i}{c RD/d} \quad \text{Eq. 2.59}$$

Evaluation of coefficient c results in the following expression for that.

$$c = \frac{N_g(N_g + 1)}{6(N_g - 1)} \quad \text{Eq. 2.60}$$

The value of the above equation for $N_g = 2$ is equal to unity which is in compliance with the result of the study on two-girder bridges. The value of the coefficient c for different number of girders is tabulated in Table 2.5-1.

N_g : Number of Girders	C Factor
2	1.000
3	1.000
4	1.111
5	1.250
6	1.400
7	1.556
8	1.714
9	1.875

Table 2.5-1. C Factor for Different Number of Girders

As the first approximation, the summation of the girders moments can be estimated by the sum of the moments due to applied loads. So, the Eq. 2.59 can be estimated by

$$V = \frac{\sum_{i=1}^{N_g} M_{iL}}{c RD/d} \quad \text{Eq. 2.61}$$

which directly gives the load applied to the outer girder at diaphragm location. The loads on the other girders can be obtained by the linear variation assumption for the loads. In this way, first based on the external loads that are applied to the bridge a set of additional shear forces on the girders is calculated. Then, the girders are analyzed to obtain the additional moments due to curvature.

2.6 Cross Frame Spacing

A criterion for cross frame spacing can be obtained from the equilibrium of horizontal forces as stated in Eq. 2.41:

$$H = \frac{M_b S}{hR} \quad \text{Eq. 2.62}$$

in which H is the horizontal force of cross frame with a spacing of S due to bending moment M_b . Therefore, if the force of the cross frame is assumed to be distributed over the spacing S , the magnitude of that force is:

$$q = \frac{H}{S} = \frac{M_b}{hR} \quad \text{Eq. 2.63}$$

Since in a bridge, usually there are several cross frames along the length of the bridge, if the force q is assumed to be uniform between adjacent cross frames, the maximum moment about the vertical axis in the flanges of the girder is:

$$M_z = \frac{qS^2}{12} = \frac{M_b S^2}{12hR} \quad \text{Eq. 2.64}$$

The moment M_z tends to bend the flanges of the girder about the vertical axis. But the direction of bending is different for top and bottom flanges, so that it causes some sort of warping in the bridge girders. The longitudinal stress due to this lateral moment is equal to the moments M_z divided by the section modulus of the flange under consideration:

$$\sigma_L = \frac{M_z}{S_f} \quad \text{Eq. 2.65}$$

where S_f is the elastic section modulus of the flange equal to:

$$S_f = \frac{t_f b_f^2}{6} \quad \text{Eq. 2.66}$$

On the other hand, the bending moment M_b causes longitudinal stresses in the flanges of the girder which can reasonably estimated as:

$$\sigma_b = \frac{M_b}{h t_f b_f} \quad \text{Eq. 2.67}$$

Substitution of the above three equations into Eq. 2.64 results in:

$$S = \sqrt{2R b_f \left(\frac{\sigma_L}{\sigma_b} \right)} \quad \text{Eq. 2.68}$$

The ratio of the stresses due to lateral bending of the flange can be presumed by designer in order to find an approximate spacing for the cross frames. Using the above equation, the designer can find the optimum spacing of the cross frames after one or two iterations.

Chapter 3

Detailed Study of Connections in an Integral Abutment

3.1 Introduction

In this chapter, the behavior of the connections in the integral abutment of a steel bridge is studied in details. For this purpose, first the general configuration of a typical integral abutment is discussed. A picture of the details for this type of abutments which is in practice in the US is presented. Then, the material models considered for steel and concrete elements are investigated. Next, the finite element modeling of the abutment is explained. And at the end, the results of the analysis are brought.

In order to study the integral abutments, finite element modeling is conducted using the software package Abaqus 6.9.1. This general-purpose program is able to analyze such structural details in the finest possible way. In the following sections, the method of analysis is explained step by step.

3.2 Abutment Configuration

A general picture of an integral abutment of a steel I-girder bridge is depicted in Figure 3.2-1. As can be seen, the concrete mass of the wall is continuous with the deck slab. This is maybe the first reason that this type of abutment is called *integral*. In these abutments, the steel girder is embedded in the concrete wall in a length of about half of the wall thickness. It is supposed that the bond between steel and concrete which is poured on it develops enough stresses for attaching the girder to the wall. Although the horizontal rebars of the wall are continued through the web of the girder. There may also be some shear studs attached to the bottom flange of the girder in the embedment length. The purpose of installing such studs is to increase the reliability of the connection to carry negative moments. The top flange of the girder is connected to the reinforced concrete deck by shear connectors which altogether provide the tension component for the presumed negative moment.

In these abutments, the piles are embedded in the concrete mass of the wall. The connection is assumed to be provided by the bond of concrete and steel. The length of embedment is typically between 2 and 4 feet. The wall rebars are so arranged that they do not intersect with the piles.

The approach slab is attached to the abutment wall by means of a pin connection detail. Therefore, it just applies a vertical load to the abutment wall and does not participate in the overall response of the abutment. Because of that, it can be eliminated from the study.

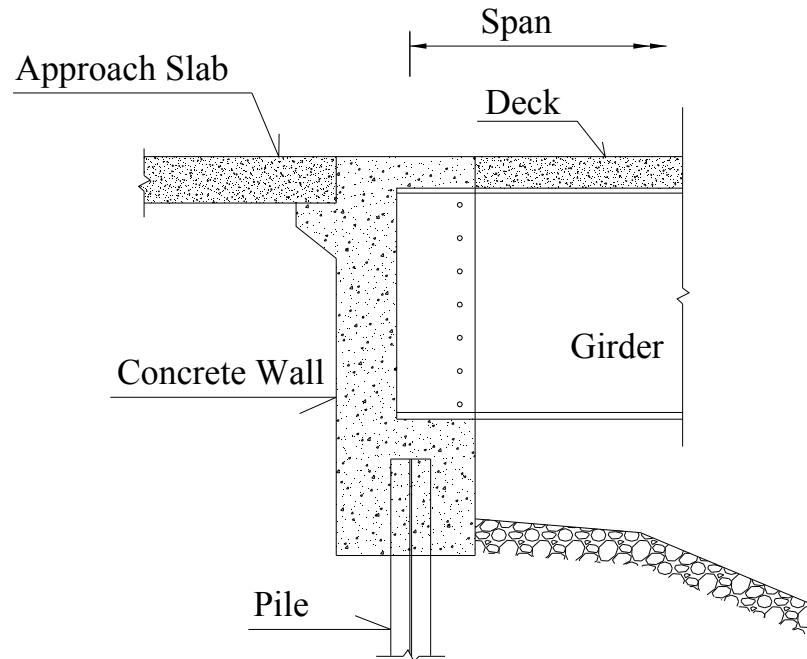


Figure 3.2-1. General Configuration of an Integral Abutment

3.3 Steel Material Modeling

The steel components of this connection include flanges and web of the girder, stiffeners, steel pile and reinforcement of the concrete elements. ASTM Grade 50 steel is assumed to be used in the girder and stiffeners. The H-piles are supposed to be of ASTM Grade 36 steel and the rebars of concrete elements are of ASTM Grade 60 steel.

The strain-stress data of steel components are obtained from standard tension tests. The results of such tests are the applied force and the strain of the specimen throughout the time span of the test. So, having the initial cross sectional area of the specimen, the resulted stress data would be based on that initial area. As for most practical engineering purposes, the strains are so small that change of area is negligible; calculating the stress based on initial area has adequate precision. The stress calculated using this method is

called “*engineering stress*”. But inspecting the ultimate resistance of a structural element using engineering strain-stress data can have a noticeable error. Strains can also have a similar problem. When the strain is evaluated based on the initial length of the specimen, named “*engineering strain*”, the result is suitable for small strain problems. But, when the problem consists of large deformations, the initial length and the length of the specimen are different so that calculating the strain based on the initial length originates some error. To compensate such errors, more exact definitions for stress and strain have been presented by researchers which can incorporate large deformation effects. To cover all the required equations in this discussion, first engineering strain and stress are defined as follows:

$$\varepsilon_{Eng} = \frac{l - l_0}{l_0} \quad \text{Eq. 3.1}$$

where l_0 and l are the initial length and the current length of the specimen. And:

$$\sigma_{Eng} = \frac{F}{A_0} \quad \text{Eq. 3.2}$$

In which F is the applied load and A_0 is the initial cross sectional area of the specimen. For true strain, the following equation can be reasonably proposed:

$$d\varepsilon_{True} = \frac{dl}{l} \quad \text{Eq. 3.3}$$

in which the increment of length is divided by the current length. Integrating over the length of the specimen results in:

$$\varepsilon_{True} = \int_{l_0}^l \frac{dl}{l} = \ln \left(\frac{l}{l_0} \right) \quad \text{Eq. 3.4}$$

This strain is also called as log-strain. Substituting the engineering strain definition into true strain definition yields a relationship between the two strains:

$$\varepsilon_{True} = \ln\left(1 + \frac{l - l_0}{l_0}\right) = \ln(1 + \varepsilon_{Eng}) \quad \text{Eq. 3.5}$$

Using the above equation, true strain can be easily calculated from the engineering strain which is the result of the tension test. The true stress is also defined using a logical equation:

$$\sigma_{True} = \frac{F}{A} \quad \text{Eq. 3.6}$$

which is the division of the current force by the current area. The problem with the true stress definition is that finding the real time area of the specimen during the tension test is not possible using the conventional tension test equipments. Therefore, despite the equation for calculating the true stress is available for engineers and designers, the evaluation of true stress is not practical. So, researchers have tried to figure out methods to estimate the true stress as precise as possible. The first recommended method to evaluate the true stress is based on assuming constant volume for the element during deformation. Using the previous equations for engineering and true strains and stresses and also assuming a constant value for the element the following formulation can be concluded for true stress:

$$\sigma_{True} = \frac{F}{A} = \frac{F}{\left(\frac{A_0 l_0}{l}\right)} = \frac{F}{A_0} \times \frac{l}{l_0} = \sigma_{Eng}(1 + \varepsilon_{Eng}) \quad \text{Eq. 3.7}$$

Using the above equation, the true stress can be easily calculated from engineering strain and stress that are results of tension test. But, the validity of this equation depends

on the validity of the constant volume assumption. Another method to find the true stress is based on the Poisson's ratio approach. If a cylindrical specimen is under tension, the area of the specimen is reduced while its length increases. If the ratio of the transverse strain to longitudinal strain is assumed to be equal to the Poisson's ratio, the current diameter of the specimen will be:

$$\begin{aligned} D &= D_o - \Delta D = D_o + \varepsilon_{transverse} D_o = D_o(1 - \nu \varepsilon_{longitudinal}) \\ &= D_o(1 - \nu \varepsilon_{Eng}) \end{aligned} \quad \text{Eq. 3.8}$$

So, the current area will be:

$$A = \frac{\pi}{4} D_o^2 (1 - \nu \varepsilon_{Eng})^2 = A_o (1 - \nu \varepsilon_{Eng})^2 \quad \text{Eq. 3.9}$$

Therefore, the true stress can be written as follows:

$$\sigma_{True} = \frac{F}{A} = \frac{F}{A_o (1 - \nu \varepsilon_{Eng})^2} = \frac{\sigma_{Eng}}{(1 - \nu \varepsilon_{Eng})^2} \quad \text{Eq. 3.10}$$

Using this equation the true stress is again evaluated as a function of engineering strain and stress. This equation is valid if the ratio of the lateral to longitudinal strains is equal to the assumed Poisson's ratio. In this case, the validity of Poisson's ratio after yielding of steel and experiencing large strains is questionable.

3.3.1 Tension Test

To have a better understanding of the state of stresses in steel materials, the strain-stress data of some actual tension tests that are conducted based the ASTM requirements are studied. The tension tests have been done on test specimens with the dimensions in

accordance to ASTM A 370. The steel material for the specimens is ASTM A709, Grade 50 which conforms to the steel material of the girders of the studied bridges.

The first step of study is to plot engineering and true strain-stress curves for the available tension test data. As there are two different definitions for the true stress, both of the formulations are plotted. Figure 3.3-1 through Figure 3.3-4 show the strain-stress curves.

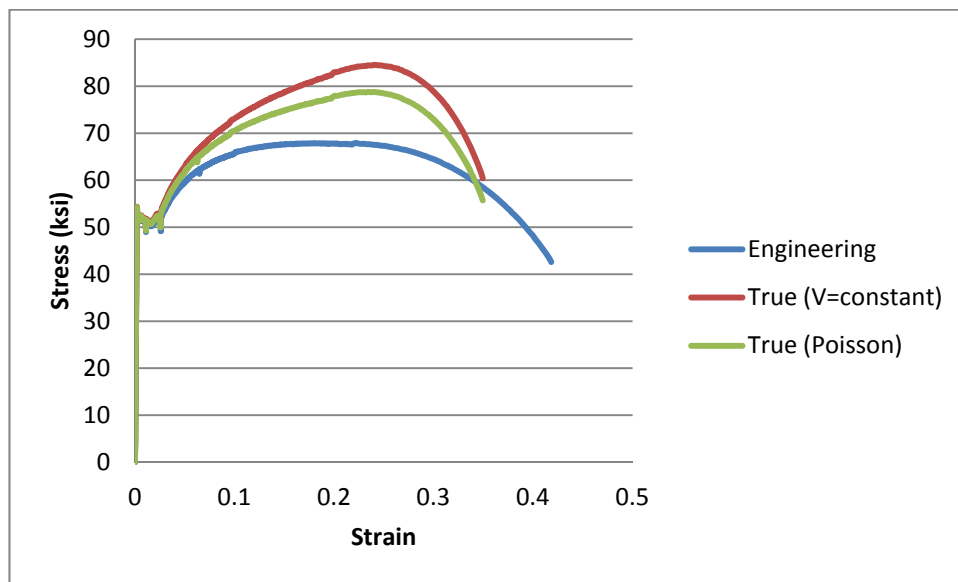


Figure 3.3-1. Strain-Stress Curves (Tension Test # 1)

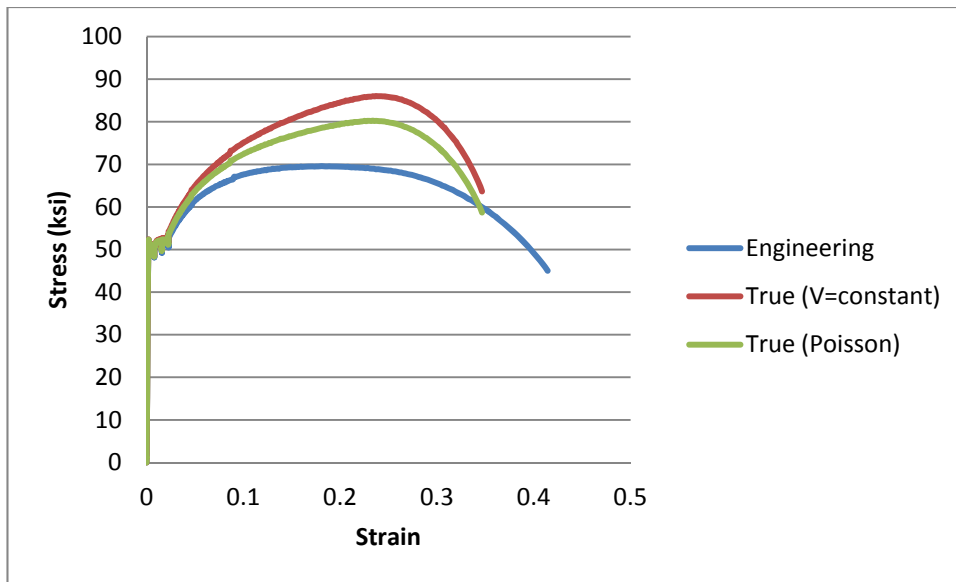


Figure 3.3-2. Strain-Stress Curves (Tension Test # 2)

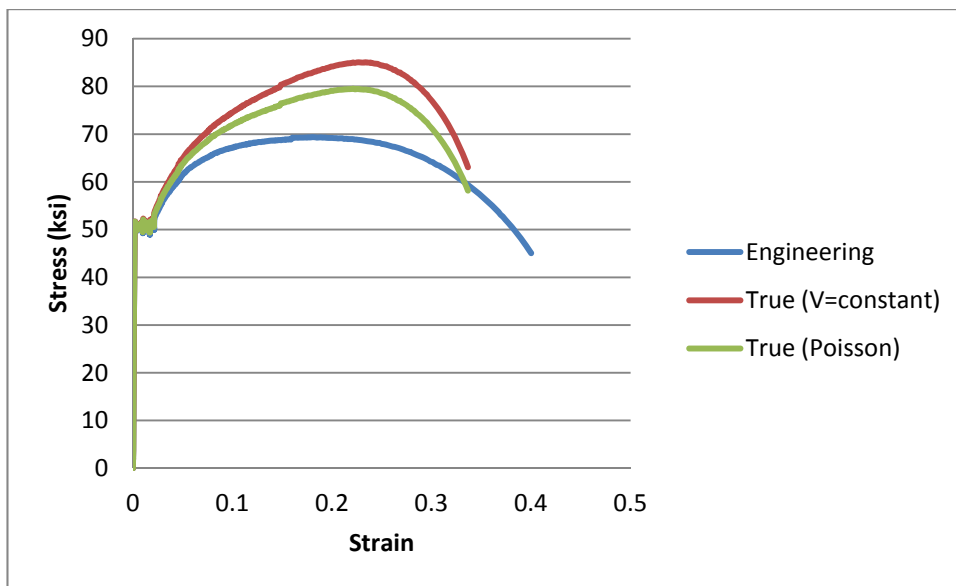


Figure 3.3-3. Strain-Stress Curves (Tension Test # 3)

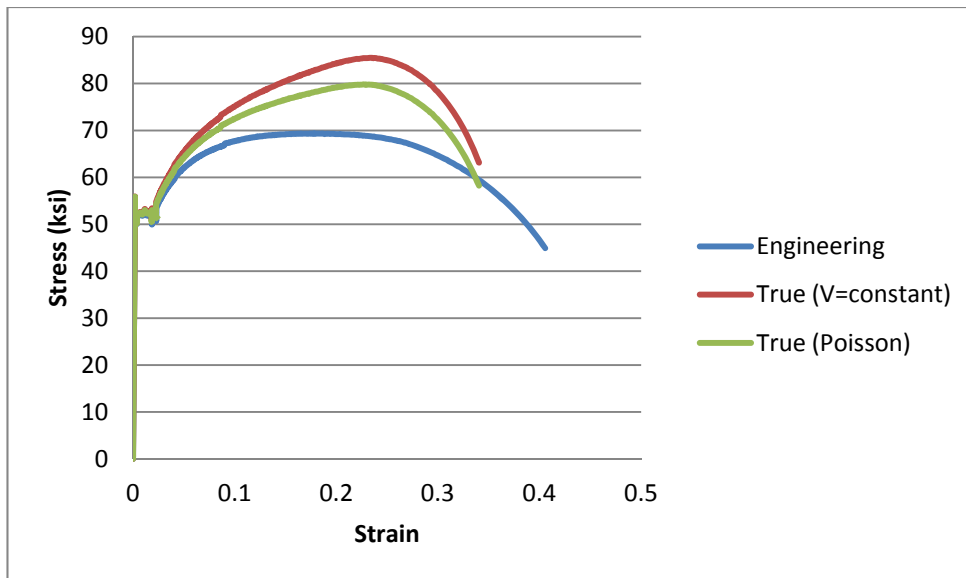


Figure 3.3-4. Strain-Stress Curves (Tension Test # 4)

As can be observed from the results of different tension tests, the equivalent true point of each point of engineering curve has smaller strain value. This is attributed to the fact that $\ln(1 + \epsilon_{Eng})$ is smaller than ϵ_{Eng} for nonzero values of strains. The other observation is that engineering definition of stress gives the smallest stress and true definition with constant volume assumption yields the largest stress among stress definitions. True stress based on legitimacy of Poisson's ratio results in stress values between the other two stress definitions. An additional fact about strain-stress curves is that all of the different approaches are approximately the same up to start of strain hardening of steel. This is a very helpful remark in the practical designs where stresses are kept below the stress plateau. The last but not the least observation from the above graphs is that the slope of true strain-stress curve at the beginning of strain hardening region is about 1.18 times of that slope in the engineering strain-stress curve. This ratio is the same for all conducted tension tests.

3.3.2 Validity of Constant Volume Assumption

Further study on these curves is initiated by looking more exactly at the failure point of the curves. As stated before, in normal tension tests, the applied force to the specimen at each moment (usually with one second intervals) is recorded, while the actual strains in the failure zone are not known. But, the cross sectional area of the specimen after break can be measured. This cross section represents the actual cross section of the specimen at the time of failure after elastic rebound of the area. Since the necked area shows a tremendously large plastic deformation, the elastic rebound of the cross section can be ignored in the calculations; however estimation of the elastic rebound is not a difficult problem. For the previously discussed tension tests, the final cross sectional area of the specimens are measured. These areas are 0.06396, 0.06558, .06710 and 0.06299 inch squared for the tests #1 through #4, respectively. Dividing the ultimate forces by these areas shows considerably different stress values at the very last moments of tension tests compared to those of true strain-stress curves. These ultimate stresses are 134.3, 141.2, 137.3 and 139.9 ksi for the tests #1 to #4, respectively. As there is not any particular assumption in calculating these stress values, it can be believed that these stresses are more exact compared to true stresses which are calculated based on some assumptions. At this point, since the true stress based on Poisson's ratio assumption gives stress values that are even less than those of the stress values based on constant volume assumption, the Poisson's ratio true stress is disregarded for the rest of the study and after this, the true stress means the stress estimated based on constant volume assumption.

Another point of interest is the point of maximum stress on the engineering strain-stress curve. As the engineering stress is obtained by simply dividing the applied force by

the initial cross sectional area, maximum stress at this point means maximum applied load. Therefore, at this point the derivative of the applied load is zero:

$$dP = 0 \quad \text{Eq. 3.11}$$

So

$$dP = d(\sigma_{True}A) = d(\sigma_{True})A + \sigma_{True}d(A) = 0 \quad \text{Eq. 3.12}$$

And therefore

$$\frac{d\sigma_{True}}{\sigma_{True}} = -\frac{dA}{A} \quad \text{Eq. 3.13}$$

On the other hand, constant volume assumption gives another expression for $\frac{dA}{A}$. As the volume is constant, its derivative is zero. So

$$dV = d(lA) = d(l)A + ld(A) = 0 \quad \text{Eq. 3.14}$$

Hence

$$-\frac{dA}{A} = \frac{dl}{l} = d\varepsilon_{True} \quad \text{Eq. 3.15}$$

The second equation in the above expression is based on Eq. 3.3 which is the definition of true strain. Thus

$$\frac{d\sigma_{True}}{\sigma_{True}} = d\varepsilon_{True} \quad \text{Eq. 3.16}$$

Or

$$\frac{d\sigma_{True}}{d\varepsilon_{True}} = \sigma_{True} \quad \text{Eq. 3.17}$$

In other words, the slope of the true strain-stress curve is equal to the value of true stress at that point. This derivation is for the point of maximum stress on the engineering

strain-stress curve. This formulation is presented by Yakel (Yakel, 2009). To verify this equation, the results of the available tension test are scrutinized. The results of tension tests show that the slope of the strain-stress curve is on average 20 percent larger than the value of true stress, at the point of maximum engineering stress.

$$\frac{d\sigma_{True}}{d\varepsilon_{True}} = 1.2\sigma_{True} \quad \text{Eq. 3.18}$$

This is another reason that the constant volume assumption is not valid for large deformations.

3.3.3 Elastic Rebound of Cross Section

In the previous section it was shown that the exact value of stress at the time of failure in tension tests is much higher than those predicted by true stress formulation based on the constant volume assumption. Those values of stress were calculated ignoring the elastic rebound of the cross section after the specimen breaks. In this section, it is tried to find the magnitude of the stresses considering the area of the specimens before the rebound.

If the dimensions of a rectangular specimen after the break at failure section are $a_{measured}$ and $b_{measured}$, the area of the cross section is $a_{measured}$ times $b_{measured}$. But the cross sectional area right before the break is smaller than that. The elastic rebound of the section can be estimated having the stress of the section at the time of the break. The elastic rebound strain for each side of the specimen is equal to the stress at the moment of break divided by the modulus of elasticity.

$$\varepsilon_{rebound} = \frac{\sigma_{just\ before\ break}}{E} \quad \text{Eq. 3.19}$$

So, the dimension of each side of the specimen just before failure is:

$$a_{just\ before\ break} = a_{measured}(1 - \varepsilon_{rebound}) \quad \text{Eq. 3.20}$$

And

$$b_{just\ before\ break} = b_{measured}(1 - \varepsilon_{rebound}) \quad \text{Eq. 3.21}$$

For circular specimens $a_{measured}$ and $b_{measured}$ are replaced by the measured diameter $d_{measured}$. Consequently, a more exact cross sectional area for the specimen at the moment of break can be obtained using the following equation:

$$A_{just\ before\ break} = a_{measured}b_{measured}(1 - \varepsilon_{rebound})^2 \quad \text{Eq. 3.22}$$

As $\varepsilon_{rebound}$ is a function of $\sigma_{just\ before\ break}$ and this stress is a function of the area just before the break, an iterative procedure can be employed to find the area at the moment of failure.

Examining the presented formulation for the available tension tests show that for tension tests #1 through #4 the first iteration results in areas equal to 0.06337, 0.06494, 0.06647 and 0.06239 inch squared, respectively. The ratios of these areas to the measured areas are 0.9907, 0.9903, 0.9905 and 0.9902. As the difference of the measured area and the calculated area of the first iteration is less than one percent, other iterations are ignored and the cross sectional area of the specimens at the time of break can be assumed to be equal to %99 of the measured area after the break. This method is used for true cross sectional area calculation for the rest of this study. Therefore the true stress at the

time of break is calculated by dividing the actual final load by %99 percent of the measured area of the section after the break.

3.3.4 Proposing a New Model for Steel Material

Based on the previous discussions on the results of tension tests, a model for the true strain-stress curve of steel material is presented in this section. The model assumes that the engineering strain-stress data are available for the material under study. The purpose is to define the true strain-stress curve. The model is described in the following steps. The key points are designated in Figure 3.3-5:

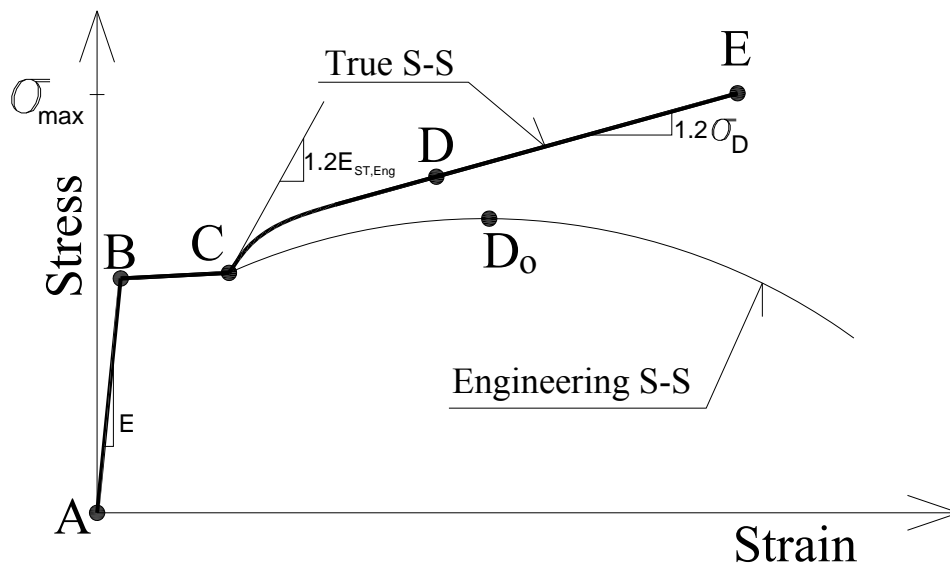


Figure 3.3-5. Designation of the Key Points on the Strain-Stress Curves

Step 1- For the points on the elastic region and yielding plateau, it is assumed that the constant volume assumption is valid and the values of true strain and true stress are obtained by Eq. 3.5 and Eq. 3.7. Therefore points A, B and C are known.

Step 2- The slope of true strain-stress curve at the beginning of strain hardening region is assumed to be 1.18 (or approximately 1.2) times of that slope for engineering strain-stress curve (as presented in Section 3.3.1).

Step 3- Point D is the corresponding true strain-true stress point for the point of maximum stress on the engineering strain-stress curve based on constant volume assumption (using Eq. 3.5 and Eq. 3.7).

Step 4- The slope of the true strain-stress curve at point D is equal to 1.2 times of the value of true stress at that point (As discussed in section 3.3.2).

Step 5- A smooth curve is fitted between points C and D knowing the coordinates of these points and the slope of the curve at these points. The curve fitting technique is offered in the next section.

Step 6- A line is extended beyond point D with the same slope as the slope of the curve at point D and terminated at point E with a stress level equal to the maximum true stress at the moment of break. As discussed in Section 3.3.3, this stress is equal to the applied load at the time of break divided by 99% of the cross sectional area after the break.

3.3.5 Curve Fitting

In the material model proposed in the previous section, a curve was needed to fit between points C and D. There are some requirements for the curve. The first one is the smoothness of the curve. Rough changes are not seen in the engineering strain-stress curve. So, a function having rough variations is not expected for the true strain-stress curve in this region. The other necessity is that the function is concave between these two

points. As there are four known parameters for the function, a first guess would be a cubic polynomial. Other researchers have suggested a more complicated function that satisfies all the requirements (Yakel, 2009). To be in harmony with the previously proposed models, a function like theirs is used in the present study. A simplifying trick is to shift the origin of the coordinate axes to the beginning point of strain hardening region and to define two new coordinate axes like $\xi = \varepsilon - \varepsilon_{St.H}$ and $\eta = \sigma - \sigma_{St.H}$, where $\varepsilon_{St.H}$ and $\sigma_{St.H}$ are the true strain and true stress at the start of strain hardening region. The function and its first derivative are as follows:

$$\psi = \xi[S_{asympt.} + \frac{S_i - S_{asympt.}}{[1 + (c\xi)^d]^{\frac{1}{d}}}] \quad \text{Eq. 3.23}$$

And

$$\psi' = S_{asympt.} + \frac{S_i - S_{asympt.}}{[1 + (c\xi)^d]^{\frac{d+1}{d}}} \quad \text{Eq. 3.24}$$

The function is plotted schematically in Figure 3.3-6. In this function, S_i is the initial slope, $S_{asympt.}$ is the asymptotic slope, c is the reciprocal of the ξ value at the intersection of the tangents and d is the smoothing exponent.

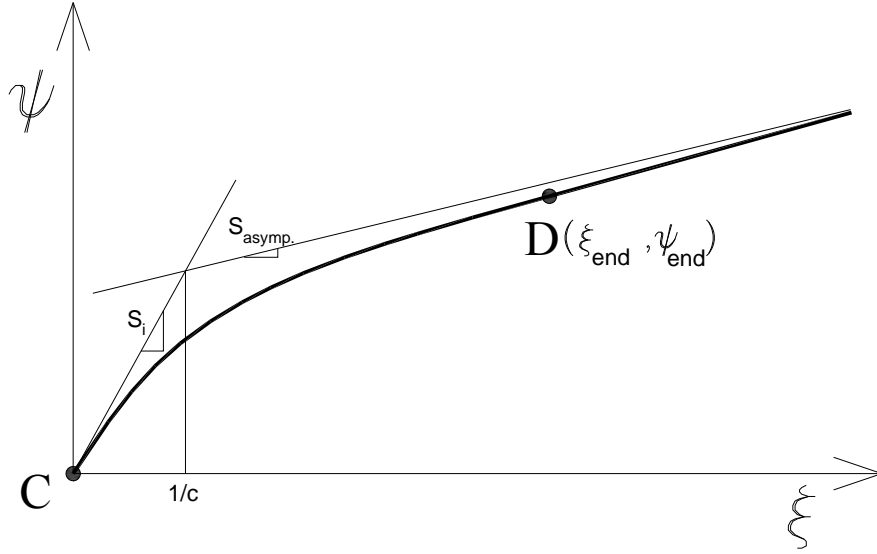


Figure 3.3-6. Scheme of Fitted Curve Between Points C and D

As there are four known values (the coordinates and the slopes at the two ends of the curve) and four unknown values of S_i , $S_{asympt.}$, c and d , it seems that four equations can be written to find the four unknown value. But, coordinates of the first end (0,0) is a trivial solution for Eq. 3.23, independent of the four unknown values. Therefore, there is one extra unknown value in this problem and assuming a value for one of them results in a solution for the other three. Plotting different curves for different values of the involved parameters shows that if the smoothing exponent is between 1 and 3, the curve fits the best as what is expected for this transition function. If the exponent is less than 1, the curve looks like a line and if it is larger than 3, the curve tends to the tangents of the two ends. So, a value between 1 and 3 is chosen for that. Let's take d equal to 2.

Among the other unknown parameters, S_i is the easiest to find. If $\xi = 0$ is plugged into Eq. 3.24, then $\psi' = S_i$ which shows S_i is simply equal to the known slope of the first end.

Now, there are two unknown parameters $S_{asympt.}$ and c and two known values which are the coordinates and slope of the end point. Plugging the coordinates of end point into Eq. 3.23 and back-calculating c yields:

$$c = \left[\left(\frac{S_i - S_{asympt.}}{\frac{\psi_{end} - S_{asympt.}}{\xi_{end}}} \right)^d - 1 \right]^{\frac{1}{d}} / \xi_{end} \quad \text{Eq. 3.25}$$

Simultaneous numerical solution of the Eq. 3.24 and Eq. 3.25, so that the slope at the end is equal to the known value of slope, yields the values of $S_{asympt.}$ and c . Figure 3.3-7 shows the curve for a smoothing exponent value of 2, an initial slope of $S_i = 444 \text{ ksi}$, a final coordinates of $(\xi, \psi) = (0.1435, 27.98 \text{ ksi})$ and an end slope of 98.2 ksi . The resulted values for $S_{asympt.}$ and c are 88.71 ksi and 22.24 , respectively. Note that the end slope and asymptotic slope are not the same.

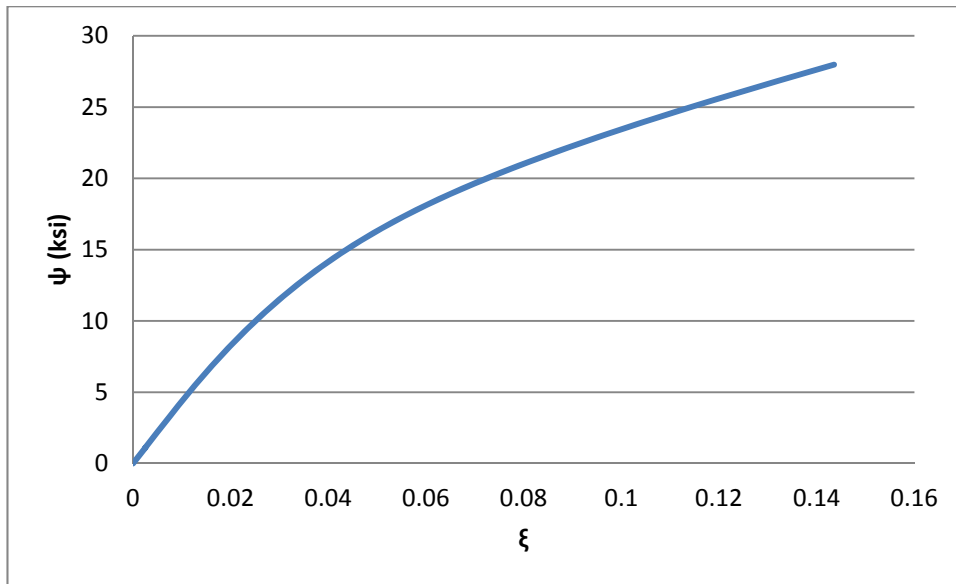


Figure 3.3-7. Fitted Curve Between Points C and D

3.3.6 A Sample Model: Grade 50 Steel

The result of all of the modeling steps for a Grade 50 steel is shown in Figure 3.3-8. In this model, the curve is linear up to a stress of 50 ksi with a slope of 29000 ksi. The strain at this point is 0.00172. After that, it has a plateau up to a strain of 0.0227. Note that the slope of plateau is not a real zero. Then, on the transition curve, it goes to a strain of 0.1663 with a stress of 82.18 ksi. After the transition, it goes up linearly to a stress level of about 141 ksi with a corresponding true strain of 0.767. Other steel materials are also modeled using the same approach.

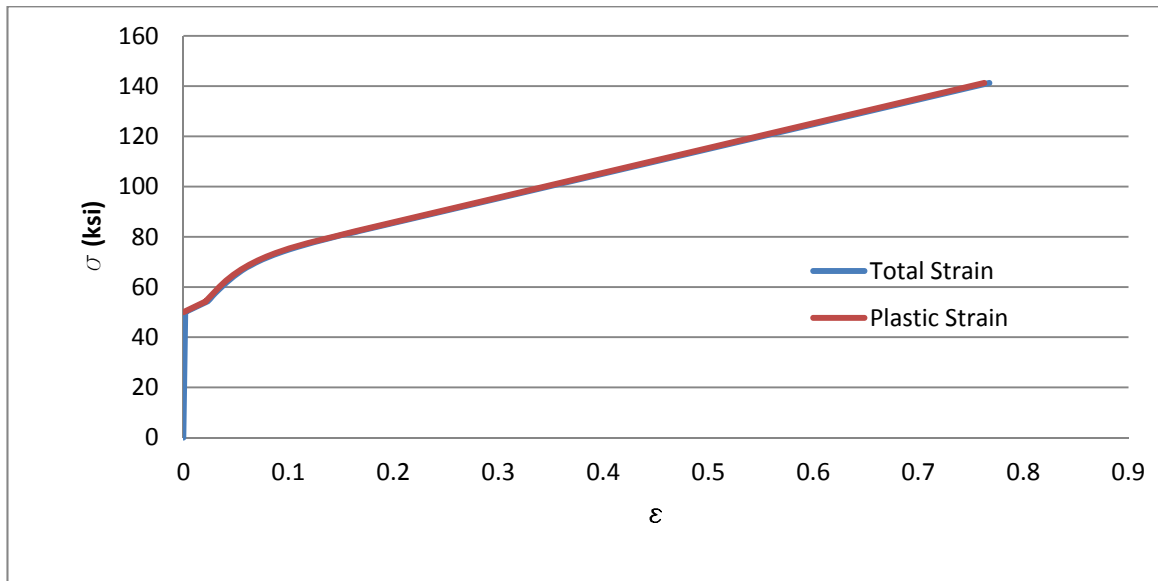


Figure 3.3-8. Material Model for Grade 50 Steel

3.4 Concrete Material Modeling

In this section, the behavior of concrete under loading is studied. Concrete shows a very complex response when imposed to different loading conditions. There are several factors that affect the response of concrete members. Concrete has totally different

behaviors under compression and tension. Multi-axial load application is also a decisive parameter. When concrete is confined by lateral compressive force, it can carry considerably higher axial load. To study the material properties of concrete, first the response of concrete under compressive forces is explained. Then the existing models to predict the strain-stress properties of concrete specimens under compression are given. Then, selecting one of the models, it is tried to illustrate how the model is perceived in the finite element program, Abaqus. This program has some different methods to model nonlinear strain-stress response of materials among which the most applicable one for concrete behavior is detailed. The same steps are taken for tensile behavior of concrete. For this purpose, first concrete response under tension is explained. Then, one of the existing models for estimating the strain-stress curve of concrete under tension is elucidated. And at the end, the technique of Abaqus to model the tensile behavior of concrete is elaborated.

3.4.1 Concrete Response under Compression

When a concrete member is under compressive force, it demonstrates a nonlinear strain-stress curve. In the first stages of loading, concrete stress goes up with an approximately linear trend as the strain increases. But under greater loads, the rate of stress increase reduces so that it reaches a maximum point. After that, the concrete stress decreases as the displacement increases. At the final point, the concrete crushes due to application of the ultimate compressive force. This behavior is not the same under different conditions. When the rate of load application changes or multi-axial load is applied to the concrete member, different strain-stress curves are resulted. The other fact

is that concretes of different strength show different crushing strains. Figure 3.4-1 shows the strain-stress curves for some concrete specimens of different compressive strength.

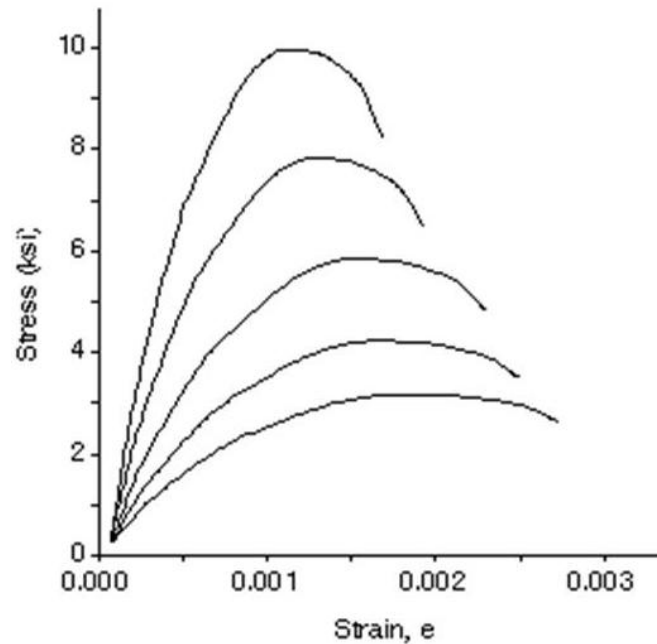


Figure 3.4-1. Strain-Stress Curves of Concrete Specimens of Different Strength

It can be observed that the compressive stress is a nonlinear function of strain. Also, the crushing strain decreases as the maximum stress increases. Finding the affecting parameters and their nonlinear relation to the compressive strength is a complex task which has been studied by several researchers. The next subsection discusses some their works.

3.4.2 Concrete Compression Response Models

Several researchers have investigated the response of concrete in compression. The result of their research has been to propose models for the strain-stress curve of concrete. In this section, first these models are described and then a comparison of the models is presented.

A) Hognestad Model

Hognestad (1951) proposed a model for the response of concrete under compression. This model describes the stress of concrete at each strain level as a function of the maximum compressive strength, f'_c , and the modulus of elasticity of concrete.

$$\sigma = f'_c \left[\frac{2\varepsilon}{\varepsilon_o} - \left(\frac{\varepsilon}{\varepsilon_o} \right)^2 \right] \quad \text{for } 0 \leq \varepsilon \leq \varepsilon_o \quad \text{Eq. 3.26}$$

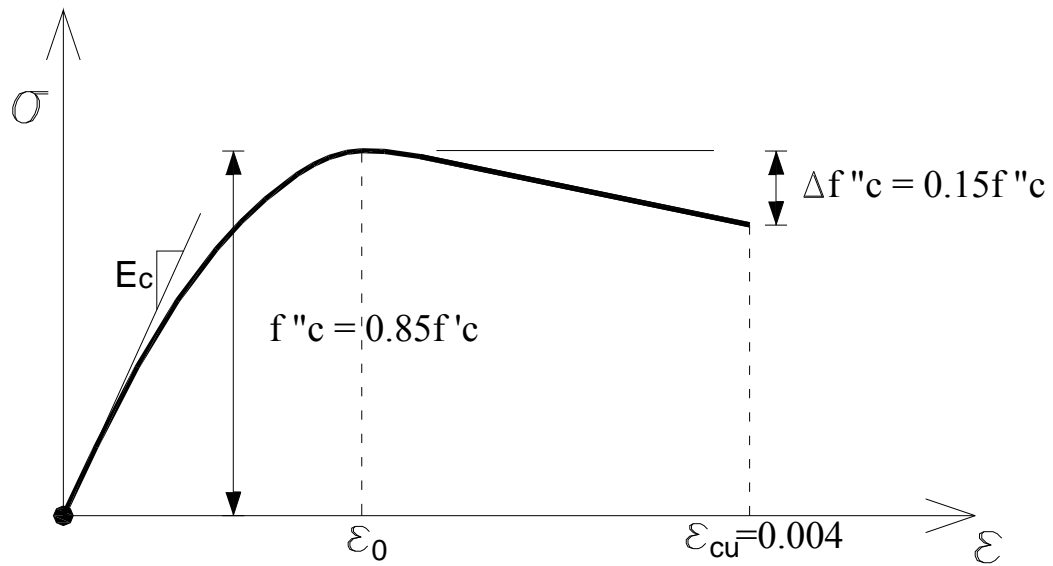


Figure 3.4-2. Hognestad Model for Strain-Stress of Concrete in Compression

And

$$\sigma = f'_c \left[1 - \frac{0.15(\varepsilon - \varepsilon_o)}{0.004 - \varepsilon_o} \right] \quad \text{for } \varepsilon_o < \varepsilon \quad \text{Eq. 3.27}$$

In which

$$\varepsilon_o = \frac{2f'_c}{E} \quad \text{Eq. 3.28}$$

B) Polynomial Model

This model describes the compressive stress of concrete as a polynomial function of its strain. To find the constants of the polynomial functions, it is required to have some assumptions. In the model, it is assumed that the maximum stress of the concrete takes place at a strain equal to 0.002 and the failure occurs at the strain of 0.003. The other assumption is on the failure stress level. In the current model it is assumed that failure stress is 60 percent of the maximum stress. Implementing the above-mentioned assumptions to a cubic polynomial, the following equation is resulted for the strain-stress of the concrete.

$$\sigma = -5 \times 10^7 f'_c \varepsilon^3 - 5 \times 10^4 f'_c \varepsilon^2 + 800 f'_c \varepsilon \quad \text{Eq. 3.29}$$

In which σ is the concrete stress and f'_c is the maximum compressive strength both in ksi.

C) Carreira and Chu Model

Carreira and Chu (1985) proposed a curve for the strain-stress relation of concrete which is composed of two parts. The first part is a line that is valid for stresses up to 30 percent of the maximum strength of the concrete. Beyond that point, a curve is suggested that predicts the stress of concrete up to crushing strain. That curve is defined as follows.

$$\sigma = \frac{f'_c \beta \left(\frac{\varepsilon}{\varepsilon_c}\right)}{\beta - 1 + \left(\frac{\varepsilon}{\varepsilon_c}\right)^\beta} \quad \text{Eq. 3.30}$$

In which ε'_c is the strain of concrete at the maximum stress of f'_c in MPA.

$$\beta = \left(\frac{f'_c}{32.4}\right)^3 + 1.55 \quad \text{Eq. 3.31}$$

In this model, ϵ'_c can be assumed to be equal to 0.002 and the crushing strain to be equal to 0.003.

D) Comparison of Different Models

In this section, different models proposed for concrete compressive behavior are compared to each other. For this purpose, the models are plotted for a concrete with compressive strength of 4 ksi. The strain corresponding to this maximum stress is assumed to be 0.002. The crushing strain is assumed to be 0.003. Figure 3.4-3 shows the strain-stress curves predicted by different models.

As can be seen, up to the point of maximum stress, the Hognestad model and Polynomial model are almost the same, while the model proposed by Carreira and Chu predicts higher stresses. Beyond that point, Hognestad Model and Carreira and Chu model have approximately the same stresses and the polynomial model drops the stresses down to 60 percent of the maximum stress which was imposed to that model as an assumption. Comparing this graph to Figure 3.4-1 shows that the stresses at the time of failure are close to 80 percent of the maximum stress which is between the stress values predicted by the polynomial model and the other two models. In the present study, the model proposed by Carreira and Chu is used in the finite element models.

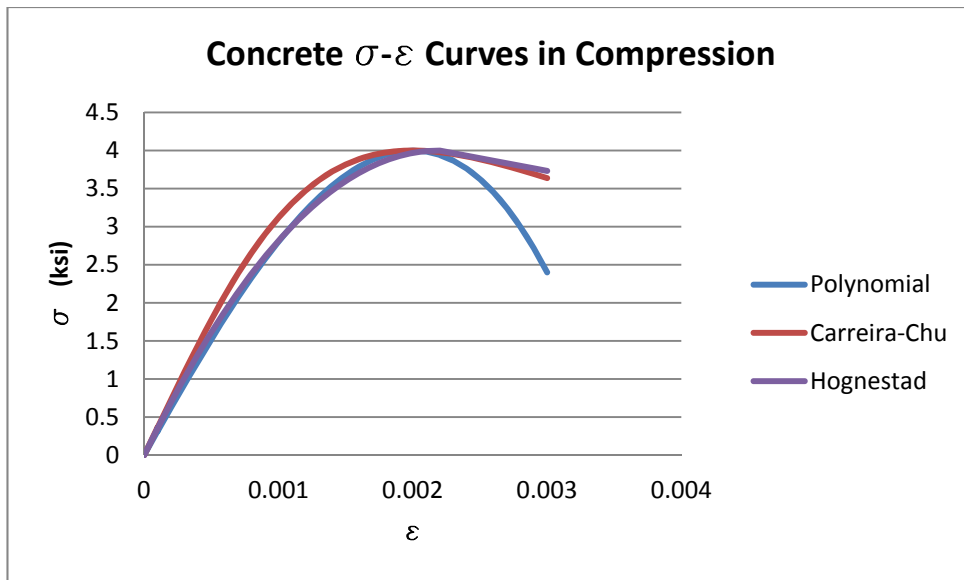


Figure 3.4-3. Strain-Stress Curves of Concrete in Compression in Different Models

3.4.3 Concrete Response under Tension

The behavior of concrete in tension is much more complicated than its behavior in compression. When tensile strains are introduced in a concrete element, the stress starts to be proportional to the magnitude of strain. For very small strains, the stress is proportional to the strain, almost similar to the response under compression. But this similarity is just for the early stages of loading. As the strain increases, complexities of tensile behavior start to show up. The reason for that is formation of micro-cracks in the body of the element in the tensile zone. The micro-cracks can unite to develop a macro-crack which grows in the process of crack propagation. If the strain and average stress are recorded during this process, it is observed that as the strain increases the average stress over the tensile element decreases. The pattern for this reduction has been the subject of study for several researchers who have recommended different models for the tension stiffening regime of concrete behavior. More difficulty comes to existence when it is tried

to express stress tensor in terms of strain tensor of at a point. Results of the studies show that for such a material the stress tensor is not just a function of the strain tensor of that point. But also, a strain field should be considered for the neighborhood of each point of the element. The next subsection presents some of the existing models for the tensile response of concrete.

3.4.4 Concrete Tension Response Models

Several researchers have studied the behavior of concrete in tension. Figure 3.4-4 shows the strain-stress curves which are proposed by some of the researchers. As can be seen, linear, bi-linear and nonlinear descriptions are the recommendation of different researchers for the tension stiffening part of concrete strain-stress curve. Bazant has proposed a line for the tension stiffening part of the curve. Gylltoft has suggested the stress as a bilinear function of the strain while some others like Scanlon, Mazars and Lin & Scordelis have recommended curvilinear functions for that region of the response.

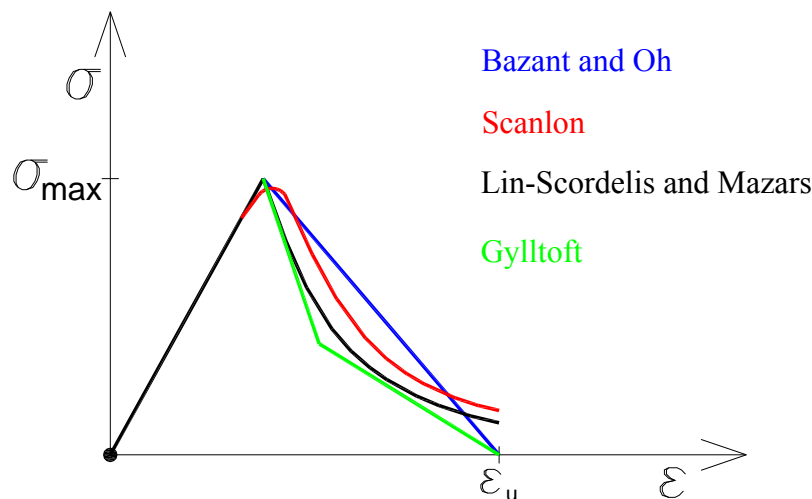


Figure 3.4-4. Strain-Stress Curves of Concrete in Tension in Different Models

In this section, one of the existing models for predicting the post-cracking response of concrete in tension is studied in more details. This method is recommended by Barros et al. and is developed to consider both linear and exponential functions for the tension stiffening of behavior of concrete (Barros, Martins, & Ferreira, 2001). That's why the formulations are given for both functions simultaneously. The assumed linear and exponential functions for strain-stress curve are as follows:

$$\sigma = \frac{f_t E}{f_t - E \varepsilon_{tu}} (\varepsilon - \varepsilon_{tu}) \quad \text{Linear Function} \quad \text{Eq. 3.32}$$

And

$$\sigma = f_t e^{-b(\varepsilon - \frac{f_t}{E})} \quad \text{Exponential Function} \quad \text{Eq. 3.33}$$

In which f_t is the initial cracking stress, E is modulus of elasticity of undamaged concrete, ε_{tu} is the ultimate strain in tension and b is the calibration coefficient for the exponential curve. If the above stress functions are plotted against strain, the schematic shapes of Figure 3.4-5 are obtained. The unknown values ε_{tu} and b are found as follows.

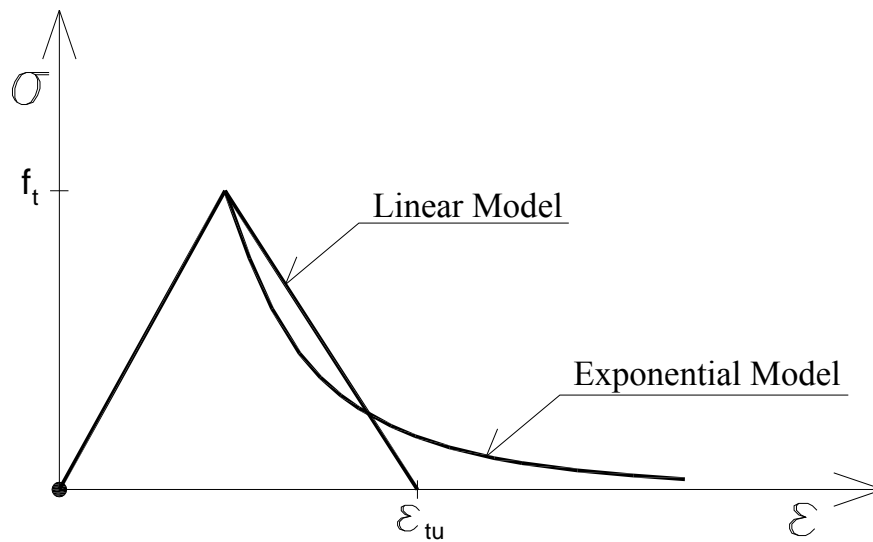


Figure 3.4-5. Schematic Strain-Stress Curve of Concrete in Tension

The area under the curves for these two functions will be equal to:

$$S = \frac{f_t}{2} \varepsilon_{tu} \quad \text{for Linear Function} \quad \text{Eq. 3.34}$$

And

$$S = \frac{f_t^2}{2E} + \int_{\frac{f_t}{E}}^{\infty} f_t e^{-b(\varepsilon - \frac{f_t}{E})} d\varepsilon = \frac{f_t^2}{2E} + \frac{f_t}{b} \quad \text{for Exponential Function} \quad \text{Eq. 3.35}$$

On the other hand, the total area of the strain-stress curve is equal to the deformation energy per unit volume, G_f . From the definitions of Fracture Mechanics, one can obtain the crack propagation energy per unit area of the crack as:

$$G_F = w \cdot G_f \quad \text{Eq. 3.36}$$

in which w is the width of the damaged region. As G_F is a material property which can be found for the customary materials in the fracture mechanics references, the area under the strain-stress curve can be set equal to the known value of G_F/w .

Ozblot and Bazant recommend that the width of the damaged region is proportional to the maximum aggregate size, which is a known parameter for any kind of concrete used in the construction industry (Ozblot & Bazant, 1996). So, w can be assumed as a known parameter as:

$$w = \alpha \cdot D_{agg}^{max} \quad \text{Eq. 3.37}$$

where α is a factor changing between 3 and 8 and D_{agg}^{max} is the maximum aggregate size.

As w and G_F are known, the area under the strain-stress curve can be set equal to the ratio of G_F/w to find the unknowns of each of the two linear or exponential approaches.

For the linear function the unknown ε_{tu} will be found as follows:

$$S = \frac{f_t}{2} \varepsilon_{tu} = G_F/w \quad \text{Eq. 3.38}$$

So

$$\varepsilon_{tu} = \frac{2G_F}{wf_t} \quad \text{Eq. 3.39}$$

And for the exponential function the parameter b will be calculated as follows:

$$S = \frac{f_t^2}{2E} + \frac{f_t}{b} = \frac{G_F}{w} \quad \text{Eq. 3.40}$$

Therefore

$$b = \frac{2wEf_t}{2EG_F - wf_t^2} \quad \text{Eq. 3.41}$$

Hence, the tension stiffening part of the strain-stress curve for concrete will be:

$$\sigma = \frac{f_tE}{f_t - \frac{2EG_F}{wf_t}} \left(\varepsilon - \frac{2G_F}{wf_t} \right) \quad \text{Linear Function} \quad \text{Eq. 3.42}$$

And

$$\sigma = f_t e^{-\left(\frac{2wEf_t}{2EG_F - wf_t^2}\right)\left(\varepsilon - \frac{f_t}{E}\right)} \quad \text{Exponential Function} \quad \text{Eq. 3.43}$$

In practical cases, the strain cannot go to infinity, while in the exponential function there is no limit for the strain. Therefore, to find an upper bound for the strain in the exponential model, the area under the curve at the maximum practical strain is set equal to 98 percent of the total area under the curve. This equality results in a strain of $\frac{4G_F}{wf_t}$ as

the maximum practical strain. So for the exponential function the range of applicability is as follows:

$$\frac{f_t}{E} \leq \varepsilon \leq \frac{4G_F}{wf_t} \quad \text{Eq. 3.44}$$

3.4.5 Concrete Response Modeling in Abaqus

To study the integral abutment connections, the finite element program Abaqus is used. The program has several capabilities, making the user able to model complex structural systems. Regarding the concrete nonlinear structural properties, two major methods are available in the program. One of them is smeared crack modeling and the other one is concrete damaged plasticity. In the present study, concrete damaged plasticity is employed as the method of analyzing the problem. The accuracy of this approach to model the behavior of reinforced concrete has been verified by many researchers in the past years.

Concrete damaged plasticity can incorporate two types of concrete failure in the model: crushing under compressive stresses and cracking under tensile stresses. Crushing and cracking are detected when certain criteria reach yield surfaces. The yield surfaces are defined by compressive and tensile equivalent plastic strains as the hardening parameters. In the coming discussion, these two parameters are shown by ε_c^{pl} and ε_t^{pl} . Figure 3.4-6 illustrates the strain-stress curves of concrete in tension and compression. It is observed that as the strain increases, the tensile stress increases linearly up to a maximum tensile stress of σ_{t0} . Beyond this point, the tension softening starts which results in reduction of stress for any increment of strain so that in very large strains the

stress of concrete tends to zero. In compression the response is different. In the beginning, the stress has a linear relationship with strain up to reaching the stress of σ_{c0} . After that, stress goes up as the strain increases in a nonlinear manner. This trend is seen up to a maximum compressive capacity of σ_{cu} . Beyond this maximum point, the strain softening part of the curve starts which results in lower stresses for larger strains. This response continues so that for very large strains, the compressive stress of concrete goes to zero.

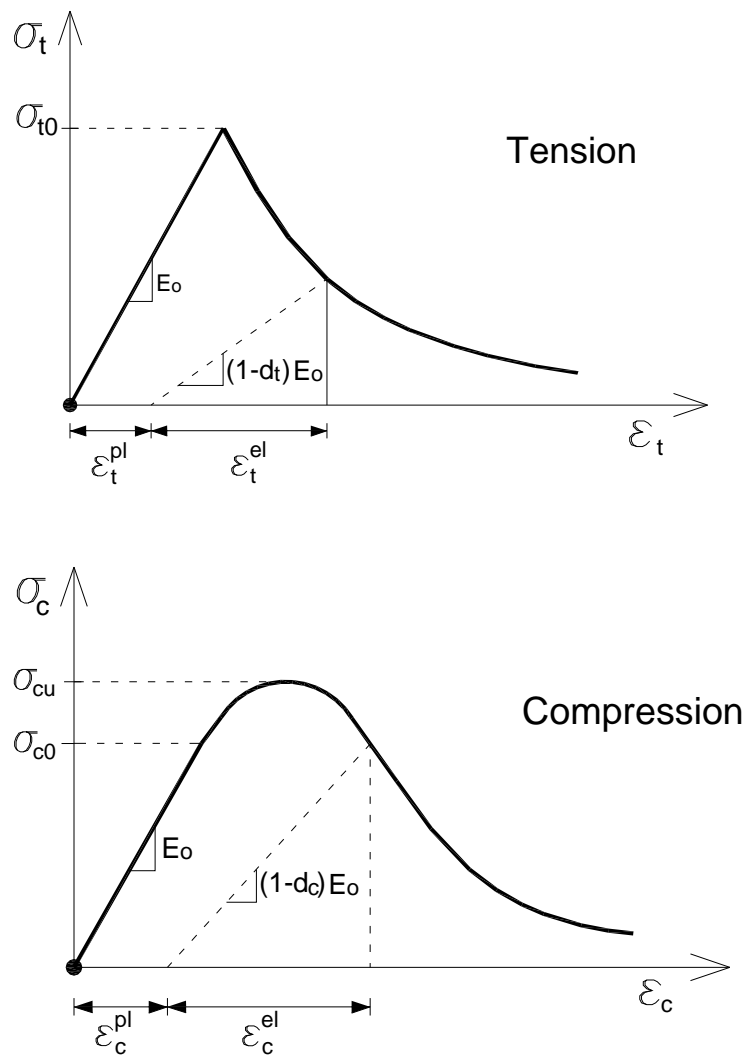


Figure 3.4-6. Strain-Stress Curves of Concrete in Tension and Compression

Concrete damaged plasticity is supposed to model damage in concrete in compression and tension. This is considered in this approach by decreasing the stiffness of concrete when strain softening starts in compression or tension. This is implemented in the model by means of damage parameters in compression and tension designated by d_c and d_t , respectively. These parameters reduce the modulus of elasticity of concrete and can be between zero and one. Values of damage parameter close to zero represent early stages of softening and values closed to one correspond to very low stiffness which is seen at large strains. Values of these parameters very close to one can lead to structural and so numerical instabilities in the problem.

The problem of concrete damage is more complex when dealing with cyclic loads. In this case, some cracks are initiated when the material is under tension. Then, compression in the next cycles of loading may result in closure of some of the cracks. Therefore, some part of the lost stiffness of the concrete may be reinstated. This complicated behavior is modeled by recovery parameters in compression or tension.

Another difficult situation occurs when concrete is under multi-axial state of stress. In this case, Abaqus makes use failure surfaces instead of failure curves. Figure 3.4-7 shows a section of the failure surface for the case of biaxial loading. In this picture the points of failure corresponding to uniaxial compression, uniaxial tension, biaxial compression and biaxial tension are demonstrated.

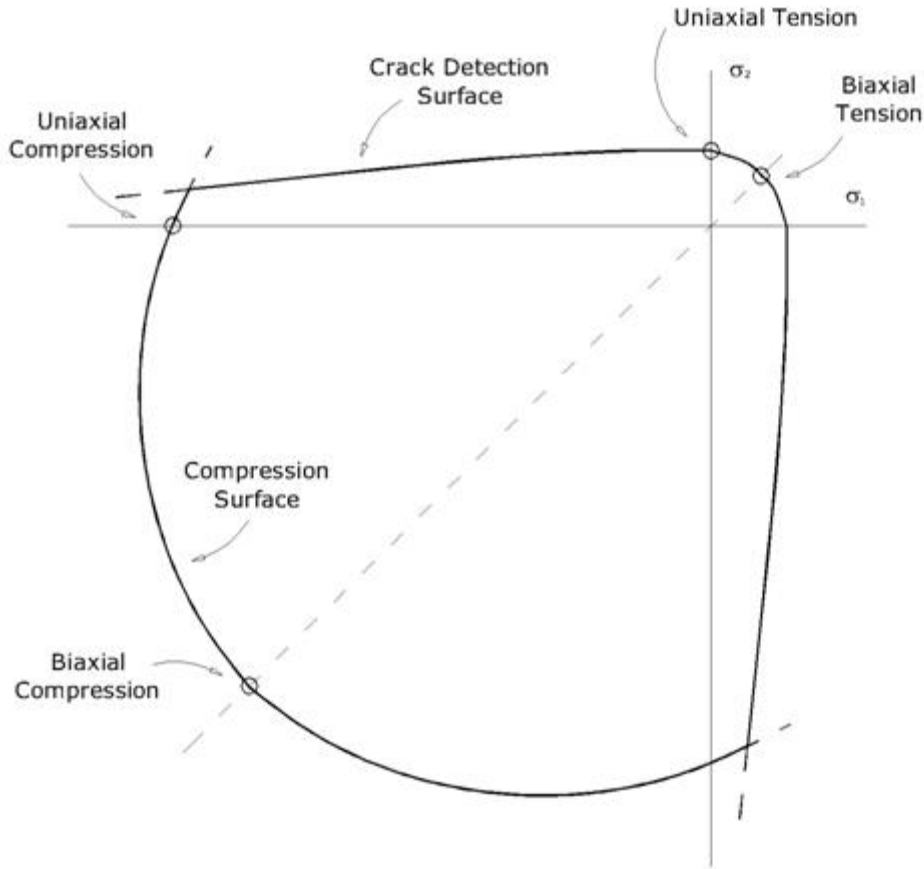


Figure 3.4-7. Biaxial Failure Surface of Concrete

In concrete damaged plasticity model, the behavior of concrete under compression is idealized by defining the inelastic strain of concrete. This strain is equal to the total strain minus the elastic strain assuming an undamaged modulus of elasticity for concrete.

$$\varepsilon_c^{in} = \varepsilon_c - \varepsilon_{oc}^{el} \quad \text{Eq. 3.45}$$

In which

$$\varepsilon_{oc}^{el} = \frac{\sigma_c}{E_0} \quad \text{Eq. 3.46}$$

Figure 3.4-8 shows the definition of compressive inelastic strain based on the above equation. Also elastic and plastic strains are illustrated in the picture, to clearly show the difference of inelastic strain and plastic strain.

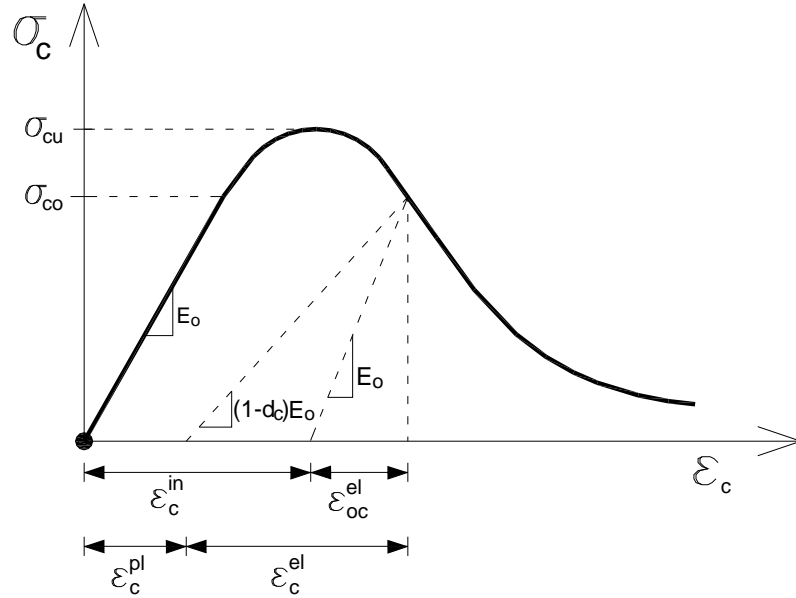


Figure 3.4-8. Definition of Compressive Inelastic strain Used for Definition of Compression Hardening Data (Abaqus Documentation)

The same approach is used for tension stiffening part of the strain-stress response of concrete. The input data of Abaqus are post-cracking stress and also cracking strain for an element in tension. The cracking strain is defined as the total tensile strain minus the elastic strain assuming undamaged modulus of elasticity for concrete. Therefore:

$$\varepsilon_c^{ck} = \varepsilon_t - \varepsilon_{ot}^{el} \quad \text{Eq. 3.47}$$

In which

$$\varepsilon_{ot}^{el} = \frac{\sigma_t}{E_0} \quad \text{Eq. 3.48}$$

Figure 3.4-9 illustrates the cracking strain based on using undamaged modulus of elasticity to obtain it from total strain. To distinguish the difference of cracking strain and plastic strain, both of them are shown in the picture. As can be seen, plastic strain is calculated using the reduced modulus of elasticity of the damaged material. An initial guess for the tension stiffening part of the curve which is recommended in Abaqus Documentation is a line originating from a strain of $10E-4$ for a stress of σ_{t0} and ending to a point of zero stress for a strain of $10E-3$. Other more accurate models for tension stiffening can be found in the literature.

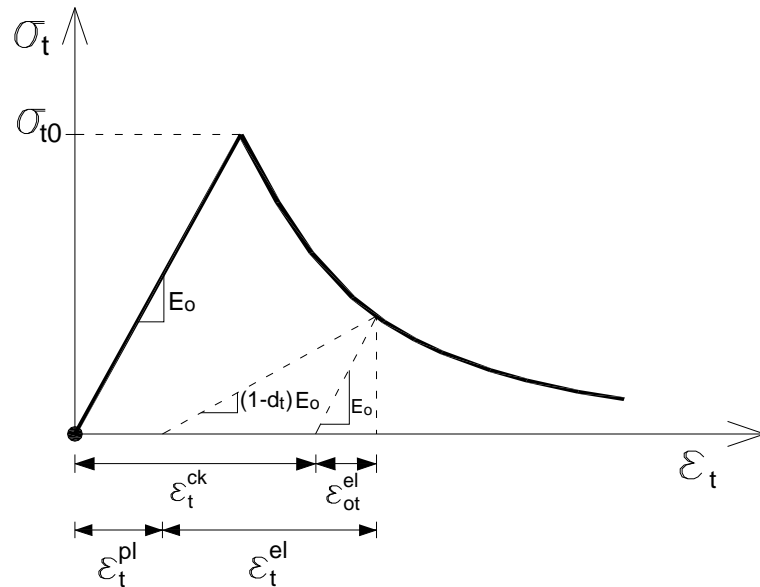


Figure 3.4-9. Definition of Tensile Cracking Strain used for Definition of Tension Stiffening Data

3.4.6 Employed Concrete Models

Based on the previous discussions on the behavior of concrete elements in compression and tension, the following models are developed for a 4ksi concrete which is used in the finite element analyses. Figure 3.4-10 shows the total strain and also the

inelastic strain of concrete in compression versus stress, which is based on Carreira and Chu model. As can be observed, there are no inelastic behavior up to the stress of 1.2 ksi.

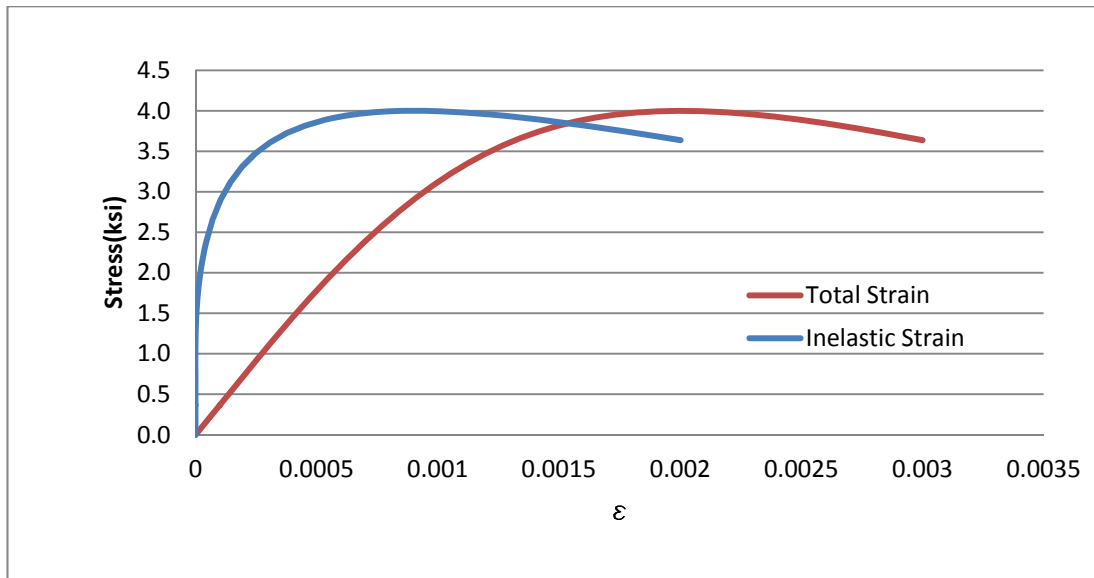


Figure 3.4-10. Total and Inelastic Strain vs. Stress for 4 ksi Concrete in Compression

Figure 3.4-11 depicts the total and cracking strain of the concrete material versus its tensile stress. The employed model in tension is an exponential one. It shows that the concrete material does not have an inelastic response up to reaching a tensile stress level of about 0.5 ksi. Then, it starts to develop cracks which results in steep drop of its tensile strength.

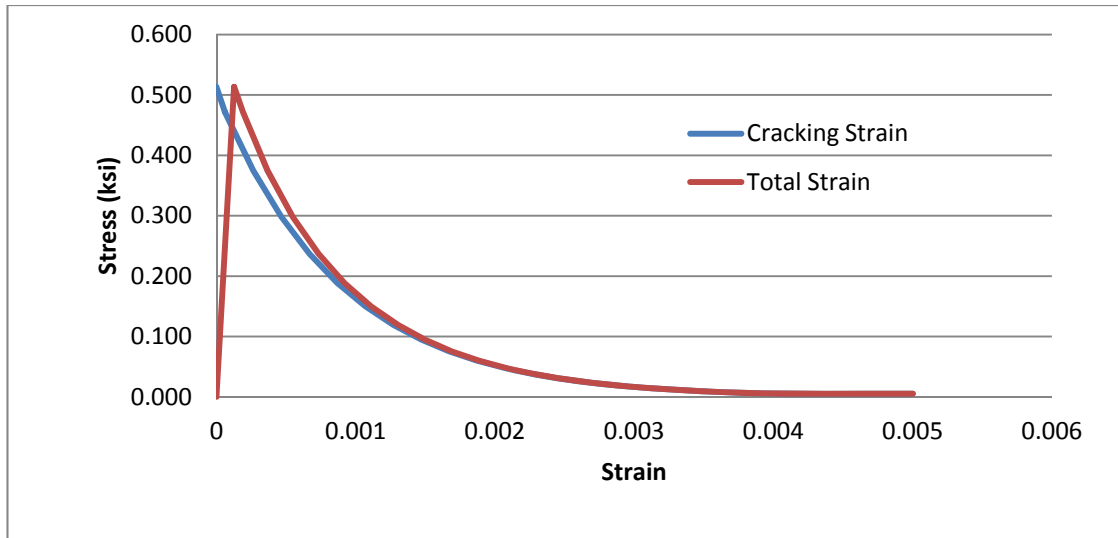


Figure 3.4-11. Total and Cracking Strain vs. Stress for 4 ksi Concrete in Tension

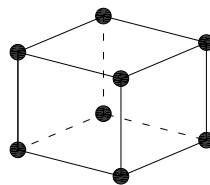
3.5 Elements

In this section, a brief explanation on the elements that are used in the finite element modeling is presented. The descriptions are based on Abaqus 6.9 HTML Documentation. For more details one can refer to the Abaqus Documentation.

3.5.1 C3D8(R)

C3D8 is an 8-node linear brick element. C3D8R is an 8-node linear brick element with reduced integration and hourglass control. These elements have three degrees of freedom at each node which are translations in x, y and z directions. Figure 3.5-1 shows a picture of these elements. The extension R stands for reduced integration. Reduced integration means an integration scheme which is one order less than the full integration scheme which is used for integration of internal forces and stiffness of the element. Reduced integration reduces the constraints introduced by an element when the continuum theory being modeled has some sort of internal constraints, like incompressibility or the

Kirchhoff transverse shear constraints when solid elements are used in order to analyze a bending problem. In these applications, full integration leads to locking which means resulting in a response that is orders of magnitude too stiff, so that the results are totally unusable. In such cases, reduced integration will often work well. In contrast, if there is no R in the element name, it is fully integrated. It means the Gauss scheme chosen will integrate the stiffness matrix of the elements with uniform material behavior exactly if the Jacobian of the mapping from the isoparametric coordinates to the physical coordinates is constant throughout the element. The meaning of this statement is that the opposite sides or faces in 3D elements must be parallel and in second-order elements the nodes must be either at the ends or middle of the element sides. Hourglassing can be a problem with first-order, reduced-integration elements, like C3D8R, in stress-displacement analyses. Since the elements have only one integration point, distortion is possible in such a way that the strains calculated at the integration point are all equal to zero, that leads to uncontrolled mesh distortion. First-order, reduced-integration elements in Abaqus include hourglass control, but reasonably fine meshes should be used for them. By distributing point loads and boundary conditions over a number of neighboring nodes, instead of one point, the hourglassing can be minimized.



8-node linear element

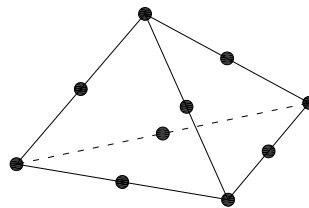
Figure 3.5-1. C3D8 Brick Element

3.5.2 C3D4

C3D4 is a 4-node first-order constant stress tetrahedral element. It is tried to avoid using this element, but in some cases making use of it has been inevitable.

3.5.3 C3D10M

C3D10M is a 10-node modified tetrahedron element with hourglass control. Figure 3.5-2 illustrates this element.



10-node modified second-order element

Figure 3.5-2. C3D10M Tetrahedron Element

3.5.4 T3D2

T3D2 is a 2-node linear displacement element. The behavior of this element is the same as truss elements in structures. It carries only axial load. No shear or bending moment is transferred by this element. This element, when embedded in a concrete mass, can be regarded as a rebar.

3.6 Stress Functions Definition

In this section, the definitions of the stress functions that are used in the following discussions are presented. The stress components at each node are assumed to be given

by the Cauchy stress tensor T which its elements are T_{ij} . The isotropic invariants of the stress tensor are defined as

$$\begin{aligned} I_{1T} &= tr(T) \\ I_{2T} &= tr(T^2) \\ I_{3T} &= tr(T^3) \end{aligned} \tag{Eq. 3.49}$$

Another set of invariants are defined as

$$\begin{aligned} J_{1T} &= tr(T) \\ J_{2T} &= \frac{1}{2}[tr^2(T) - tr(T^2)] \\ J_{3T} &= det(T) \end{aligned} \tag{Eq. 3.50}$$

If the principal stresses of T are T_1 , T_2 and T_3 , the above six invariants can be written in terms of these stresses as

$$\begin{aligned} I_{1T} &= T_1 + T_2 + T_3 \\ I_{2T} &= T_1^2 + T_2^2 + T_3^2 \\ I_{3T} &= T_1^3 + T_2^3 + T_3^3 \end{aligned} \tag{Eq. 3.51}$$

And

$$\begin{aligned} J_{1T} &= T_1 + T_2 + T_3 \\ J_{2T} &= T_1T_2 + T_2T_3 + T_3T_1 \\ J_{3T} &= T_1T_2T_3 \end{aligned} \tag{Eq. 3.52}$$

The deviatoric stress which has a crucial role in plasticity theory is defined as the difference of Cauchy stress and the spherical stress as

$$S = T - T_{\text{avg}}I \quad \text{Eq. 3.53}$$

In which the average stress is

$$T_{\text{avg}} = \frac{1}{3} \text{tr}(T) = \frac{1}{3} I_1 T \quad \text{Eq. 3.54}$$

A useful property of the deviatoric stress is that its trace is equal to zero.

$$\text{tr}(S) = \text{tr}(T - T_{\text{avg}}I) = \text{tr}(T) - T_{\text{avg}}\text{tr}(I) = \text{tr}(T) - \frac{1}{3}\text{tr}(T) \times 3 = 0 \quad \text{Eq. 3.55}$$

The isotropic invariants can also be defined for the deviatoric stress in the same way as defined for the Cauchy stress:

$$\begin{aligned} I_{1S} &= \text{tr}(S) \\ I_{2S} &= \text{tr}(S^2) \\ I_{3S} &= \text{tr}(S^3) \end{aligned} \quad \text{Eq. 3.56}$$

And the second set of invariants as follows:

$$\begin{aligned} J_{1S} &= \text{tr}(S) = 0 \\ J_{2S} &= \frac{1}{2} [\text{tr}^2(S) - \text{tr}(S^2)] = -\frac{1}{2} \text{tr}(S^2) = -\frac{1}{2} S_{ij} S_{ji} \\ J_{3S} &= \det(S) \end{aligned} \quad \text{Eq. 3.57}$$

The latter set of invariants of deviatoric stress are written in terms of the invariants of Cauchy stress as

$$J_{1S} = 0 \quad \text{Eq. 3.58}$$

$$J_{2S} = -\frac{1}{3}[J_{1T}^2 - 3J_{2T}]$$

$$J_{3S} = \frac{1}{27}(2J_{1T}^3 - 9J_{1T}J_{2T} + 27J_{3T})$$

One of the most celebrated yield criteria for ductile metals is the Von Mises Yield function as follows

$$f = f(\boldsymbol{\sigma}) - \sigma_{yo} \quad \text{Eq. 3.59}$$

In which σ_{yo} is the yield stress of the ductile metal material and $f(\boldsymbol{\sigma})$ is Von Mises stress potential defined as

$$f(\boldsymbol{\sigma}) = \sqrt{\frac{3}{2}S:S} = \sqrt{\frac{3}{2}S_{ij}S_{ji}} \quad \text{Eq. 3.60}$$

Plugging $S_{ij}S_{ji}$ from Eq. 3.57 into Eq. 3.60 yields

$$f(\boldsymbol{\sigma}) = \sqrt{-3J_{2S}} \quad \text{Eq. 3.61}$$

Substituting J_{2S} from Eq. 3.58 into Eq. 3.61 and making use of Eq. 3.52 to convert invariants of Cauchy stress into principal stresses gives Von Mises stress potential as a function of principal stresses as

$$f(\boldsymbol{\sigma}) = \sqrt{T_{11}^2 + T_{22}^2 + T_{33}^2 - T_{11}T_{22} - T_{22}T_{33} - T_{33}T_{11}} \quad \text{Eq. 3.62}$$

One of the most significant advantages of the above equation is that it proves that Mises stress potential can be smaller or larger than the principal stresses and when one of the principal stresses is much larger than the other two, Mises stress is close to the *absolute value* of that larger stress.

As the Mises stress potential is always equal to or greater than zero, another equivalent stress definition by means of which the direction of traction vector can be distinguished is

also required. This criterion can be achieved using the third invariant of the deviatoric stress tensors. This third invariant is defined as

$$f(\mathbf{S}) = \sqrt[3]{\frac{9}{2} \mathbf{S} : \mathbf{S} : \mathbf{S}} \quad \text{Eq. 3.63}$$

This value is a useful representation of the stress values at a specific location which its sign can be positive or negative. In the following study, this third invariant of deviatoric stress will be used to distinguish tensile or compressive stresses when required.

3.7 Finite Element Modeling

An elaborated technique is employed to model the abutment details in Abaqus 6.9.1. The abutment wall, deck slab, haunch, girder, stiffeners and piles are modeled using 3D solid elements. Rebars are modeled by means of 2-node 3D truss elements. Figure 3.7-1 shows a general picture of the abutment which consists of different elements.

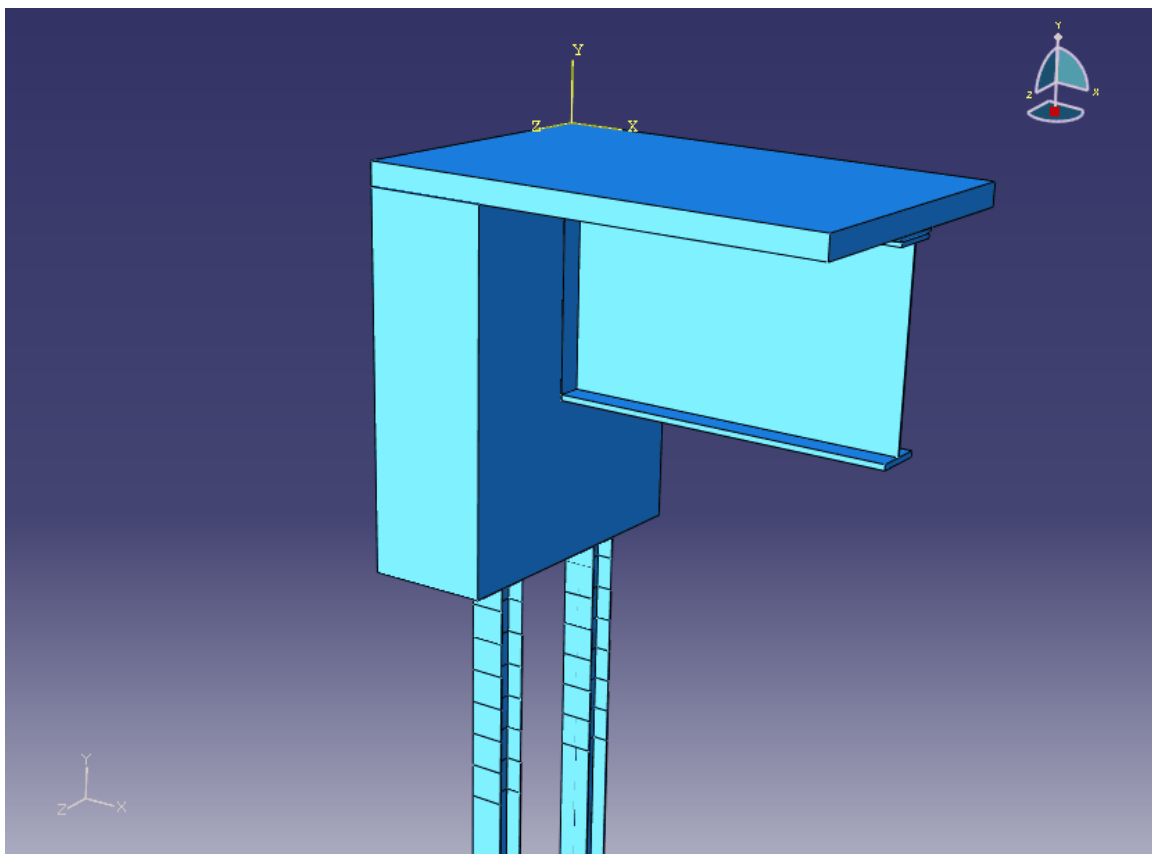


Figure 3.7-1. General Configuration of the Integral Abutment Model

Figure 3.7-2 shows the girder element of the connection. The girder is made of Grade 50 steel. It has an 18"x1.5" top flange, a 66"x0.5" web and an 18"x2" bottom flange. The girder may have two stiffener plates at the face of the concrete wall. The stiffener size is 66"x8.75"x0.5" on each side.

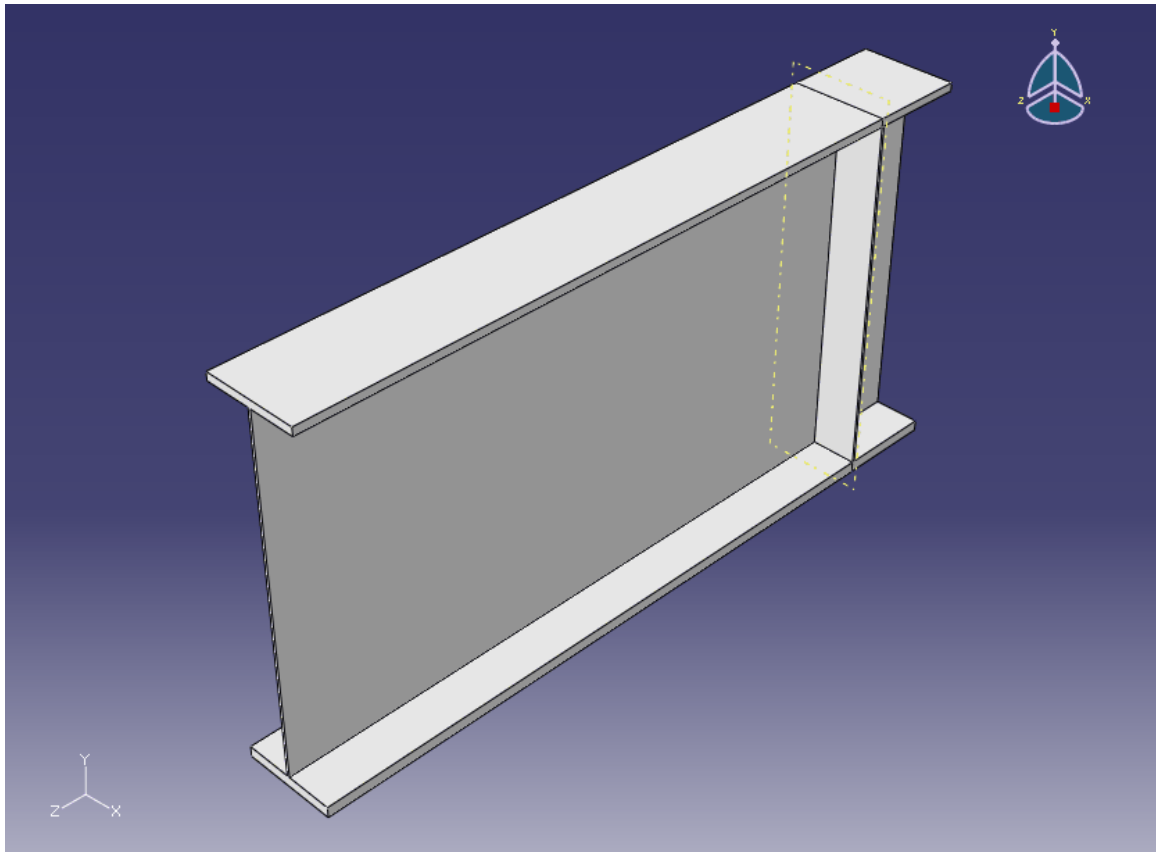


Figure 3.7-2. Girder Element of the Connection

The girder is 18 inches embedded in the abutment wall. Figure 3.7-3 illustrates the end of the girder which is embedded in the wall and cannot be seen clearly in the other pictures. One of the features of such connections is that the rebars of the abutment wall go through the web of the girder. This requires the web of the girder be drilled to provide the holes for rebars to go through. As the two top rebars are #7 and the lower five rebars are #5, the upper two holes are larger than the lower ones.

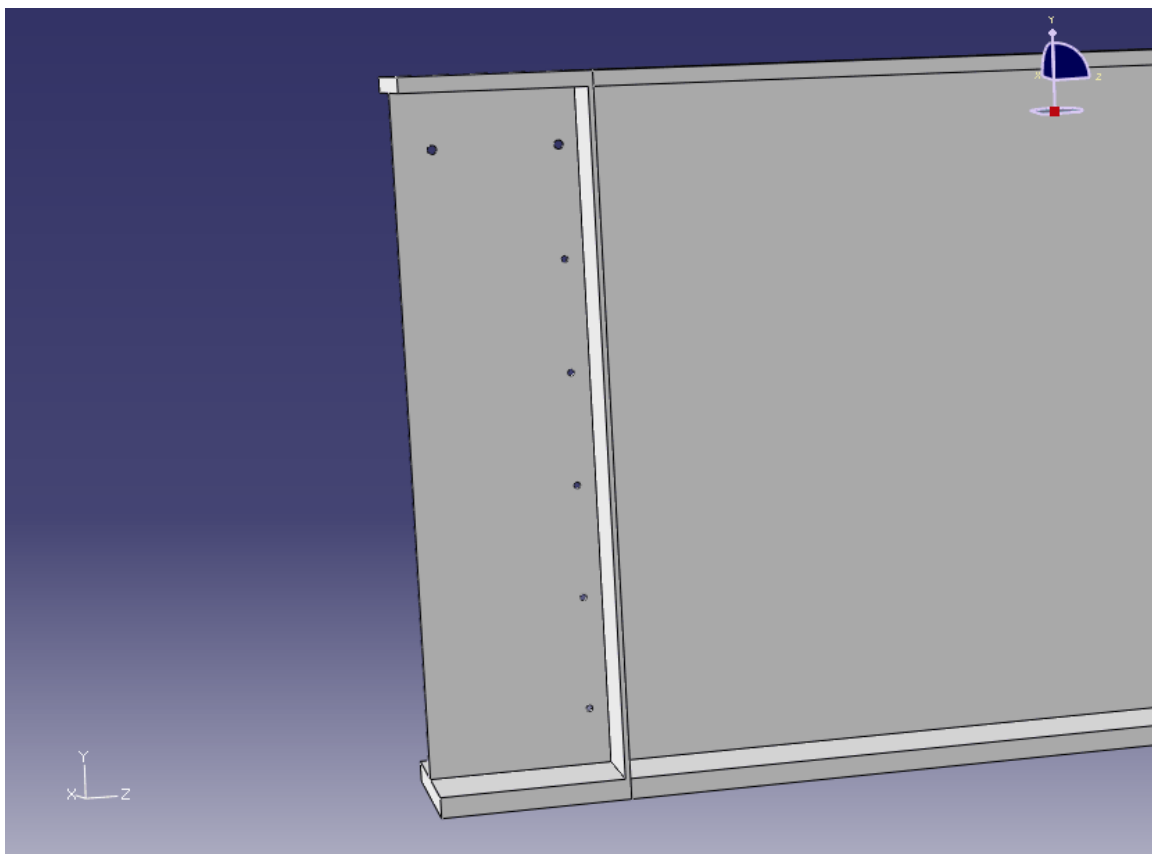


Figure 3.7-3. Embedded End of the Girder

Figure 3.7-4 shows the highlighted picture of the girder in the connection. The boundaries of the girder element can be visibly seen in this picture.

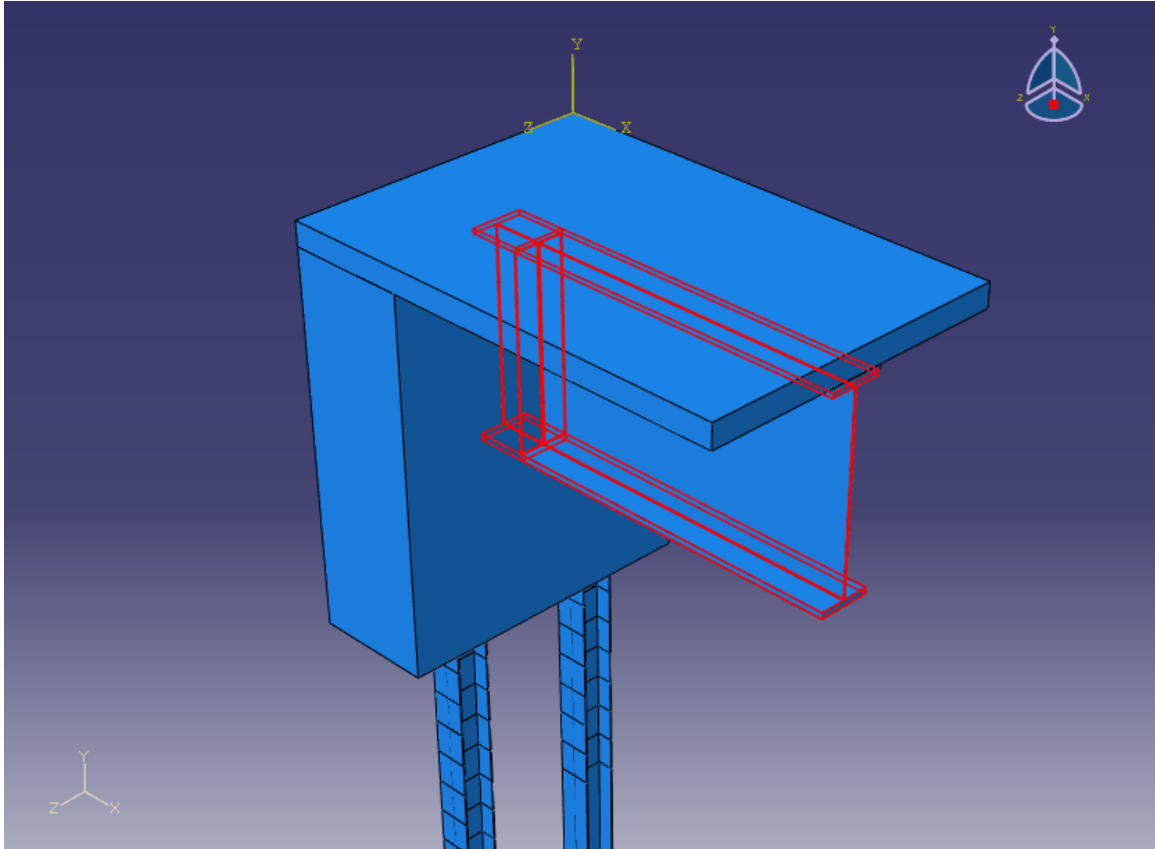


Figure 3.7-4. Highlighted Position of the Girder Element

Figure 3.7-5 shows the abutment wall part of the connection. It is made of concrete material with a characteristic strength of 4 ksi. It has a width of 42", a length of 108" and a height of 136". The place of girder and piles embedment is cut into the wall using the outstanding features of Abaqus. As the girder stiffeners are assumed to be inside the mass of concrete, their place is also cut in the wall element.

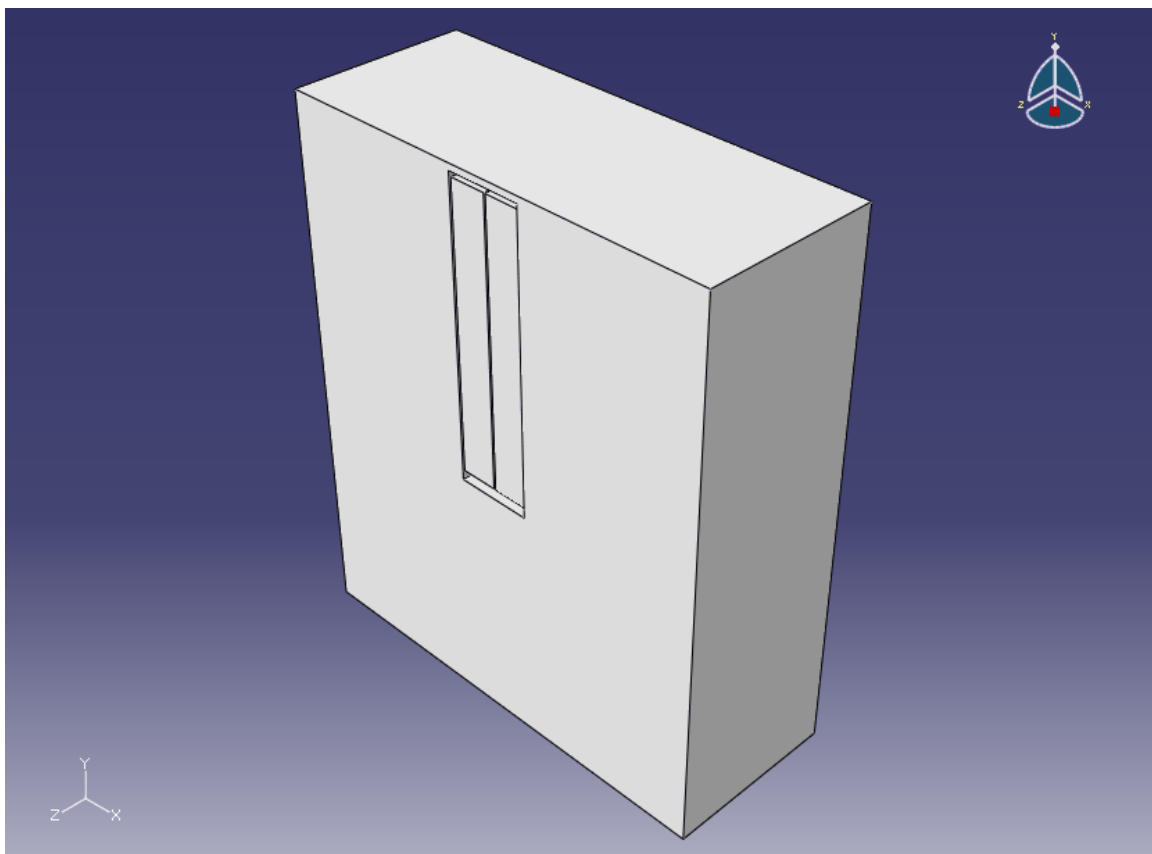


Figure 3.7-5. Concrete Wall of the Abutment

Figure 3.7-6 illustrates the highlighted picture of the abutment wall which more clearly shows its boundaries and also the place of piles embedment in the wall.

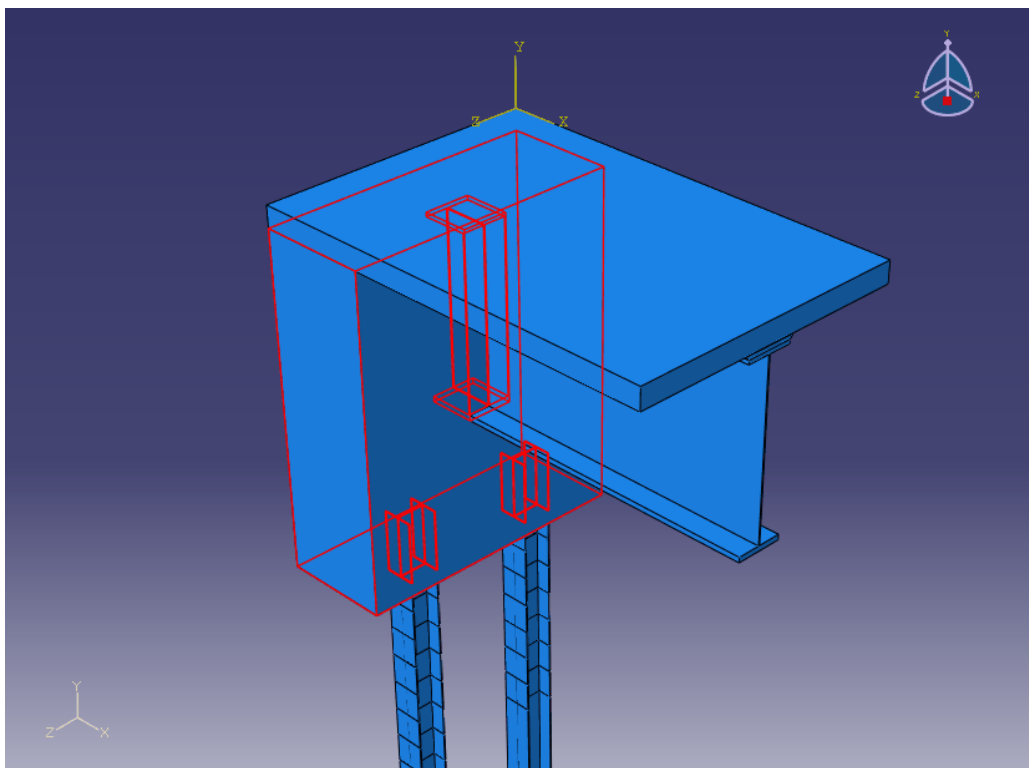


Figure 3.7-6. Highlighted Position of the Abutment Wall

Figure 3.7-7 shows the highlighted position of the deck in the abutment assembly. Like the abutment wall, it is made of class BD47 4 ksi concrete. The deck has an 8" thickness and has a tributary width of 108" for each girder.

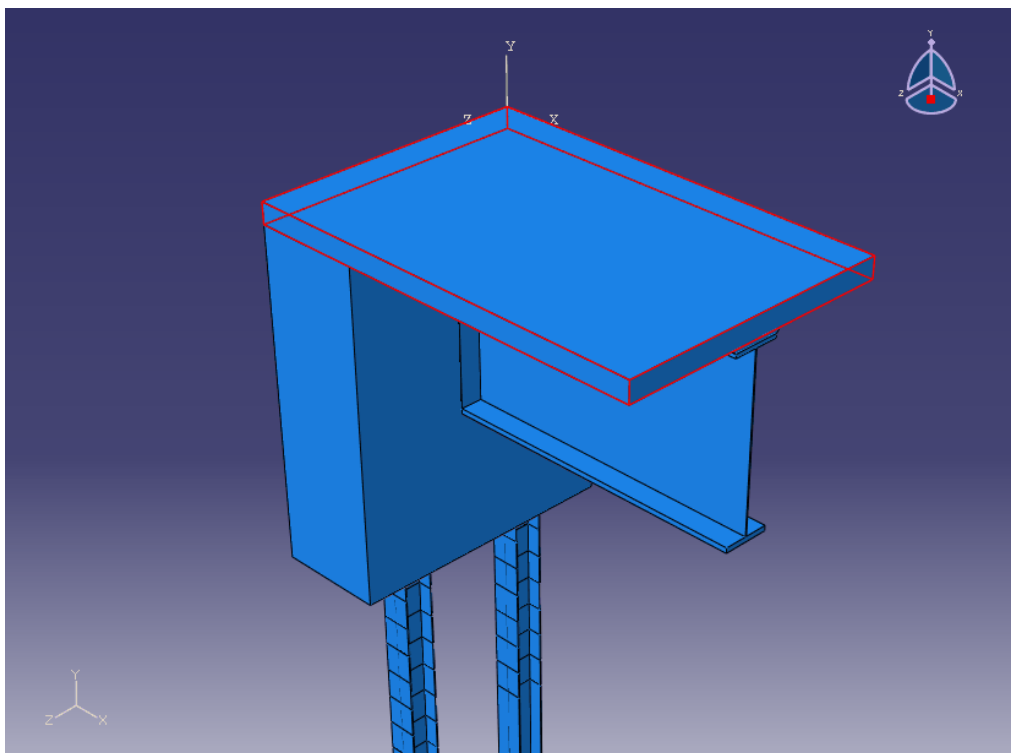


Figure 3.7-7. Highlighted Position of the Deck Slab

Figure 3.7-8 illustrates the haunch between the girder and the deck slab elements. The haunch is of the same material as the deck slab and has a thickness of 1.5 inches. The lower width of the haunch is 18 inches which is the width of the girder top flange and the upper width is 21 inches that provides a 1:1 slope for the edges. Figure 3.7-9 shows the highlighted position of the haunch element in the abutment.

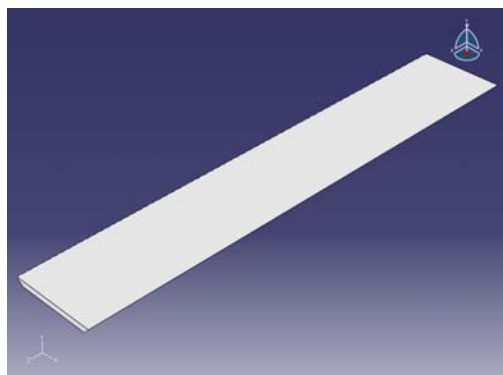


Figure 3.7-8. Haunch Element of the Connection

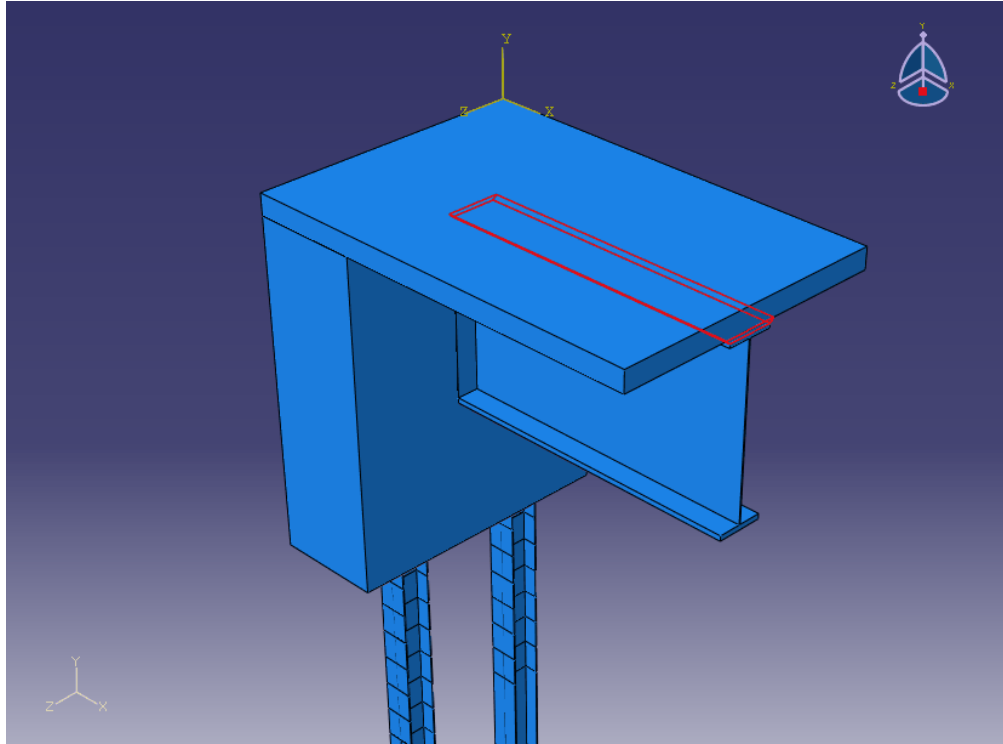


Figure 3.7-9. Highlighted Position of the Haunch

Figure 3.7-10 shows the pile element of the abutment. The section of the piles is H12x53 which is made of Grade 36 steel. The piles are modeled 3 feet below the point of fixity. The abutment is supported by two piles which are 54 inches apart. The center of the piles is 12 inches away from the front face of the wall. The surrounding soil of the piles is modeled using the spring element in Abaqus. The stiffness of the springs is 4 k/in per linear foot of the piles.

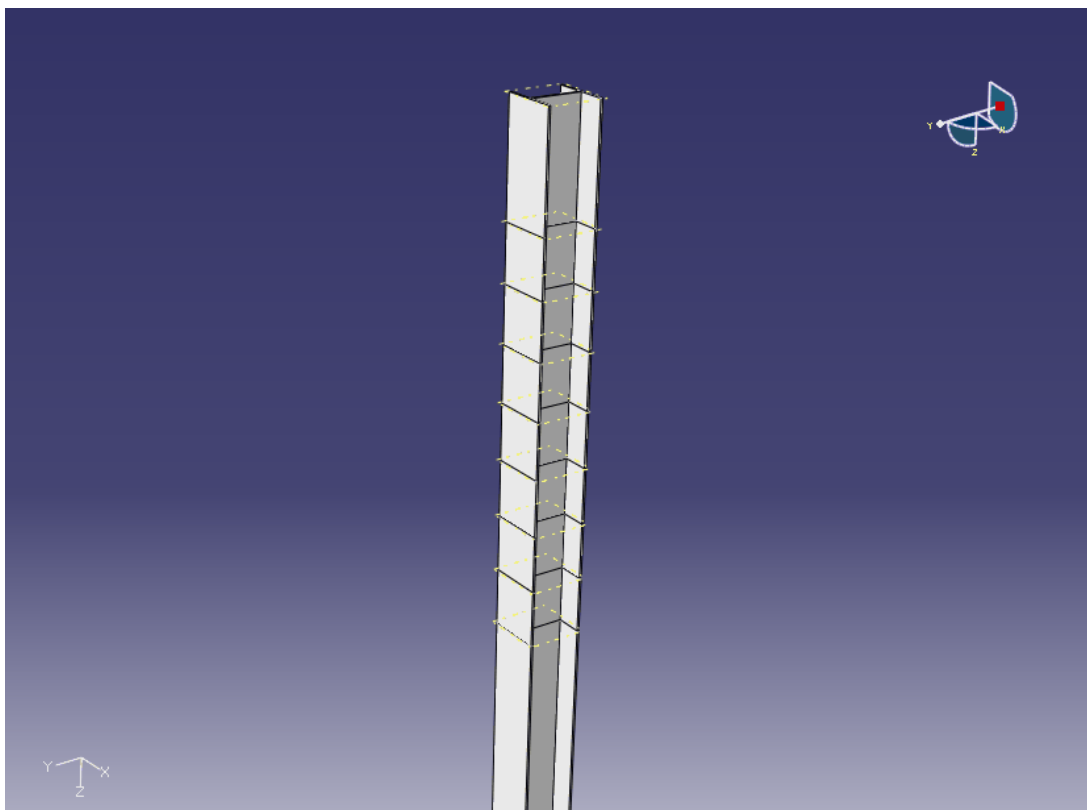


Figure 3.7-10. H- Pile Element of the Connection

Figure 3.7-11 shows the highlighted picture of the piles in the abutment assembly. The embedded length of the pile in the abutment wall can be obviously detected in this picture.

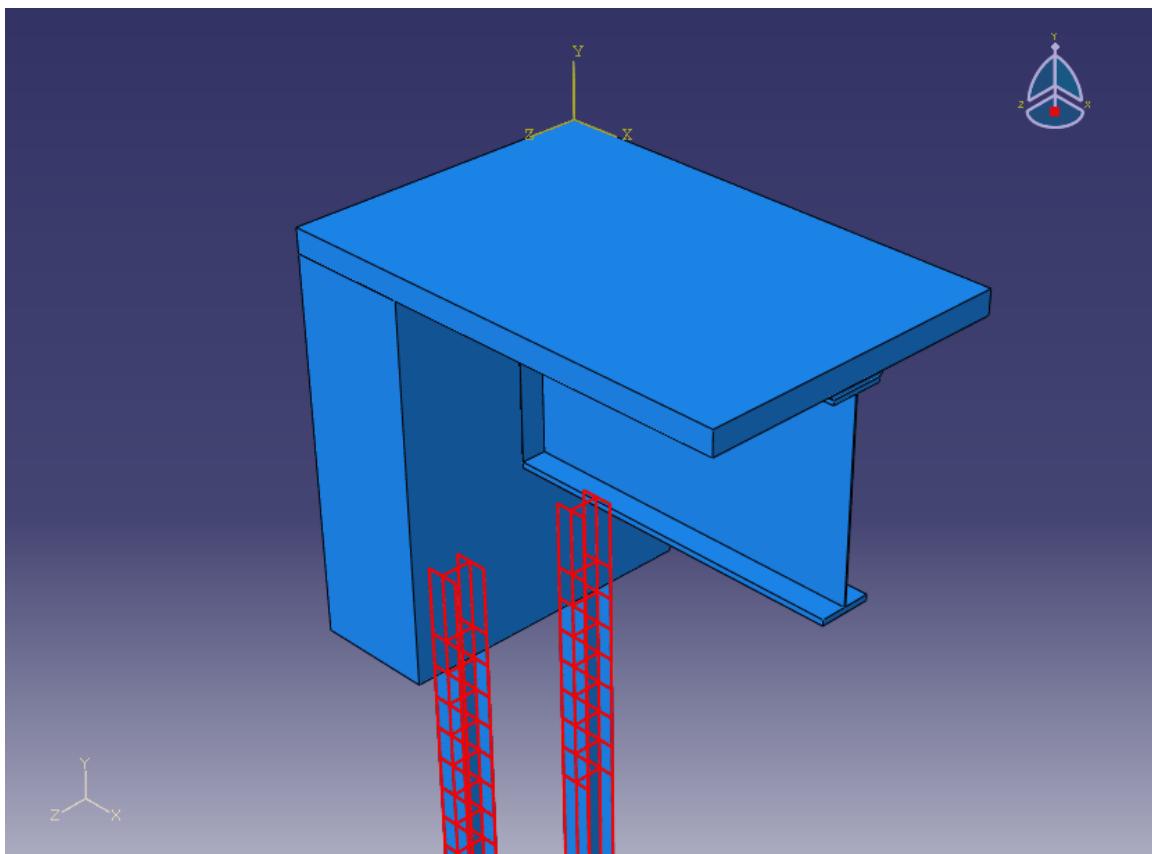


Figure 3.7-11. Highlighted Position of the H-Piles

Figure 3.7-12 shows the highlighted rebars of the concrete deck slab. The longitudinal bars are #5 placed at 8" spacing at top and bottom layers. The transverse bars are #5 at 12" spacing again at both top and bottom layers. The cover above the upper transverse rebars is 2 inches and the cover below the lower transverse rebars is 1 inch.

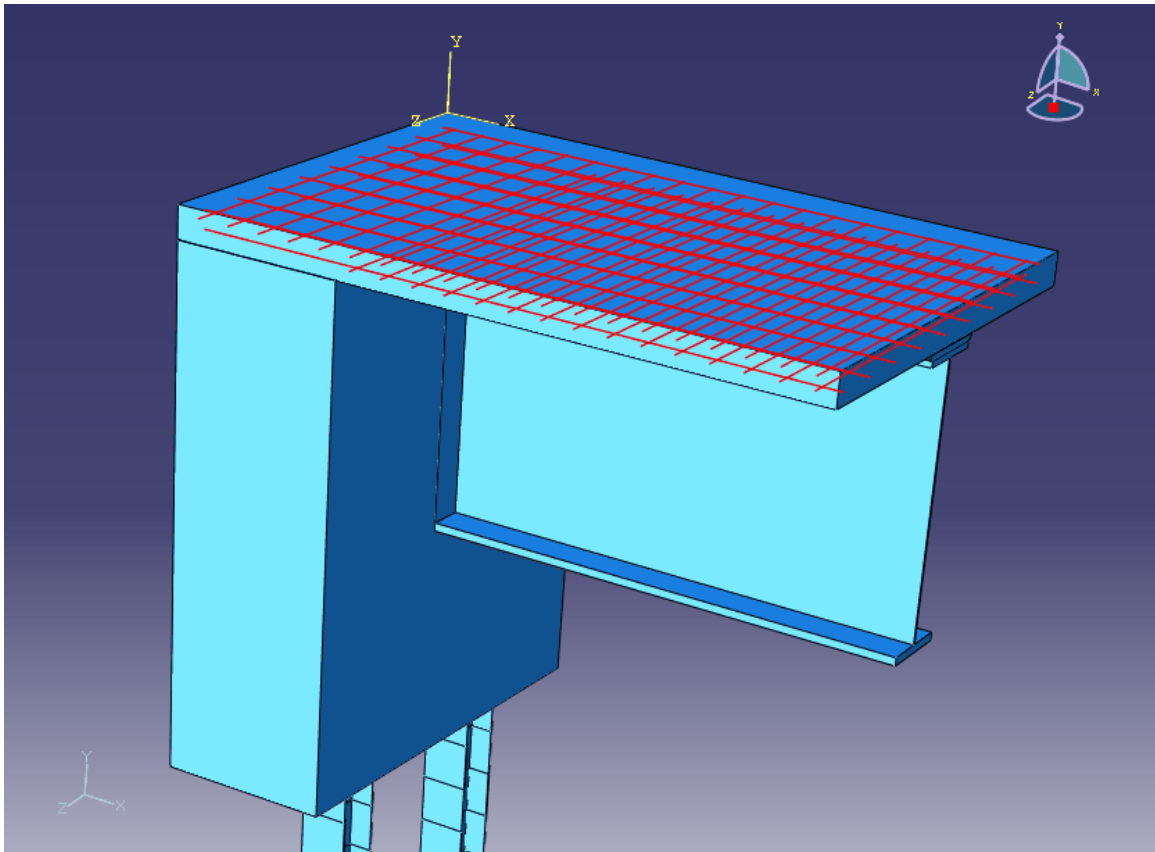


Figure 3.7-12. Highlighted Rebars of the Deck Slab

Figure 3.7-13 illustrates the abutment wall cage of reinforcement. The top and bottom layer of bars along the length of the abutment consist of 4#7 rebar. The size of all other rebars of the wall is #5. The rebars are not evenly distributed to minimize the intersection with the girder or the piles. Although, some of them that are parallel to the wall face go through the girder web as explained before. The clear concrete cover for the lower and back face of the wall is 3 inches, while it is 2 inches for the front face of the wall. The vertical rebars of the wall enter the deck slab to guaranty the load transfer between the deck and the wall. However, a considerable portion of the load is supposed to be transferred through the girder which is attached both to the deck and the wall.

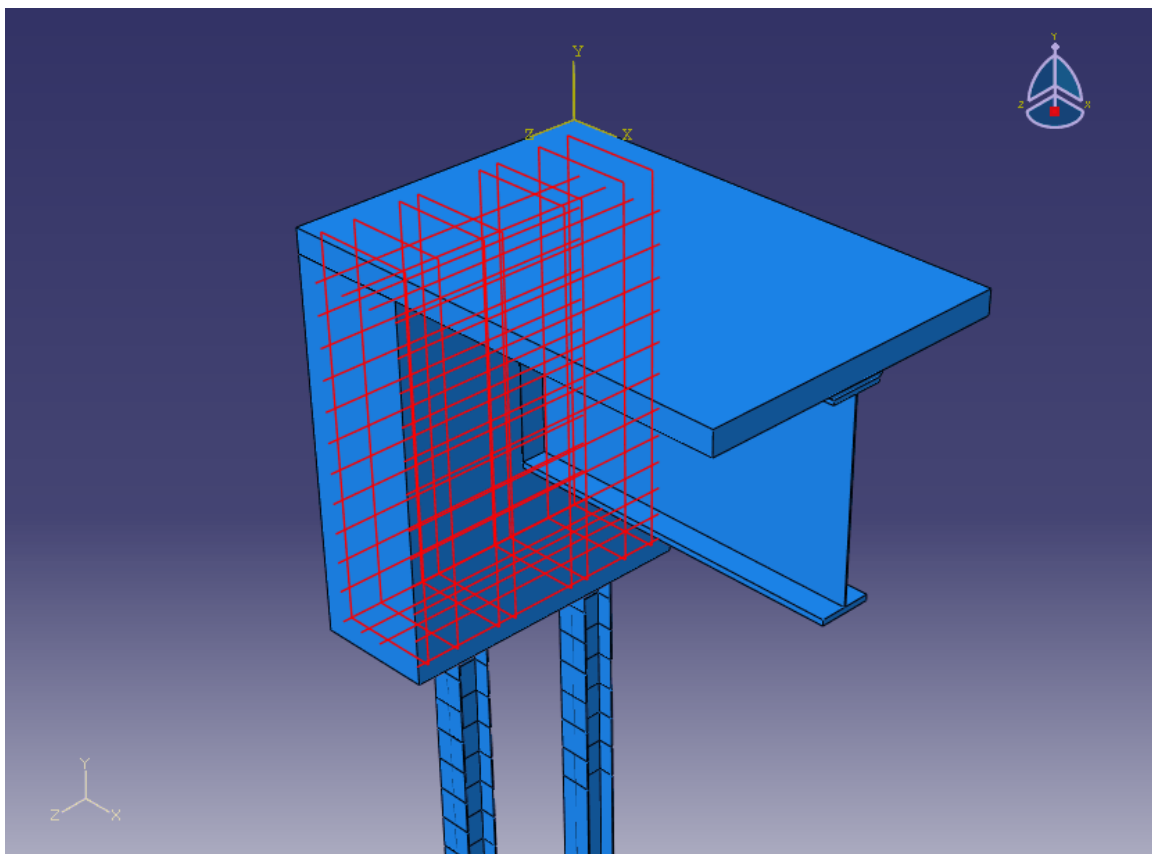


Figure 3.7-13. Highlighted Rebars of the Abutment Wall

The effect of shear studs on the bottom flange of the girder in the embedded length is also studied. Figure 3.7-14 shows two pictures of the shear studs below the bottom flange.

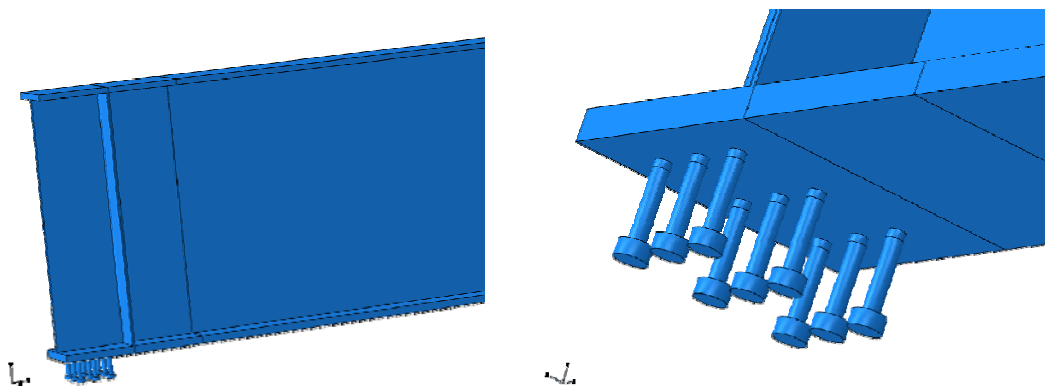


Figure 3.7-14. Shear Studs Attached to the Girder Bottom Flange

Using the above-mentioned elements two different models have been made. The first one is a single span bridge of 100 feet length which has integral abutments at the two ends. The piles in this model are not modeled and a fixed support is provided for the abutment wall. Using this model one is able to apply the ultimate gravity load to the bridge and observe the behavior of the I-girder to abutment wall connection. The other model is a 30 feet cantilever composite I-girder that is integrally connected to the abutment. In the latter study, the piles are included in the modeling. So, it is possible to investigate the pile-to-wall connection which is another area of interest. The following sections of this chapter describe the results of analyzing these two models.

3.8 Moment Capacity of the Superstructure

Before proceeding to the results of finite element analysis, to have a measure of the capacity of the superstructure section that is attached to the abutment wall, a moment-curvature analysis of the section is performed using the defined material properties. A MATLAB code is provided to analyze the section. The implemented approach in the program is to increase the bending strain in the section incrementally and calculate the imposed curvature and the developed moment in the section. This MATLAB program has been a huge project by its own, and for brevity more explanation is avoided and the program is brought in Appendix B.

Figure 3.8-1 shows the superstructure section for which the moment capacity is calculated and Figure 3.8-2 illustrates the moment-curvature diagram of that section. It is seen that the yielding moment of the section is about 160,000 k.in and the ultimate moment capacity of the section is approximately 175,000 k.in.

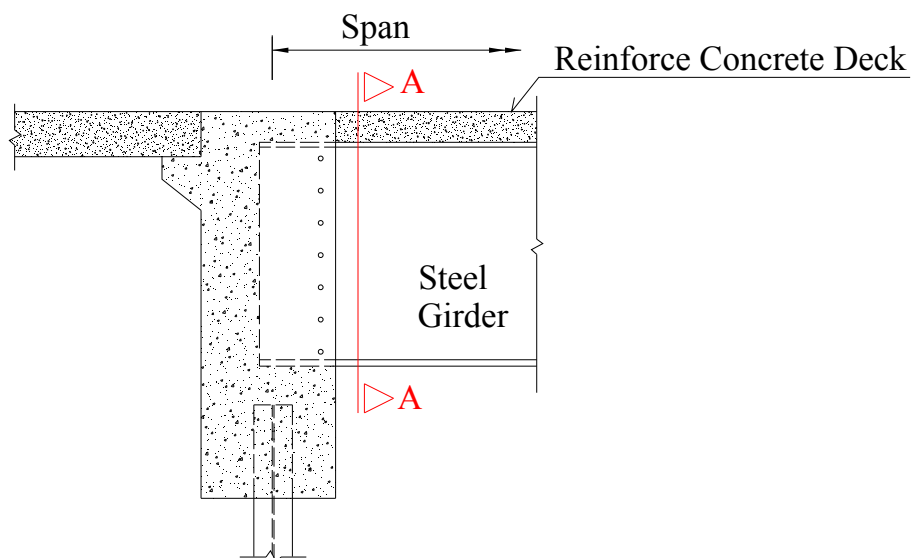


Figure 3.8-1. Superstructure Section at the Vicinity of Abutment Wall (Section A-A)

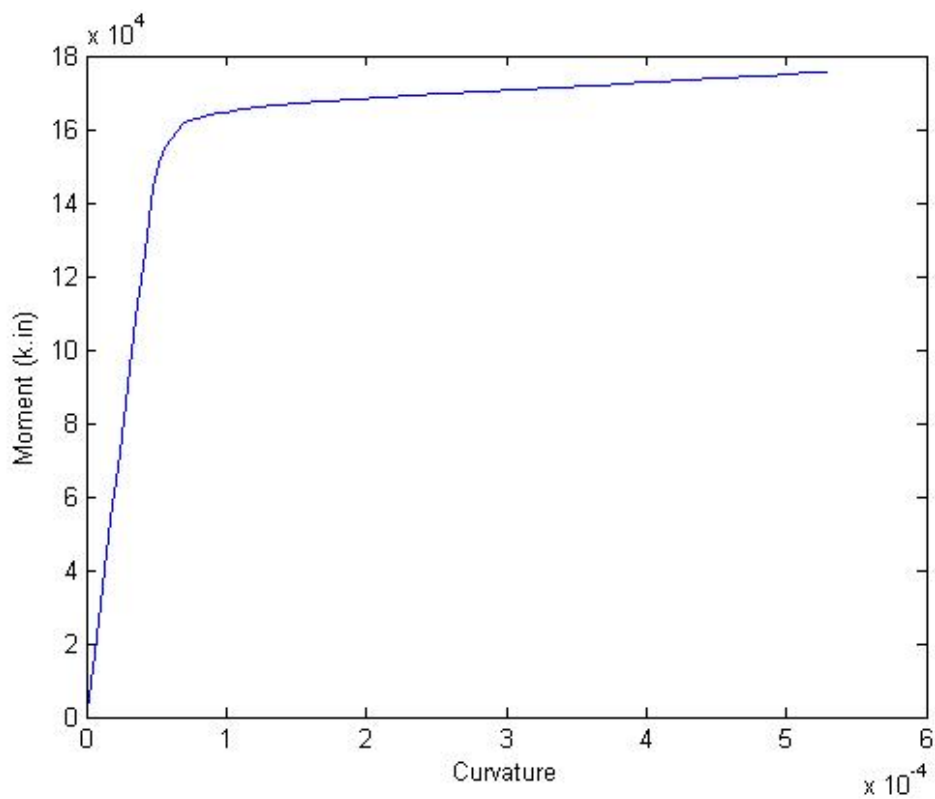
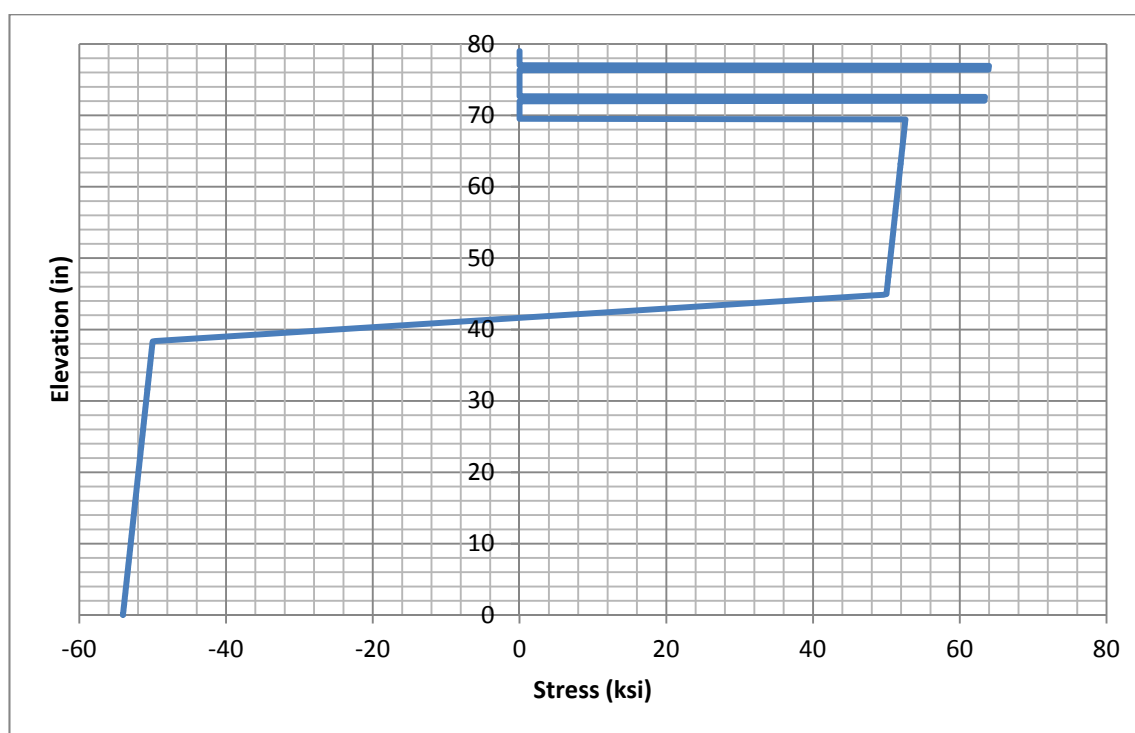


Figure 3.8-2. Moment-Curvature of the Superstructure at Section A-A

Figure 3.8-3 shows the stress distribution in the superstructure section when the maximum moment is reached. It is observed that the neutral axis is 42 inches above the bottom fiber of the girder. Other than about 3.5 inches below and above this neutral axis, all other parts of the girder are yielding which have stresses equal or greater than 50 ksi. Concrete deck is fully cracked and the upper and lower layers of rebars in the deck are yielding. The stress of the rebars is more than 60 ksi. Note that the slope of the plateau region in the presented steel material models in section 3.3 is not zero. That's why the stresses after yielding get larger than 50 and 60 ksi for Grade 50 and Grade 60 steel, respectively.



**Figure 3.8-3. Stress Distribution in the Superstructure at the Vicinity of Abutment Wall
Corresponding to Maximum Moment Capacity**

3.9 Results of Analysis

The results of nonlinear finite element analysis of the studied integral abutment detail are presented in this section. First, the steel I-girder stresses are discussed. This includes the girder stresses at the vicinity of the abutment wall face, both in the embedded region and outside of the wall. Then, the concrete deck stresses are shown. In the next step, a discussion on the stresses of the abutment wall is presented. As a result, the effect of girder stiffener right at the wall front face section is investigated. After that comes another outcome of this study which is to show the effect of shear studs attached to the bottom flange of the girder. One more investigation is on the pile stresses. Stresses of abutment wall at the neighborhood of the pile are then illustrated followed by an argument on necessity of a pile stiffener at that location.

3.9.1 Girder Stresses

In this section, the stress state of a girder integrally attached to an abutment wall is studied. First, a 100-foot span bridge is analyzed in which the girder has no stiffener and no bottom flange shear connectors. The Mises stresses for such a girder are depicted in Figure 3.9-1. It is seen that the maximum stress happen in the web above the wall face. At the level of loading corresponding to this picture, the concrete in contact to the end of the bottom flange started crushing while the stress in the girder flange is much lower than its yield capacity. To find a solution to decrease the web stresses and shift them to the bottom flange, two usual details are described in the following sections.

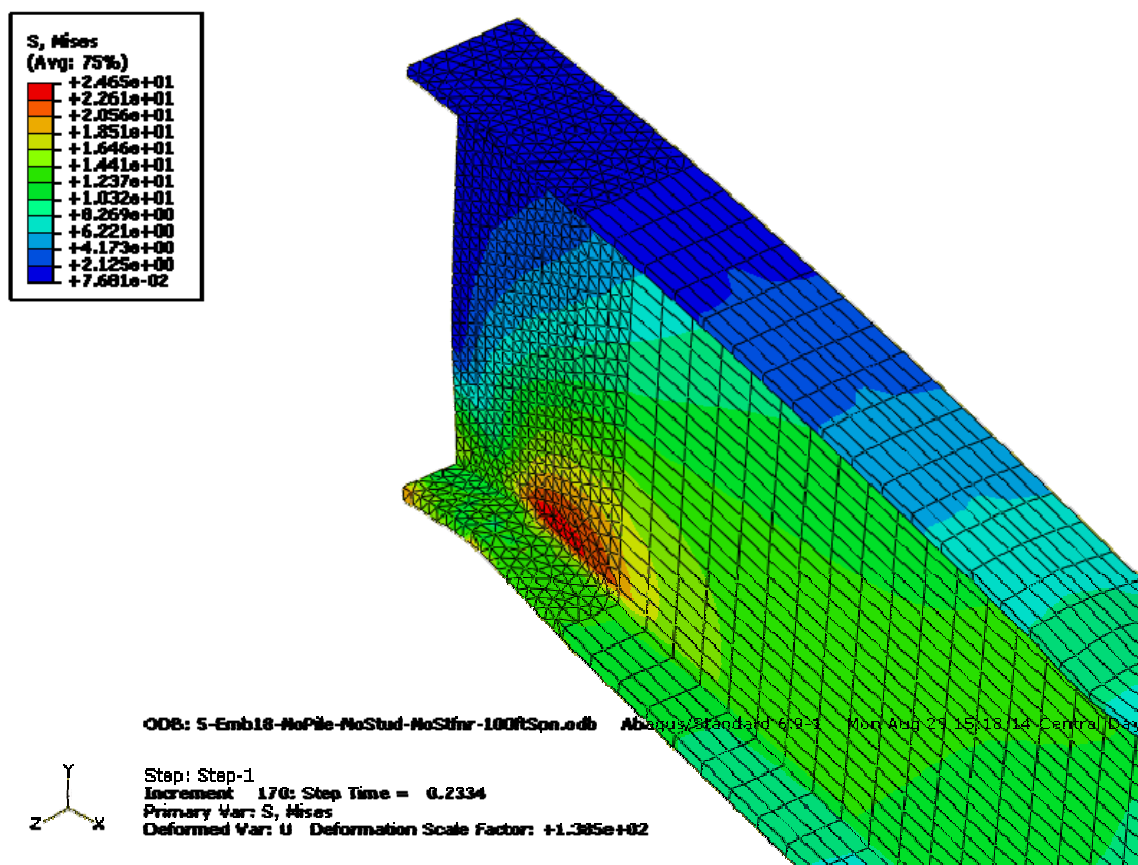


Figure 3.9-1. Mises Stresses of Girder without any Stiffener or End Shear Stud

A) Effect of Girder Stiffener

In this part of the study, a transverse stiffener is added to the girder right above the wall front face and the single span bridge is analyzed. Figure 3.9-2 describes the stresses after adding the stiffener. It is observed that the stiffener reduces the web stresses to some extents. But, as expected, the stiffener is not able to move the maximum stresses to the bottom flange. That's why some designers think about connecting shear studs to the bottom flange to increase the moment carrying capacity of the girder. This problem is discussed in the next section. The effect of the stiffener on the abutment wall stresses is studied in section 3.9.2.

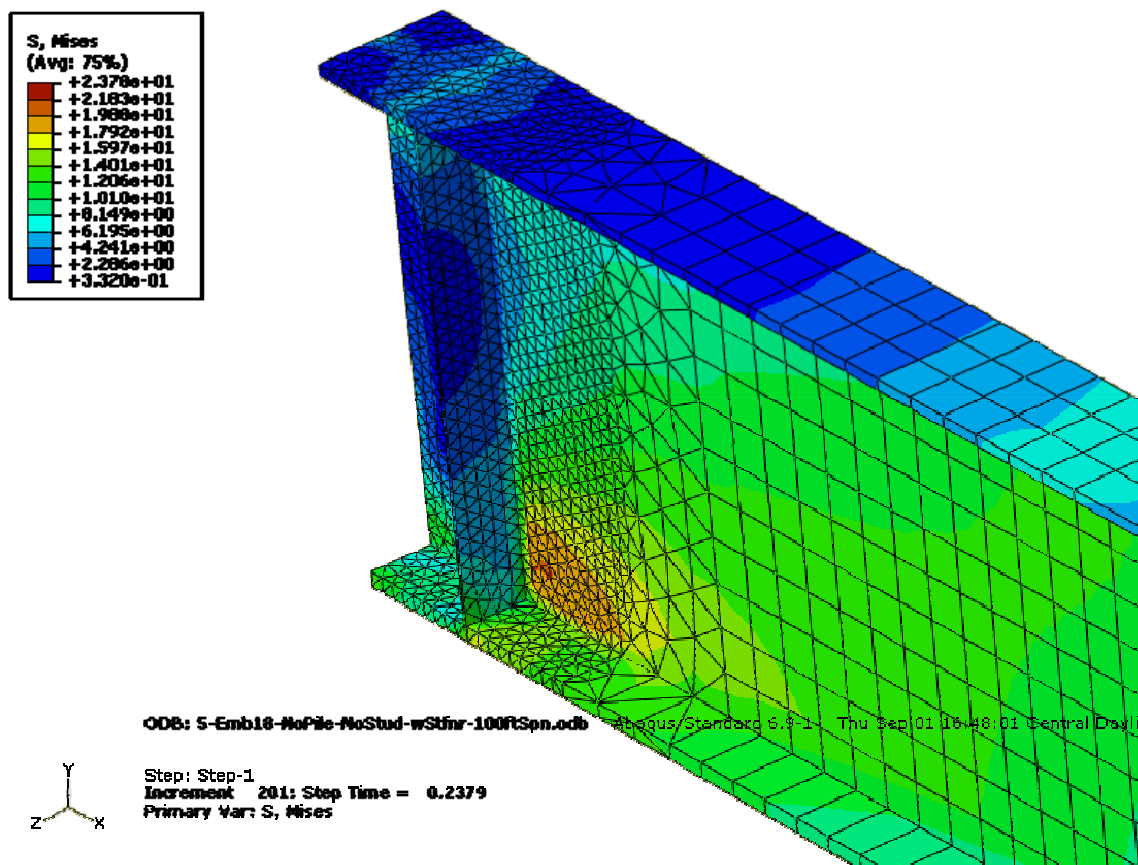


Figure 3.9-2. Mises Stresses of Girder with Stiffener without End Shear Stud

B) Effect of Girder End Shear Studs

Another idea is to connect shear studs to the bottom flange of the girder in the embedded length to offer it a more pronounced role in carrying loads. Nine shear studs of 6 inches length and 1 inch diameter are tied to the lower face of the bottom flange. Figure 3.9-3 shows the Mises stresses of the girder end. Comparing to Figure 3.9-1, it can be observed that there is not a noticeable difference between the state of stress of the girder with and without shear connectors. The maximum stress occurs in the web while

the shear studs are not able to give the bottom flange an added value. The effect of the shear studs on the state of stress in the abutment wall is discussed in section 3.9.2.

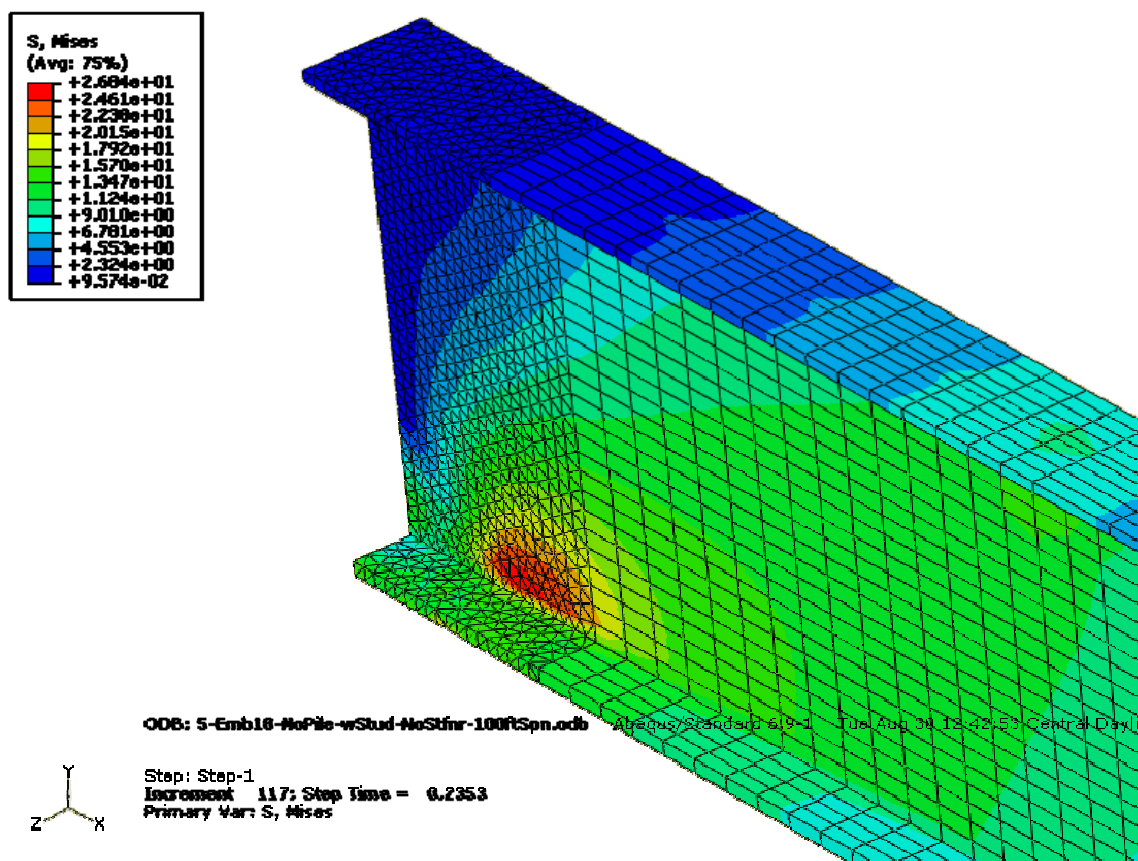


Figure 3.9-3. Mises Stresses of Girder with End Shear Stud without Stiffener

C) Ultimate Loading

Another job is to analyze the single span bridge under heavy gravity loads and observe the behavior of the connection. The loading and analysis are continued up to reaching plastic moment capacity in the middle of the 100-foot span. As can be observed in Figure 3.9-4, the Mises stresses in the girder are about 50 ksi from the bottom fiber of the section up to upper portion of the web. Figure 3.9-5 is showing the Mises stresses of the concrete deck. The concrete stress at mid-span is close to 4 ksi which is the maximum

strength of concrete. This configuration for stresses at mid-span corresponds to the plastic capacity with the neutral axis below the top flange of the girder.

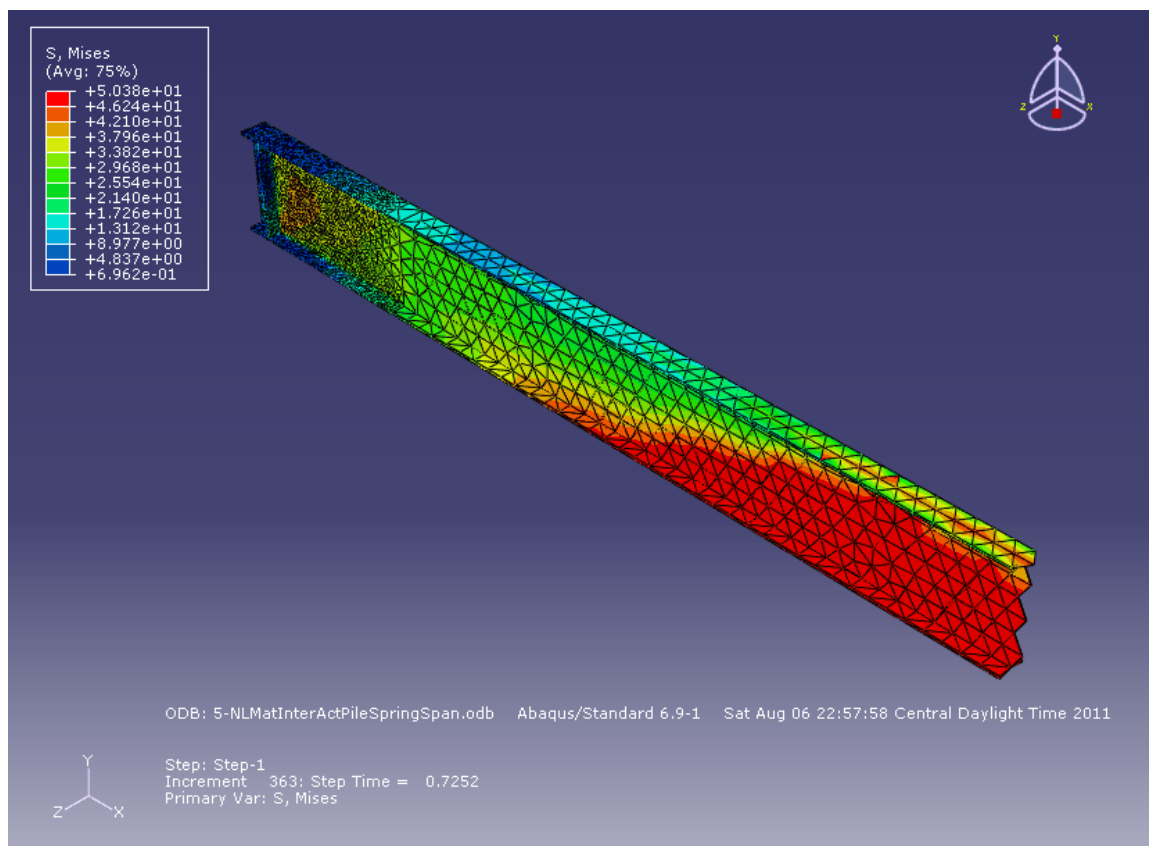


Figure 3.9-4. Mises Stresses of Half of the Girder

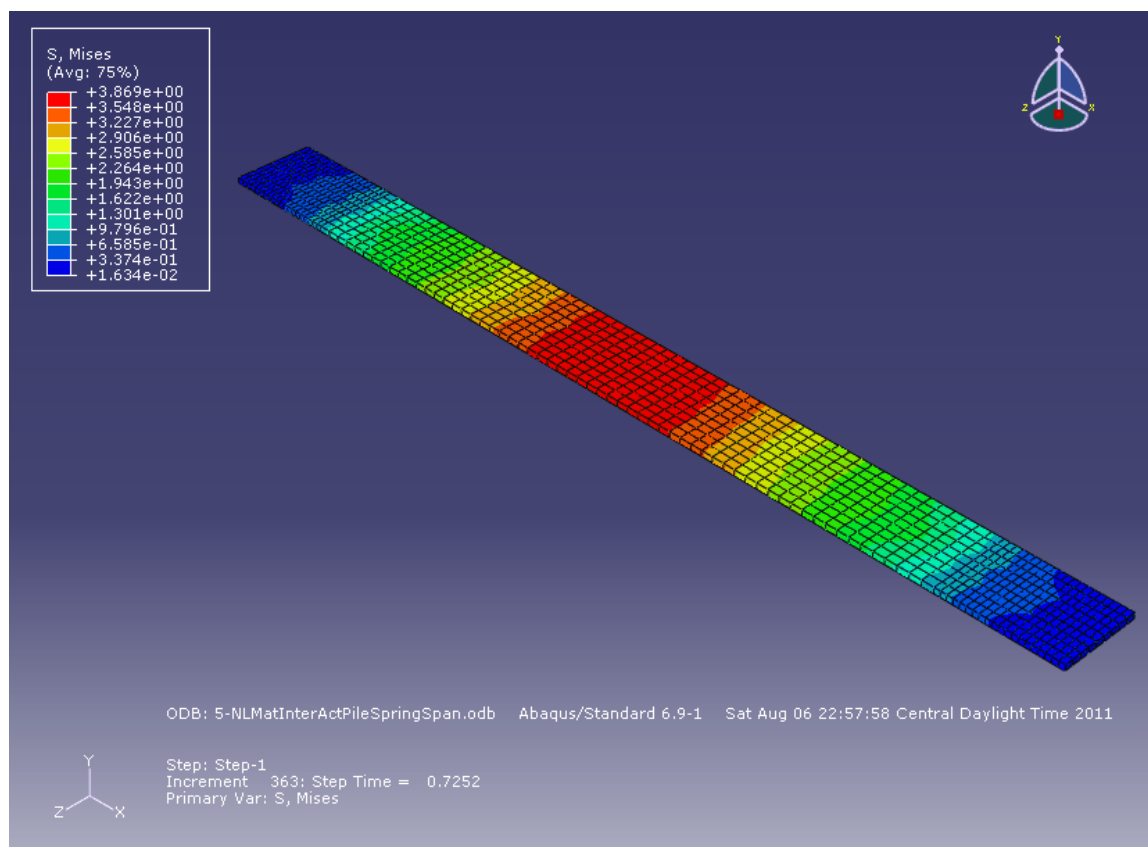


Figure 3.9-5. Mises Stresses of Concrete Deck

A closer look at the stresses of girder ends demonstrates that the girder has low stresses at the ends, despite of plastification at mid-span. And another weird observation is that the maximum stresses of the girder at the ends do not form in the top or bottom flange. In integral abutment connections, the maximum stress at the girder end is in the web above the wall front face. Figure 3.9-1 through Figure 3.9-3 show initiation of high stresses in the web instead of flanges in such a connection. This is attributed to the occurrence of knife edge phenomenon. In such connections, the girder web tends to cut the face of the concrete wall like a knife. The other characteristic of these connections is that the responsibility of developing the longitudinal stresses in the bottom flange of the girder is with the surrounding concrete of the flange in the short practical lengths of

embedment. As the maximum supporting stress at the end face of the flange is the capacity of concrete and the mobilized stress over the surfaces of the flange in the embedded region is the friction and bond between steel and concrete, these two cannot create stresses comparable to yield stress of steel material. Figure 3.9-6 shows the Mises stresses of the girder end as the load is increased. It is observed that application of a large load creates high shear stresses in the web of the girder while the stress in the bottom flange of the girder is still low.

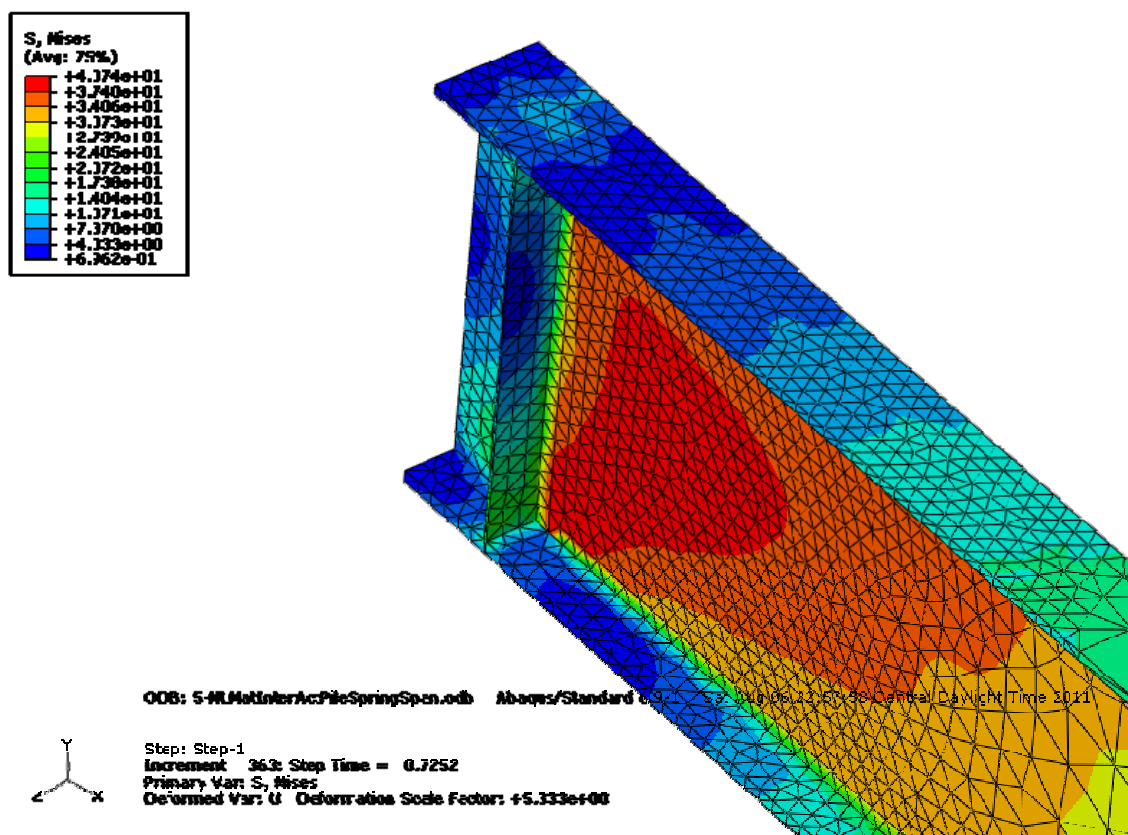


Figure 3.9-6. Mises Stresses of Girder's End Corresponding to Mid-span Plastification

3.9.2 Abutment Wall Stresses At Girder Embedment Zone

In this section, the concrete abutment wall stresses are studied in more details. The first point of interest in the wall is the contact region of the steel girder and the wall. This region is in charge of transferring the girder end shear and moment to the abutment structure. As shown in Figure 3.9-7, maximum stresses are developed right below the girder web at the face of the concrete wall. This picture is of wall supporting an unstiffened girder. This region is subject to the vertical shear force and the horizontal friction and bond between steel and concrete. This part of the abutment structure is potential to failure because of this high stress and the limited confinement of concrete.

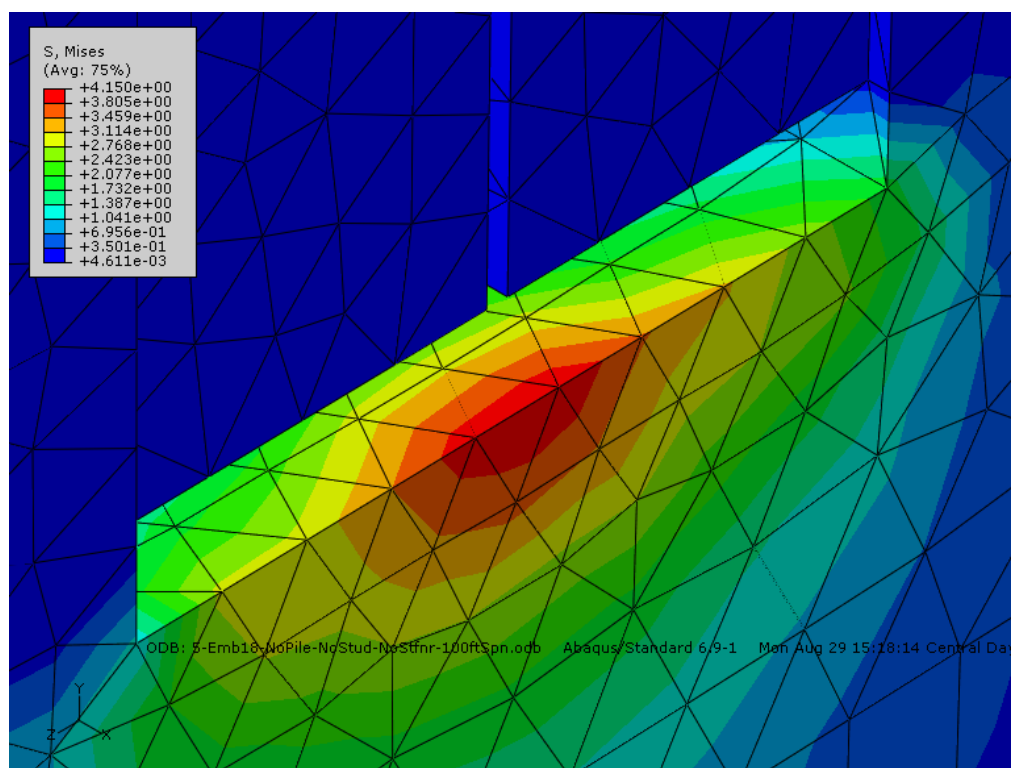


Figure 3.9-7. Mises Stresses of Abutment Wall Supporting an Unstiffened Girder

A) Effect of Girder Stiffener on Wall Stresses

Figure 3.9-8 shows the stresses at the front face of abutment wall below the bottom flange of a girder with bearing stiffener. Comparison to Figure 3.9-7 demonstrates that if the girder has no bearing stiffener, there is a point of high stress below the web of the girder. But, if the girder is provided with bearing stiffener, for the same amount of loading the stress is more distributed over the contact area with a lower maximum value. This analysis shows the necessity of girder bearing stiffener for this type of connections.

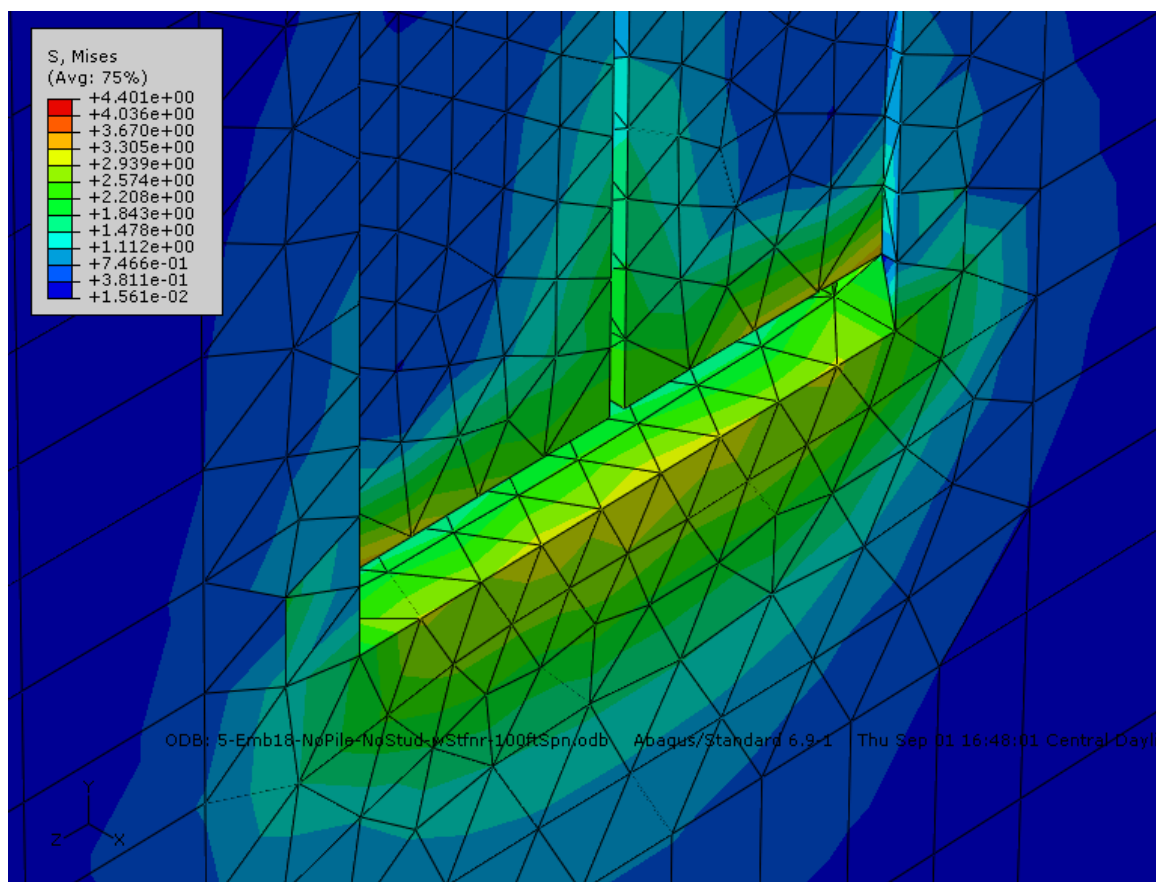


Figure 3.9-8. Mises Stresses of Abutment Wall Supporting a Stiffened Girder

B) Effect of Girder End Shear Studs

Another study is to investigate the effectiveness and necessity of girder end shear studs. In this study, the role of bottom flange shear connectors in changing the wall stresses is examined. The Mises stresses of the girder and abutment wall in two different cases of with and without shear studs are shown in Figure 3.9-9 and Figure 3.9-10. It demonstrates that if shear studs are added to the bottom flange of the girder, the concrete stresses at the end of the bottom flange decrease from 6.69 ksi to 4.61 ksi. In section 3.9.1, it was shown that girder stresses are not affected considerably by the end shear studs. But, the results for abutment wall stresses show that the shear studs are effective in mitigating the wall stresses.

A closer look at the wall stresses in this zone reveals that the maximum stress occurs where the end of the bottom flange pushes the adjacent concrete. As the friction and bond between the surfaces of the bottom flange do not mobilize high values of stress in the bottom flange, development of stress in the bottom flange is mainly done by the concrete in contact to the end face of the flange. While adding shear studs to the bottom flange, helps engage a larger chunk of concrete in developing flange stresses.

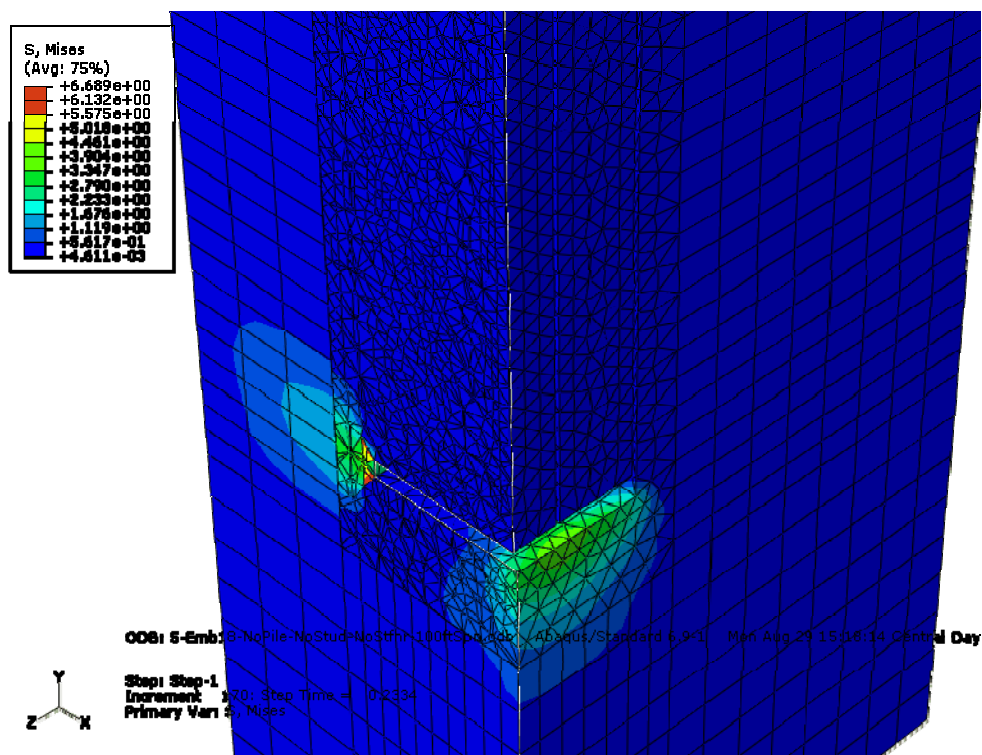


Figure 3.9-9. Mises Stresses of Abutment Wall - Girder without End Shear Studs

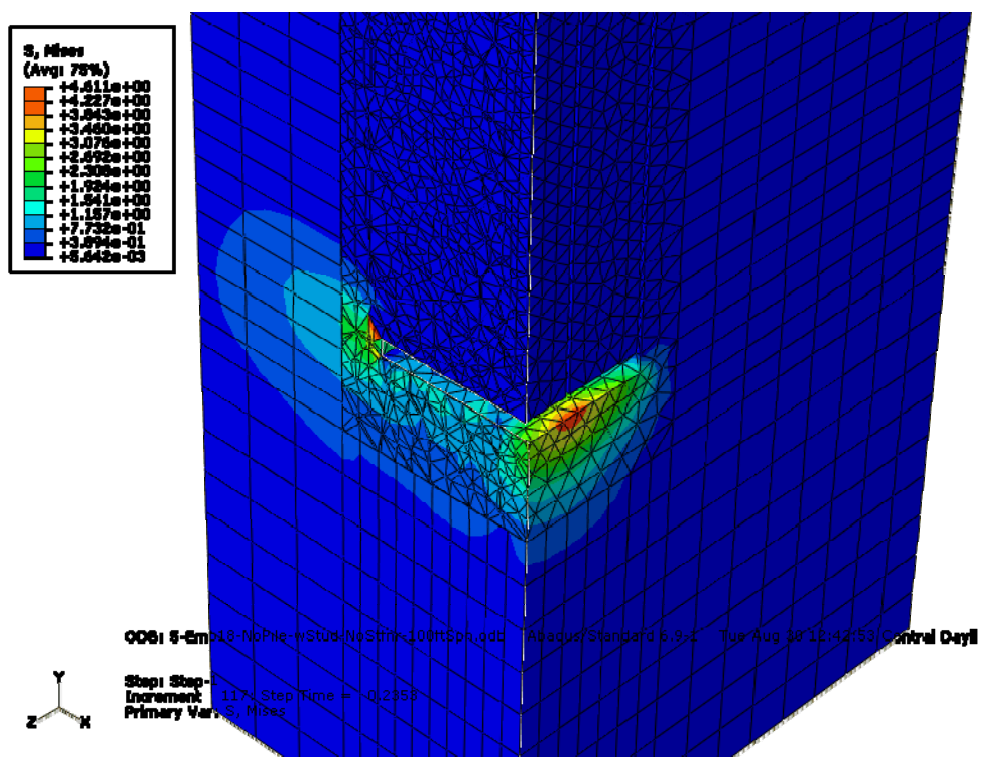


Figure 3.9-10. Mises Stresses of Abutment Wall - Girder with End Shear Studs

3.9.3 Abutment Wall Stresses At Pile Embedment Zone

In the case of girder to wall connection, it was observed that the stresses in the concrete wall at the points of contact to steel girder were so large. Therefore, it is also expected that the stresses in the concrete in contact with steel piles to be high. Figure 3.9-11 shows the stresses of concrete around the piles. As anticipated, large compressive stresses are created at the lower face of the wall. Although there is a great gradient of the stresses in depth, these stresses are so huge that are able to crush the concrete. Hence, a detail to prevent the crushing is required. A suggestion can be to add stiffeners to the pile at the concrete face section which will be discussed in the following section.

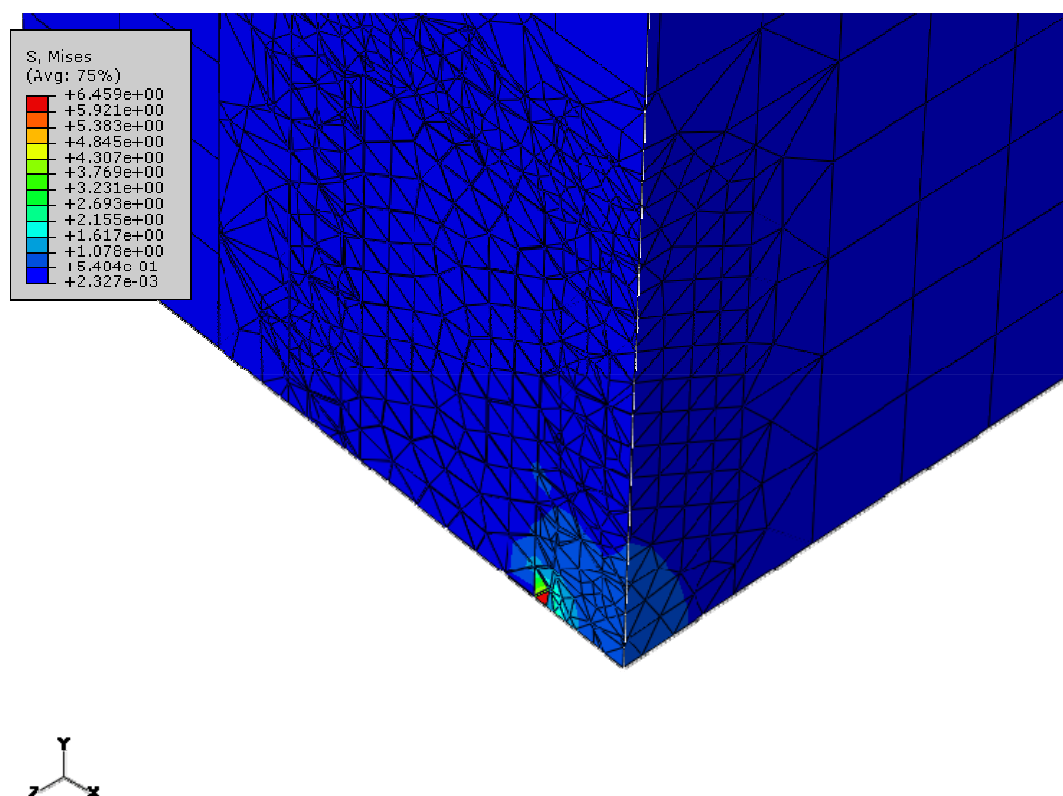


Figure 3.9-11. Mises Stresses of the Concrete Wall Around the Piles

A) Effect of Pile Stiffener

The finite element model of the abutment is run again by adding a pair of stiffeners to the HP sections of the pile at the concrete lower face section. Figure 3.9-12 shows a picture of pile stiffener. The stiffener has 0.5 inch thickness.

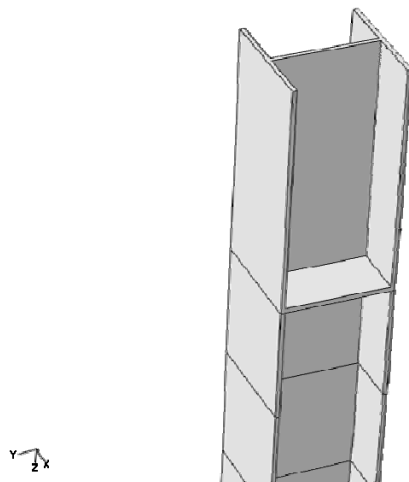


Figure 3.9-12. Stiffened Pile at the Wall Lower Face Section

As can be observed from Figure 3.9-13, the maximum stress of the concrete wall reduces to 5.31 ksi. It shows about 18 percent of reduction of the stresses. These stiffeners do not have a magnificent role in distributing the stresses in the concrete. As opposed to the case of girder-to-wall connection, this time adding stiffeners is not so effective.

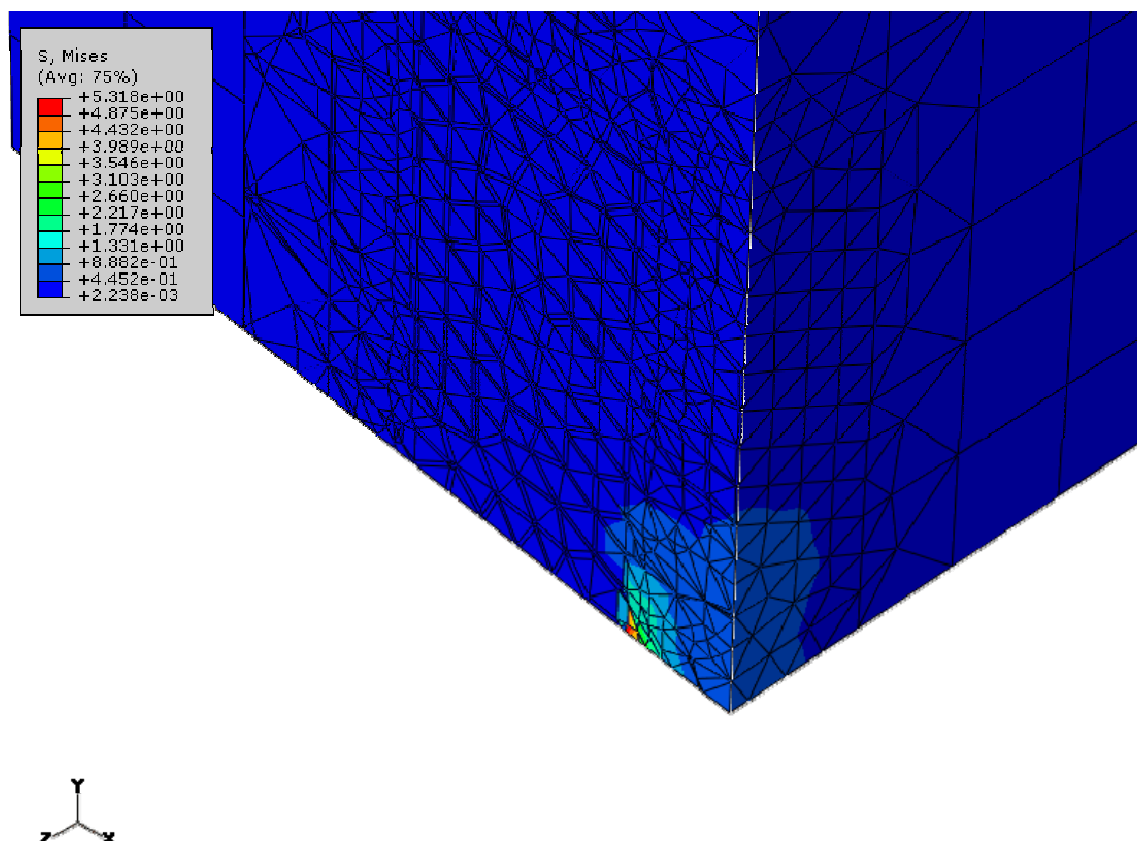


Figure 3.9-13. Mises Stresses of the Concrete Wall Around the Piles with Stiffener

3.9.4 Pile Stresses

In the conventional detail for integral abutments, the weakest elements are the piles. These piles are usually HP sections. The strongest HP section is HP14x117 which compared to the other attached elements which are the girders and abutment wall is tiny. That's why these abutments absorb a small negative moment in comparison with the capacity of the girders. Figure 3.9-14 shows the Mises stresses of the piles. The stresses illustrate a full plastic hinge in the piles just below the lower face of the concrete wall. The pile stresses start to reduce inside the wall as the distance to the concrete face gets larger. The stress at the top section of the pile is close to zero.

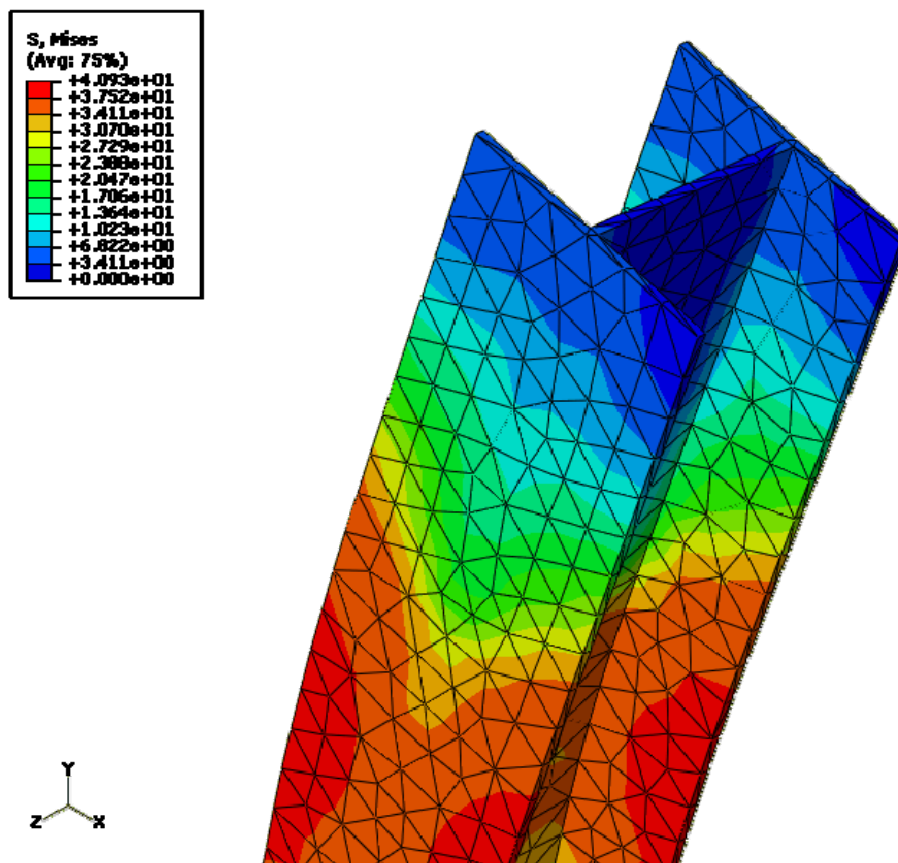


Figure 3.9-14. Mises Stresses of Abutment Piles

A) Effect of Pile Stiffener

The stresses of the piles after adding the stiffeners are illustrated in Figure 3.9-15. Comparing to Figure 3.9-14 reveals that there is a slight difference between the pile stresses with and without stiffeners. This is similar to the results for the girder stresses. In the case of the stiffened pile, the pile stresses decrease gradually inside the concrete mass so that they are almost zero at the top of the pile.

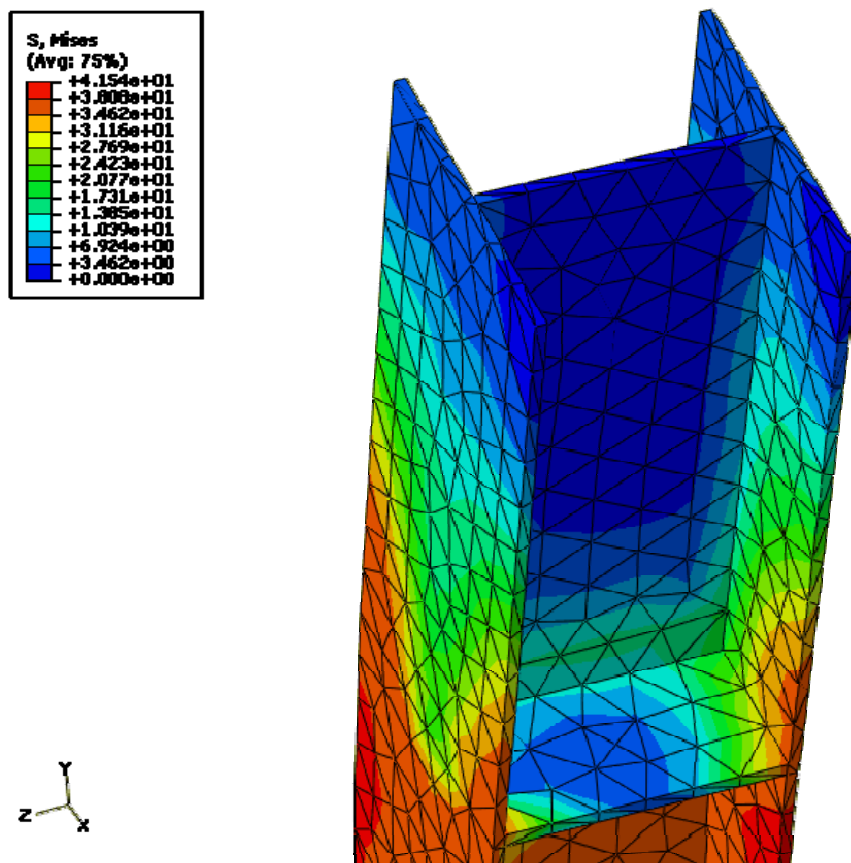


Figure 3.9-15. Mises Stresses of Abutment Piles with Stiffener

Chapter 4

Effect of Curvature on Steel I/A Bridges

4.1 Introduction

In this chapter the effect of bridge horizontal curvature on the response of integral steel I-girder bridges is studied. The baseline bridge for this part of the investigation is the I-480 Bridge in Omaha, NE. To perform such an investigation, based on that real-life bridge, several finite element models of curved integral bridges with different lengths and radii of curvature are analyzed. These bridge models have a composite steel I-girder superstructure, two integral abutments at the two ends of the bridge and one or more intermediate piers which are isolated from the bridge superstructure by means of bearings. All abutments and piers are supported on steel H-piles. More explanations on the modeled bridges are brought in the following sections. Figure 4.1-1 shows a picture of a curved steel I-girder bridge similar to the bridges that are studied in this research.



Figure 4.1-1. A Curved Steel I-girder Bridge Similar to the Studied Bridges

4.2 Bridge Configuration

The shape and dimensions of the components of the studied bridges including superstructure, abutments and piers are explained in the following subsections.

4.2.1 Superstructure

The bridge superstructure is composed of seven steel I-girders, composite concrete deck, parapets at the sides which are compositely connected to the deck and a two-inch concrete overlay which is considered as the wearing surface and is not a structural component. Figure 4.2-1 shows the cross section of the superstructure.

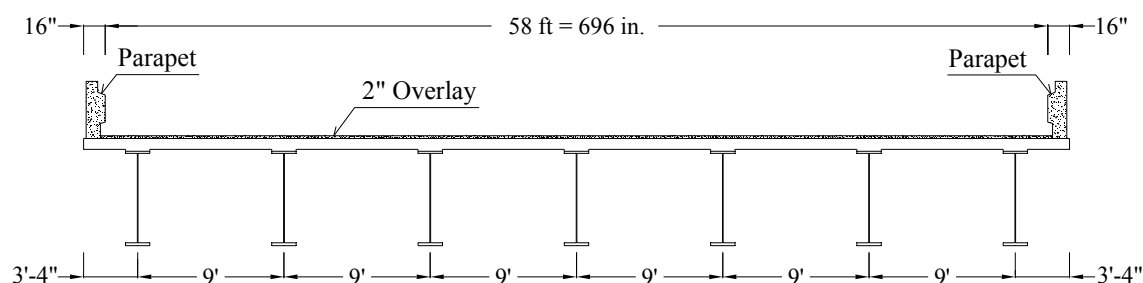


Figure 4.2-1. Cross Section of the Composite Steel Superstructure

The girders have two different cross sections at mid-span and over piers. Dimensions of different girder sections are illustrated in Figure 4.2-2. As can be seen, the depth of the web is equal to 66 inches throughout the length of the girders, but other dimensions are different for positive and negative moment regions. The total height of the steel section is 69.5 and 70.25 inches at mid-span and over the piers, respectively. The spacing of the girders is 9 feet. There is a concrete haunch of variable thickness between the girders and the deck which provides a 6% superelevation over the top flange of the girders with its variable thickness. The average thickness of the haunch is 1.5 inches over the entire length of the girders except a length of 15 feet at each side of the piers that the thickness reduces to 1 inch.

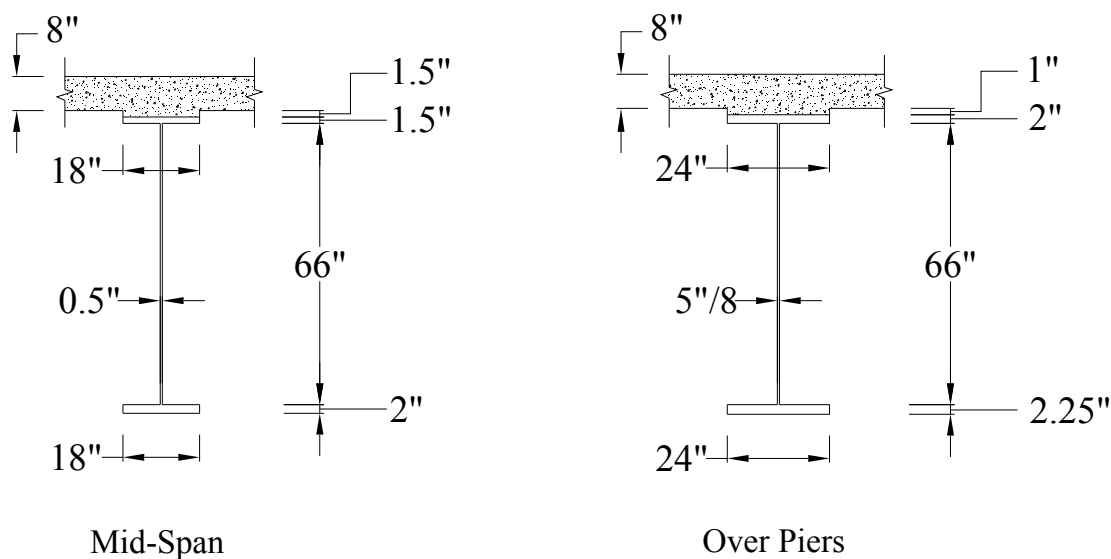


Figure 4.2-2. Steel I-Girder Dimensions

The thickness of the concrete deck is 8 inches and its width is 60'-8". The effective roadway width of the bridge is 58 feet. At the two sides of the superstructure, there are two concrete parapets which are connected to the deck using rebars. The width and height of each parapet are 16 and 42 inches, respectively.

4.2.2 Abutments

The abutments of the modeled bridges are integrally connected to the superstructure which is the main characteristic of this type of bridges. Each abutment is consisted of a concrete wall with a thickness of 3'-5 13/16" and a varying height between 9'-4" to 13'. The wall is sitting on a row of seventeen HP12x53 steel piles with a length of 70 feet and spacing of 3'-6". The wing walls of the studied bridges are separated from the abutment wall with a joint so that from a structural stand point, they are not affecting the behavior of the bridges. Also, the approach slabs are connected to the abutment wall using a pin joint detail. So, the only reaction force from the approach slab is a vertical load that is

applied to the abutment walls and then transmitted to the steel piles and the surrounding soil.

There are several details for connecting an abutment to bridge superstructure integrally, which can be found in the references. For composite steel superstructures, the integral connection can be achieved by continuing the steel girders in the concrete wall and connecting these two elements using rebars that go through the web of the girders. Figure 4.2-3 shows the details of such an integral connection.

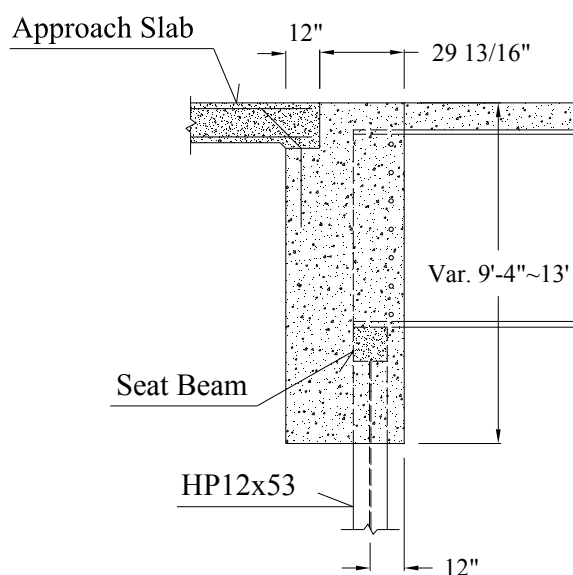


Figure 4.2-3. Abutment Integral Details

4.2.3 Piers

The piers of the studied bridges consist of two hammerhead columns, a cap beam and two pile caps each of them resting on two rows of five steel H-piles. All the components of the piers other than the H-piles are made of reinforced concrete. The columns have a 3'-6" by 10'-9" rectangular cross section and a length of 38 feet. At the top, the width of each column is gradually widened to 29'-9". The cap beam which connects the columns

to each other has a length of 59'-6", a width of 4'-6" and a varying depth from 4' to 7'-7" which provides a 6% superelevation for the bridge. The pile cap of each column is a 21x7.5x4 cubic feet concrete mass which is supported on ten HP14x89 steel piles with 95 feet length. Figure 4.2-4 shows a general picture of the piers of the studied bridges.

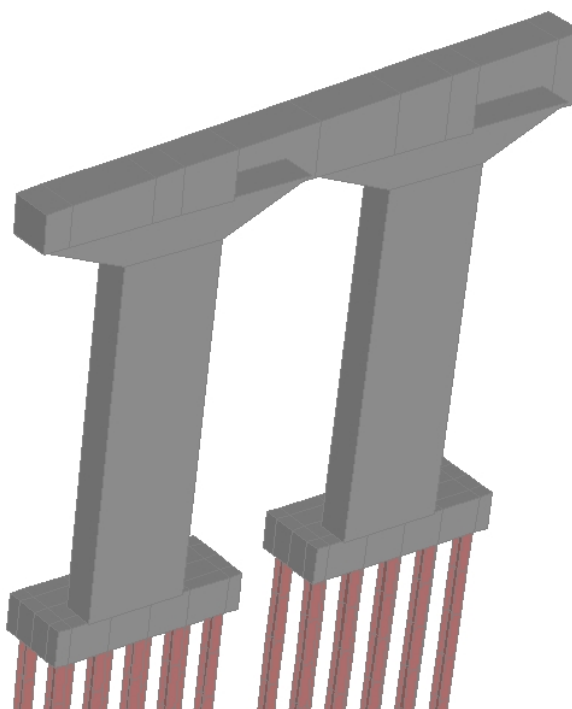


Figure 4.2-4. Pier Configuration

The superstructure is resting on piers by means of bearings which can be either elastomeric, sliding, fixed pot or guided pot. In the fixed pot bearings, the horizontal movement of the superstructure and the cap beam at the point of connection is tied to each other and the other four degrees of freedom are provided by means of an elastomeric layer which is in the pot. These elements are modeled using nonlinear gap springs. In the guided pot bearings, using a stainless steel PTFE plate and a shear key, the horizontal movement is set so that it is free in one horizontal direction and fixed in the other horizontal direction (perpendicular to the free DOF). The other four degrees of freedom

are provided by the elastomeric layer and are modeled by gap elements, similar to fixed pot bearings. Figure 4.2-5 shows the springs modeling the bearings of the piers.

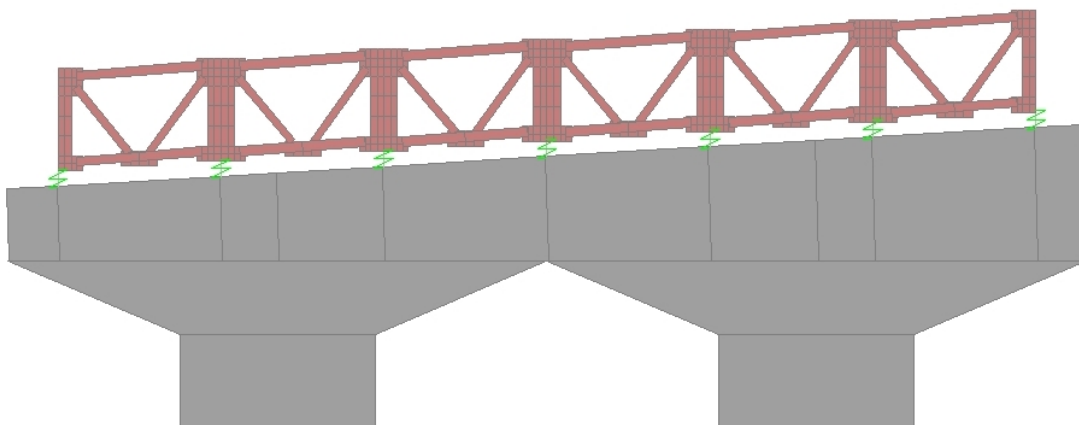


Figure 4.2-5. Springs Modeling the Bearings of the Piers

4.3 Finite Element Modeling

In this section, the characteristics of the finite element models of the studied curved steel integral abutment bridges are explained. These characteristics include material properties, loading, soil-structure interaction and the employed elements in the finite element models.

4.3.1 Material Properties

In the studied bridges, the material for I-girders flanges and webs, braces, stiffeners and all splices conforms to the requirements of ASTM A709/A709M, Grade 50 weathering steel. The steel material for H-piles conforms to ASTM A709, Grade 36. All structural steel materials have a unit weight of 490 lb/ft³, a coefficient of thermal expansion of 6.5×10^{-6} /°F, a modulus of elasticity of 29000 ksi and a Poisson ratio of 0.3.

Other components including deck slab, parapets, abutment walls, columns, cap beams and pile caps are reinforced concrete parts with a 28-day compressive strength equal to 4 ksi. These parts have a unit weight of 150 lb/ft³, a coefficient of thermal expansion of 6×10^{-6} /°F, a modulus of elasticity of 3644 ksi and a Poisson ratio of 0.2.

4.3.2 Loading

In this section, the applied loads to the modeled bridges are reviewed. These loads include the self weight of the bridge components, the weight of the wearing surface and railing, the effects of live load including gravity, braking and centrifugal forces, the pressure of soil to the abutments, the thermal loads including expansion, contraction and temperature gradient through the thickness of superstructure and the effect of concrete shrinkage. An explanation of each of these loads is presented in the following subsections.

A) Dead Load (DC)

Assuming a unit weight of 150 lb/ft³ for the reinforced concrete components and a unit weight of 490 lb/ft³ for steel components of the bridges, the dead load of the modeled bridges is applied to all elements through calculating the volume of each element.

B) Wearing Surface Load (DW)

Considering a 2-inch thick future concrete overlay with a unit weight of 145 lb/ft³, the weight of wearing surface which is equal to 1.678E-4 ksi is applied to the bridges decks. Also, the cross sectional area of each concrete side railing is assumed to be 498

in^2 , which results in a weight of 519 lb/ft along the edges of the bridges. A schematic picture of the wearing surface components is shown in Figure 4.3-1.

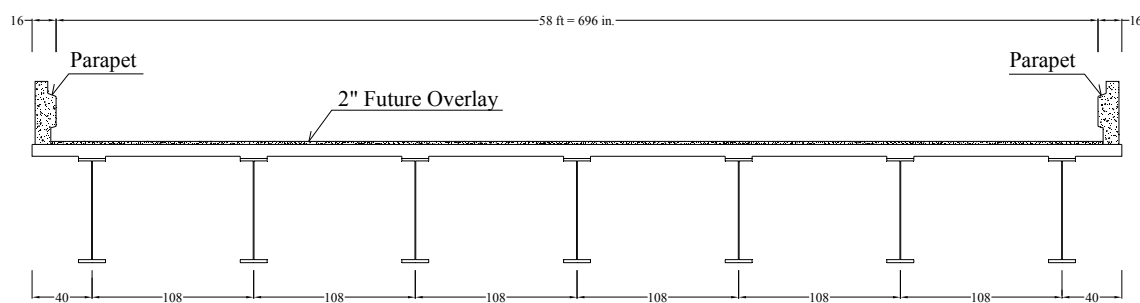


Figure 4.3-1. Wearing Surface of the Modeled Steel Bridges

C) Earth Pressure (EH)

The pressure of the backfill soil is applied to the modeled bridges assuming a cohesionless soil with a unit weight of 125 lb/ft^3 and an angle of internal friction of 30 degrees. In this way, the soil pressure is:

$$p_{soil} = k_o \gamma h = 3.617 \times 10E - 5 \times h \quad \text{Eq. 4.1}$$

In which h is depth of the soil layer in inches and p_{soil} is the soil pressure in ksi. Elaborate explanations on how the soil pressure is applied to the structure are presented in Section 4.3.4 (Soil-Structure Interaction).

D) Live Load (LL)

Live load is applied to the models based on the AASHTO LRFD Bridge Design Specifications (American Association of State Highway and Transportation Officials, 2010). According to the specifications four different loads should be considered for such continuous superstructures:

- Design truck plus the lane load
- Design tandem plus the lane load
- For negative moments and piers reaction: 90 percent of dual design trucks plus the lane load
- And again for the negative moments and piers reaction: dual tandem plus the lane load

An impact factor of 1.33 is applied to all live loads except the lane loads. In addition, a multiple lane presence factor is applied which is derived from Table 4.3-1.

Number of Loaded Lanes	Multiplication Factor
1	1.20
2	1.00
3	0.85
> 3	0.65

Table 4.3-1. Multilane Presence Factors

The live loads are applied in the most critical place in each lane so that the maximum effects are concluded. Figure 4.3-2 shows the positioning of the live load on the modeled bridge decks.

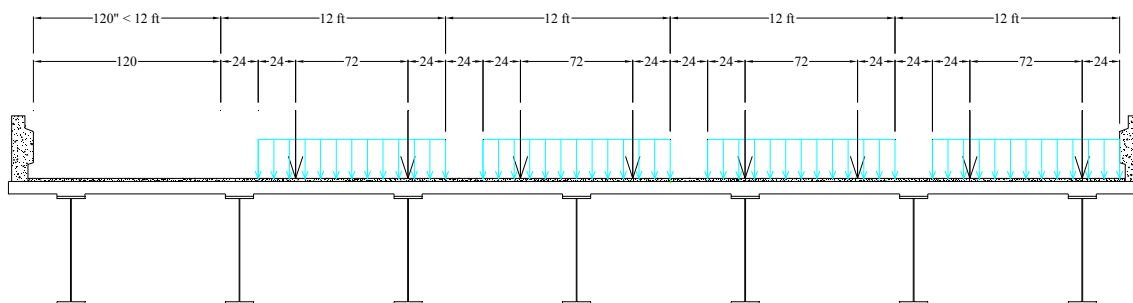


Figure 4.3-2. Positioning of the Live Load

E) Braking Force (BR)

As per AASHTO LRFD Bridge Design Specifications, the braking force for each lane is the maximum of 25 percent of the design truck weight or 5 percent of the design truck plus lane load weight. This force is calculated for different bridge lengths and applied for different positions of the live load.

It should be noted that as there are four lanes on the modeled bridges and the simultaneous braking of the live load of all the lanes is considered, a multilane presence factor based on Table 4.3-1 is applied to the braking forces. It should also be mentioned that for bridges with length of less than 450 feet, the braking force of a truck which is 25 percent of its weight is governing and this force is equal to 11.7 kips per lane:

$$F_{BR} = 72 \text{ kip} * 0.25 * 0.65 = 11.7 \text{ kip/lane}$$

For bridges with lengths more than 450 feet, the braking force based on truck plus lane loading is governing which depends on the length of the bridge:

$$F_{BR} = 0.05(72 \text{ kip} + 0.64 * L) * 0.65 = (2.34 + 0.0208 * L) \text{ kip/lane}$$

F) Centrifugal Force (CE)

When a bridge has horizontal curvature, an important lateral load which is applied to the bridge superstructure is the centrifugal force of the moving loads. Based on AASHTO LRFD Bridge Design Specification 2010, this radial force is the product of the weight of design truck or tandem and a C factor defined as:

$$C = f \frac{v^2}{Rg} \quad \text{Eq. 4.2}$$

where f is equal to 4/3 for all limit states other than fatigue, v is the design speed, R is the radius of curvature of the design lane and g is the gravitational acceleration equal to 32.2 ft/s^2 . If the parameters in this equation are in a consistent set of units, the C factor will be unitless. Actually based on Eq. 1.4 and Eq. 4.2, the centrifugal force factor should be equal to

$$C = \frac{4(e + f)}{3} = 0.28 \quad \text{Eq. 4.3}$$

But for design purposes, the structural design speed may be assumed slightly more than the geometrical design speed. Table 4.3-2 shows the values of C factor and equivalent centrifugal forces for different radii of curvature at design speeds from 35 to 60 mph. In the calculations, a multilane presence factor of 0.65 is applied for four lanes of loading. Note that the assumed design speeds are about 5 mph more than the speed given by Eq. 1.4.

Radius of Curvature (ft)	Geometrical Design Speed (mph)	Structural Design Speed (mph)	C Factor	Centrifugal Force (kips per lane)
300	30.7	35	0.364	17.04
538	41.2	45	0.335	15.68
1000	56.1	60	0.324	15.16

Table 4.3-2. C Factor for Different Radii

As can be seen, the value of the C factor is almost constant ranging from 0.324 to 0.364.

G) Wind Load (WS)

The wind load is applied to the modeled bridges based on the AASHTO LRFD Bridge Design Specification. The pressures of the wind load are assumed to be caused by a base design wind which has a speed of 100 mph. The wind pressure has a horizontal direction and is uniformly distributed over the areas of the bridge exposed to the wind as seen in the elevation view.

The pressure of design wind, P_D , is calculated using the following equation in ksf:

$$P_D = P_B \left(\frac{V_{DZ}}{V_B} \right)^2 \quad \text{Eq. 4.4}$$

in which P_B is the base wind pressure specified in Table 4.3-3, V_{DZ} (mph) is the design wind velocity at design elevation and V_B is the base wind velocity equal to 100 mph at 30.0 feet height.

Structural Component	Windward Load (ksf)	Leeward Load (ksf)
Beams	0.05	NA
Trusses, Columns and Arches	0.05	0.25
Large Flat Surfaces	0.04	NA

Table 4.3-3. Base Wind Pressure, P_B Corresponding to $V_B = 100 \text{ mph}$

The wind loading shall not be less than 0.30 klf on beam and girder components like the superstructure of the bridges.

As the bridge superstructure's elevation is more than 30 feet (the height is ranging from 43 feet to 56.44 feet), there should be an adjustment on the V_{DZ} as follows:

$$V_{DZ} = 2.5 V_o \left(\frac{V_{30}}{V_B} \right) \ln\left(\frac{Z}{Z_o}\right) \quad \text{Eq. 4.5}$$

where:

V_o : Friction velocity taken as specified in Table 4.3-4

V_{30} : Wind velocity at 30 feet above low ground or design water level assumed to be equal to $V_B = 100 \text{ mph}$

Z : Height of the structure at which wind load are being calculated measured from low ground or water level (> 30 feet)

Z_o : Friction length of upstream fetch taken as specified in Table 4.3-4

Condition	Open Country	Suburban	City
V_o (mph)	8.20	10.9	12.0
Z_o (ft)	0.23	3.28	8.20

Table 4.3-4. Values of V_o and Z_o for Various Upstream Conditions

Where the wind direction is not perpendicular to the structure, the base wind pressure P_B shall be modified as specified in Table 4.3-5.

Skew Angle of Wind (Degrees)	Girder Lateral Load (ksf)	Girder Longitudinal Load (ksf)
0	0.050	0.000
15	0.044	0.006
30	0.041	0.012
45	0.033	0.016
60	0.017	0.019

Table 4.3-5. Base Wind Pressure, P_B for Various Angles of Attack

The forces directly applied to the substructures shall be calculated using a base wind pressure of 0.040 ksf. Also, a vertical upward wind pressure of 0.020 ksf should be applied to the horizontal surfaces of the bridges.

Now, using the above equations the wind pressures on the studied bridges are calculated as follows. Assuming an open country condition for the bridge which is the most severe case, V_o will be 8.20 mph and Z_o will be 0.23 foot. As the average height of the superstructure is 49.72 feet, the design wind velocity will be:

$$V_{DZ} = 2.5 V_o \left(\frac{V_{30}}{V_B} \right) \ln \left(\frac{Z}{Z_o} \right) = 2.5 \times 8.20 \times \left(\frac{100}{100} \right) \times \ln \left(\frac{49.72}{0.23} \right) = 110.2 \text{ mph}$$

Since for the girder structures the base wind pressure, P_B , is 0.05 ksf, pressure of design wind will be:

$$P_D = P_B \left(\frac{V_{DZ}}{V_B} \right)^2 = 0.05 \left(\frac{110.2}{100} \right)^2 = 0.0607 \text{ ksf}$$

Therefore the forces on different elements of the modeled bridges will be:

$$0.0607 \text{ ksf} = 4.22 \times 10^{-4} \text{ ksi} \quad : \text{ On the vertical surface of girders and parapets}$$

$$0.020 \text{ ksf} = 1.39 \times 10^{-4} \text{ ksi} \quad : \text{ On the horizontal surface of deck}$$

$$0.040 \text{ ksf} = 2.78 \times 10^{-4} \text{ ksi} \equiv 0.01168 \frac{k}{in} \quad : \text{ On the vertical surfaces of columns}$$

As this study is mainly focused on curved bridges and there are no unique longitudinal and transverse directions for such bridges, especially for highly curved ones, after choosing the direction of the wind, the pressures should be calculated and applied to the vertical surfaces based on the different angles of attack for different parts. With a pressure of design wind equal to 0.0607 ksf, the pressures applied to the parts in an average height of 49.72 ft will be as presented in Table 4.3-6.

Skew Angle of Wind (Degrees)	Girder Lateral Load (ksi)	Girder Longitudinal Load (ksi)
0	4.22×10^{-4}	0.000
15	3.71×10^{-4}	0.51×10^{-4}
30	3.46×10^{-4}	1.01×10^{-4}
45	2.79×10^{-4}	1.35×10^{-4}
60	1.43×10^{-4}	1.60×10^{-4}

Table 4.3-6. Wind Pressure, P_D for Various Angles of Attack

H) Uniform Temperature Changes (TU)

Seasonal temperature changes are applied to the modeled bridges based on the contour maps that are given in AASHTO as the more precise method of determining the temperature changes for each region. For a steel girder bridge composite with concrete deck, a maximum design temperature of 120°F and a minimum design temperature of -30°F can be a worst case scenario that can be envisioned. An assumed construction temperature between 60°F and 70°F results in an increase of +60°F and a decrease of -100°F for the bridge structure. These two temperature changes are applied to the modeled bridges as the uniform temperature loading.

I) Temperature Gradient (TG)

The temperature gradient loading is applied to the modeled bridges based on the provisions of AASSTO LRFD Specifications. Figure 4.3-3 illustrates the considered pattern for positive gradient. Assuming a solar radiation zone “1” for the location of the modeled bridges, the temperatures T1 and T2 are equal to 54°F and 14°F, respectively.

For composite steel girder bridges, the value of A is 12 inches and t is the thickness of concrete deck. Based on these assumptions a non-uniform temperature gradient is obtained for the concrete deck and there will be no gradient in the steel girders. The negative temperature gradient is obtained by multiplying the values of positive gradient by -0.30 . These two gradient patterns are applied to the computer models.

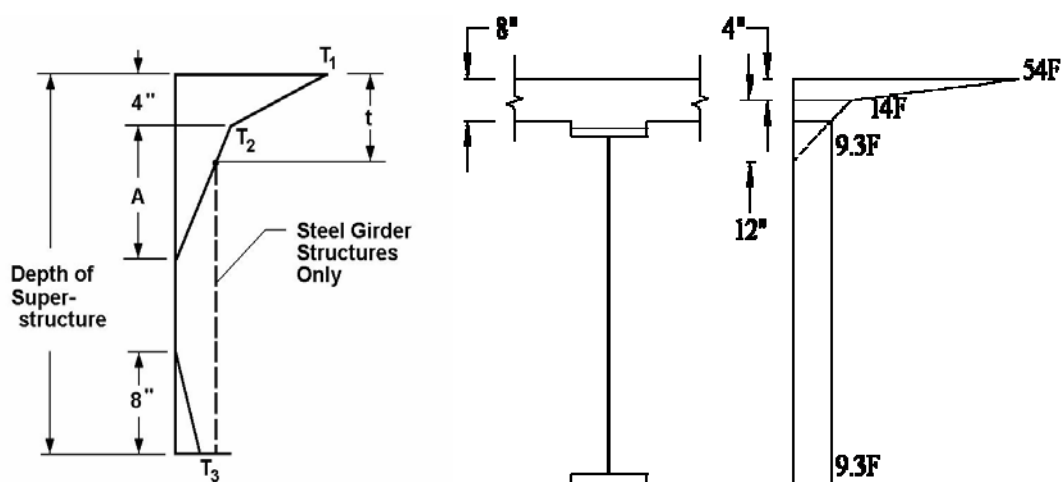


Figure 4.3-3. Positive Temperature Gradient in the Superstructure Section

J) Shrinkage (SH)

To account for the effect of concrete shrinkage in the models, first the strain due to concrete shrinkage is calculated and then the equivalent temperature decrease which causes the same amount of strain is found. In this way, the effect of concrete shrinkage is simulated by applying a temperature decrease to the concrete parts.

To calculate the strain in concrete due to shrinkage, the method presented by AASHTO LRFD is used (American Association of State Highway and Transportation Officials, 2010). In the code, the shrinkage strain is obtained using the following equation:

$$\varepsilon_{sh} = k_s k_{hs} k_f k_{td} 0.48 \times 10^{-3} \quad \text{Eq. 4.6}$$

in which:

$$k_s = 1.45 - 0.13(V/S) \geq 1.0$$

$$k_{hs} = 2 - 0.014 H$$

$$k_f = \frac{5}{1 + f'_{ci}}$$

$$k_{td} = \frac{t}{61 - 4f'_{ci} + t}$$

where:

H = relative humidity (%). In the absence of better information, H may be taken from Figure 4.3-4.

k_s = factor for the effect of the volume-to-surface ratio of the component

k_f = factor for the effect of concrete strength

k_{hs} = humidity factor for shrinkage

k_{td} = time development factor

t = maturity of concrete (day), defined as age of concrete between the end of curing and the time being considered for shrinkage effects

t_i = age of concrete at time of interest (day)

V/S = volume-to-surface ratio (in.)

f'_{ci} = specified compressive strength of concrete at time of prestressing for pre-tensioned members and at time of initial loading for non-prestressed members. If concrete age at time of initial loading is unknown, f'_{ci} may be taken as $0.80 f'_c$ (ksi).

AASHTO LRFD 2010 states that if the concrete is exposed to drying before 5 days of curing have elapsed; the shrinkage strain should be increased by 20 percent.

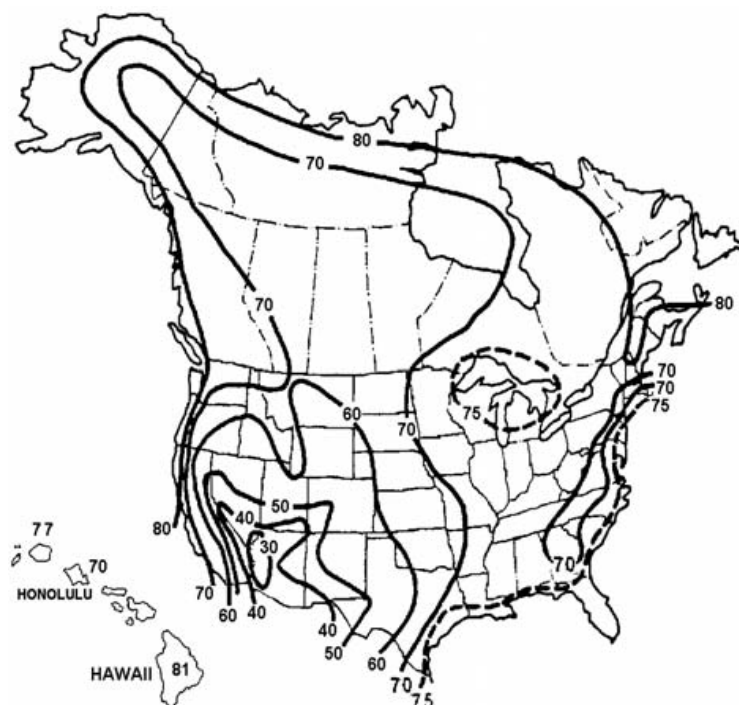


Figure 4.3-4. Annual Average Ambient Relative Humidity in Percent

For concrete deck of the superstructure, assuming a relative humidity of 70 percent for the location of the bridge under consideration, a V/S ratio equal to 4.0 inches, an f'_c of 4 ksi for superstructure concrete and a time of infinity for calculation of the time development factor, the following values are obtained:

$$\frac{V}{S} = \frac{12 \times 12 \times 8}{12 \times 12 \times 2} = 4.0$$

$$k_s = 1.45 - 0.13 \left(\frac{V}{S} \right) = 1.45 - 0.13 \times 4 = 0.93 < 1.0 \rightarrow k_s = 1.0$$

$$k_{hs} = 2 - 0.014 H = 2 - 0.014 \times 70 = 1.02$$

$$k_f = \frac{5}{1 + f'_{ci}} = \frac{5}{1 + 0.80 \times 4} = 1.19$$

$$k_{td} = \frac{t}{61 - 4f'_{ci} + t} = \frac{\infty}{61 - 4 \times 4 + \infty} = 1.0$$

For parapets the $\frac{V}{S}$ ratio and k_s are calculated as follows:

$$\frac{V}{S} = \frac{42 \times 12}{42 + 12 + 42} = 5.25$$

$$k_s = 1.45 - 0.13 \left(\frac{V}{S} \right) = 1.45 - 0.13 \times 5.25 = 0.77 < 1.0 \rightarrow k_s = 1.0$$

For abutment walls the $\frac{V}{S}$ ratio and k_s are calculated as follows:

$$\frac{V}{S} = \frac{728 \times 158 \times 48}{728 \times 158 + 158 \times 48 \times 2 + 728 \times 48} = 33.4$$

$$k_s = 1.45 - 0.13 \left(\frac{V}{S} \right) = 1.45 - 0.13 \times 33.4 = -2.89 < 1.0 \rightarrow k_s = 1.0$$

And for the pier columns the $\frac{V}{S}$ ratio and k_s are equal to:

$$\frac{V}{S} = \frac{129 \times 42}{(129 + 42) \times 2} = 15.8$$

$$k_s = 1.45 - 0.13 \left(\frac{V}{S} \right) = 1.45 - 0.13 \times 15.8 = -0.60 < 1.0 \rightarrow k_s = 1.0$$

The other coefficients including k_{hs} , k_f , k_{td} are the same as those of deck and so the shrinkage strain can be calculated as:

$$\varepsilon_{sh} = 1.0 \times 1.02 \times 1.19 \times 1.0 \times 0.48 \times 10^{-3} = 583 \times 10^{-6}$$

Now, the equivalent temperature decrease can be evaluated using the following equation:

$$\alpha \Delta T_{equiv} = -\varepsilon_{sh}$$

Hence:

$$6 \times 10^{-6} \Delta T_{equiv} = -583 \times 10^{-6}$$

$$\Delta T_{equiv} = -97.2 \text{ } ^\circ F$$

The effect of shrinkage of the concrete deck, parapets, abutment wall and pier columns is applied to the modeled bridges by assuming a contraction of -97.2°F for these parts. In this case of loading, there is no temperature change in the other elements of the bridge.

4.3.3 Load Combinations

The load combinations used for studied bridges are based on Table 3.4.1-1 of AASHTO LRFD. In general, a factored load effect can be taken as:

$$Q = \sum \eta_i \gamma_i Q_i \quad \text{Eq. 4.7}$$

in which η_i 's are load modifiers that are taken equal to unity, γ_i 's are the load factors from Table 3.4.1-1 of AASHTO LRFD and Q_i 's are the load effects. Among all the possible load combinations given in Eq. 4.7, some of them realized to be critical for the studied bridges that are discussed as follows.

For Strength I Limit State, Eq. 4.7 results in:

$$Q_{ST,I} = \gamma_p DC + \gamma_p DW + \gamma_p EH + 1.75(LL + I) + 1.75BR + 1.75CE \\ + (0.5 \text{ or } 1.2)TU + (0.5 \text{ or } 1.2)SH \quad \text{Eq. 4.8}$$

Where

$$\gamma_{p,DC} = 1.25 \text{ or } 0.90$$

$$\gamma_{p,DW} = 1.5 \text{ or } 0.65$$

$$\gamma_{p,EH} = 1.35 \text{ or } 0.90$$

The possible rational load combinations comes from maximizing or minimizing $DC + DW$, maximizing or minimizing EH , maximizing or minimizing $TU + SH$. The following eight load combinations are the final result from Eq. 4.8.

$$Q_{ST,I} = (1.25DC + 1.5DW) \text{ or } (0.9DC + 0.65DW) + (1.35 \text{ or } 0.9)EH \\ + 1.75(LL + I) + 1.75BR + 1.75CE + (0.5 \text{ or } 1.2)(TU \\ + SH) \quad \text{Eq. 4.9}$$

For the term $(TU + SH)$, it is observed that contraction and shrinkage act in the same direction, while expansion is opposite to shrinkage. Therefore, a more simplification is to take $(1.2TUE + 0.5SH)$ and $(1.2TUC + 1.2SH)$. However, the more general expression arises less questions about the possible critical combinations.

For Strength III Limit State, Eq. 4.7 yields:

$$Q_{ST,III} = (1.25DC + 1.5DW) \text{ or } (0.9DC + 0.65DW) + (1.35 \text{ or } 0.9)EH \\ + 1.4WS + (0.5 \text{ or } 1.2)(TU + SH) \quad \text{Eq. 4.10}$$

In addition to strength limit states, the bridges are also studied in service limit states. Eq. 4.7 gives the following Service I Limit State combinations:

$$Q_{Srv,I} = 1.0DC + 1.0DW + 1.0EH + 1.0(LL + I) + 1.0BR + 1.0CE + 0.3WS + 1.0WL + (0.5 \text{ or } 1.2)(TU + SH) + \gamma_{TG}TG$$

Eq. 4.11

In which γ_{TG} is equal to 0.5 for the load combinations that have live load included and equal to 1.0 when live load is not considered. These load combinations are regarded in this study on the integral bridges.

4.3.4 Soil-Structure Interaction

This section presents detailed explanation on the employed methods for calculation of the interaction forces between the elements of the modeled bridges and the adjacent soil. Based on theories of soil mechanics, the soil pressure depends on the magnitude and direction of the structure displacement. If the structure is pushed against soil, the pressure changes nonlinearly between at-rest and passive pressure. And if the structure is moving away from neighboring soil, the interaction pressure decreases nonlinearly from at-rest to active soil pressures, depending on the magnitude of the movement. To predict these nonlinear responses, there are some available methods in literature which will be used in the finite element models.

As the soil exists all around the piles of abutments or piers, but in the case of abutment walls, the soil is just in one side of the wall, there are two different soil pressure response curves for these two cases which will be explained separately in the following subsections.

A) Soil-Abutment interaction

In soil mechanics, lateral soil pressure is generally defined as a ratio of vertical earth pressure. This ratio that is known as the earth pressure coefficient is a variable that changes based on the state of interest which can be active, at-rest, passive or something between. For a wall supported laterally by soil, Clough G. W. and Duncan J. M. have performed a series of finite element analyses to perceive the soil behavior (Clough, Duncan, University of California, & Dept. of Civil Engineering, 1971). They developed a relationship between the wall movement and the soil pressure which is shown in Figure 4.3-5. As can be observed the soil pressure changes from passive pressure to active pressure based on the direction and magnitude of the wall displacement. In the present study, the curve that they have presented for an internal friction angle of 30 degrees is entered as the response curve into the finite element models.

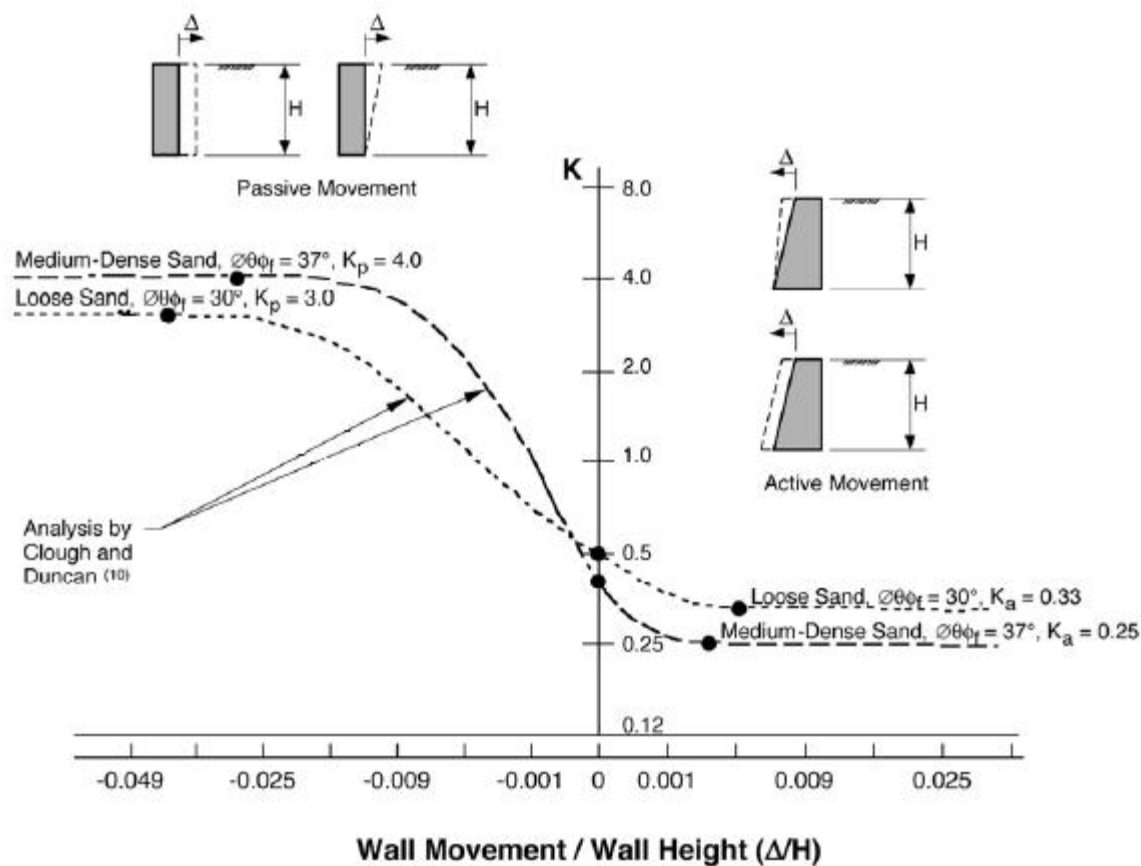


Figure 4.3-5. Relationship of Wall Movement vs. Soil Pressure

Based on the earth pressure coefficients presented in Figure 4.3-5, for an abutment wall height of 13'-2", a backfill soil with a unit weight of 125 lb/ft^3 , an internal friction angle of 30 degrees and for springs of one square foot tributary area located at different depths, the force-displacement curves of Figure 4.3-6 are obtained which are used in the finite element models.

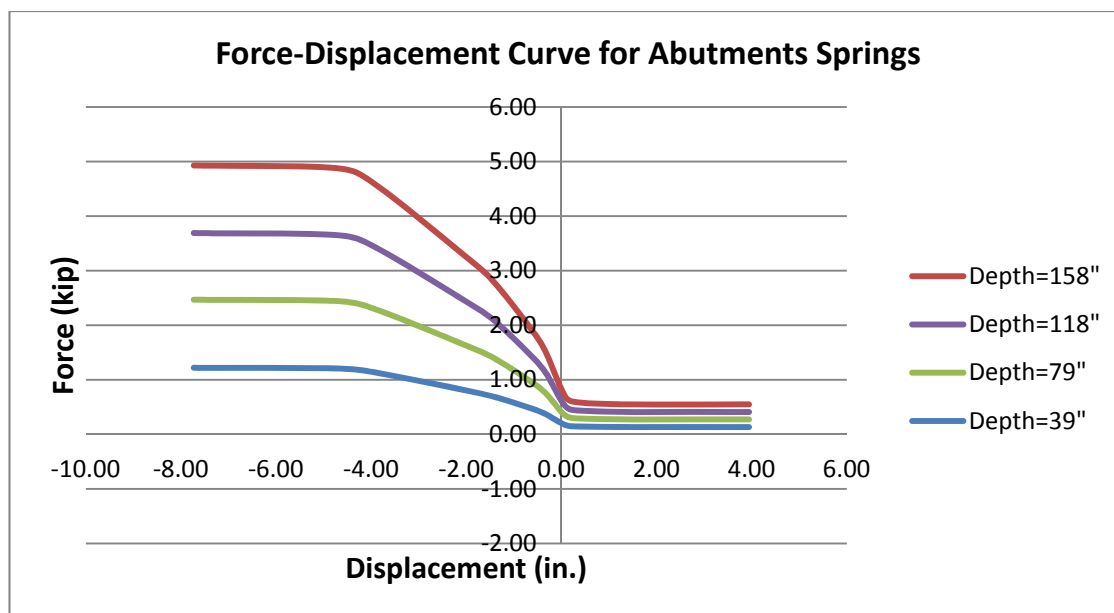


Figure 4.3-6. Force-Displacement Curves of the Abutment Backfill Springs

As the backfill of the bridge abutments are generally composed of granular soils, the response curve for abutment springs is only presented for cohesionless soils and therefore cohesive soil behavior for abutment backfill is ignored.

B) Soil-Pile Interaction

The response of the soil interacting with piles of piers or abutments is different than that for abutment walls because the piles are fully embedded in soil or in other words the soil completely surrounds the piles. So the pile movement in all directions results in pushing a mass of soil. In this way, if one wants to study this problem in 2D, for each point of the pile if the pile is not moving, the at-rest pressures of the two sides are equal and the total pressure on the pile is equal to zero. And if the pile moves in a direction, the value of the soil pressure is equal to the pressure value resulted from a displacement of the same magnitude but in the opposite direction. This 2D reasoning is valid for all horizontal directions in a 3D space and therefore displacement versus pressure curves that

are presented by the researchers is skew-symmetrical with respect to zero pile displacement.

One of the sources for solution of this problem is the recommendations of American Petroleum Institute which proposes soil response curves for both cohesive and cohesionless soils (American Petroleum Institute, 2005). The following subsections describe the API recommendations.

B1) Lateral Load-Deflection in Soft Clay

The response of soft clay under lateral loading is generally a nonlinear behavior. API proposes a p-y curve for short term static loading which may be generated from Table 4.3-7.

p/p_u	y/y_c
0	0
0.23	0.1
0.33	0.3
0.5	1
0.72	3
0.98	8
1	∞

Table 4.3-7. Proposed API p-y Curve for Soft Clay

in which:

p : actual lateral pressure

p_u : lateral bearing capacity of soft clay

y : actual lateral deflection

$$y_c = 2.5\varepsilon_c \cdot D$$

ε_c : strain which occurs at one half of the maximum stress on laboratory unconsolidated undrained compression tests of undisturbed soil samples

D : pile diameter

The lateral bearing capacity of soft clay has been found to be between $8c$ and $12c$ except at shallow depths which failure mode changes due to lack of enough overburden pressure. In the present study, this capacity is assumed to be equal to $9c$ for deep elements of the pile and for shallower positions, i.e. at depth smaller than reduced resistance zone (X_R), it is linearly increased between $3c$ and $9c$:

$$\begin{aligned} p_u &= 3c + \gamma X + J \frac{cX}{D} & \text{for } x < X_R \\ p_u &= 9c & \text{for } x \geq X_R \end{aligned} \quad \text{Eq. 4.12}$$

c : undrained shear strength for undisturbed clay samples

γ : effective unit weight of soil

J : a dimensionless empirical constant with values ranging from 0.25 to 0.5

X : depth below soil surface

X_R : depth below soil surface to bottom of reduced resistance zone. For constant soil strength with depth:

$$X_R = \frac{6D}{\frac{\gamma D}{c} + J}$$

Based on the above mentioned equations, the force-displacement curves for the springs of abutment piles are obtained which are plotted in Figure 4.3-7. These graphs correspond to the response for HP12x53 piles with spring spacing of 5 feet, soil unit weight of 125 lb/ft³, undrained cohesion of 2 ksf, J value of 0.4 and ϵ_c equal to 0.01.

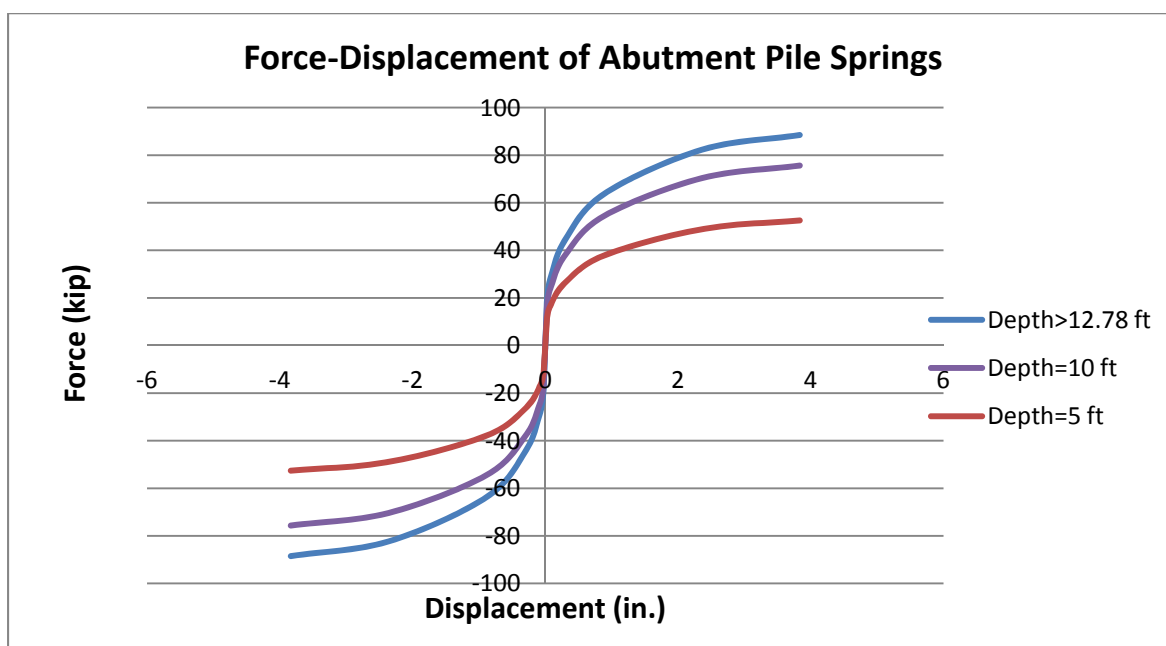


Figure 4.3-7. Force-Displacement Curves of the Springs of Piles of Abutments in Soft Clay

Also for piles of piers with HP14x89 sections, for springs of five feet spacing and the same soil properties and same J and ϵ_c values, the force-displacement curves of Figure 4.3-8 are found.

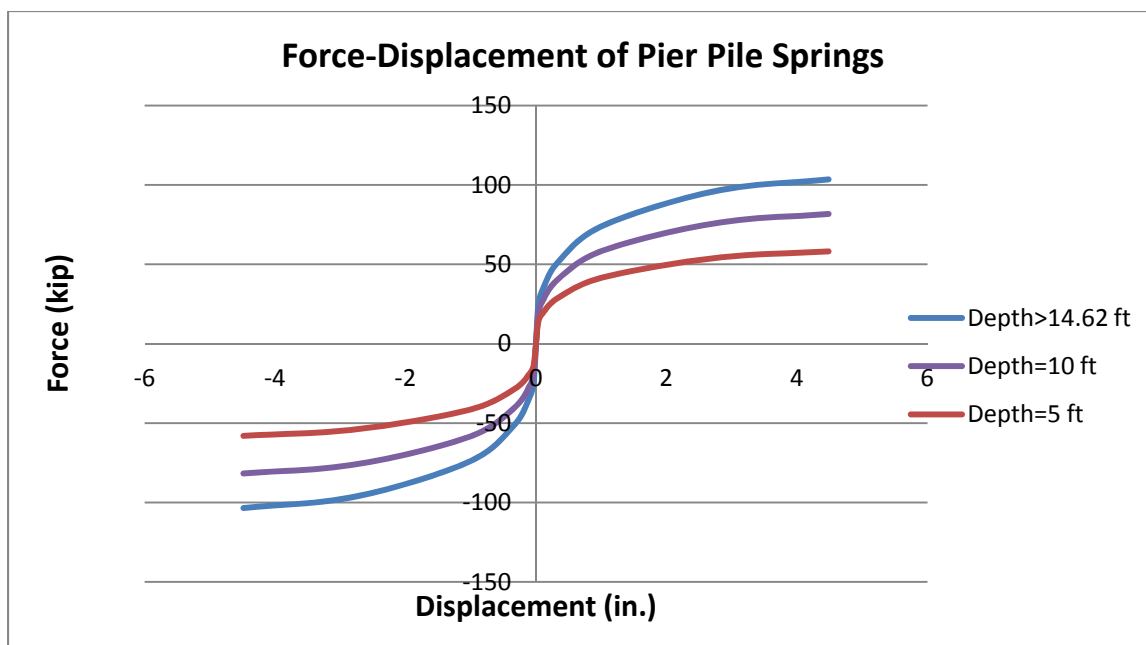


Figure 4.3-8. Force-Displacement Curves of the Springs of Piles of Piers in Soft Clay

B2) Lateral Load-Deflection in Sand

API recommends a hyperbolic tangent equation for the lateral force-displacement curve of the piles in sand as follows:

$$F_{spring} = C_0 \cdot p_u \cdot \Delta z \cdot \tanh\left(\frac{k z y}{\alpha p_u}\right) \quad \text{Eq. 4.13}$$

Where:

F_{spring} : Lateral soil resistance in a length of Δz of pile (force)

C_0 : An empirical correction factor, $C_0 = 3 - 0.8 \left(\frac{z}{D}\right) \geq 0.9$

p_u : Estimated ultimate lateral soil resistance (force/unit length)

Δz : Length of the pile section

k : Initial modulus of subgrade reaction from Figure 4.3-9

z : Depth from the top of the soil layer

y : Displacement in the horizontal direction

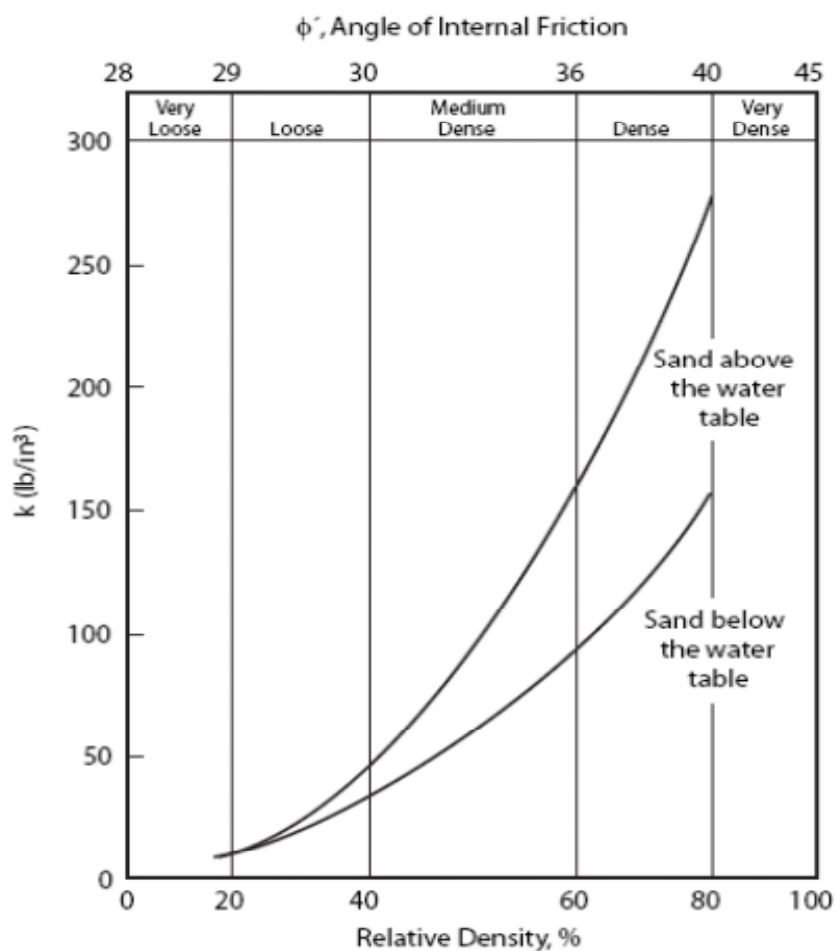


Figure 4.3-9. Initial Modulus of Subgrade Reaction

The ultimate soil lateral resistance can be obtained based on the equations given in API recommendations as the minimum of:

$$p_{us} = (C_1 z + C_2 D) \cdot \gamma' \cdot z \quad \text{Eq. 4.14}$$

And

$$p_{ud} = C_3 \cdot \gamma' \cdot D \cdot z \quad \text{Eq. 4.15}$$

where:

p_{us} : Ultimate sand lateral resistance at shallow depths (force/unit length)

p_{ud} : Ultimate sand lateral resistance at deep depths (force/unit length)

D : Pile Diameter

γ' : Effective soil density

φ : Angle of internal friction

$$C_1 = K_o \frac{\tan\varphi \tan\beta}{\tan(\beta-\varphi)\cos\alpha} + \frac{\tan^2\beta \tan\alpha}{\tan(\beta-\varphi)} + K_o \tan\beta (\tan\varphi \sin\beta - \tan\alpha)$$

$$C_2 = \frac{\tan\beta}{\tan(\beta-\varphi)} - \tan^2\left(45 - \frac{\varphi}{2}\right)$$

$$C_3 = K_o \tan\varphi \tan^4\beta + K_a(\tan^8\beta - 1)$$

$$\alpha = \varphi/2$$

$$\beta = 45 + \frac{\varphi}{2}$$

K_a : Active earth pressure coefficient

K_o : At-rest earth pressure coefficient

The values of constants C_1 , C_2 and C_3 can be found from Figure 4.3-10. This figure may also be used to check the values obtained from the relevant equations.

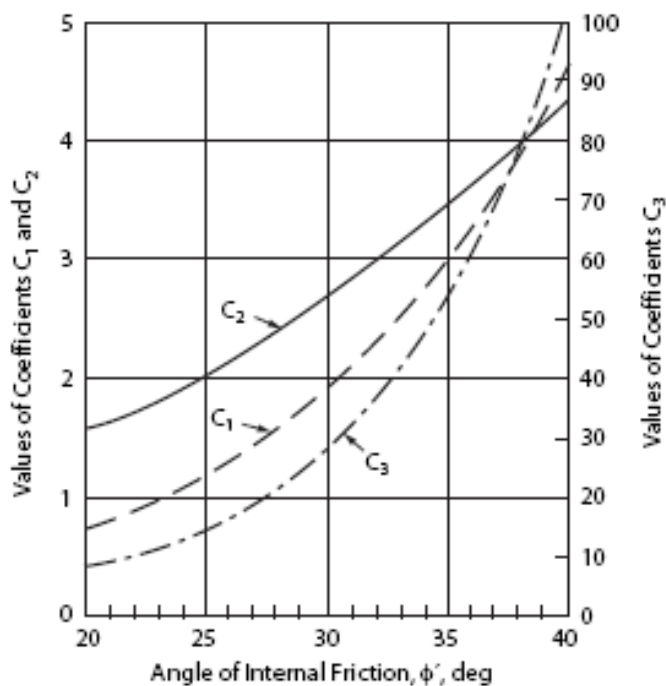


Figure 4.3-10. Values of Coefficients C_1 , C_2 and C_3 as a Function of Angle of Friction

Using the above equations and considering a width of 13.8 inches for HP14x89 piles of piers, a soil unit net weight of 125 /ft^3 , an angle of internal friction of 30 degrees and a one foot spacing for the pile springs, a k value of 45 lb/in³ is obtained from Figure 4.3-9, which results in the force-displacement curves of Figure 4.3-11 for the pile springs. As shown in these two graphs, the force-displacement curves strongly depend on the depth of the springs.

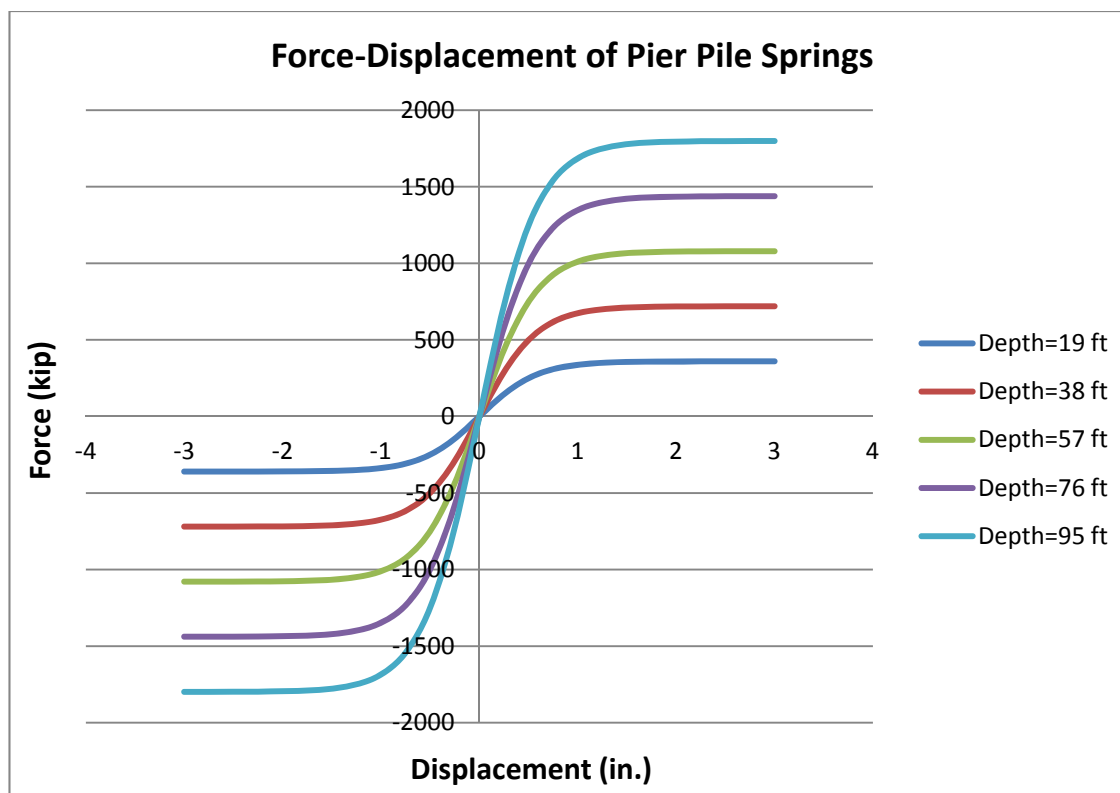


Figure 4.3-11. Force-Displacement Curves of the Springs of Piles of Piers in Sand

The response of the springs of the HP12x53 piles of the abutments can be plotted by employing the same values as used for the pier piles in the related equations and considering a width of 11.8 inches for the piles. Figure 4.3-12 shows the force-displacement curves for these springs.

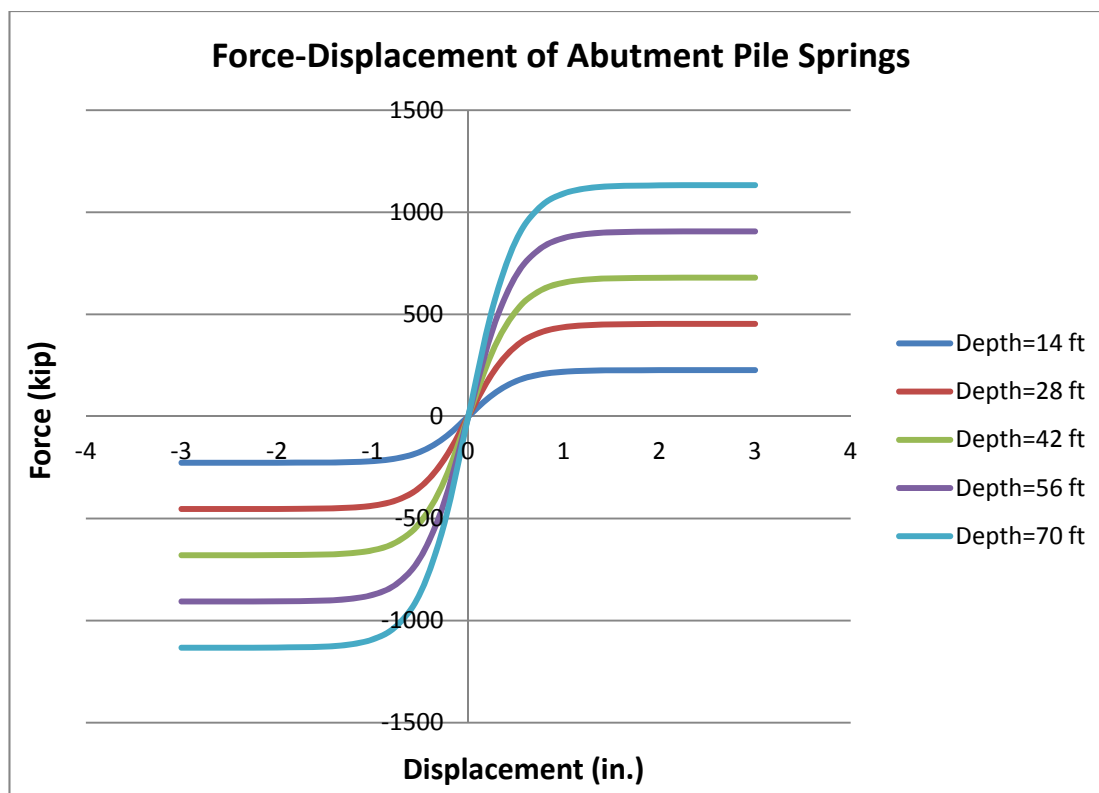


Figure 4.3-12. Force-Displacement Curves of the Springs of Piles of Abutments in Sand

4.3.5 Elements

The structures studied in this chapter are curved steel I-girder bridges with flexible integral abutments interacting with soil, having at least one intermediate pier made of concrete columns, cap beam and pile caps supported on steel piles. The piles of the piers are also in contact with the supporting soil. As can be observed, the bridge behavior is controlled by several structural elements that need different finite elements to be used for elaborate modeling. An explanation of the employed finite elements is brought in the following subsections.

A) Beam Element

To model the superstructure braces, pier columns, cap beams and also the piles of the piers and abutments, two-node frame elements are used. The frame elements have a general three dimensional beam column formulation. In these elements the effects of axial deformation, biaxial bending, torsion and biaxial shear can be modeled. A frame element is a straight line between two points. Each element has its own local coordinate system for assigning element properties and loads. Another characteristic of these elements is end offset which enables one to more accurately model the intersection of two elements, such as intersection of the columns of these bridges with the relatively rigid pile caps. The rigidity of end offsets can vary by setting a parameter called rigid zone factor to model partial to full rigidity. These elements can be loaded by gravity, multiple concentrated loads, multiple distributed loads, temperature induced loads and strain and deformation loads.

B) Shell Element

Several parts of the modeled bridges including the deck slab, parapets, flanges and webs of the I-girders, stiffeners, abutment walls and pile caps are modeled using shell elements. A shell element is a three- or four-node formulation which combines membrane and plate behaviors.

For defining material properties and loads and for getting output, each shell element has its local axes. Different types of loadings are possible in these elements including gravity and uniform loads, surface pressure on the side faces and also the top, bottom

surfaces and temperature loads. In these elements temperature-dependent, orthotropic material properties can also be defined.

Shell elements use a four-point numerical integration formulation. Stresses and internal forces and moments are calculated at the 2-by-2 Gauss integration points and then extrapolated to the joints of the element. From the difference in values of stresses or internal forces calculated from different elements attached to a common joint, an estimate error in the solution can be approximated. This is an indication of the accuracy of a given finite-element meshing and can then be used as the basis for optimizing the mesh for a new and more accurate solution.

C) Nonlinear Link Element

Nonlinear link elements are used to connect two joints together with specified nonlinear properties. Each link element may show up to three types of behavior based on the required properties and the analysis type. These properties include: linear, nonlinear and frequency-dependent.

In the modeled bridges, these link elements are used to simulate the elastomeric bearings connecting the piers to the superstructure. The properties assigned to these link elements are described here. In design of the elastomeric bearings, it is assumed that the area of the bearing should be chosen so that the pressure on the elastomeric bearing is not less than a specified value, namely one third or one fourth of the maximum allowed pressure on the bearing. This assumption yields to the fact that these types of bearings shall not in tension in any of the load combinations. On the other hand, as the maximum applied pressure on the elastomer is limited by the manufacturers (typically to 2 ksi), the

stiffness of the link element in the six degrees of freedom can be determined using the following equations. In these equations, the gravity direction of the neoprene is assumed as direction 1 and the two horizontal directions are named 2 and 3. The elastomers are circular with radius of 14 inches and have a thickness of 4 inches. The modulus of elasticity of elastomeric material is 85.3 ksi and it has a shear modulus of elasticity of 0.142 ksi.

Axial stiffness:

$$k_1 = \frac{EA}{T} = 6565 \text{ kip/in}$$

Shearing stiffness:

$$k_2 = k_3 = \frac{GA}{T} = 10.9 \text{ k/in}$$

Torsional stiffness:

$$k_{11} = \frac{GJ}{T} = 268 \text{ k.in/rad}$$

Bending stiffness:

$$k_{22} = k_{33} = \frac{EI}{T} = 80'427 \text{ k.in/rad}$$

Where:

A is the cross sectional area, E is axial modulus of elasticity, T is the rubber thickness, G is the shear modulus of elasticity, J is the torsional constant (equal to $\frac{\pi D^4}{32}$ for circular elastomers) and I is the moment of inertia of the section of the elastomeric bearing.

In this way, six stiffnesses of the bearings are calculated and entered into the finite element model. A picture of the bearing springs modeled in a pier is shown in Figure 4.3-13.

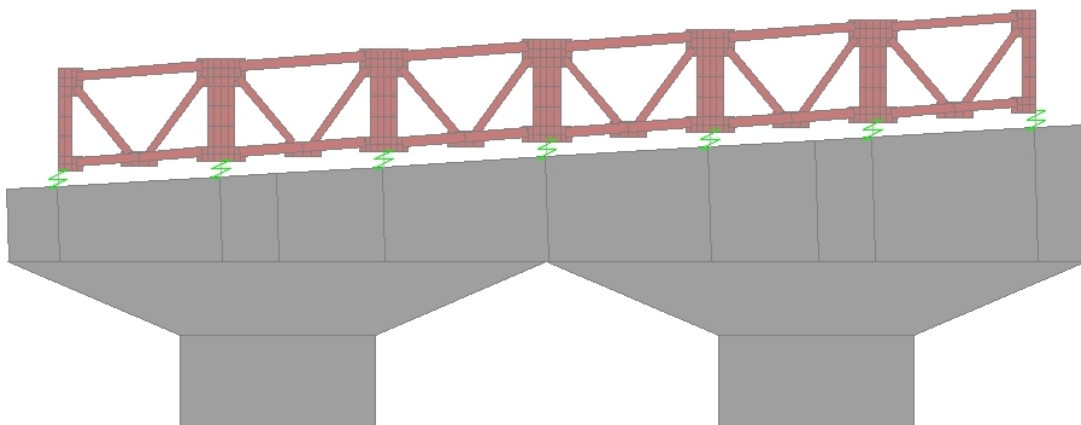


Figure 4.3-13. Modeling of the Bearings

Later in this study, the effects of fixed and guided pot bearings are also examined. For those types of bearings, if the elastomeric layer of the pot is assumed to have a circular shape with the radius of 18 inches and thickness of 1 inch, then the stiffness in the six degrees of freedom will be calculated as follows:

Axial stiffness:

$$k_1 = \frac{EA}{T} = \frac{85.3 \text{ ksi} \times \pi/4 \times 18^2 \text{ in}^2}{1 \text{ in}} = 21'700 \text{ kip/in}$$

Shearing stiffness (for fixed pots):

$$k_2 = k_3 = \infty$$

Shearing stiffness (for guided pots in the guided direction):

$$k_2 = 0$$

Shearing stiffness (for guided pots perpendicular to guided direction):

$$k_3 = \infty$$

Torsional stiffness:

$$k_{11} = \frac{GJ}{T} = \frac{0.142 \text{ ksi} \times \pi/32 \times 18^4 \text{ in}^2}{1 \text{ in}} = 1463 \text{ k.in/rad}$$

Bending stiffness:

$$k_{22} = k_{33} = \frac{EI}{T} = \frac{85.3 \text{ ksi} \times \pi/64 \times 18^4 \text{ in}^2}{1 \text{ in}} = 439'551 \text{ k.in/rad}$$

D) Nonlinear Support Element

To model the effect of the soil support which acts on the abutment walls and the surface of the piles, nonlinear support elements are used. These elements are one-node grounded nonlinear springs.

As two different types of properties are supposed to be analyzed with these elements which are soil-abutment interaction and soil-pile interaction, two different sets of properties are defined for the elements.

The first set of properties for nonlinear support elements is based on the force-displacement curves of Figure 4.3-6 which are assigned to the nonlinear springs of the abutment walls. The second set of assigned properties to nonlinear springs is based on the force-displacement curves of section 4.3.4B) which are considered for the springs that are supposed to model the behavior of the surrounding soil of the pile of abutments and piers. As the piles are embedded in the soil, the springs have the same nonlinear response in tension and compression.

4.3.6 Finite Element Models

Based on the information provided in the previous sections, a comprehensive finite element analysis study is conducted using the Nonlinear Finite Element Analysis Program SAP 2000. In the analyses, the movements and internal forces of curved integral abutment bridges are evaluated and compared to the responses of straight bridges.

In order to conduct such analyses, several finite element models of curved I-girder steel bridges with radius of curvature equal to 300, 538 and 1000 feet are analyzed. For each of these radii, the bridge is modeled in different lengths, namely; 308, 501, 694 and 887 feet. Additionally, the equivalent straight bridge of each curved model is simulated with exact same characteristics as the curved bridge except the curvature. The span length in the modeled bridges is 154 feet for the end spans and 193 feet for the middle spans. As shown before, the width of all the bridges is 60'-8". Figure 4.3-14 illustrates typical models that are made in this study.

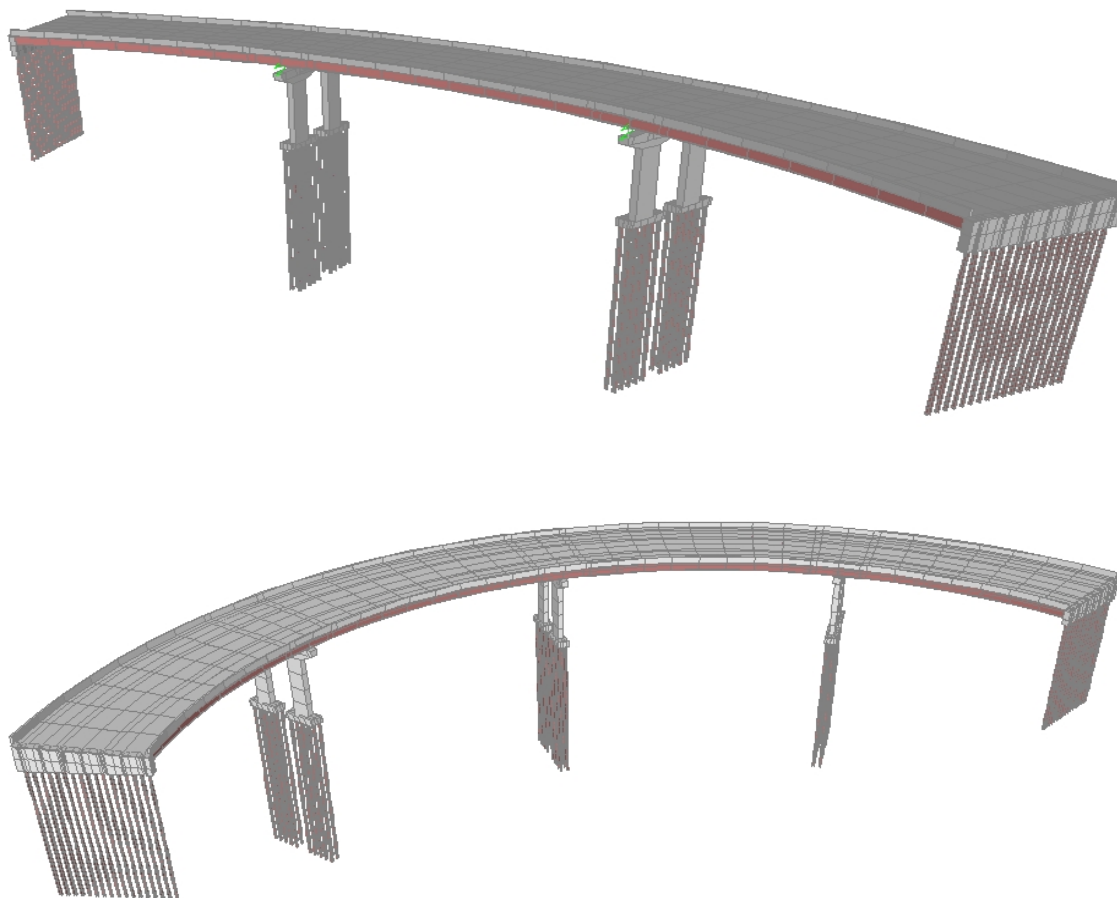


Figure 4.3-14. Typical Finite Element Models of the Studied Bridges

4.4 Results of FE Analysis

In this section, the results of the conducted finite element analyses are presented. In the analyses, different aspects of the behavior of steel I-girder integral abutment bridges are studied. These studies include:

- **Effect of Length and Curvature on Load Responses:**

A diverse set of loads are applied to the modeled bridges. The effect of bridge curvature and bridge length on the response of different elements under each load

is examined. As the critical forces in an element are determined based on factored load, the loads are combined based on the load combinations of Section 4.3.3 and the effect of length and curvature is also presented for the envelope of load combination effects.

- **Bridge Movement:**

First, it is tried to distinguish the different parameters affecting the bridge end displacement. It is observed that the maximum bridge end displacement occurs due to contraction and shrinkage. The reduction of the bridge length (or bridge shortening) due to these effects is calculated. In the case of long straight bridges, the summation of end displacements is equal to the bridge shortening. But, in curved bridges end displacements are a function of bridge shortening. A geometrical relationship is presented between shortening and displacement in curved bridges. The effect of bridge width is also included.

- **Abutment Pile Orientation:**

The orientation of abutment piles is a problem that is studied in deep for steel bridges. Researchers have two different opinions regarding the pile orientation. Some believe the piles should be oriented for strong axis bending. Some others prefer a weak axis bending. An analytical solution for this problem is presented for the case of straight bridges. For curved bridges, several finite element analyses for different bridge configurations are performed. Based on the results, a general solution to find the optimum pile orientation is presented.

- **Effect of Bearing Type and Orientation:**

First, different bearing types used in bridge industry are surveyed. The different types that are found are categorized based on their structural performance. The effect of elastomeric, fixed, guided and sliding bearings on the internal forces of the studied bridges is investigated. And the final recommendations on the bearing orientation are provided.

In the following sections, all of the above-mentioned problems are developed elaborately.

4.4.1 Effects of Length and Curvature on Load Responses

In this section, the effect of different loads on the responses of the studied integral abutment bridges is displayed. The piers of the bridges are isolated from the superstructure by means of *elastomeric* bearings. The loads and load effects that are considered include the self weight of the bridge, the weight of superstructure, live load, braking force, centrifugal force, horizontal earth pressure, expansion, contraction, positive and negative temperature gradient and finally concrete shrinkage. Since the studied bridges are composed of several elements, the examined elements should be limited to those elements that are the most critical from the design standpoint. The other factor is the inspected output. As each element has a number of different outputs such as axial or in-plane forces and also bending moments and shear forces in different directions, the study should be narrowed down to a number of the most influential output types.

With the above introduction, since the abutment piles are the most critical elements in design of integral bridges, they are chosen for the study. For those elements, the resultant bending moment and shear force are investigated as the desired output types. The following subsections show the results of the finite element studies on these element outputs.

The other problem is the magnitude of the internal forces in each element due to each load. It should be noticed that the responses are totally different in a manner that the responses under some of the loads are tens of times of the response due to some other loads. So, all loads should not be considered of the same effectiveness. A weight function is defined for each response of the elements which shows the significance of that type of loading for that set of elements. The definition of the weight function is as below:

$$\text{Internal Force Ratio} = \frac{\text{Factored Response}}{\text{Maximum Response in Different Load Combinations}}$$

For example the weight function for dead load moment of pile of abutments is:

$$\text{Dead Load Moment Ratio} = \frac{\text{Factored Dead Load Moment}}{\text{Maximum Moment in Different Load Combinations}}$$

And then the average of the internal force ratios is calculated for different bridge as follows:

$$\text{Average Ratio} = \text{Average of the Ratios for Different Bridge lengths and Radii}$$

And the normalized weight factor for each load case is obtained using the following equation:

$$\text{Normalized Weight Factor of a Load} = \frac{\text{Average Ratio of the Load}}{\text{Sum of the Average Ratios of All Loads}}$$

A) Bending Moment of Abutment Piles

As the piles of abutment are assumed to be integrally connected to the abutment wall, the maximum moment is produced in the upper section of each pile. And since due to application of different loads, there are bending moments in both longitudinal and transverse directions of the bridge, the resultant moment is calculated for each pile. In the following parts, this resultant moment due to each of the considered loads are studied. The loads are presented based on their weight functions. The normalized weight factors are tabulated in Table 4.4-1.

Load Case	Normalized Weight Factor
Contraction	31
Expansion	14
Live Load	12
Wind Load	11
Dead Load	11
Shrinkage	8
Earth Pressure	6
Centrifugal Force	3
Weight of Wearing Surface	2
Braking Force	1
Temperature Gradient (+)ve	0
Temperature Gradient (-)ve	0

Table 4.4-1. Normalized Weight Factors for Bending Moment of Abutment Piles

The fact that should be mentioned about these weight factors is that these factors are not the percentage of participation of the load compared to other loads in a load combination. These factors show the relative magnitude of the moments due to different load. For example, in some bridges factored contraction moment can be about 95 percent of the critical load combinations moment, while its normalized weight factor is 31.

A1) Contraction

Contraction with a normalized weight factor of 31 is the most effective loading for the studied bridges. In straight bridges, contraction moments in abutment piles have an increasing trend with increase of bridge length. Figure 4.4-1 shows the curves of moment versus length for different radii. In curved bridges with large radius of curvature, i.e. radius of 1000 feet, the moments due to contraction tend to increase as the length increases, but the increase is not as strict as the case of straight bridges. For bridges with radius of 300 and 538 feet, the moment increases up to length of about 500 to 600 feet, then it starts to decrease for longer bridges.

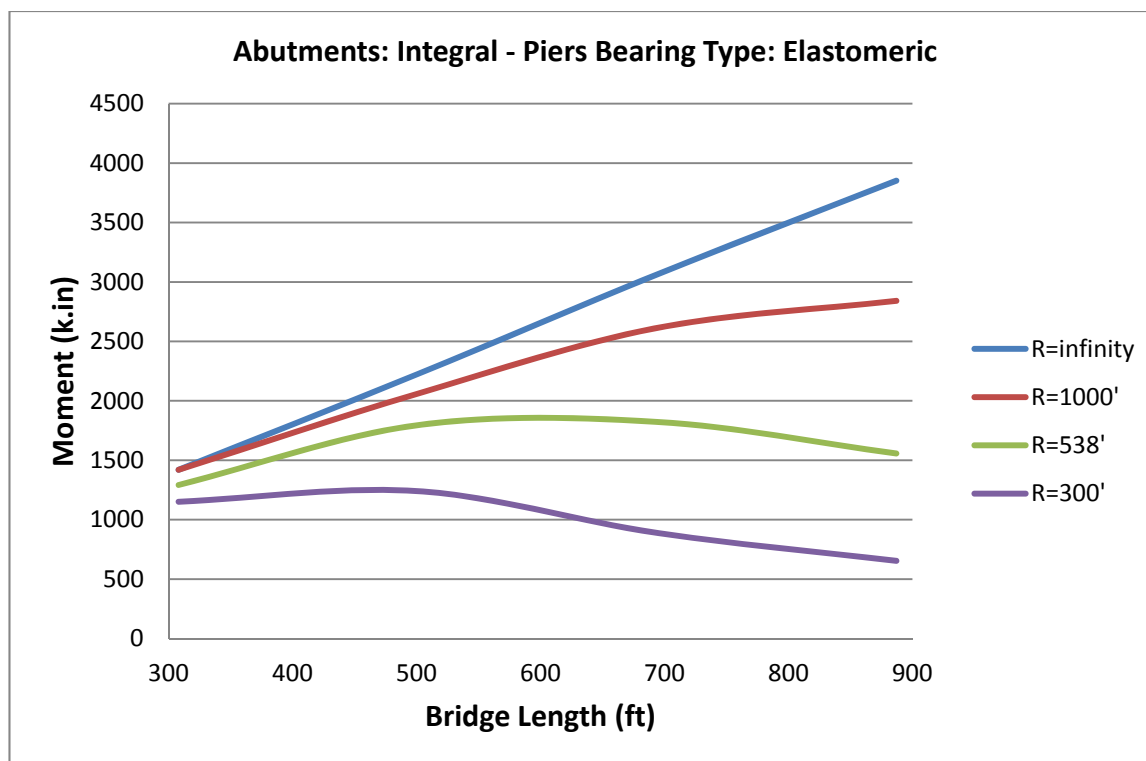


Figure 4.4-1. Maximum Moment in Abutment Piles Due to Contraction

To have a better understanding of how the moments reduce for long bridges, the moments in piles of bridges of different radii are divided by the moment of the straight bridge of the same length. In this way, a set of Normalized moments are calculated which are plotted in Figure 4.4-2.

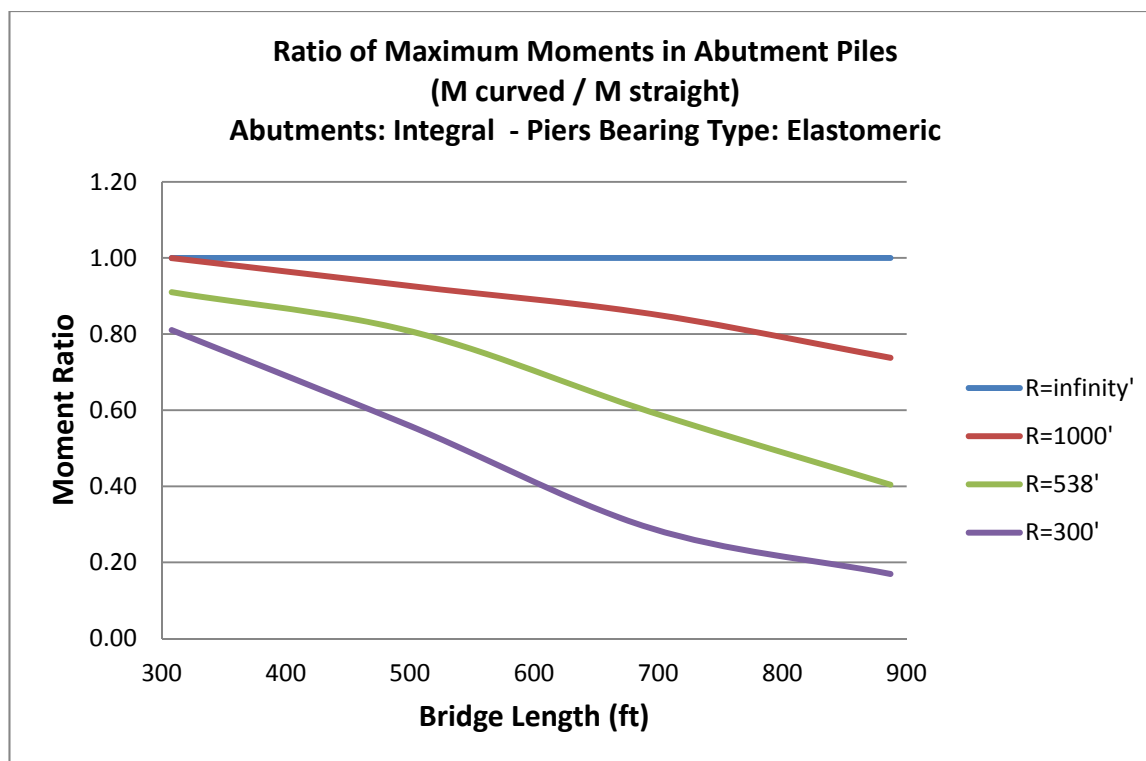


Figure 4.4-2. Normalized Moment in Abutment Piles Due to Contraction

As can be observed from the above graph, the pile moments in a bridge with $R=300'$ and $L=887'$ is about 17 percent of the pile moment in a straight bridge of the same length. This shows that the abutment pile moments due to contraction not only do not necessarily increase as the bridge length increases but also they may be reduced considerably for long bridges.

A2) Expansion

Expansion is the second load that is studied because it has the second greatest weight factor. The bending moment in abutment piles of straight bridges show a strictly increasing trend as the length of the bridge increases. But in curved bridges, the moments of the abutment piles get larger values due to increase in the length of short bridges. But beyond a specific length which depends of the radius of curvature, the moments start to

drop off. The other noticeable point is that the values of pile moments in expansion are considerably lower than those due to contraction. There are two reasons for this difference. The first one is the magnitude of the considered temperature changes. The temperature increase is $+60^{\circ}\text{F}$ while the temperature decrease is -100°F . The other reason for lower moments compared to contraction is the soil resistance. When bridge expands, the abutment walls are pushed against the backfill soil, and soil tries to decrease the movement of bridge ends. That's why in a straight bridge with $L=887$ feet, the pile moment due to expansion is about 1100 k.in and that moment caused by contraction is about 3800 k.in.

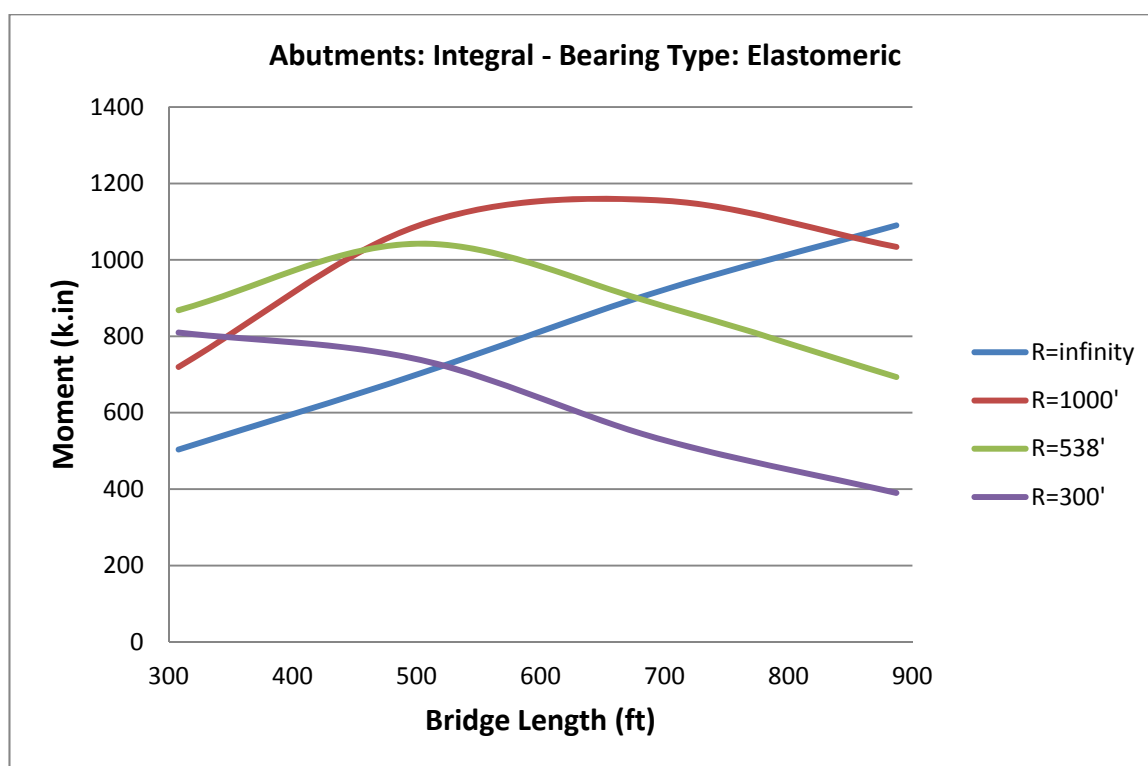


Figure 4.4-3. Maximum Moment in Abutment Piles Due to Expansion

In order to have a better view of the relative values of the moments of the studied bridges due to expansion, a normalized graph of the curves is presented in Figure 4.4-4.

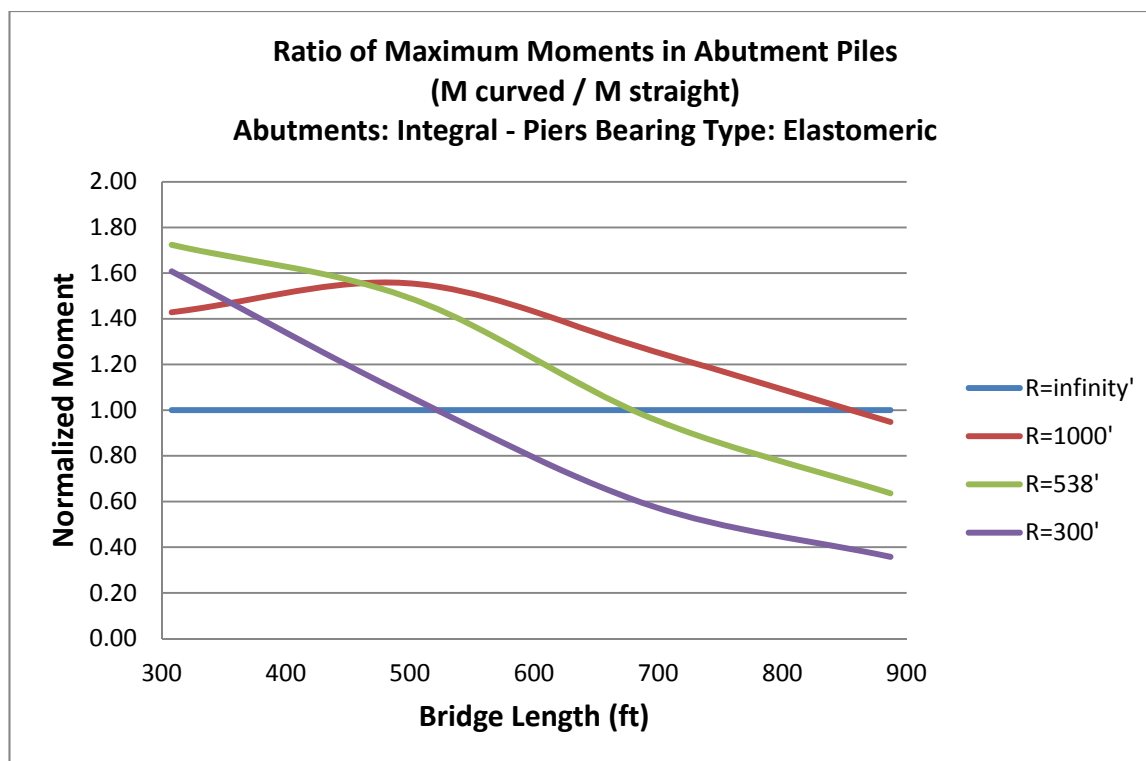


Figure 4.4-4. Normalized Moment in Abutment Piles Due to Expansion

The observable fact from Figure 4.4-4 is that the magnitude of abutment pile expansion moments in a long curved bridge ($L=887$ feet) with a radius of 300 feet is less than 40 percent of that of a straight bridge. In shorter bridges, the pile moments of curved bridges are greater than those of straight bridges. The reason of larger moments in shorter curved bridges is the lateral displacement of the abutment wall due to bridge expansion which bends the piles about their strong axes and causes large moment in piles. In the case of straight bridges, because of symmetry there is not large lateral displacement due to expansion.

A3) Live Load

In the table of weight factors live load is in the third place which shows the relatively high values of internal moments developed by live load in the abutment piles. As can be

seen in Figure 4.4-5, these moments cover a range between 450 k.in and 650 k.in. The important problem about live load moments is that the values of live load moments increase as the number of spans increases from two to three. The moments reach a plateau for bridges with three or more spans. This is because of patterned loading of the live load.

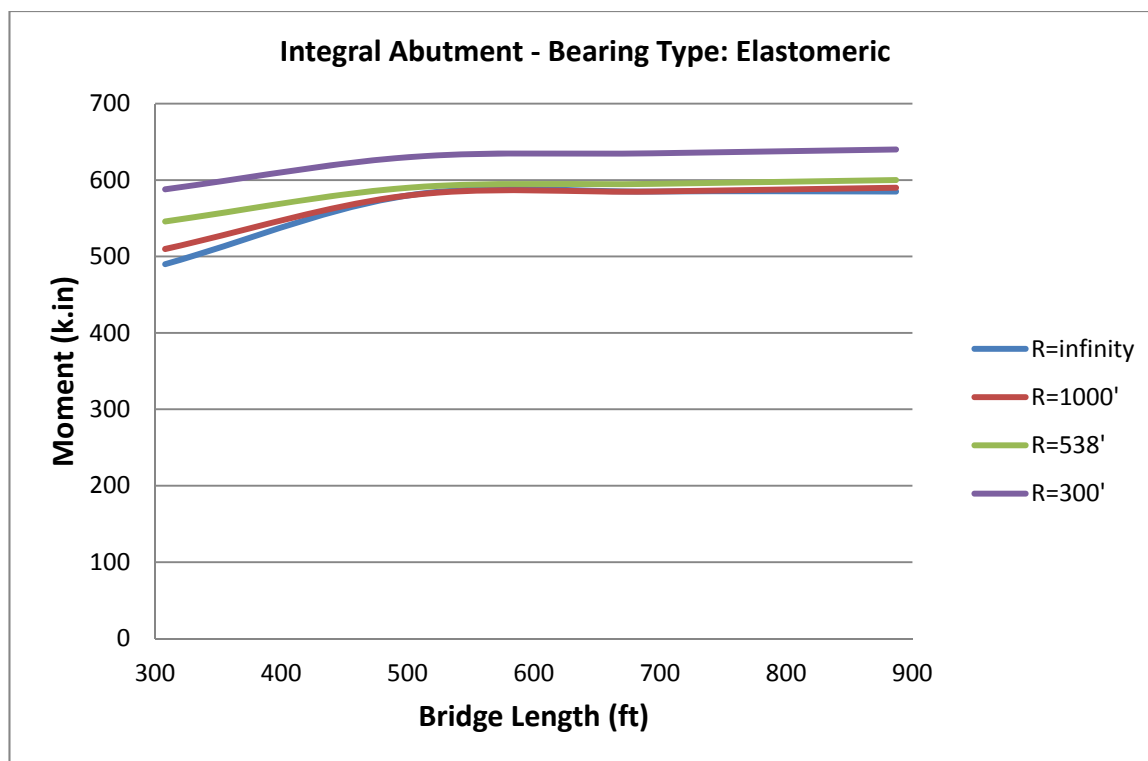


Figure 4.4-5. Maximum Moment in Abutment Piles Due to Live Load

By dividing the pile moments of bridges of different radii to the moment of the piles of straight bridge of the same length, a normalized moment graph is produced which is depicted in Figure 4.4-6. The moments are at most 20 percent larger than the moments of straight bridges for shorter bridges and are within 10 percent of those of straight bridges for long bridges.

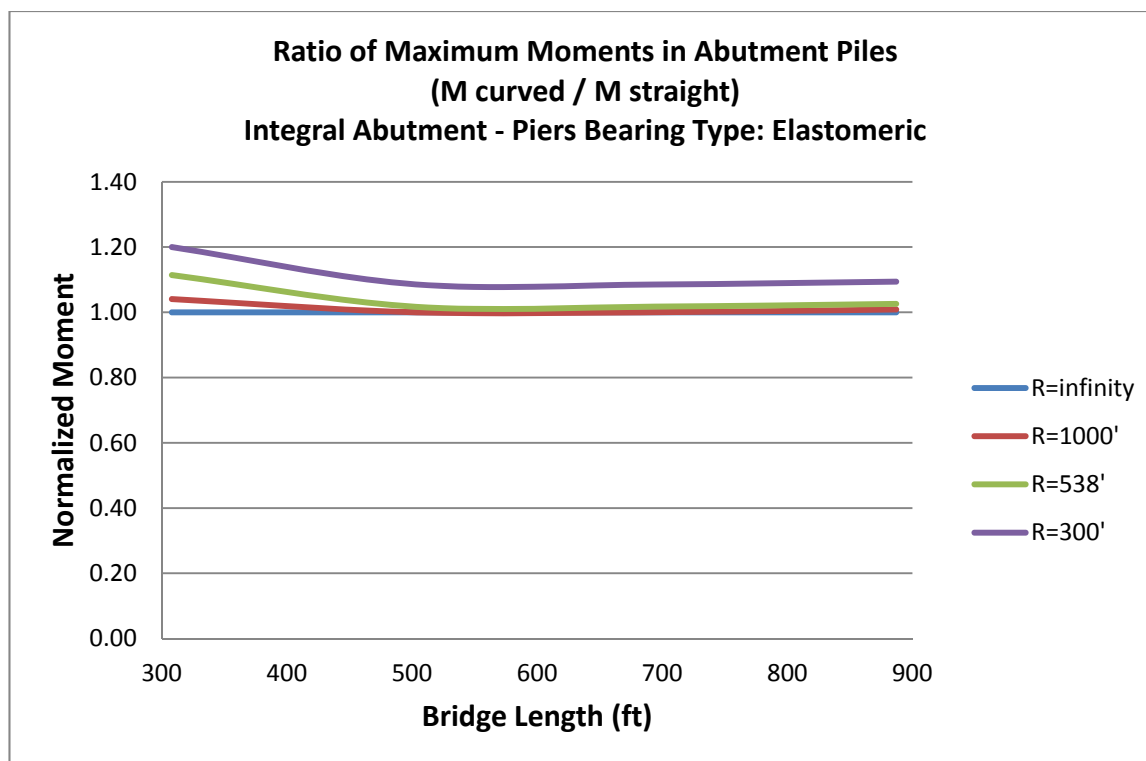


Figure 4.4-6. Normalized Moment in Abutment Piles Due to Live Load

A4) Wind Load

Lateral load transfer mechanism in integral abutment bridges is totally different than that of jointed bridges. That's why wind load has such a high weight factor in integral bridges. As the piers of the studied bridges are assumed to be connected to the superstructure by means of elastomeric bearings, and the abutments are integrally connected to the superstructure, the larger stiffness of the abutments absorbs almost all the lateral loads applied to the bridge. This problem is more magnified when the length of the bridge increases. As shown in Figure 4.4-7, the moments in the abutment piles of bridges of $L=300$ feet have a maximum of about 400 k.in and for length of about 900 feet, the maximum is about 900 k.in. This could lead to high stresses in the piles if there were live load and centrifugal force on the bridge simultaneously. But the load

combinations that include stormy conditions assume no live load on the bridge. Because of this approach, which is reasonable, wind load is not a terribly critical load case on integral abutment bridge. However, the current studies show that the wind load combinations should always be considered for abutment piles.

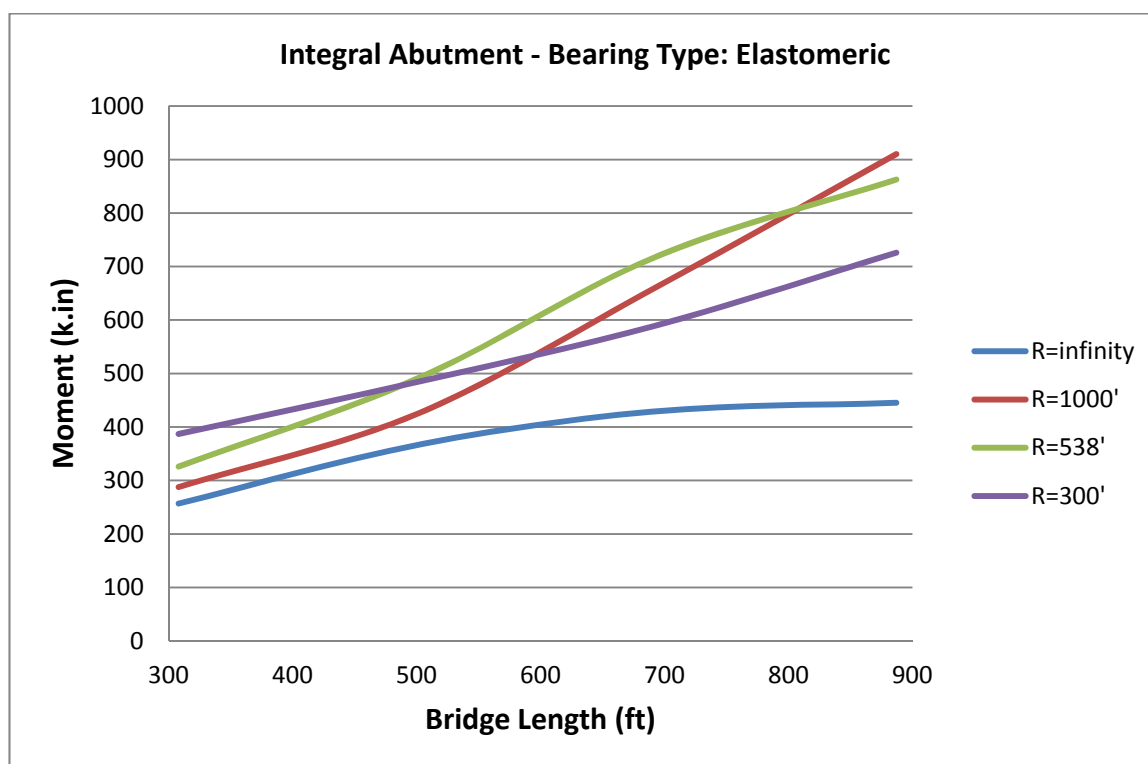


Figure 4.4-7. Maximum Moment in Abutment Piles Due to Wind Load

A graph of the ratio of the moments of curved bridges to the moment of the straight bridge of the same length is shown in Figure 4.4-8. These ratios have a maximum of about 1.5 for shorter bridges and a maximum of 2 for longer bridges which shows the vulnerability of curved bridges to wind load. It's because the wind major effect on the abutment of straight bridges is in lateral direction and the abutment stiffness in lateral direction is much larger than the stiffness in longitudinal direction. Wind can have a

major component in the longitudinal direction of curved bridges which causes larger displacement and so larger moments in the abutment piles.

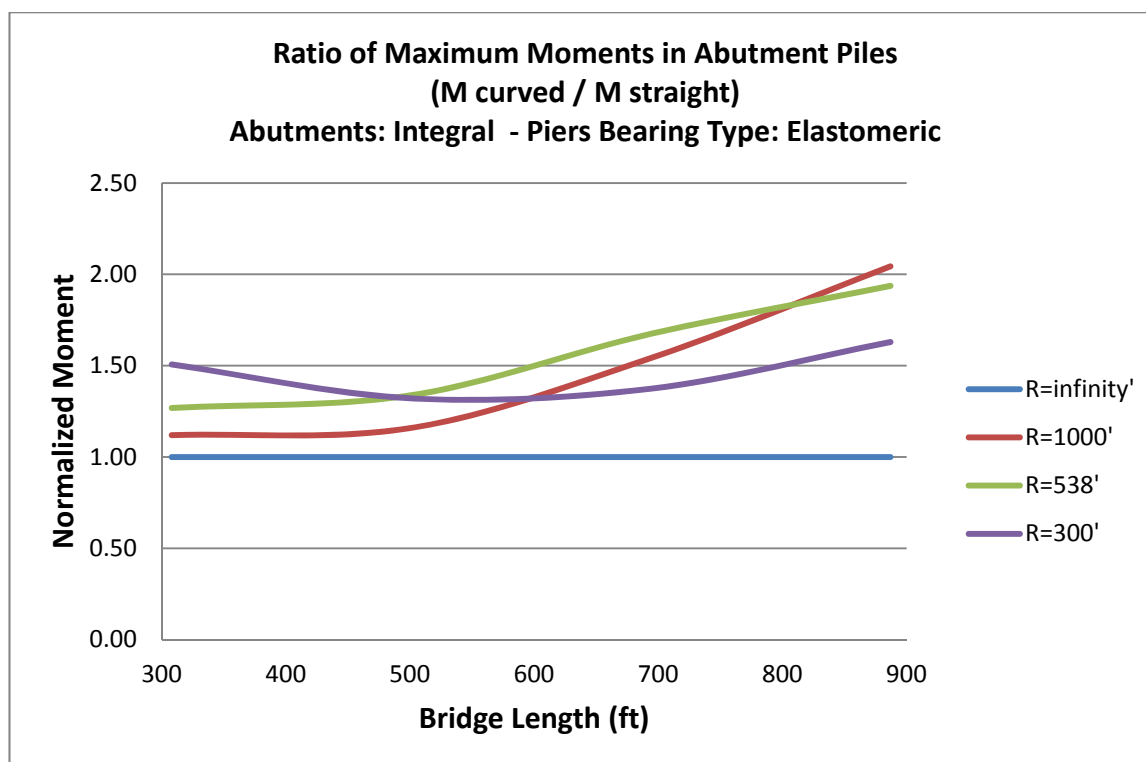


Figure 4.4-8. Normalized Moment in Abutment Piles Due to Wind Load

A5) Dead Load

Dead load effect on the abutment of bridges depends on the sequence of the construction. Based on the stages that a bridge is constructed, the internal forces in the components can be totally different. In a bridge which most of the end span is covered by the elements cantilevered to piers, the dead load effects on the abutment are minimal at the end of construction. But in a bridge with a large number of temporary supports that are removed at the end of construction, the forces in the abutment can be much larger. In the studied bridges, the dead weight of the bridge is applied to the models in a single stage which simulates the second example with temporary supports. The shapes of the

curves of the piles dead load moments versus bridge length are illustrated in Figure 4.4-9.

It shows that the moments decrease as the bridge length increases.

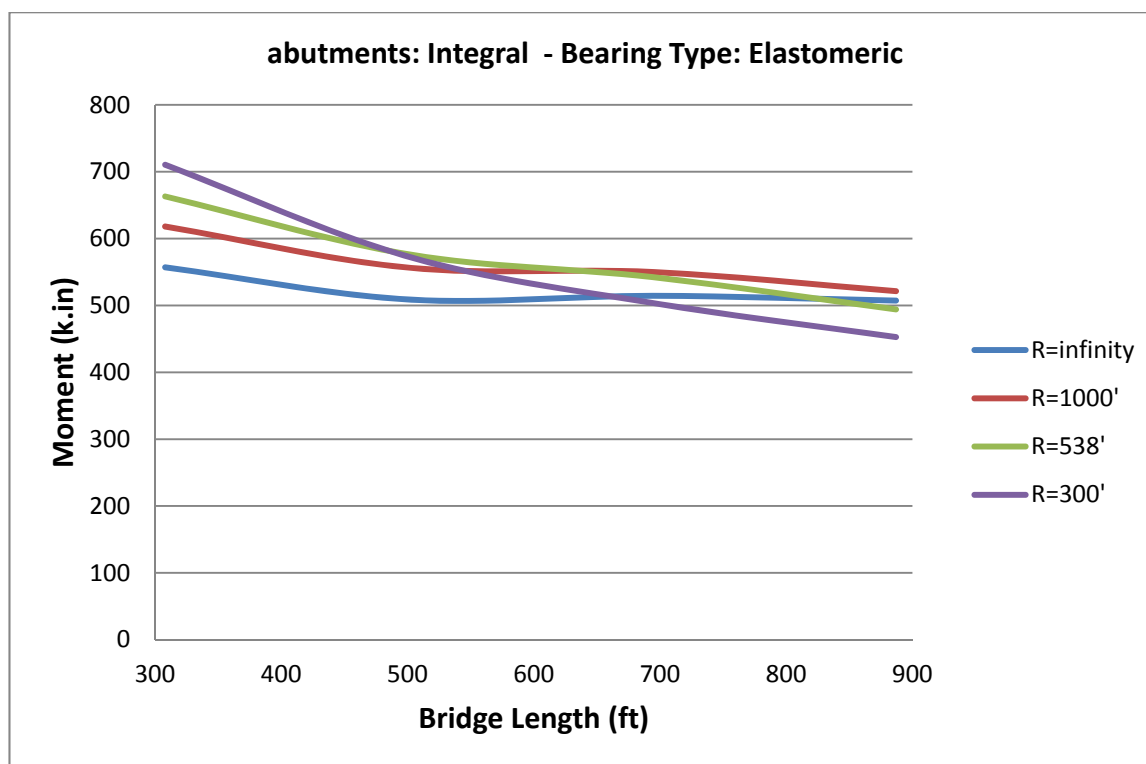


Figure 4.4-9. Maximum Moment in Abutment Piles Due to Dead Load

The magnitude of dead load moment reduction can be seen in Figure 4.4-10. The maximum decrease is for the bridge with the smallest radius which decreases from 1.3 times of equivalent straight bridge moment to about 0.9 times of that.

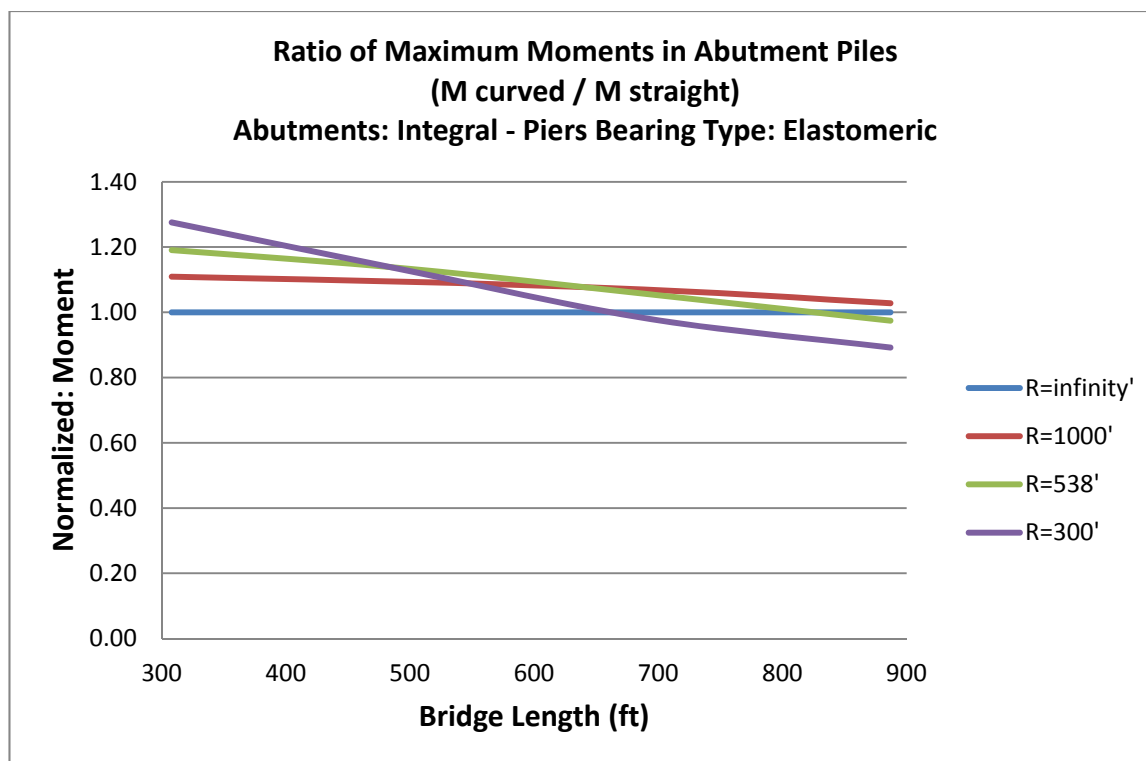


Figure 4.4-10. Normalized Moment in Abutment Piles Due to Dead Load

A6) Concrete Shrinkage

In the literature related to structural effects of concrete deck shrinkage in composite steel bridges, this phenomenon is regarded as a secondary effect in bridge structures. But in the studied bridges, concrete shrinkage showed a noticeable effect on the abutment piles. It can be observed from Figure 4.4-11 that shrinkage can cause moments up to about 1100 k.in in the abutment piles of straight bridges which is a large moment. This behavior is seen, but not of the same severity, in bridges with a radius of 1000 feet. But in bridges with a radius of 300 or 538 feet, the pile moments are not increasing for bridges longer than 500 or 600 feet. In these bridges, a maximum moment of about 660 k.in is read which shows the better performance of highly curved bridges under shrinkage load effects.

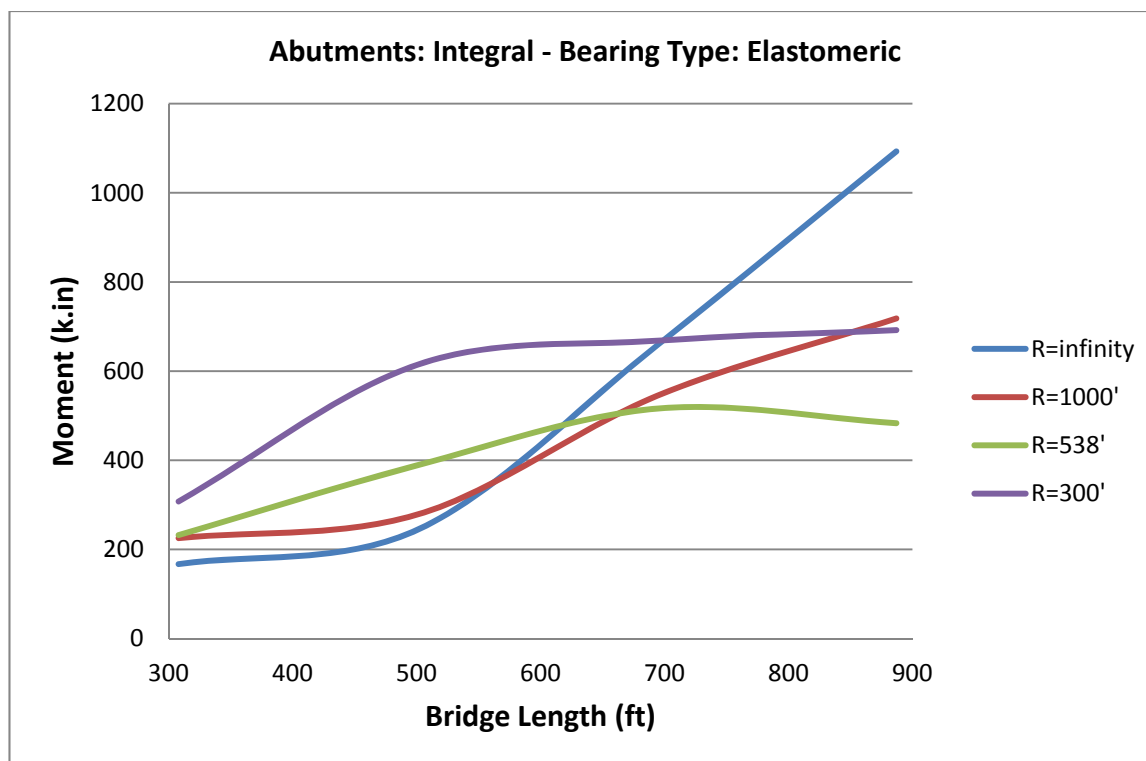


Figure 4.4-11. Maximum Moment in Abutment Piles Due to Concrete Shrinkage

The pattern of changes of moments versus length for different radii shows that for shorter bridges shrinkage creates larger moments compared to straight bridges. But, as illustrated in Figure 4.4-12, in longer bridges ($L=887'$), shrinkage moments are less than 70 percent of those of straight bridges.

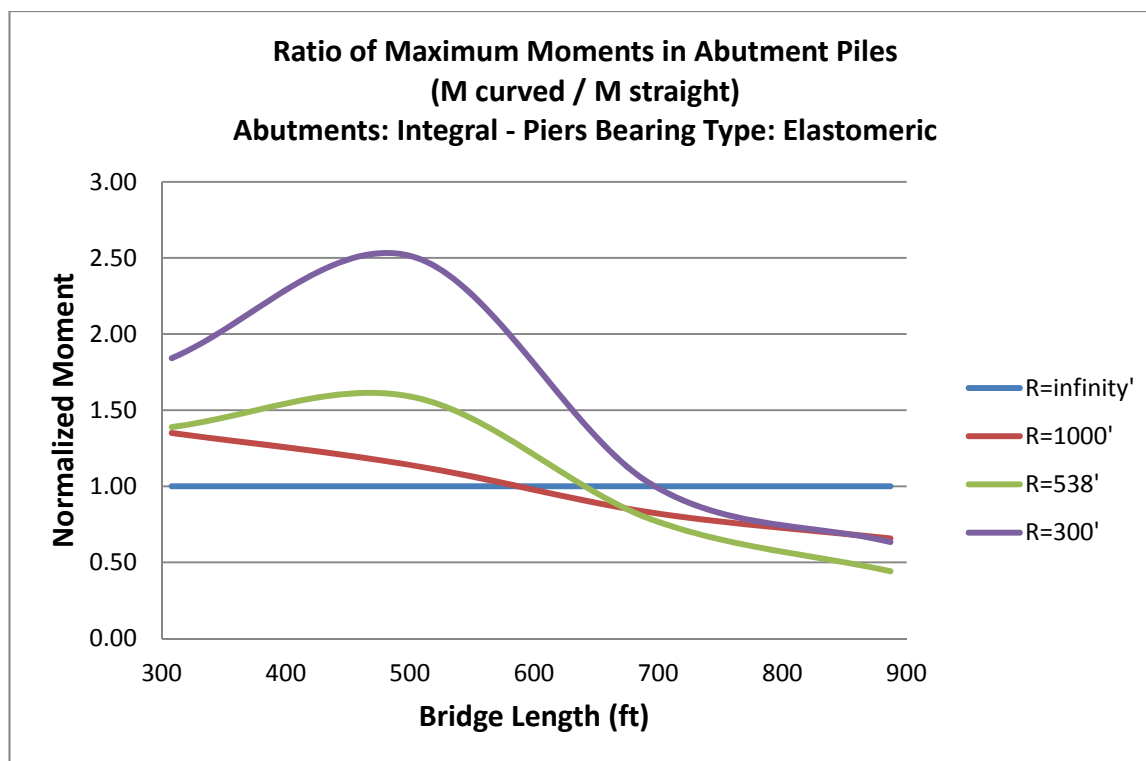


Figure 4.4-12. Normalized Moment in Abutment Piles Due to Concrete Shrinkage

A7) Horizontal Earth Pressure

Study of integral abutment bridges shows that earth pressure produces larger internal forces in curved bridges compared to straight bridges. This response is attributed to the movement of curved bridges due to earth pressure. When earth pressure is applied to the abutments of a straight bridge, the only source of displacement is the compression of the superstructure due to the applied pressure and bending of the abutments and superstructure. As the displacements due to compression of the superstructure are negligible, bending is responsible for all movements. But in curved bridges, earth pressure can be assumed to have two components: one in the direction of the bridge chord and the other perpendicular to the first one. The components in the direction of the chord line balance each other, while there is no balancing force for the other component

other than the soil reaction on the bridge piles. Consequently, horizontal earth pressure on the abutments causes lateral bending of the piles in addition to all the effects that exist in a straight bridge. That's why in Figure 4.4-13, as the bridge radius reduces, the pile moments blow up.

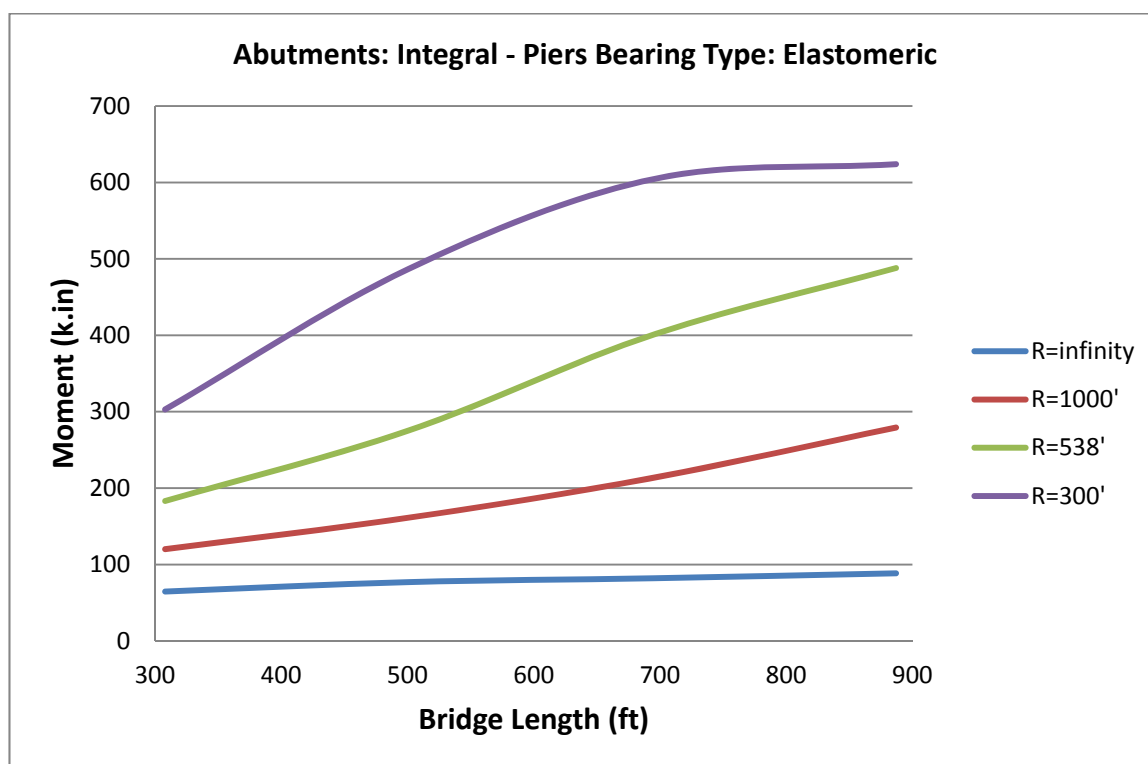


Figure 4.4-13. Maximum Moment in Abutment Piles Due to Horizontal Earth Pressure

The ratio of the pile moment increase for curved bridges compared to equivalent straight bridges can be extracted from Figure 4.4-14. As one can observe, the pile moments in highly curved bridges can be up to seven times of those of corresponding straight bridges. Even in bridges with a radius of 1000 feet, the pile moments are at least twice of those for straight bridges.

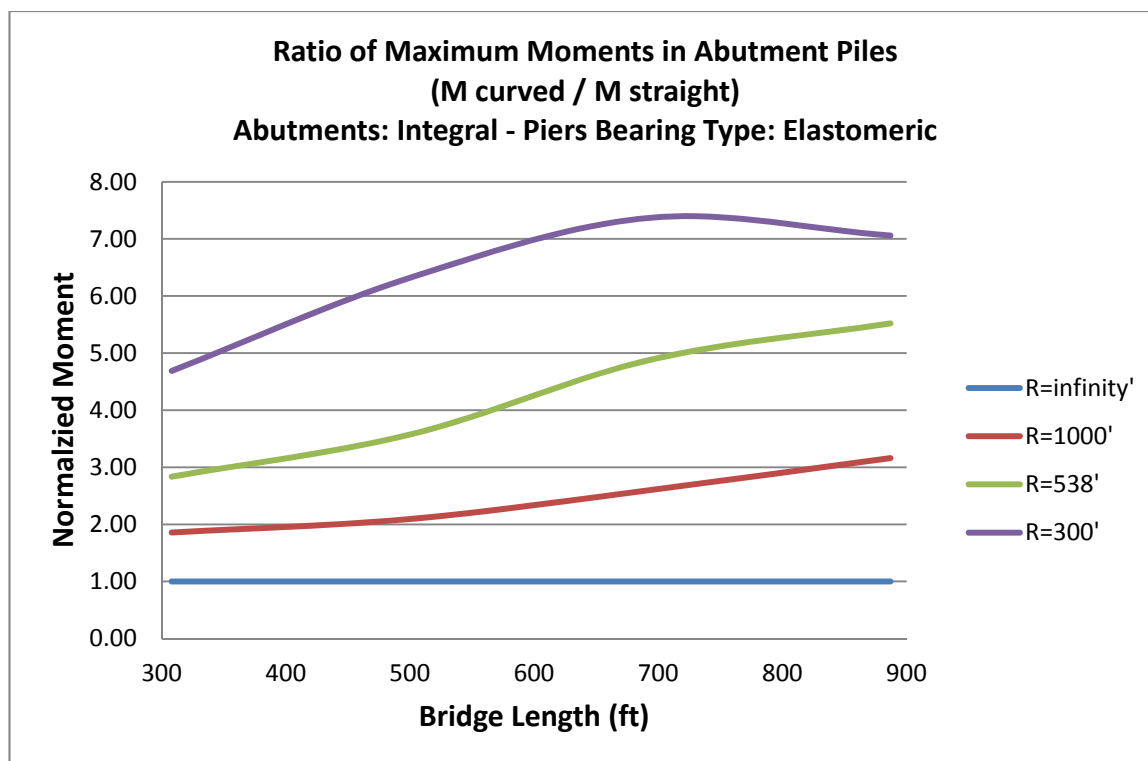


Figure 4.4-14. Normalized Moment in Abutment Piles Due to Horizontal Earth Pressure

A8) Centrifugal Force

The results of the study show that the bending moment in the abutment piles due to centrifugal force is not highly dependent on the radius of curvature or the length of the bridge. As can be observed in Figure 4.4-15, when the radius of the bridge varies from 300 feet to 1000 feet or the length of the bridge changes between 300 feet and 900 feet, the pile moments change from 120 to 150 k.in. It means three times of change in radius or length causes about 25 percent of difference in abutment pile moments. If the centrifugal force factor was chosen equal to 0.28 for all radii, the pile moments were even closer to each other.

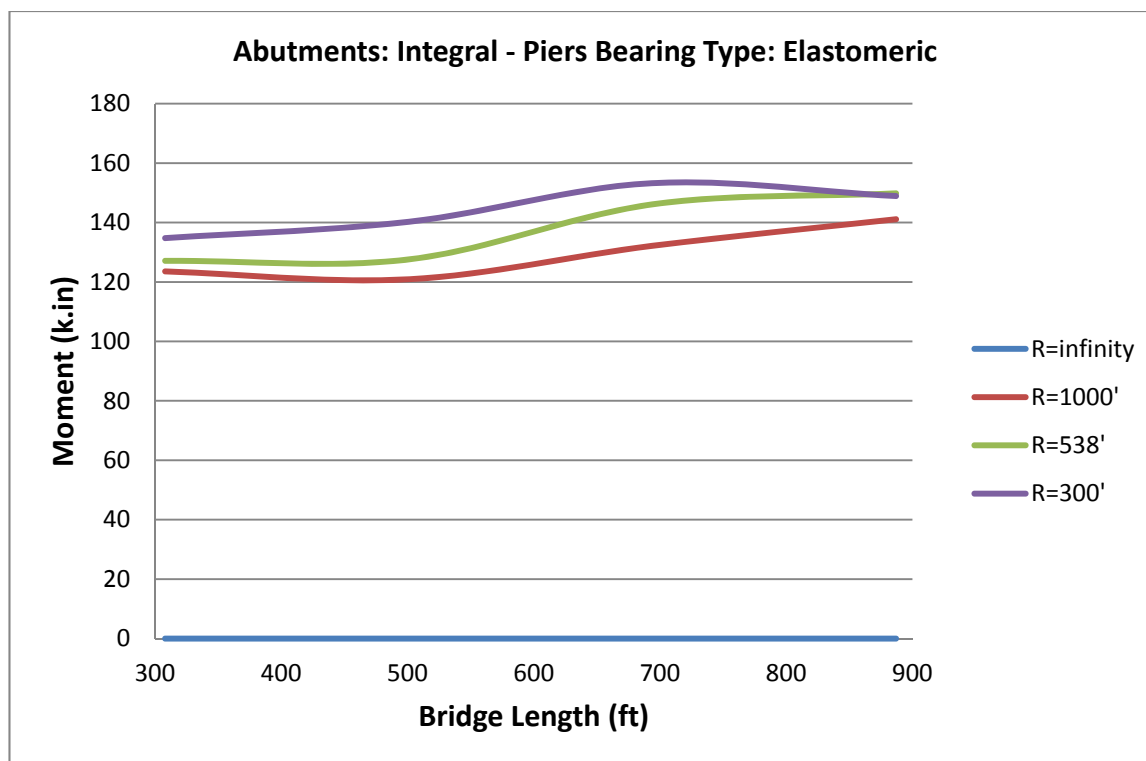


Figure 4.4-15. Maximum Moment in Abutment Piles Due to Centrifugal Force

A9) *Weight of Wearing Surface*

The response due to the weight of wearing surface has the same style as that of dead load. As observed in Figure 4.4-16, the pile moments have a decreasing trend as the length of bridge increases. But the magnitudes of the moments are much smaller. This can also be interpreted from its weight factor which is equal to two versus the weight of dead load that is eleven.

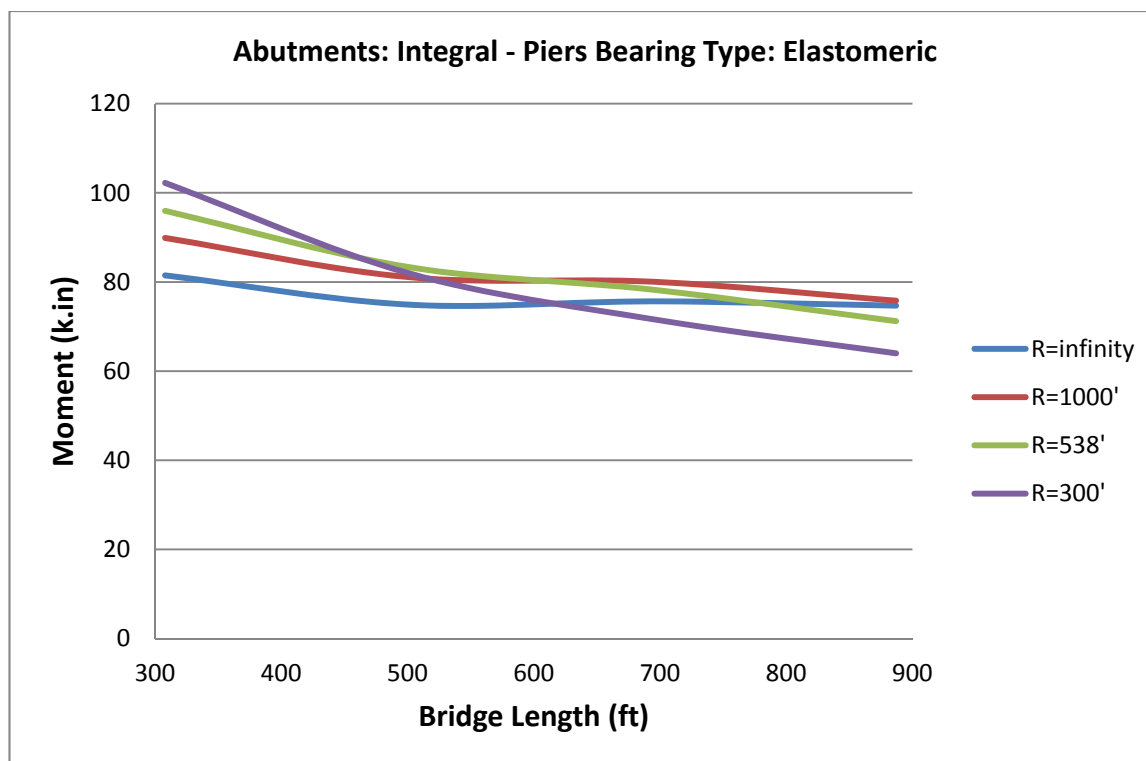


Figure 4.4-16. Maximum Moment in Abutment Piles Due to Weight of wearing Surface

The ratios of the pile moments for wearing surface weight are shown in Figure 4.4-17.

As the values of the pile moments in this case are not so large, these ratios are not of great importance from a design point of view.

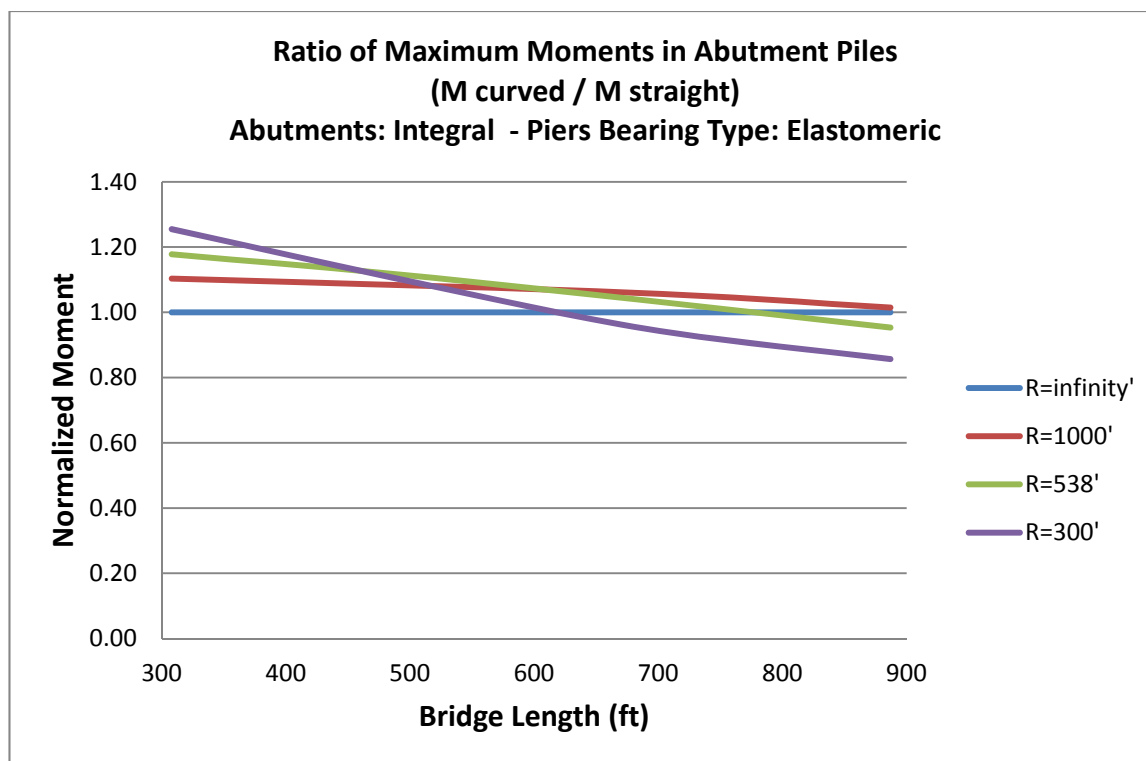


Figure 4.4-17. Normalized Moment in Abutment Piles Due to Weight of Wearing Surface

A10) Braking Force

Braking force shows to be one of the least important load types applied to an integral bridge. Having a normalized weight factor equal to one implies this minimal effect. Figure 4.4-18 illustrates the variation of bending moment of the abutment piles versus bridge length. For all different radii, the braking pile moment increases when the length of the bridge increases. Another observation is that the braking response for length greater than 450 feet is different than that of shorter bridges. This is attributed to the way the loading code defines the braking force. For more evidence one can refer to the loading section. The other fact is that as the radius of curvature of the bridge increases, the abutment pile moment due to braking load reduces.

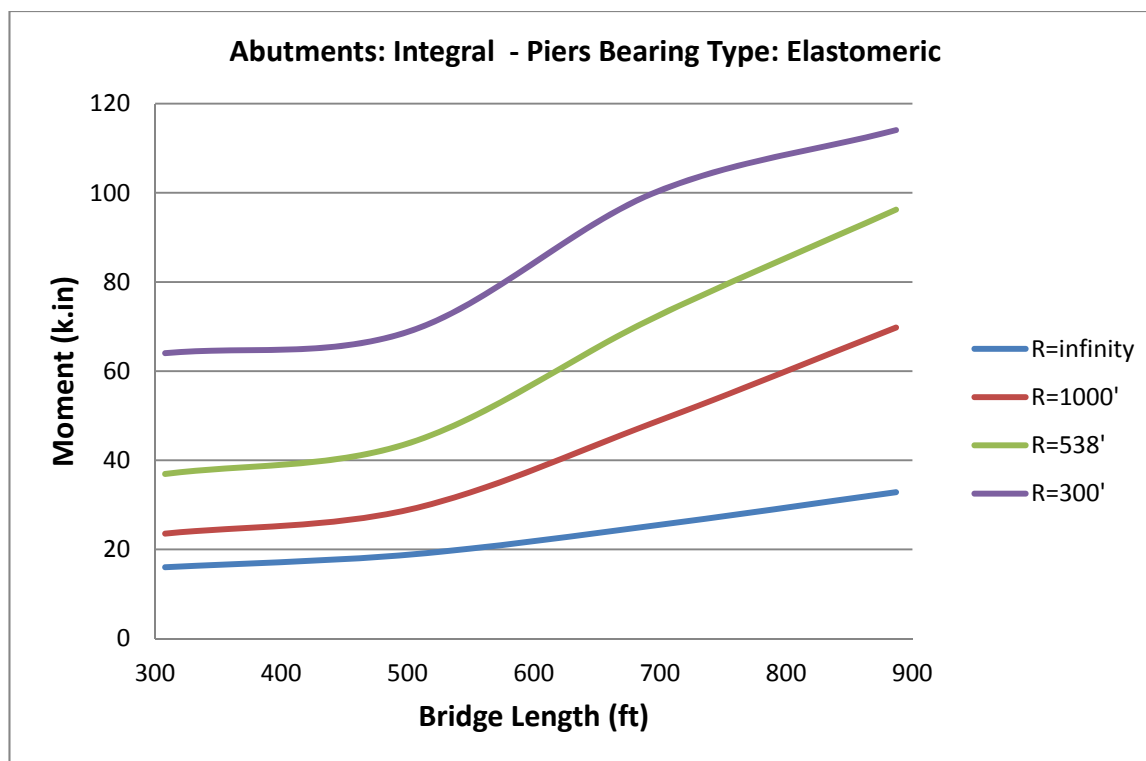


Figure 4.4-18. Maximum Moment in Abutment Piles Due to Braking Force

Figure 4.4-19 depicts the normalized moment of abutment piles for different bridge lengths and radii. It shows that the pile braking moment of a highly curved bridge is about four times of that of equivalent straight bridge. But, regarding the fact that the braking load is of little significance in integral bridges, this increase in the moments is not so effective in changing the pile design moments.

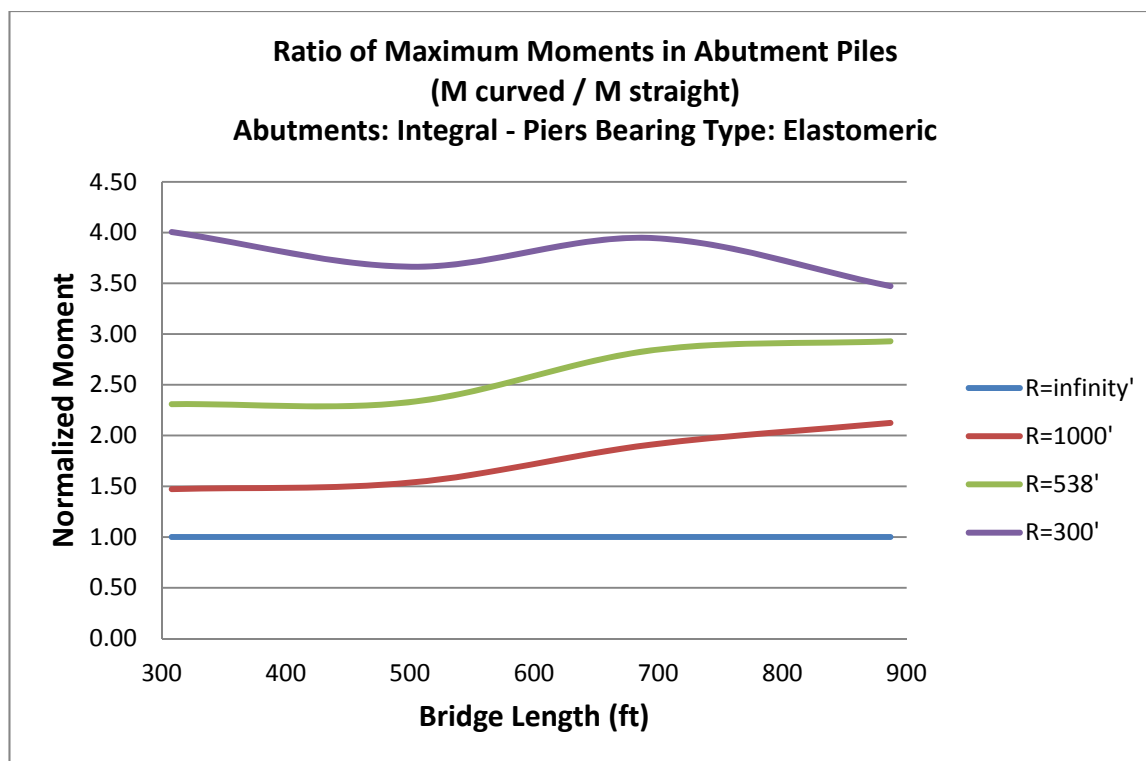


Figure 4.4-19. Normalized Moment in Abutment Piles Due to Braking Force

A11) Positive Temperature Gradient

The abutment pile moments and the ratios of the moments to the moments of equivalent straight bridge caused by positive temperature gradient are illustrated in Figure 4.4-20 and Figure 4.4-21, respectively. As can be observed, for longer bridges, this moment is independent of the bridge length. But, the most important thing about these moments is that their magnitudes are negligible compared to other moments created in the piles. This can also be concluded from the normalized weight factor of this loading which was close to zero. From this study, it is resulted that all the complex procedures presented by design codes, including AASHTO LRFD Bridge Design Specifications, to more accurately model temperature gradient do not change the design moment of abutment piles noticeably.

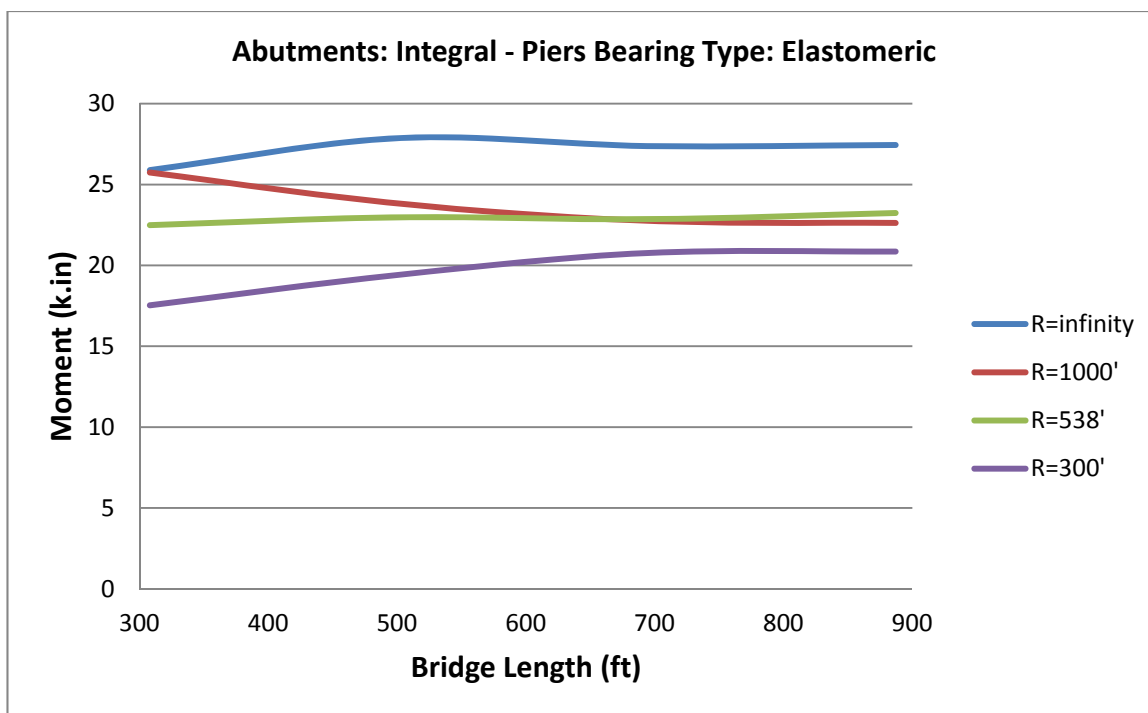


Figure 4.4-20. Maximum Moment in Abutment Piles Due to Positive Temperature Gradient

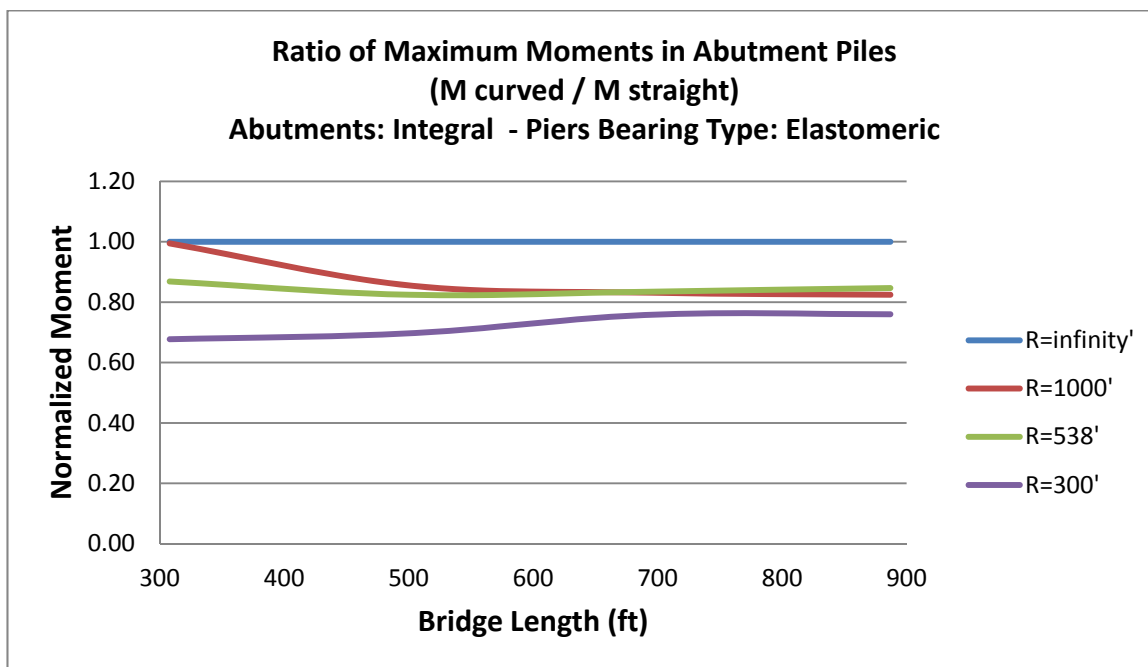


Figure 4.4-21. Normalized Moment in Abutment Piles Due to Positive Temperature Gradient

A12) *Negative Temperature Gradient*

The pile moments and normalized moments in the abutments due to negative temperature gradient are illustrated in Figure 4.4-22 and Figure 4.4-23. Similar to positive temperature gradient, again the values of bending moments are trifling. The comment on positive temperature gradient is repeated that complicated modeling for this type of loading does not distinctly change the design moments.

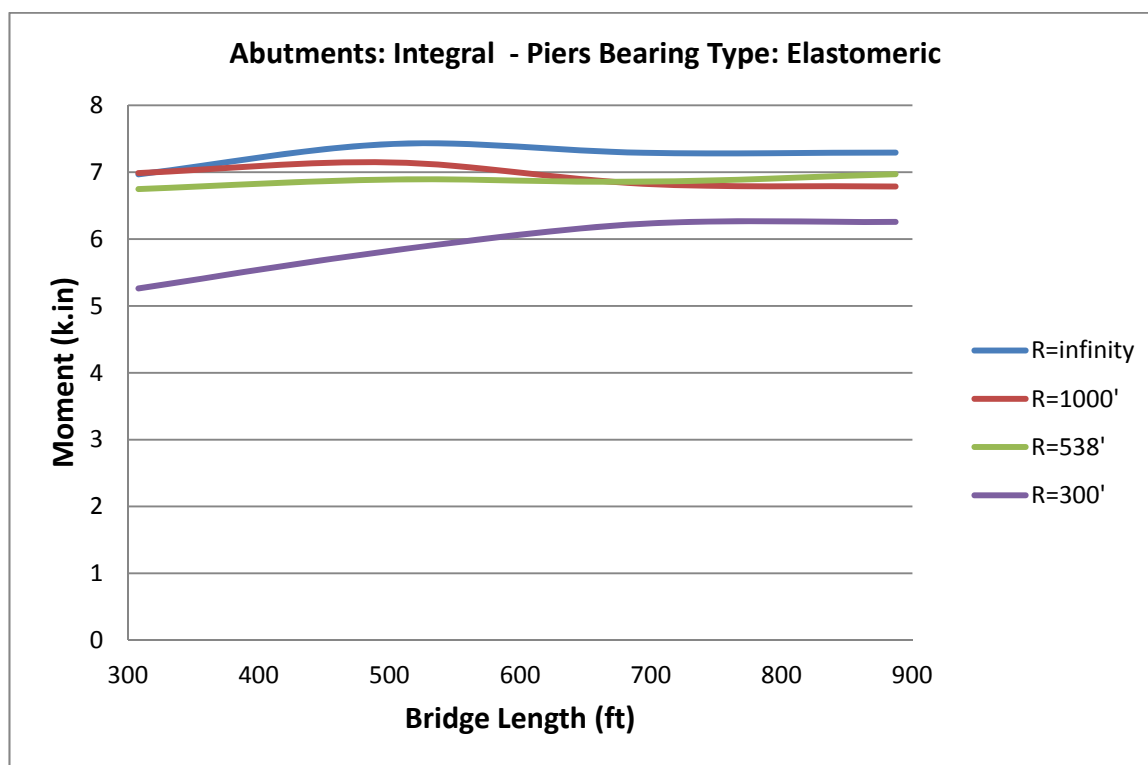


Figure 4.4-22. Maximum Moment in Abutment Piles Due to Negative Temperature Gradient

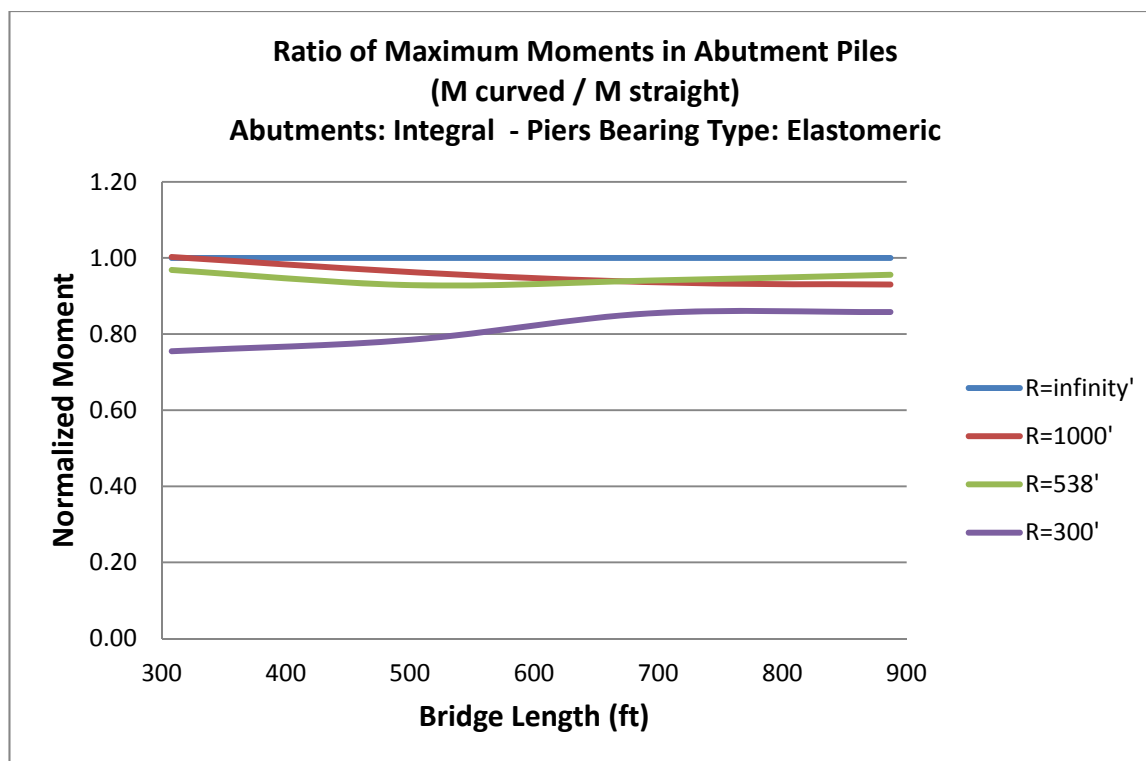


Figure 4.4-23. Normalized Moment in Abutment Piles Due to Negative Temperature Gradient

A13) Combination of the Loads

The bending moment in the abutment piles are calculated based on the load combinations of section 4.3.3. As there are several different combinations, study of responses in all of the combinations may be exhausting. Therefore, the envelope of the moments in all of those combinations is studied instead. The envelope moments are plotted for different radii and lengths in Figure 4.4-24. It can be observed that generally as the radius reduces, the slope of the curves reduces as well. Therefore, in spite of the larger moments for shorter curved bridges, the moments in curved bridges are finally smaller than those of the corresponding straight bridge. The other fact is that the envelope

pile moments of bridge with small radius of curvature, $R < 600$ feet, is almost independent of the bridge length. This is a significant result that can be concluded from this graph.

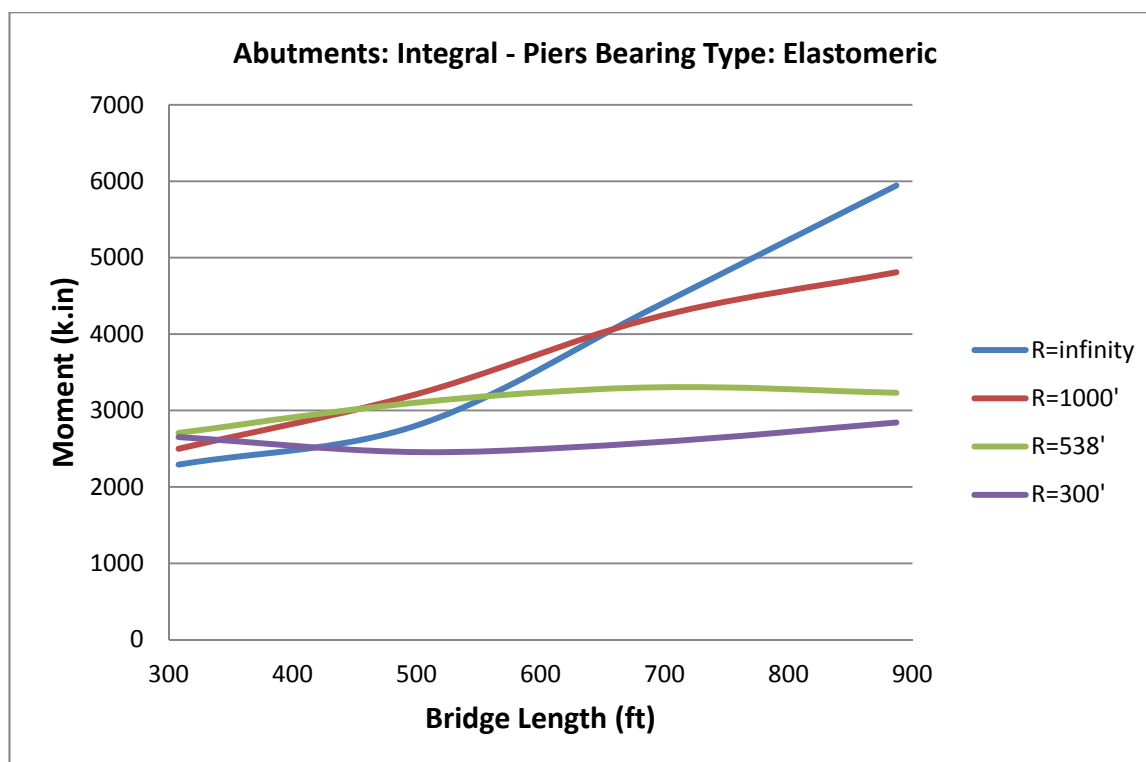


Figure 4.4-24. Maximum Moment in Abutment Piles in Load Combinations Envelope

Similar to what was done for each load case; the normalized moments are plotted versus bridge length for different radii of curvature in Figure 4.4-25. In this graph, it is shown that in bridges of length less than 500 feet, pile design moment in curved bridges are at most 20 percent larger than those of straight bridges. But as the length of the bridge increases, the moments reduce in a manner that in bridges of length equal to about 900 feet and radii equal to 300, 538 and 1000 feet, the pile moments are 0.48, 0.54 and 0.81 times of those of equivalent straight bridge, respectively.

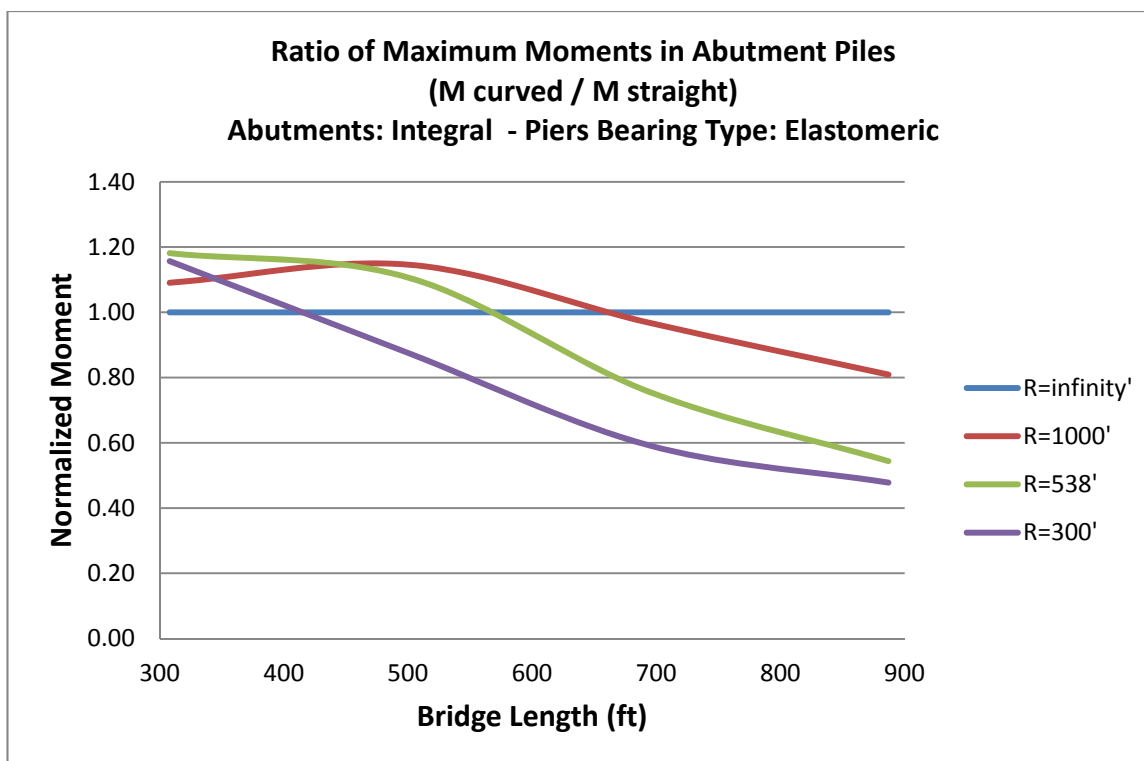


Figure 4.4-25. Normalized Moment in Abutment Piles in Load Combinations Envelope

B) Shear Force of Abutment Piles

A study similar to what is done for abutment piles bending moment is carried out on the shear forces of the piles. The results show that the design shear force of piles which is the envelope of the shear in different load combinations is increasing in straight bridges as the length of the bridge increases. But in curved bridges, such a general conclusion cannot be made. The response depends on the radius of curvature of the bridge. It is observed that for bridges with large radius, the behavior is similar to that of straight bridges. In the bridges of high curvature, the slope of shear curves is much smaller than that of bridges with large radius so that the shear forces can even be decreasing versus length. In long bridges with small radius, the design shear can be as small as 40 percent of that of equivalent straight bridges.

For brevity of the main text, the complete discussions and graphs of shear forces in abutment piles are presented in Appendix A.

4.4.2 Bridge Movement

Bridge movement is a major concern in design of integral bridges. When the superstructure of a bridge is integrally connected to the abutments, all effects that can cause a displacement or rotation at the ends of the bridge create internal forces both in abutment and in superstructure. The most important source of displacing the end of a bridge is temperature change. Expansion and contraction are the most known causes of change of bridge length. The other significant reason for bridge movement is the shrinkage of concrete deck. In fully concrete superstructures, shortening of the bridge length can also be caused by creep of concrete. However, in composite steel bridges creep cannot have such a role in moving the ends of the bridge. When there is a movement in the bridge ends, all the bridge elements including abutment wall, abutment piles, steel girders and deck should tolerate the induced forces. The pavements should also accommodate the movement so that there is not uncontrolled cracks or bumps in the road.

In order to determine the displacements of bridge ends, all the engaged factors should be studied. These include:

- the factors dependent on the location and type of the bridge: maximum and minimum temperatures that the bridge experiences over its life span, the temperature gradient in the bridge elements, construction temperature of the bridge

- the factors dependent on material properties: coefficients of thermal expansion of steel and concrete, creep and shrinkage properties of concrete
- the factors affecting the bridge movement based on the structural characteristics of the bridge

The first set of problems which are mainly climatic problems have been studied by several researchers. As these problems depend on many parameters including shade temperature, solar radiation and wind speed, the success in this area has been limited. But reasonable data are available in references including “Climatic Atlas of the United States” (Visher, 1954) and “Climatography of the United States” (United States, Environmental Data Service, & National Climatic Center, 1900s). In the present study, an increase of +60 °F and a decrease of -100 °F are taken which are based on AASHTO LRFD contour maps for a typical location in the US. But site specific temperatures should be used for each bridge which can be obtained from climatological resources or design codes.

The second set of problems which is determination of the material properties is also studied by several researchers, including the investigations of Tadros et al. on the creep and shrinkage properties of concrete (Al-Omaishi, Tadros, & Seguirant, 2009; Huo, Al-Omaishi, & Tadros, 2001; Tadros et al., 2003).

But the third problem which is analysis of bridges for movements due to assumed temperature changes and assumed material properties needs much more attention. What is generally known in bridge engineering is that the bridge movement is the summation of the movements due to temperature, shrinkage and creep:

$$\Delta_{total} = \Delta_{thermal} + \Delta_{shrinkage} + \Delta_{creep} \quad \text{Eq. 4.16}$$

The thermal displacement is equal to the thermal strain times the initial length:

$$\Delta_{thermal} = \varepsilon_{thermal} \times L_o \quad \text{Eq. 4.17}$$

In which thermal strain is the product of temperature change ΔT and the coefficient of thermal expansion α . The shrinkage and creep displacements are also calculated in the same way:

$$\Delta_{shrinkage} = \varepsilon_{shrinkage} \times L_o \quad \text{Eq. 4.18}$$

and

$$\Delta_{creep} = \varepsilon_{creep} \times L_o \quad \text{Eq. 4.19}$$

To calculate the shrinkage and creep strains there are some available methods, one of them the equations presented by AASHTO LRFD Bridge Design Specifications (American Association of State Highway and Transportation Officials, 2010). But regarding the usage of these equations, some questions may come to the mind of a bridge engineer:

- Are these equations able to predict the bridge movement with enough precision?
- Aren't there any other factors affecting the bridge displacement at pavement level?
- What should be done to find the displacements of a curved bridge?

In this section, using the finite element models of the studied composite steel curved bridges, it is tried to answer the above questions. First, a discussion is presented to clarify the involved factors and the difference of bridge shortening and bridge end displacement. Then, based on the results of finite element analyses, two factors are introduced to more

exactly calculate the change of length of bridge due to temperature variation and shrinkage. Then, the total change of bridge length is calculated using previously obtained parameters and a new modification factor. And finally, a new method is presented to find the bridge end displacement as a function of the change of bridge length which is applicable to both straight and curved bridges. To develop the new method, the effect of bridge width and also the direction of the displacement which is a major unknown in curved bridges are studied. At the end, an example for the recommended procedure is presented.

This procedure is applicable when a bridge is not designed using 3D finite element analysis, or when an engineer wants to calculate the movements of an existing bridge to design the expansion joints or for retrofit purposes.

A) Factors Affecting Bridge Displacement

In this section, three subjects are discussed. The first one is to clarify the difference of bridge shortening/elongation and the bridge end displacement. In a straight bridge with a large length-to-width ratio, the summation of the bridge end displacements is equal to the change of bridge length. But in a curved bridge or in a straight bridge with smaller length-to-width ratio, the sum of end displacements is not the same as the shortening or elongation of the bridge length. The reason for that is clearly illustrated for a sample curved bridge in Figure 4.4-26. As can be seen, the end displacements are not in the same direction to be added to each other. On the other hand, the change in the bridge length occurs in a curved line for which definition of a direction is not possible.

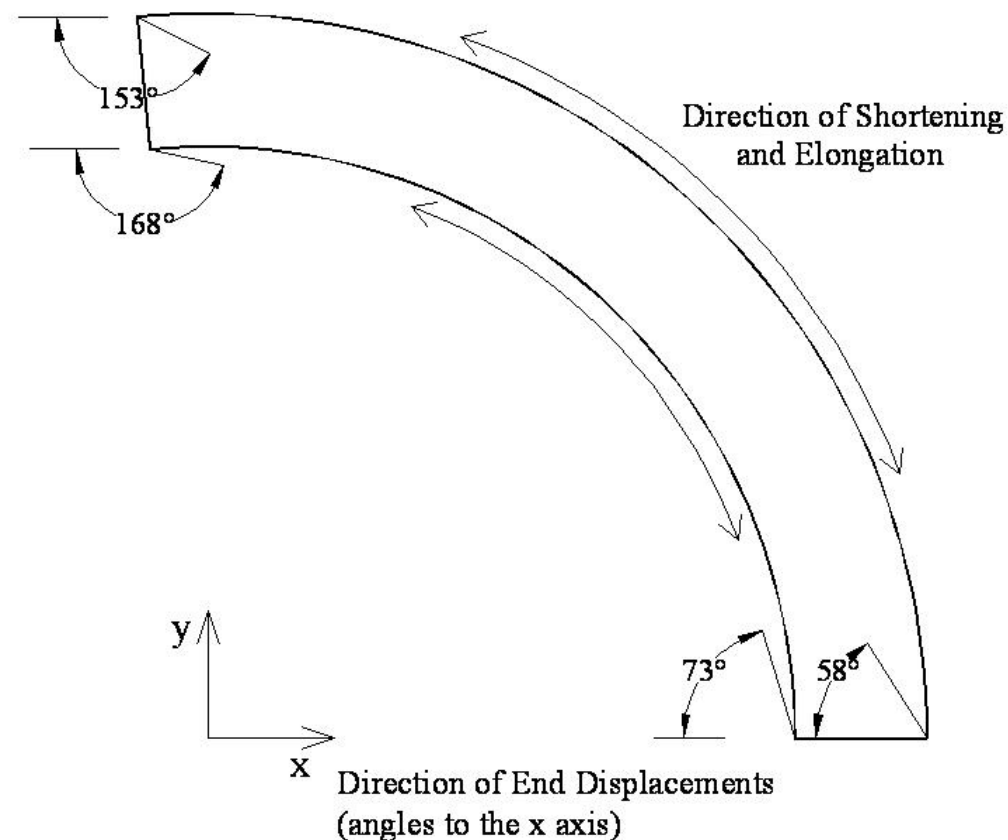


Figure 4.4-26. Directions of End Displacements in A Curved Bridge

The second problem is to investigate the reasons for “movement” of bridge ends. Among the applied loads and load effects to a bridge, some of them like temperature variation change the bridge length. It is obvious that when the length of a bridge changes, at least one of the bridge ends moves. But this kind of movement is not the only source for bridge end displacement. The bridge ends can displace due to rotation of the bridge ends without noticeable change in bridge length. This rotation is more understandable as a source of movement when the load do not change bridge length, like gravity loads. Figure 4.4-27 shows a picture of bridge end movement due to translation and rotation.

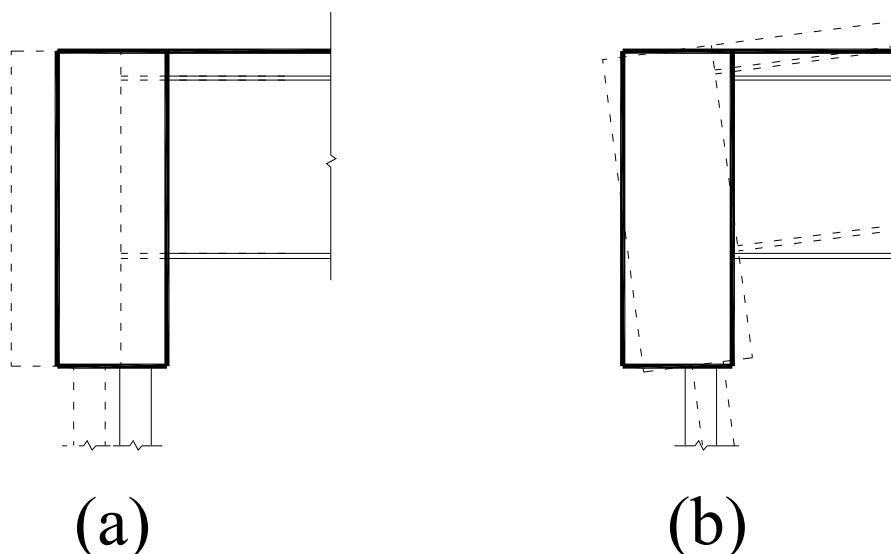


Figure 4.4-27. Bridge End Movement- a) Pure Translation -b) Rotation

The third problem is to explain the effect of different loads on bridge length. In the literature, it can repeatedly be found that the only parameters involved in bridge displacement are temperature change, shrinkage and creep. But the results of 3D finite element analysis of the studied composite steel bridges show that almost all loads participate in displacing the bridge ends. The other issue is consideration of each displacement in combination with other displacements. These load combinations are defined by design codes. In the present study, AASHTO LRFD load combinations are used. The effect of each load is as follows:

- **Contraction:** bridge contraction is the major cause for bridge shortening. Most of the displacement is because of translation, but a smaller portion of that is caused by end rotation.
- **Shrinkage:** concrete deck shrinkage is another main source for bridge shortening. In composite steel bridges, it occurs only in the deck, not in the girders. So, in

addition to reducing the length of the bridge, it causes rotation of the ends more profoundly compared to bridge contraction.

- **Creep**: the effect of concrete creep is ignorable in composite steel bridges. However in prestressed concrete bridges, it is an important reason for bridge shortening.
- **Expansion**: bridge expansion is another significant source of displacing the bridge ends. In section 4.4.1A2), two reasons were presented for smaller abutment pile moments due to expansion compared to contraction. For exact same reasons, the displacements due to expansion are smaller than those of contraction. In addition, contraction, shrinkage and creep create displacements that are in the same direction (or at least approximately in the same direction). But expansion movement is almost in the opposite direction. In the conducted finite element analyses, expansion load combinations do not create the maximum end displacements. For these reasons, the main focus of the present study is to calculate the bridge movements in contraction load combinations.
- **Gravity Loads** including dead load, weight of wearing surface and live load: all gravity loads cause bridge end displacement. As gravity loads do not change the bridge length, this displacement is mainly due to rotation of the bridge ends.
- **Lateral loads**: these loads such as centrifugal load and wind load are analyzed in the finite element models. The results demonstrate that the movements due to this type of loads are not of great importance. Although all of these displacements are taken into account.

- **Earth pressure:** finite element analyses of the studied bridges show that earth pressure has a minimal effect on end displacement of straight bridges. But in the case of curved bridges, its effect become more visible which is considered in the models.
- **Braking force:** the results show that live load braking force has a minimal effect on bridge movement.
- **Temperature gradient:** all model either straight or curved show that the displacements due to temperature gradient in superstructure in approximately zero. So, if a bridge designer ignores the complicated modeling of temperature gradient, no noticeable displacement is missed.

B) Bridge Shortening Due to Contraction

To calculate the reduction of the bridge length due to a uniform temperature decrease of -100 °F, the equivalent coefficient of thermal expansion (in this case contraction) should be evaluated. This coefficient is calculated as follows:

$$\alpha_{equivalent} = \frac{(EA\alpha)_{deck} + (EA\alpha)_{girder}}{(EA)_{deck} + (EA)_{girder}} \quad \text{Eq. 4.20}$$

in which the values of modulus of elasticity, E, cross sectional area, A, and coefficient of thermal expansion, α , for concrete deck and steel girder should be plugged in. Then, the change of bridge length can be calculated using the following equation:

$$\Delta_{contraction} = \alpha_{equivalent} \cdot \Delta T \cdot L_o \quad \text{Eq. 4.21}$$

where ΔT is equal to -100 °F and L_o is the initial length of the bridge (or $L_o = \sqrt{L^2 + W^2}$ where L and W are the undeformed bridge length and width to account for the

effect of bridge width). Based on the location of point of zero movement, this value may be multiplied by a fraction like $\frac{1}{2}$. For curved bridges, two different lengths for inner and outer arc of the bridge are considered. Comparison of the bridge length reductions resulted from 3D finite element analyses and hand calculations based on the above equations shows differences that are mainly due to bending moments in the cross section. The ratio of the lengths resulted from finite element analyses and the lengths based on hand calculations are defined as a modification factor γ_{TUC} that is plotted versus the radius of curvature in Figure 4.4-28. For simplicity, in hand calculations, the actual distance to the point of zero movement, which is an oblique line in straight bridges and an unknown curve in curved bridges, is ignored and the modification factors are found based on the length of the bridge edges.

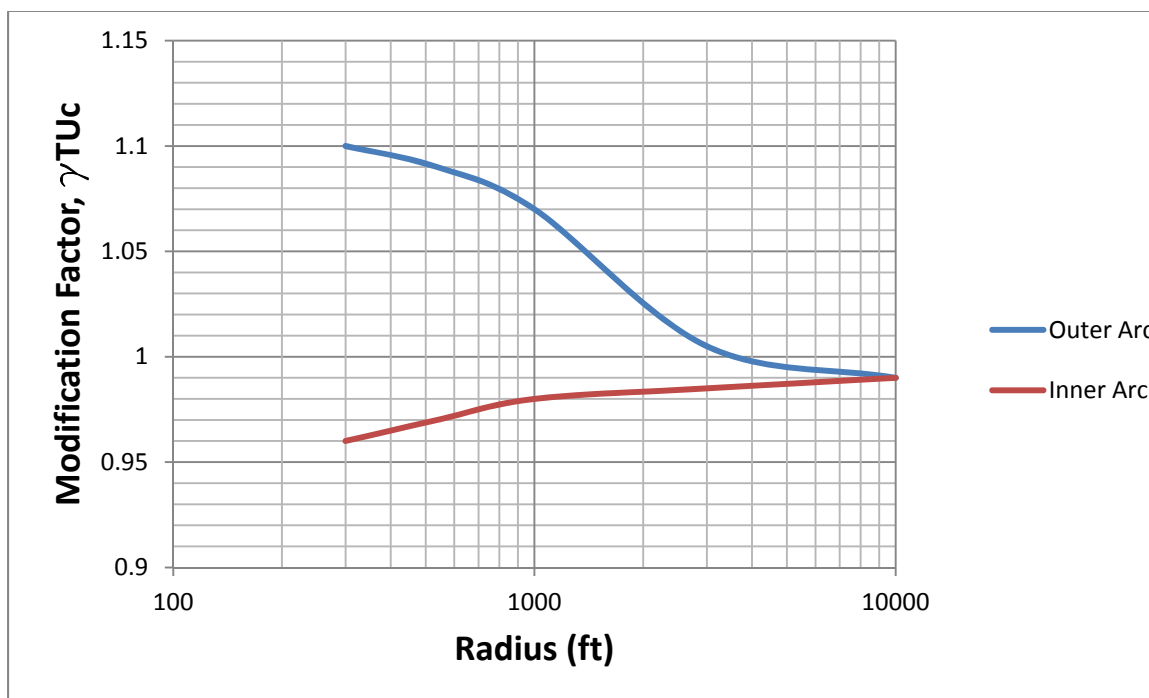


Figure 4.4-28. Modification Factor for Bridge Shortening Due to Contraction

C) Bridge Shortening Due to Shrinkage

To calculate the change in bridge length because of shrinkage of concrete, the equivalent shrinkage strain of superstructure due to shrinkage of different components should be determined as follows:

$$\varepsilon_{sh, equivalent} = \varepsilon_{sh, girder} + (\varepsilon_{sh, deck} - \varepsilon_{sh, girder}) \frac{(EA)_{deck}}{(EA)_{deck} + (EA)_{girder}} \quad \text{Eq. 4.22}$$

The shrinkage strain for each component should be calculated based of the recommendations of 4.3.2J). It should be noted that $\varepsilon_{sh, girder}$ for steel girders is equal to zero. Then the change in bridge length is calculated as follows:

$$\Delta_{shrinkage} = \varepsilon_{sh, equivalent} \times L_o \quad \text{Eq. 4.23}$$

in which L_o is the bridge length in straight bridges and the inner and outer arc length in curved bridges (or $L_o = \sqrt{Length^2 + Width^2}$ or a fraction of this value). Comparison of the results of these calculation and the bridge lengths resulted from 3D finite element analyses shows that the hand calculations need a modification factor to account for all of the other participating factors that are not seen in these simplified calculations. This factor, named γ_{sh} , is plotted versus radius of curvature for the modeled bridges.

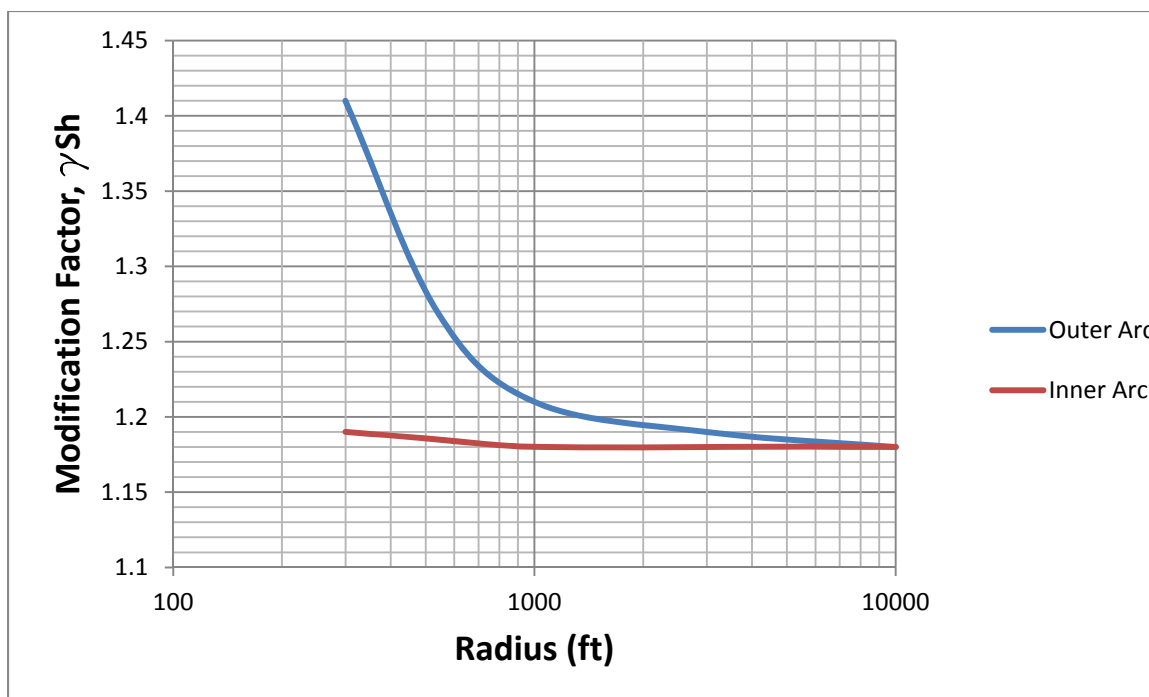


Figure 4.4-29. Modification Factor for Bridge Shortening Due to Shrinkage

D) Total Bridge Shortening

The total bridge shortening can be found as the shortening due to contraction and shrinkage are available from previous sections. The changes in lengths of the bridges are obtained based on AASHTO LRFD Service I load combinations. In these load combinations, temperature and shrinkage can have a load factor of 1.2 to yield the maximum response. So, the values of bridge length reduction obtained from finite element analyses are compared to the values of length reduction found from 1.2 times of contraction and shrinkage calculation. The values of bridge length reduction of 3D models are obtained from drawing of the deformed shapes of the bridges in AutoCAD. Finding bridge length using these two different methods again demonstrates that hand calculations miss the effect of some other parameters that exist in a real bridge. These parameters include other loads such as gravity and lateral loads and also earth pressure.

To account for these parameters another modification factor is defined which is plotted versus radius in Figure 4.4-30.

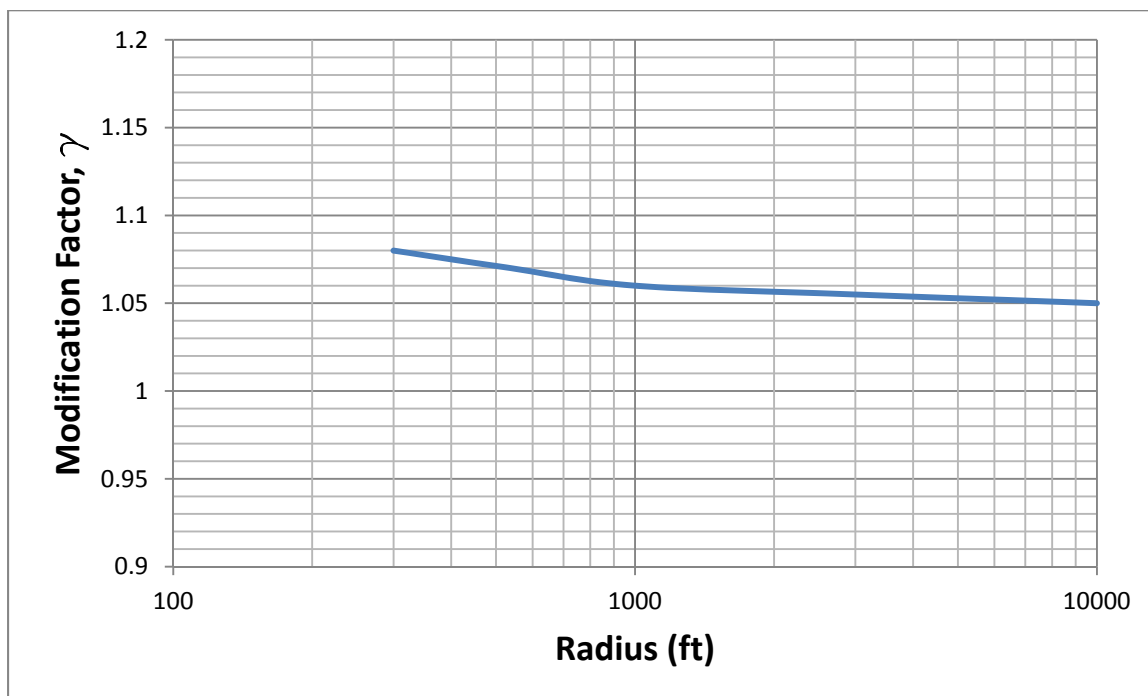


Figure 4.4-30. Modification Factor for Bridge Shortening Applied to Total Shortening

As can be observed, the summation of contraction and shrinkage shortenings should be increased from 5 to 8 percent to make up for the effect of other loads. So, the total shortening of a bridge, either straight or curved, is computed using the following equation:

$$\Delta_{total} = 1.2\gamma (\gamma_{TUC} \Delta_{thermal} + \gamma_{Sh} \Delta_{shrinkage}) \quad \text{Eq. 4.24}$$

If the modification factor given by Figure 4.4-30 is assumed to be equal to 1.08 for all bridges, then the Eq. 4.24 is simplified to:

$$\Delta_{total} = 1.3 (\gamma_{TUC} \Delta_{thermal} + \gamma_{Sh} \Delta_{shrinkage}) \quad \text{Eq. 4.25}$$

Now the total bridge shortening is found and the next task to calculate the bridge end displacement is to understand the direction of that displacement.

E) Effect of Bridge Width on the Displacement Direction

To find the direction of end displacement, first the effect of bridge width is studied. The width effect is investigated in three different problems as follows.

E1) Effect of Width on Contraction End Displacement

Since the bridge contracts in all dimensions, as shown in Figure 4.4-31, the angle of end displacement is obtained from the following equation:

$$\alpha_1 = \alpha_2 = \tan^{-1}\left(\frac{W}{L_c}\right) \quad \text{Eq. 4.26}$$

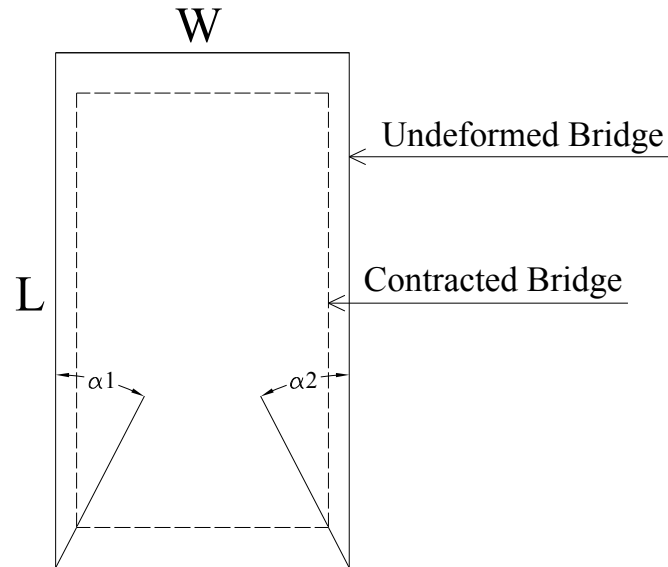


Figure 4.4-31. Direction of End Displacement Due to Contraction

where L_c is the length of bridge centerline. The angles obtained from the above equation exactly match the results of finite element analyses.

E2) Effect of width on Shrinkage End Displacement

The direction of shrinkage end displacement is more complicated. Since the girders are continuous in the longitudinal direction of the bridge and discrete in the transverse direction, the following equation can be imagined for the direction of the displacement:

$$\alpha_1 = \alpha_2 = \tan^{-1} \left(\frac{W}{L_c \left(\frac{(EA)_{deck}}{(EA)_{deck} + (EA)_{girder}} \right)} \right) \quad \text{Eq. 4.27}$$

These angles are also compared to the finite element results which show reasonable and practical precision.

E3) Effect of width on Total End Displacement

The effect of bridge width on the total bridge displacement is much more complicated than the previous cases and derivation of a closed form solution for that is not easily possible. Therefore, a finite element solution is employed. Based on the results of the finite element analyses, the data presented in Table 4.4-2 are gathered that are used to find the effect of bridge width on the total displacement of bridges.

L (ft)	W/L	α_{in} (deg.)	$\alpha_{in}/90^\circ$	α_{out} (deg.)	$\alpha_{out}/90^\circ$
308	0.197	105	1.17	75	0.83
501	0.121	100	1.11	80	0.89
694	0.087	98	1.09	82	0.91
887	0.068	96	1.07	84	0.93
Infinity	0.000	90	1.00	90	1.00

Table 4.4-2. Direction of Total Displacement (Results of FE Analyses) (W=60'-8")

The angles α_{in} and α_{out} are shown in Figure 4.4-32.

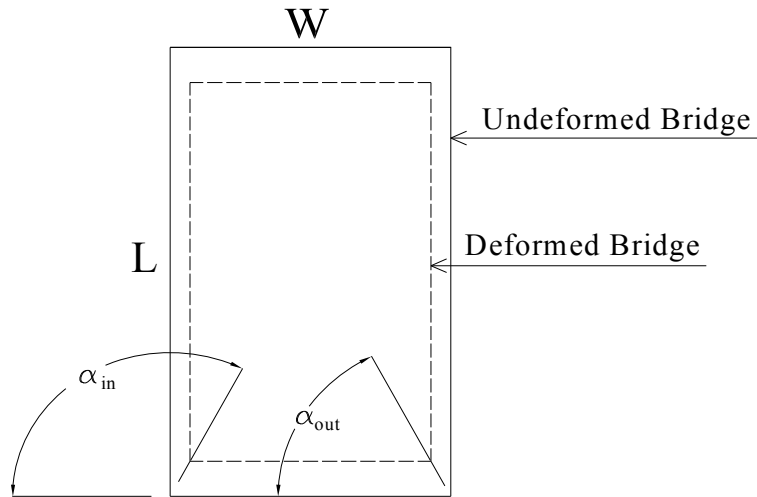


Figure 4.4-32. Angles α_{in} and α_{out} in Total Displacement

If the values of $\alpha_{in}/90^\circ$ and $\alpha_{out}/90^\circ$ are plotted versus W/L , as shown in Figure 4.4-33, it is observed that these values can be estimated by two lines with a good correlation. The following two equations are presented for these two lines:

$$k_{in} = 1 + 0.84 \frac{W}{L_c} \quad \text{Eq. 4.28}$$

$$k_{out} = 1 - 0.84 \frac{W}{L_c} \quad \text{Eq. 4.29}$$

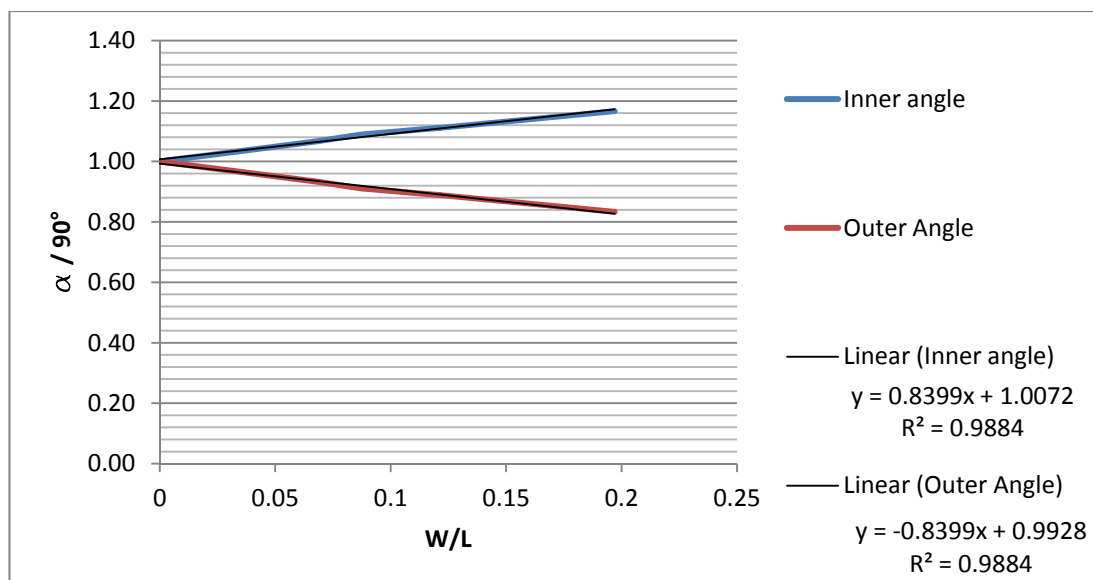


Figure 4.4-33. Values $\alpha/90^\circ$ versus W/L_c

The values of the above two equations are deviation of the direction of displacements from 90 degrees because of the width of the bridge. These equations can be considered as the effect of width on the direction of total displacement. The ratio of W/L_c should be limited to 0.33 for these equations.

F) Direction of Displacement

In this section, it is tried to find the direction of the bridge end displacements based on the results of the finite element analyses of the modeled bridges and also the findings the previous section on the effect of bridge width.

In the previous section the factors k_{in} and k_{out} were found that represent the effect of bridge width on the direction of end movements. If the angles of displacement are divided by these factors, the effect of bridge width is excluded from displacement direction. So, the obtained angles can be more easily handled as the effect of curvature on displacement direction. Based on this finding, the direction of movements for the studied

bridges are derived from finite element models and by dividing those angles by the factors k_{in} and k_{out} , it is tried to find a relationship for the modified directions. Table 4.4-3 shows the angles of displacement direction for different bridges and the modified directions to eliminate to effect of width.

L	R	L/R	α_{in}	$\alpha_{in,modified}$	α_{out}	$\alpha_{out,modified}$
308	300	1.03	91	78.0	67	80.0
501	300	1.67	77	69.0	60	68.0
694	300	2.31	68	62.4	57	63.0
887	300	2.96	68	64.0	58	62.0
308	538	0.572	102	87.0	73	87.0
501	538	0.931	86	77.5	70	78.8
694	538	1.29	82	75.0	68	75.0
887	538	1.649	76	71.0	65	69.6
308	1000	0.308	104	89.5	74	89.0
501	1000	0.501	94	84.7	76	85.5
694	1000	0.694	88	80.7	75	82.3
887	1000	0.887	85	79.4	75	80.4
308	Infinity	0	105	90.0	75	90.0
501	Infinity	0	100	90.0	80	90.0
694	Infinity	0	98	90.0	82	90.0
887	Infinity	0	96	90.0	84	90.0

Table 4.4-3. Angles and Modified Angles of Total Displacement Direction

The values of modifies angles are plotted versus the ratio L/R in Figure 4.4-34.

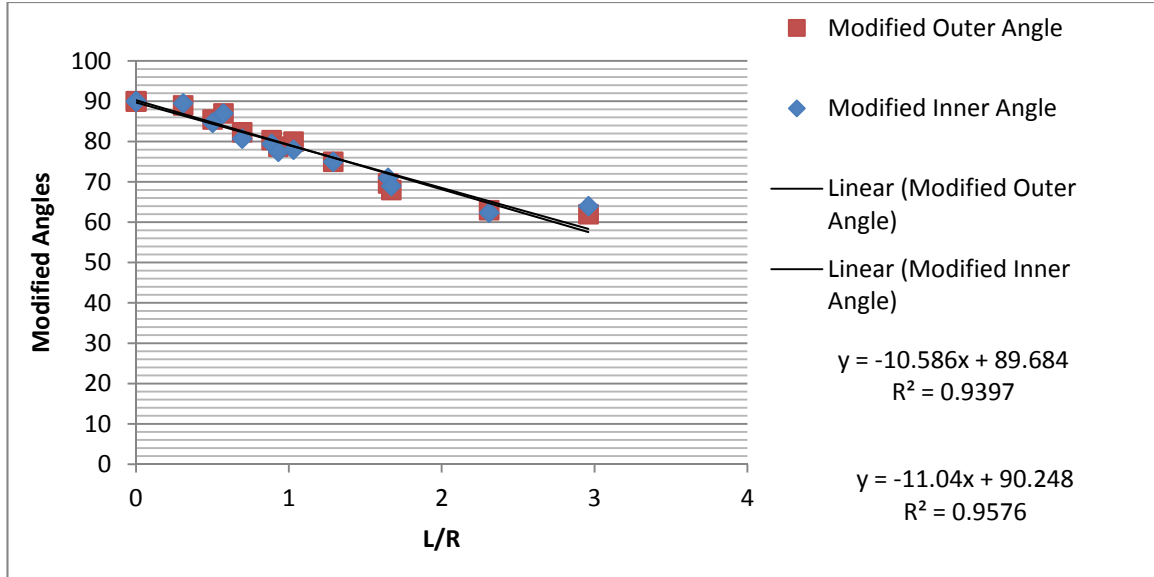


Figure 4.4-34. Modified Displacement Directions versus L/R

As observed in Figure 4.4-34, the modified inner and outer angles surprisingly coincide. If a line is fitted to the data series of the modified angles, a unique equation is obtained which is displayed in Eq. 4.30.

$$\alpha_{modified} = 90^\circ - 11 \left(\frac{L}{R} \right) \quad \text{Eq. 4.30}$$

Then the actual values of inner and outer angles can be calculated using the following equations:

$$\alpha_{in} = k_{in} \cdot \alpha_{modified} \quad \text{Eq. 4.31}$$

$$\alpha_{out} = k_{out} \cdot \alpha_{modified} \quad \text{Eq. 4.32}$$

In this way, the direction of end displacement of a curved bridge can be determined.

G) Bridge End Displacement

In the previous sections, the magnitude of the total shortening of bridges which is a function of contraction and shrinkage shortening and some modification factors and also

the direction of the end displacements of the corners of a curved bridge were found. In this section, the goal is to calculate the total end displacements of a bridge, based on the previous findings. For that purpose, one of the arcs of the bridge, either inner or outer, is considered. The problem needs a geometrical solution to find a new arc which has a specific length and its end lies on a specific line. The specific length is the length of the deformed bridge and the specific line is the direction of the end displacement, which both of them are known. The geometry of the problem is shown in Figure 4.4-35. In this picture, the undeformed configuration is known which consists of the length L , the radius R and the center of curvature O . So, the coordinates of all of the points on the curve are known. Desired is to locate the deformed curve which means finding O' and R' knowing the new length L' and the line AA'' as the geometrical location for A' .

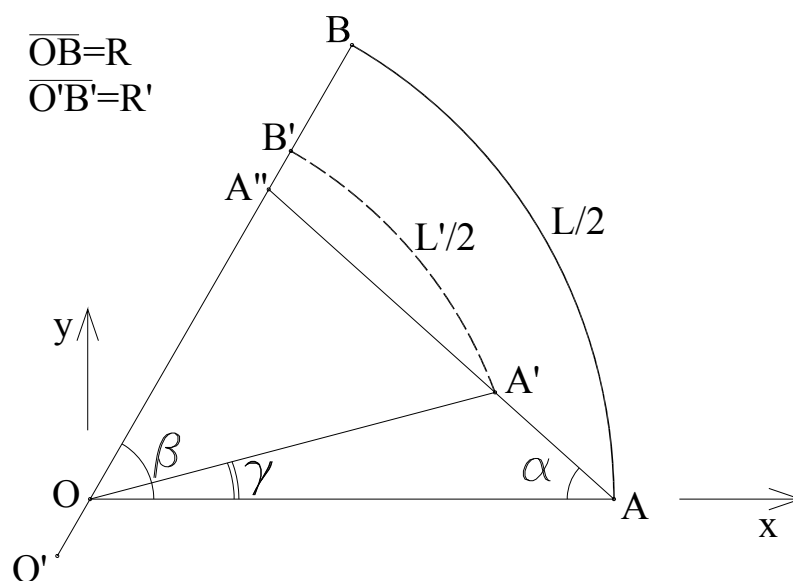


Figure 4.4-35. Deformed Bridge General Configuration

After trying to solve this problem, it was found out that this problem does not have a unique solution. So, one more constraint should be added to the problem. Drawing the

deformed and undeformed shape of all the studied bridges showed that the centers of curvature for the undeformed and deformed bridges approximately coincide. Therefore, if coincidence of the centers of curvature is added to the problem as a constraint, the simplified geometry will be as depicted in Figure 4.4-36.

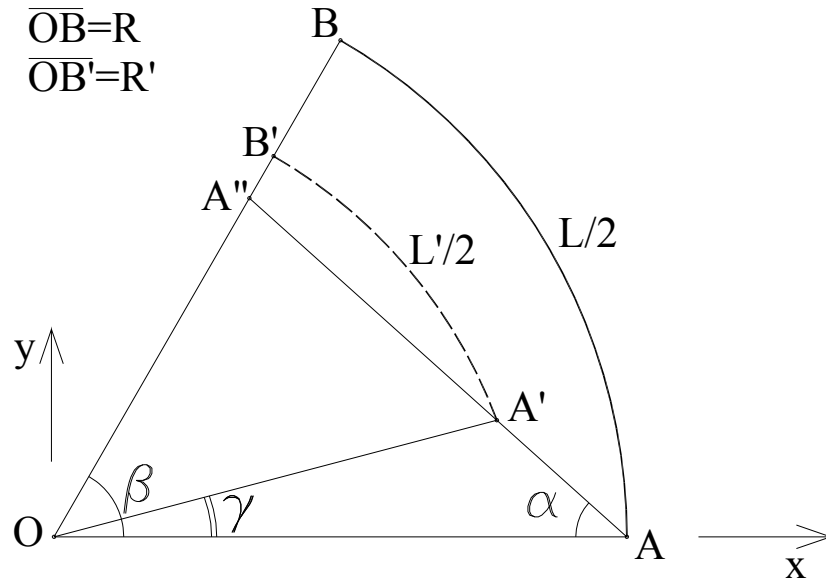


Figure 4.4-36. Deformed Bridge Simplified Configuration

To solve this problem, first the equation of line AA'' and the circle of deformed arc are derived. The equation of line AA'' is:

$$y = -\tan \alpha \cdot x + R \tan \alpha \quad \text{Eq. 4.33}$$

And the equation of deformed arc is:

$$x^2 + y^2 = R'^2 \quad \text{Eq. 4.34}$$

The coordinated of point A' can be found by solving the above two equation for x and y:

$$x_{A'} = (-ab + \sqrt{a^2b^2 - (b^2 - R'^2)(1 + a^2)})/(1 + a^2) \quad \text{Eq. 4.35}$$

$$y_{A'} = a x_{A'} + b \quad \text{Eq. 4.36}$$

Where

$$a = -\tan \alpha \quad \text{Eq. 4.37}$$

$$b = R \tan \alpha \quad \text{Eq. 4.38}$$

So the slope of line OA' will be:

$$\gamma = \tan^{-1}\left(\frac{y_{A'}}{x_{A'}}\right) \quad \text{Eq. 4.39}$$

The length of the deformed arc is equal to:

$$L' = 2R'(\beta - \gamma) \quad \text{Eq. 4.40}$$

In which

$$\beta = \frac{L}{2R} \quad \text{Eq. 4.41}$$

The above equations can be solved numerically to find R'. This can be done easily in Excel, MathCAD, MATLAB or any other program capable of solving equations. The Excel is maybe the easiest one. Note that in these equations, L is the total length, not half of it.

Using the presented method, the end displacements of a curved composite steel bridge are found which is of great importance to design such a bridge. This method is also helpful to have a sense of magnitude and direction of displacements to design the bridge-to-pavement connection devices like the expansion joints.

H) Step by Step Procedure

Based on the investigations of the present study, the following steps are recommended to calculate the maximum displacements of a curved or straight bridge:

Step 1- Determine the point of zero movement and therefore the length of the bridge that participates in end displacement. For symmetric bridges, it can be assumed to be equal to half of the length of bridge. Otherwise, other methods found in the literature can be employed. To account for the effect of width, L_o can be replaced by $\frac{1}{2} \sqrt{L^2 + W^2}$ or a similar function of bridge length and width.

Step 2- Determine the effective coefficient of thermal expansion using Eq. 4.20.

Step 3- Calculate the bridge shortening due to contraction using Eq. 4.21.

Step 4- Find the modification factor for bridge shortening due to contraction using Figure 4.4-28.

Step 5- Determine the equivalent shrinkage strain using Eq. 4.22 and recommendations of 4.3.2J).

Step 6- Calculate the bridge shortening due to shrinkage using Eq. 4.23.

Step 7- Find the modification factor for bridge shortening due to shrinkage using Figure 4.4-29.

Step 8- Find the modification factor for total bridge shortening using Figure 4.4-30.

Step 9- Calculate the total bridge shortening using Eq. 4.24.

Step 10- Calculated the bridge width effect factor using Eq. 4.28 and Eq. 4.29.

Step 11- Find the direction of the bridge corners displacements solving Eq. 4.30 through Eq. 4.32.

Step 12- Knowing the total bridge shortening found in step 9 and the directions found in step 11, solve equations Eq. 4.35 through Eq. 4.41 to find the new location of bridge corners.

Using this method, the x and y components of bridge end displacements are found.

I) Example

In this section, the x and y components of the end displacement of the inner corner of a curved composite steel bridge of length, width and radius of curvature respectively equal to 887, 60.667 and 538 feet are calculated.

Assumptions:

$$E_{deck} = 3644 \text{ ksi}$$

$$A_{deck} = 864 \text{ in}^2$$

$$\alpha_{deck} = 6.0 * 10^{-6} / ^\circ\text{F}$$

$$E_{girder} = 29000 \text{ ksi}$$

$$A_{girder} = 99.35 \text{ in}^2$$

$$\alpha_{girder} = 6.5 * 10^{-6} / ^\circ\text{F}$$

1- It is assumed that point of zero movement is located in the middle of the bridge.

$$L = \frac{887}{538} * \left(538 - \frac{60.667}{2} \right) * 12 = 10043.88 \text{ feet}$$

$$\frac{L}{2} = 5021.94 \text{ feet}$$

2- Equivalent coefficient of thermal expansion:

$$\alpha_{equivalent} = \frac{(EA\alpha)_{deck} + (EA\alpha)_{girder}}{(EA)_{deck} + (EA)_{girder}} = \frac{3644*864*6.0e-6 + 29000*99.35*6.5e-6}{3644*864 + 29000*99.35} = 6.24 \times 10^{-6}/^{\circ}\text{F}$$

3- Contraction shortening is equal to:

$$\Delta_{contraction} = \alpha_{equivalent} \cdot \Delta T \cdot \frac{L}{2} = 6.24 \times \frac{10^{-6}}{^{\circ}\text{F}} * 100^{\circ}\text{F} * 5021.94 = 3.134 \text{ inches}$$

4- From Figure 4.4-28:

$$\gamma_{Tuc} = 0.97$$

5- Equivalent shrinkage strain:

$$\varepsilon_{sh,girder} = 0$$

$$\varepsilon_{sh,deck} = 538 * 10^{-6} \text{ (From section 4.3.2J)}$$

$$\varepsilon_{sh,equivalent} = \varepsilon_{sh,girder} + (\varepsilon_{sh,deck} - \varepsilon_{sh,girder}) \frac{(EA)_{deck}}{(EA)_{deck} + (EA)_{girder}} = 538 * 10^{-6} * \frac{3644*864}{3644*864 + 29000*99.35} = 304.5 * 10^{-6}$$

6- Shrinkage shortening:

$$\Delta_{shrinkage} = \varepsilon_{sh,equivalent} \times L/2 = 304.5 * 10^{-6} * 5021.94 = 1.529 \text{ inches}$$

7- From Figure 4.4-29:

$$\gamma_{Sh} = 1.185$$

8- From Figure 4.4-30:

$$\gamma = 1.07$$

9- Total shortening is:

$$\Delta_{total} = 1.2\gamma (\gamma_{TUC} \Delta_{thermal} + \gamma_{Sh} \Delta_{shrinkage}) = 1.2 * 1.07(0.97 * 3.134 + 1.185 * 1.529) = 6.23 \text{ inchs}$$

10- Effect of width on displacement direction:

$$k_{in} = 1 + 0.84 \frac{W}{L_c} = 1 + 0.84 * \frac{60.667}{887} = 1.057$$

11- Direction of displacement:

$$\alpha_{modified} = 90^\circ - 11 \left(\frac{L_c}{R} \right) = 90 - 11 * \frac{887}{538} = 71.7^\circ$$

$$\alpha_{in} = k_{in} \cdot \alpha_{modified} = 1.057 * 71.7 = 75.8^\circ$$

12- Solving equations Eq. 4.35 through Eq. 4.41:

$$x_{A'} = 6090.70 \text{ in.}$$

$$y_{A'} = 5.15 \text{ in.}$$

So:

$$\Delta_x = x_{A'} - x_A = 6090.70 - \left(538 - \frac{60.667}{2} \right) * 12 = -1.30 \text{ in.}$$

$$\Delta_y = y_{A'} - y_A = 5.16 - 0 = 5.16 \text{ in.}$$

Δ_x and Δ_y are the components of displacement of the inner corner of the bridge.

4.4.3 Pile Orientation

There are two different opinions on the orientation of abutment piles among the researchers of this field. A first approach to pile orientation in integral bridges, asks for the weak axis bending for the piles. The supporters of such an attitude have the following reasoning for their opinion: As the bridge tends to move longitudinally and as this

movement depends on the length of the bridge which can be hundreds of feet, in order to facilitate the bridge end displacement, the stiffness of the abutments should be minimized. One of the most effective methods to reduce the stiffness of the abutments is to align the piles of the abutment such that the bending moment due to longitudinal movement occurs about the weak axis of the piles. This philosophy has led several departments of transportation to require a weak-axis bending orientation for the abutment piles. But, in contrast to this interpretation, another approach regards the problem mainly as a classic bending problem in which larger section modulus of an element results in smaller normal stresses. Founded on the latter reasoning, some other departments of transportation necessitate strong axis orientation for the abutment piles. Figure 4.4-37 illustrates the weak- and strong-axis orientations for the abutment piles.

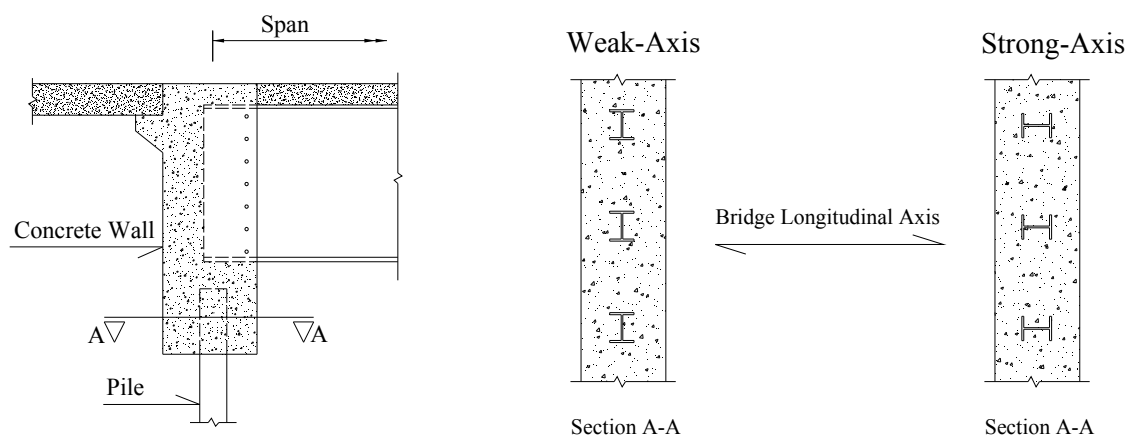


Figure 4.4-37. Critical Load Combination Type

It is observed that there is disagreement on the pile orientation among bridge researchers. The first approach has more supporters. In a report submitted to Virginia Department of Transportation, it is clearly written that: “Steel H-piles are often oriented

for weak-axis bending to better accommodate bridge displacements. For a given deflection, weak-axis bending generates less stress in the piles than does strong-axis bending.” Or “In order to build longer integral bridges, pile stresses should be kept low. In addition to weak-axis bending orientation of piles, additional provisions can be made” (Arsoy et al., 1999). It seems that the writers have assumed the same fixity depth and the same section modulus for the piles oriented in weak and strong axes in order to so easily conclude that weak orientation develops less stresses. If two elements have the same length and different moment of inertia, due to equal lateral displacement, the bending moment in that one which has smaller moment of inertia will be smaller. This relation can be clearly seen in Eq. 4.42.

$$M = \frac{6EI\Delta}{L^2} \quad \text{Eq. 4.42}$$

But such two piles embedded in soil do not have the same points of fixity. As the moment of inertia increases, the fixity point will be deeper. On the other hand, the section modulus of the weak axis is smaller than that of the strong axis. And the stress is directly related to section modulus, not the moment of inertia. So even if it is definitely known that the bending moment about the weak axis is smaller than the strong axis, it cannot be concluded that the stress level in the pile is lower.

According to the above explanations, it is clear that pile orientation is a more complicated problem than what apparently assumed by some designers. More complexity comes to existence when the bridge has some sort of irregularity such as horizontal curvature.

As stated earlier, this problem depends on some factors including bridge configuration and soil properties. The other factor is the loading that is dictated by the design code. To

be able to have a closer approach to this problem, first, the studied bridges are analyzed with usual weak axis orientation for the piles, assuming a moderate stiffness for the soil as explained in Section 4.3.4. Then, all bridges are analyzed with the piles aligned so that their strong axis is parallel to abutments. After studying the resulted internal forces, a method for orienting the abutment piles of a general curved bridge in the optimized direction is derived. In the proposed method, the goal is to minimize the stresses of the piles. It is also explained that why minimizing the stresses is in agreement with LRFD approach for design of piles, because one may think of it as an allowable stress design methodology.

A) Analysis of Modeled Bridges with Weak and Strong Orientation for Abutment Piles

In this section, first, to have a better understanding of the effect of pile orientation on the developed stresses in the bridge elements and particularly in the abutment piles, all the modeled bridges are analyzed in both usual cases for pile orientation. Since the baseline bridge had a weak axis parallel to abutments, all the original finite element models have weak axis orientation for the piles. So, the results presented in section 4.4.1 are for weak axis orientation. The piles of all models are rotated 90 degrees so that the H-Piles strong axes become parallel to the abutments. These new models are analyzed and the maximum stresses in the piles of all bridges are calculated using the following equation:

$$\sigma = \frac{P}{A} + \frac{M_{22}}{S_{22}} + \frac{M_{33}}{S_{33}} \quad \text{Eq. 4.43}$$

In the above equation, P is the axial load of the pile, A is the cross sectional area of the pile, M_{22} , S_{22} , M_{33} and S_{33} are the bending moment and section modulus of the pile about the weak axis and strong axis, respectively. The ratios of the maximum stresses of the piles in the original weak axis oriented models to those of the new models with strong axis orientation are shown in Table 4.4-4.

L (ft) \ R (ft)	308	501	694	887
300	0.84	0.87	0.76	0.80
538	0.86	0.90	1.23	1.20
1000	0.96	0.96	1.40	1.60
Infinity	1.65	1.48	1.60	1.71

Table 4.4-4. Ratios of Abutment Pile Stresses (Weak Axis Orientation to Strong Axis Orientation)

As can be observed from the above table, in some cases the weak-axis bending leads to lower stresses and in some other cases strong-axis orientation yields smaller stress values. So, a general conclusion cannot be made at this stage. The other important observation is that in straight bridges, the ratio is greater than unity, no matter what is the length of the bridge. It means lower stresses for strong-axis orientation. This can be theoretically proven regarding the fact that bridge end displacement is almost independent of the substructure stiffness. So, the parameter Δ in Eq. 4.42 is equal for all pile orientations. Besides, normal stress due to bending is equal to:

$$\sigma = \frac{Mc}{I} \quad \text{Eq. 4.44}$$

in which c is half of the depth of a symmetric section. Substituting M from Eq. 4.42 into Eq. 4.44 yields:

$$\sigma = \frac{6Ec\Delta}{L^2} \quad \text{Eq. 4.45}$$

As the depth and width of HP sections are approximately equal, the parameter c is the same for weak and strong axes bending ($c_{weak} = c_{strong}$). The length L is the distance

from top of the pile to the point of fixity which is calculated using the following equations for different soil properties:

$$L = 1.4 \sqrt[4]{\frac{EI}{k_{soil}}} \quad \text{for constant } k_{soil} \quad \text{Eq. 4.46}$$

And

$$L = 1.8 \sqrt[5]{\frac{EI}{k_{soil}}} \quad \text{for linearly increasing } k_{soil} = n_h z \quad \text{Eq. 4.47}$$

Therefore, assuming the same soil properties, L is larger for strong axis orientation. Therefore, based on Eq. 4.45, as $Ec\Delta$ is the same for both orientations, σ will be smaller for strong axis bending. In HP sections strong axis moment of inertia is about three times of that of weak axis. So, L is about 30 percent larger for the strong axis and so the stress is about 25 percent lower. This difference is only due to horizontal displacement. Other factors such as pile rotation due to earth pressure or any other participating factor can also affect the stresses. That's why larger differences are read from Table 4.4-4 for straight bridges.

To further investigate the effect of pile orientation, the condition under which a load combination produces the maximum stress in the abutment piles is studied. To have such a discussion, first the individual loads are considered. Gravity loads including dead load, live load and weight of future wearing surface are the first set of loads that create noticeable stress levels in the abutment piles. In a bridge of simple geometry like a straight bridge, these loads apply an axial load and a negative moment to the abutment piles. Temperature and shrinkage are the second set of loads that cause considerable amount of stress in the piles. In this set, expansion applies negative moment to the abutments, while contraction and shrinkage apply positive moment to the abutments. If

other loads such as centrifugal force, braking force, earth pressure, wind load and temperature gradients are ignored, the positive and negative moments of the piles can be written as follows:

$$M^{-} = M_{gravity}^{-} + M_{EXP}^{-} = -A.L_s^2 - B.L.\Delta T^{+} \quad \text{Eq. 4.48}$$

And

$$M^{+} = M_{gravity}^{-} + M_{CONT\&SH}^{+} = -A.L_s^2 - B.L.\Delta T^{-} + C.L \quad \text{Eq. 4.49}$$

In which L_s is the span length, L is the total length of the bridge, ΔT is the uniform temperature change and A , B and C are constants. Plugging in the values of temperature changes, the above two equations can be rewritten as:

$$M^{-} = M_{gravity}^{-} + M_{EXP}^{-} = -A.L_s^2 - 60B.L \quad \text{Eq. 4.50}$$

And

$$M^{+} = M_{gravity}^{-} + M_{CONT\&SH}^{+} = -A.L_s^2 + 100B.L + C.L \quad \text{Eq. 4.51}$$

The last two equations show that for short bridges the negative moment is greater than the positive moment but as the length of the bridge increases, the positive moments due to contraction becomes dominant. It should be noted that the axial force stresses are added to the bending stresses, independent of the bending moment direction. Therefore, the load combinations can be divided into two types:

- The load combinations that include bridge expansion (denoted as EXP.).
- The load combinations that include bridge contraction (denoted as CONT.).

With this background on the developed stresses in the piles, using the results of finite element analyses, the governing load combination category for each model is determined. The results for weak-axis bending pile orientation are shown in Table 4.4-5.

L (ft) R (ft)	308	501	694	887
300	EXP.	EXP.	CONT.	CONT.
538	EXP.	CONT.	CONT.	CONT.
1000	EXP.	CONT.	CONT.	CONT.
Infinity	EXP.	CONT.	CONT.	CONT.

Table 4.4-5. Critical Load Combination Category for Abutment Pile Stresses

Table 4.4-5 shows that bridges of short length have an expansion-based critical load combination and in other bridges the load combinations that include contraction dominate the stresses. In bridges of very small radius of curvature, the criticality of expansion load combinations extends more into longer bridges, but as the length increases, contraction becomes governing again. On this basis, a graph can be plotted for determining the governing load combination in the studied bridges that is shown in Figure 4.4-38.

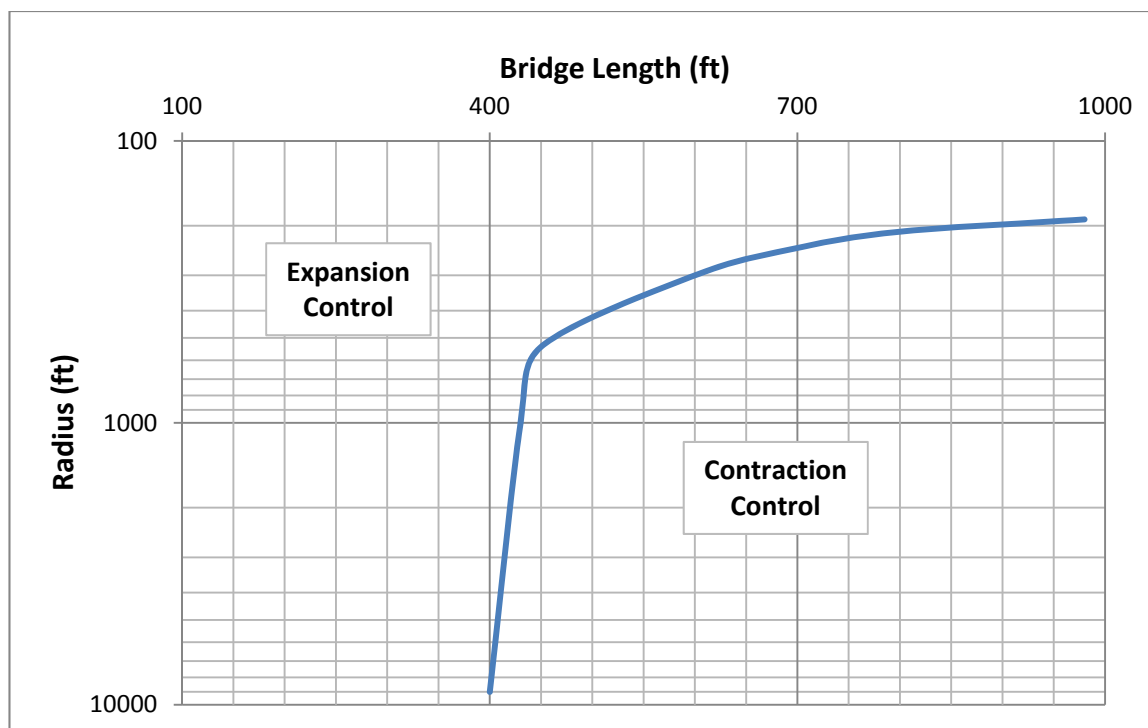


Figure 4.4-38. Critical Load Combination Type

The fact that in some bridges weak-axis bending leads to lower stresses and in the other bridges strong-axis bending creates smaller values of stress draws the attention to finding the optimum orientation for abutment piles. This problem has several contributing factors such as bridge length, bridge radius, stiffness of superstructure, stiffness of abutment wall and piles, height of the abutment wall and also some other factors such as soil properties. Thus, presenting an analytical solution for that is not easily possible. A numerical solution for this problem can be reached by making use of the finite element models. To do that, first the direction of the displacement of the node located at the top of the abutment piles is determined. To find this direction, the x and y components of the displacements of that node is extracted from the models in all load combinations. Then using the following equation, the angle of displacement direction with respect to x axis is determined:

$$\alpha = \tan^{-1}(U_y/U_x) * 180/\pi$$

Eq. 4.52

Figure 4.4-39 shows the direction of displacement for a typical pile top node.

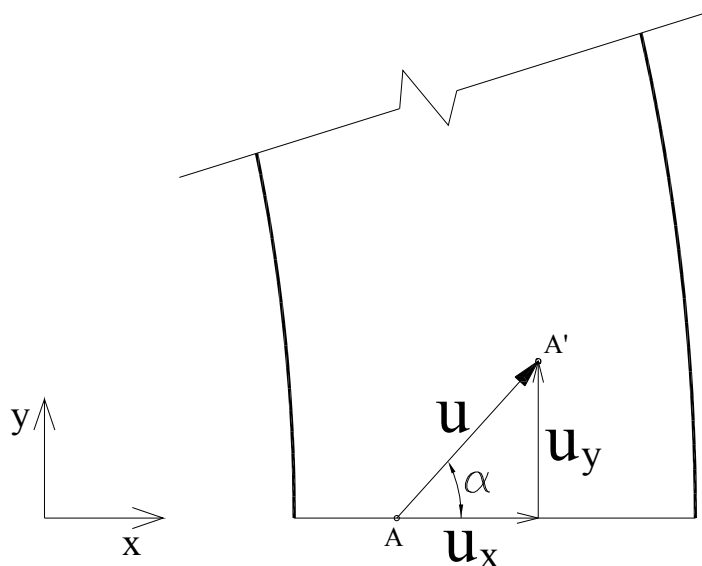


Figure 4.4-39. Direction of Pile Displacement

There are 17 piles under each abutment and 16 load combinations in which these directions are calculated. The average of these directions for expansion combinations and contraction combinations are calculated and plotted versus L/R ratios in Figure 4.4-40.

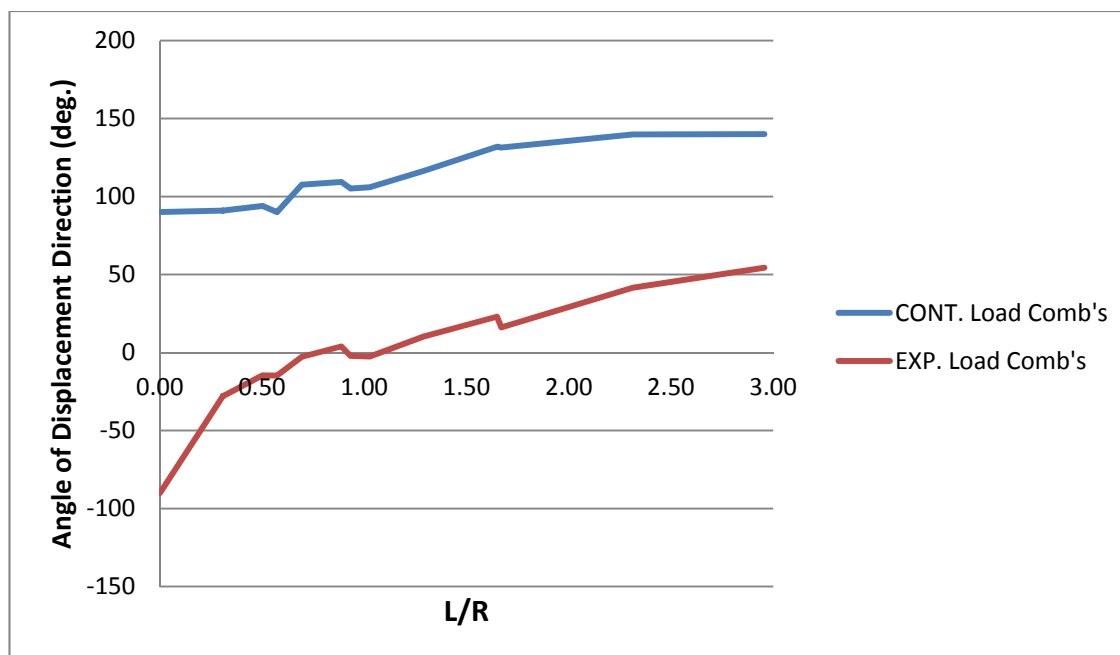


Figure 4.4-40. Average Displacement Directions of Abutment Piles Top Node

There are some fluctuations for the displacement directions in the above graph, but the general trend can be perceived. In expansion load combinations, for an L/R ratio of zero which is for a straight bridge, a displacement direction of -90° is read that means the piles move toward the backfill soil. For larger values of L/R, the angle increases gradually up to a mean angle of displacement of about $+55^\circ$ for highly curved bridges of L/R equal to 3. This shows that in highly curved bridges, even in expansion load combinations, the piles move away from the backfill which is because of other participating factors like earth pressure on the abutment wall. For contraction load combinations, the average angle of displacement starts from $+90^\circ$ for L/R equal to zero that indicates separation of abutment wall from backfill. As the ratio of L/R increases, this angle increases to $+140^\circ$ that can be interpreted by moving of the abutments toward the center of the bridge when the bridge contracts. Based on the previous graph which is the result of finite element

analysis of several bridges, approximate smooth curves can be imagined for design purposes like those displayed in Figure 4.4-41.

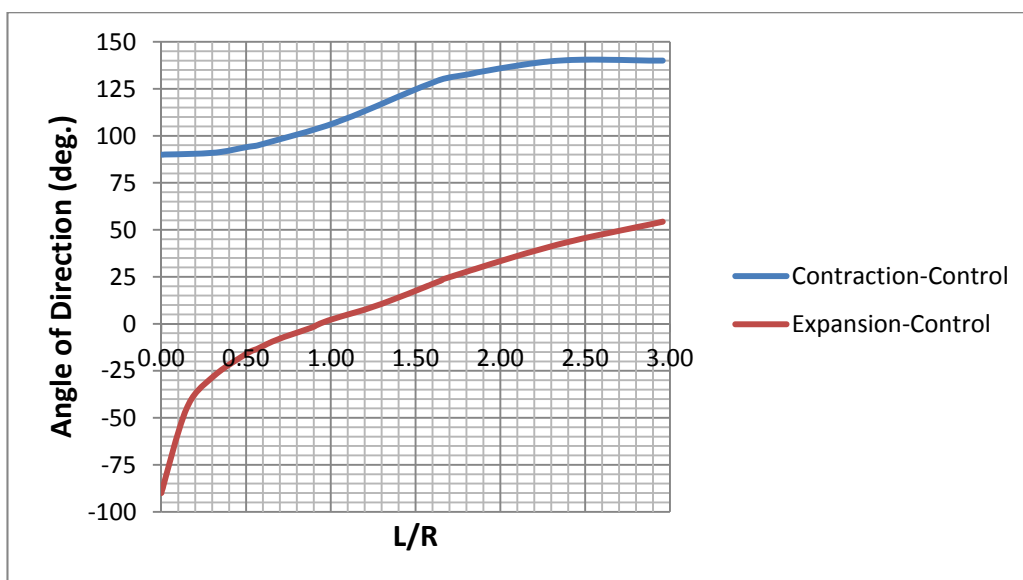


Figure 4.4-41. Design Displacement Directions of Abutment Piles Top Node

Using the above graph, the orientation of the abutment piles of the studied bridges is changed so that the critical displacement of the abutment causes strong-axis bending in the piles and the models are run again. Orienting the piles for strong-axis bending in the direction of maximum displacement is based on the results of modeling of straight bridges in which the direction of displacement was known and strong-axis bending showed better performance in lowering the stresses. After the analyses, the resulted pile stresses, which are called optimized stresses, are compared to the stresses of weak-axis and strong-axis orientation for the piles. For this purpose, the ratios of these stresses to the optimized stress are calculated and tabulated in Table 4.4-6 and Table 4.4-7:

$$\text{Stress Ratio} = \frac{\sigma_{Weak}}{\sigma_{Optimized}} \text{ or } \frac{\sigma_{Strong}}{\sigma_{Optimized}} \quad \text{Eq. 4.53}$$

L (ft) \ R (ft)	308	501	694	887
300	1.00	1.00	1.00	0.89
538	1.06	1.04	1.75	1.56
1000	1.06	1.00	1.40	1.50
Infinity	1.65	1.48	1.60	1.71

Table 4.4-6. Ratio of Piles Weak-axis Orientation Stress to Optimized Stress

L (ft) \ R (ft)	308	501	694	887
300	1.19	1.13	1.31	1.12
538	1.23	1.17	1.42	1.31
1000	1.10	1.04	1.00	0.93
Infinity	1.00	1.00	1.00	1.00

Table 4.4-7. Ratio of Piles Strong-axis Orientation Stress to Optimized Stress

As can be seen, in 15 out of 16 bridge models, this method of optimization leads to stresses less than or equal to the stresses obtained from usual weak-axis or strong-axis pile orientation stresses. Weak-axis pile orientation which is the most commonly adopted orientation can cause up to 75% larger stresses and strong-axis orientation can develop more than 40% greater stresses compared to the optimized solution. So, the presented method can be put into practice to find the optimal pile orientation for curved integral abutment bridges. A step by step procedure for this purpose is brought in the following subsection.

B) The Procedure to Find the Optimal Pile Orientation

According to the presented analyses and discussions for optimizing the abutment pile orientation, the following steps are recommended for design purposes:

Step 1- Using Figure 4.4-38, try to find the critical type of load combinations between expansion- and contraction-based combinations.

Step 2- Using Figure 4.4-41, find the direction of piles displacement based on the critical type of load combinations found in Step 1.

Step 3- Orient the strong axis of the abutment piles perpendicular to the displacement direction found in Step 2.

Step 4- Analyze the bridge based on the recommended pile orientation. Since the validity of the recommended graph for distinguishing the criticality of expansion versus contraction is limited to the current study, a more conservative approach is to find the displacement direction for both expansion-critical and contraction-critical assumptions and analyze two different models for these two pile orientations and find the optimal orientation to have the minimum stress in the piles. In the latter procedure, the minimum stress is guaranteed, even though taking the simpler procedure and trying to find the critical type of load combinations is much better than choosing the weak- or strong-axis bending without these considerations.

4.4.4 Effect of Bearing Type and Orientation

There are several types of bearings that are used in bridges. Each type of bearing has its own characteristics. For example, each type has a specific arrangement for setting the

degrees of freedom free, fixed or in between. Since in an integral bridge, the superstructure is resting on piers by means of a bearing device, it is necessary to study the effect each bearing type on the responses of the bridge. Different types of bearings and the status of the degrees of freedom for each of them are tabulated in Table 4.4-8.

Bearing Type	U _x Longitudinal	U _y Transverse	U _z	R _x	R _y	R _z
Plain or Reinforced Elastomeric	k	k	k	k	k	K
Fixed Pot or Fixed Disc	Fix	Fix	k	k	k	k
Guided Pot or Guided Disc	0 or k	Fix	k	k	k	k
Sliding (Elastomer or Pot or Disc)	0	0	k	k	k	0
Rocker or Cylindrical	0	Fix	Fix	Fix	0	Fix
Spherical	Fix	Fix	Fix	0	0	0

Table 4.4-8. Different Bearing Types and the Associated DOF's

In this table, “k” means that the DOF has a specific stiffness between zero and infinity. A free DOF that has zero stiffness and a fixed DOF with a stiffness of infinity are the two bounds indicated by “0” and “Fix”, respectively.

In the present study, the effects of four different types of bearings which are more commonly used in integral bridges are studied. These bearings consist of elastomeric, fixed, guided and sliding bearings. The responses that are studied include the bending moment of abutment piles and pier columns. For abutment piles, the resultant bending moment which is the square root of sum of squares of the longitudinal and transverse

moments is studied and for the pier columns, the longitudinal and transverse moments are investigated separately.

A) Effect of Bearing Type on Abutment Pile Moments

To study the effect of different bearing types on the bending moment of abutment piles, several finite element analyses are conducted on the studied bridges with different bearings. As there are several load cases applied to the bridges and also several load combinations, quite a few sets of outputs are resulted. For brevity, only the envelope of bending moments in different load combinations is presented in Figure 4.4-42.

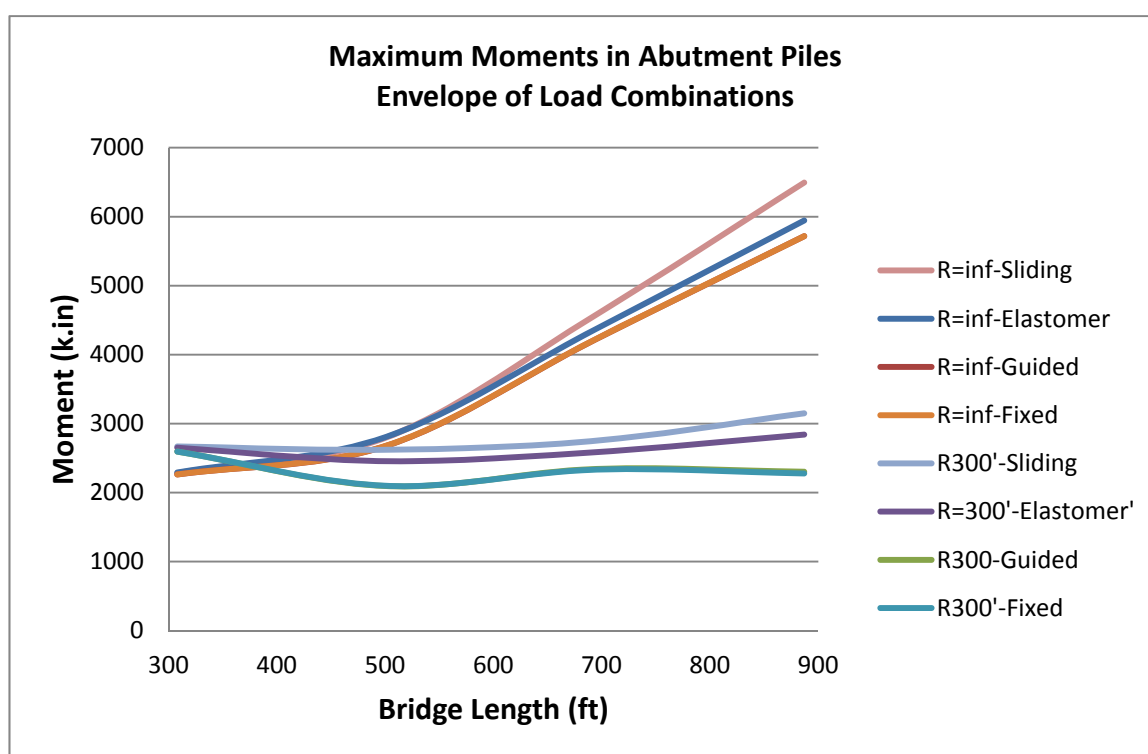


Figure 4.4-42. Bending Moment of Abutment Piles with Different Bearing Types

In bridges with the radius of 300 feet, the bridges with sliding bearings have larger moments compared to those with elastomeric, fixed or guided pot bearings. The moments for the bridges with fixed and guided pot bearings are very close to each other. These two

types of bearing cause smaller moments in the abutment piles. The other observation on highly curved bridges is that the maximum abutment pile moment is almost independent of the length of the bridge. As can be seen, the moment for the bridges with the length of about 900 feet is approximately equal to the moments in bridges with 300 feet length.

In straight bridges, the general response is similar to that of curved bridges. The abutment pile moments in bridges with sliding bearings are greater than those in the bridges with other types of bearings. Fixed and guided pot bearings create slightly smaller moments compared to the elastomeric bearings, which is attributed to the restraint that the massive piers have developed against the movements. Abutment pile moments are increasing as the length of the bridge increases. The other fact is that in short bridges either curved or straight, the maximum abutment pile moment is approximately the same for bridges with different types of bearings.

In both straight and curved bridges, the change in the abutment pile moments due to using different types of bearings is less 20 percent.

B) Effect of Bearing Type on Pier Columns Moments

The moments created in the pier columns are divided into longitudinal and transverse components that are discussed separately. In this context, the transverse moment means a moment that causes bending of pier elements in the plane of the pier. The longitudinal moment causes bending perpendicular to the transverse moment. In the case of curved bridges, longitudinal moment bends the pier about the radial axis.

The longitudinal moments in straight bridges decrease as the stiffness of the bearing reduces. It is shown in Figure 4.4-43 that the bridges with fixed bearings have the largest

moment values. When the bearings have the properties of elastomers, the moments decrease and if the bearings are sliding or guided, with sliding direction along the length of the bridge, the longitudinal moments reduce drastically. In the latter case, the longitudinal stiffness of the bearings is zero and it may be expected that the moments should be equal to zero. But, the moments are not equal to zero because of the rotational stiffness of the bearings. The rotation of the superstructure above the pier and the rotational stiffness of the bearings build up a moment in the pier in the longitudinal direction. Another sources of the longitudinal moments can be the loads that are applied to the pier itself, like wind load if applicable.

In the case of curved bridges, a similar pattern is observed. Bridges with fixed bearings have the largest moments in the pier columns. If the bearings are elastomeric, the maximum moment of pier columns reduce compared to those with fixed bearings. And when the bearings are sliding or guided the moments are considerably smaller.

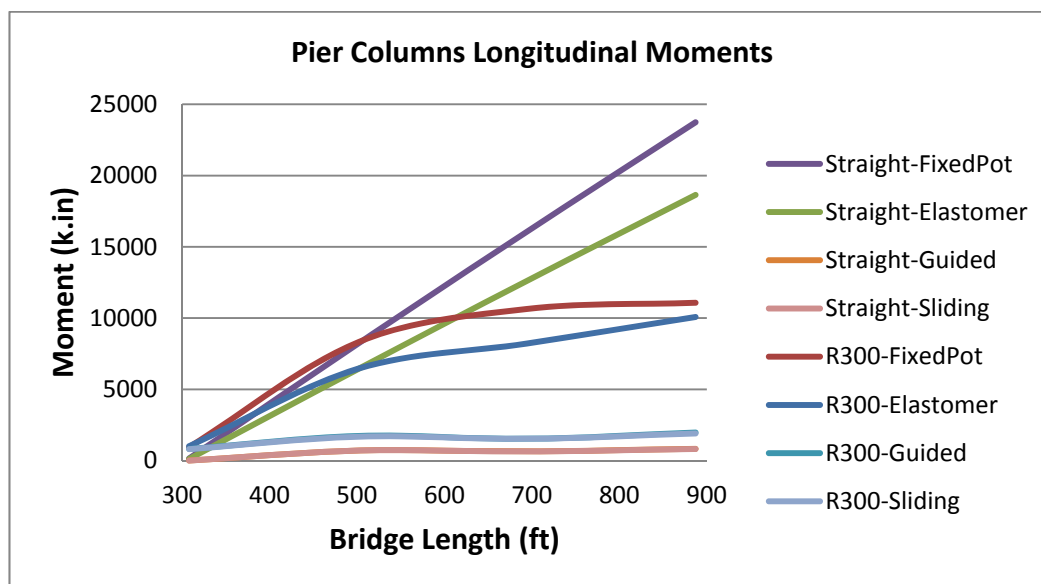


Figure 4.4-43. Longitudinal Bending Moment of Pier Columns with Different Bearing Types

The transverse moment of pier columns are plotted versus bridge length for different radii in Figure 4.4-44. It is observed that curved bridges with fixed bearings have transverse moments very close to those of the bridges with guided bearings. This is attributed to the reason presented for the case of abutment piles. If the bearings are changed to elastomeric ones, the moments drop significantly. In the case of elastomeric bearing, the transverse moments are on average 60 percent of the moments of bridges with fixed or guided bearings. If sliding bearings are used, the moments reduce to the transverse moments that are caused by the pier structure itself, like expansion, contraction and shrinkage of the pier frame.

In straight bridges, the pier columns transverse moments are mainly due to frame action of the pier structure, not the behavior of the whole bridge structure. So, it is generally independent of the bearing type or the length of the bridge. These moments are very close to the moments if the pier is analyzed alone. The result is that such a pier configuration itself creates moments about 55000 k.in. In such cases, it can be recommended that use of massive pier columns in pier bents should be avoided in favor of multiple slender columns.

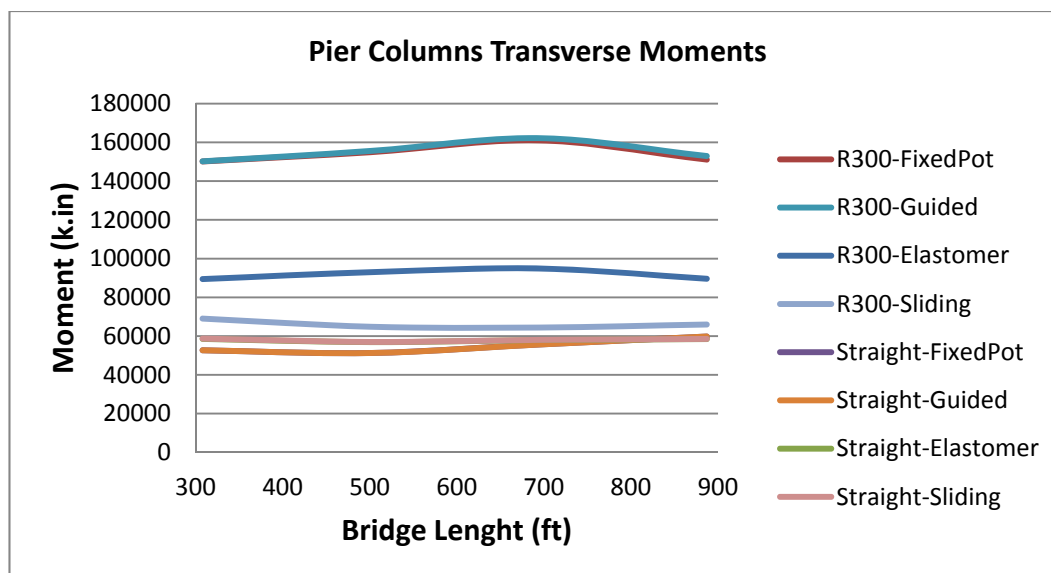


Figure 4.4-44. Transverse Bending Moment of Pier Columns with Different Bearing Types

C) Bearing Orientation

The response of elastomeric, fixed and sliding bearings can be considered like an axisymmetric material in which the response is the same in all horizontal directions. But guided bearings are fixed in one horizontal direction while having sliding or elastomeric response in the perpendicular direction. The directional dependence of the response demands choosing an optimal orientation for the bearing. In jointed bridges, since the superstructure is attached to substructure only by means of bearings, the optimal orientation for guided bearings can be defined based on assuming a point of zero movement for the superstructure and orienting all bearings in radial directions with the point of zero movement as the center. Figure 4.4-45 shows this idea.

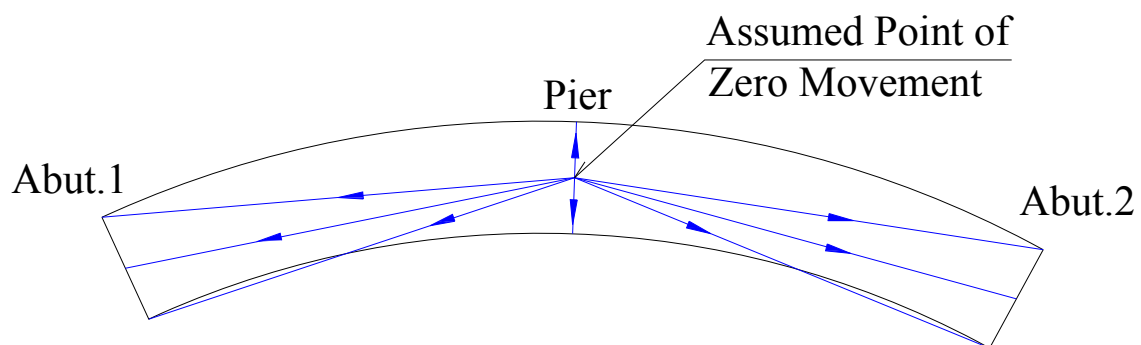


Figure 4.4-45. Guided Bearing Orientation in Jointed Bridges

The presented method for finding the optimal orientation of the bearings is valid provided that there is no restraint for the bridge movement. If there are some restraints like fixed bearings or integral abutments, the point of zero movement should be found by assuming a point as the point of zero movement, orienting the guided bearings along the rays coming out of that point, analyzing the bridge to find the internal forces of the elements and optimizing the internal forces by trial and error on the position of the zero movement point. Figure 4.4-46 shows the rays of alignment for a trial point.

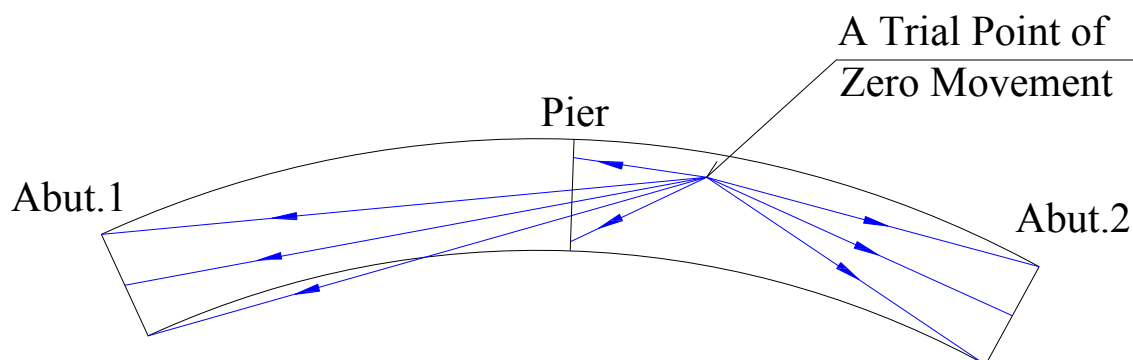


Figure 4.4-46. Guided Bearing Orientation in Bridges with Restraint Superstructure for a Trial Point

Adopting such an iterative method can be time-consuming if not a waste of time when there are other bearing types to be used in conjunction with integral bridges. A better recommendation is to use elastomeric or sliding bearings in the case of integral bridges. For elastomeric bearings, use of circular bearings is recommended to completely eliminate the problems arising from bearing direction.

Chapter 5

Effect of Curvature on Concrete IA Bridges

5.1 Introduction

In this chapter, the effect of horizontal curvature on the response of concrete curved integral abutment bridges is studied. To perform such an investigation, several finite element models of concrete integral bridges with different lengths and radii of curvature are analyzed. Each of the studied bridges has a concrete voided slab superstructure, two integral abutments at the two ends of the bridge and one or more intermediate piers which their connection to the superstructure is either integral or bearing isolated. All abutments and piers are supported on concrete piles. More explanations on the modeled bridges are brought in the following sections. Figure 5.1-1 shows a picture of a concrete curved integral bridge similar to the bridges that are studied in this section.



Figure 5.1-1. A Concrete Curved Integral Bridge Similar to the Studied Bridges

5.2 Bridge Configuration

The components of the studied bridges include superstructure, abutments and piers. The shape and dimensions of these elements are explained in the following subsections.

5.2.1 Superstructure

In the studied bridges, the superstructure is a concrete voided slab with a total width of 40 feet. This concrete deck consists of two solid concrete side cantilevers of 5 feet length with the thickness of 12 inches and a voided concrete slab of 44 inches depth. The diameter of voids is 28 inches and their center to center spacing is 38 inches. Figure 5.2-1 depicts the cross section of the superstructure. As shown in the picture, the bridge has two curbs at the two sides of the roadway each of them with a width of 24 inches.

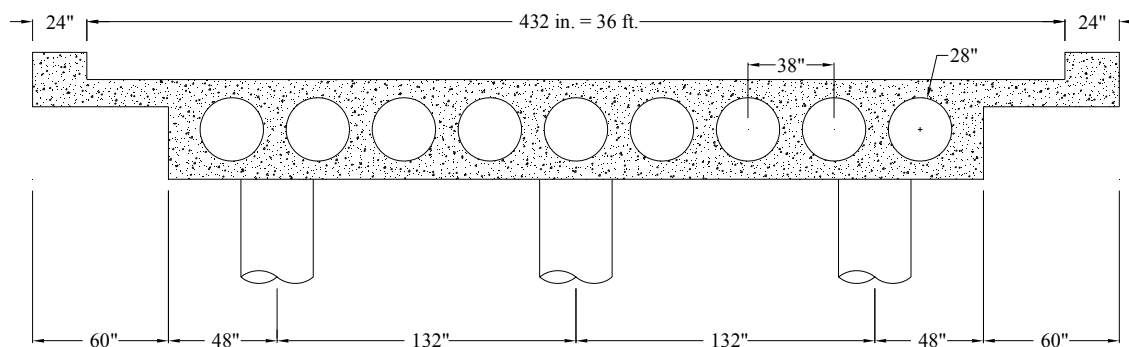


Figure 5.2-1. Cross Section of the Superstructure of the Modeled Bridges

5.2.2 Abutments

The abutments of the modeled bridges are integrally connected to the superstructure which is the main characteristic of this type of bridges. Each abutment is consisted of a 50-inch high concrete wall with a thickness of 44 inches which is resting on a row of three circular concrete shafts. The diameter of each shaft is 40 inches and their length is 50 feet. (In this chapter, the terms shaft and pile are used interchangeably.) As the thickness of both voided slab and the abutment wall are 44 inches, the connecting zone has a 44 by 44 square inches cross sectional area which transfers the forces between superstructure and the abutment.

There are several details for connecting abutments to bridge superstructures integrally, which can be found in the references. For voided slab superstructures, the integral connection can be achieved easily by splicing the rebars of the deck and the abutment

together and casting monolithic concrete for the two adjacent components. Figure 5.2-2 shows such a typical integral connection.

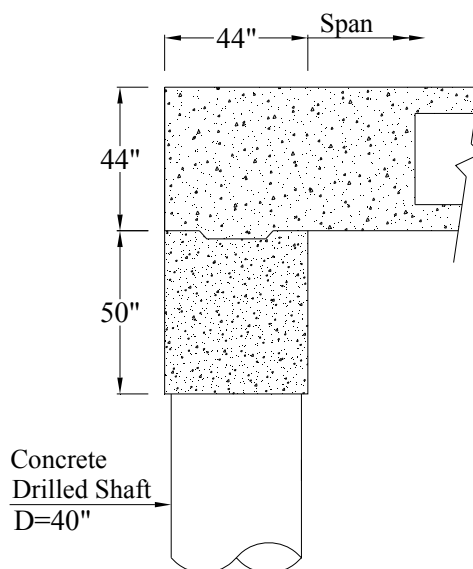


Figure 5.2-2. A Typical Integral Connection for Voided Slab Bridges

5.2.3 Piers

Piers of the modeled bridges consist of three concrete columns of circular cross section with a radius of 32 inches which are supported on concrete shafts with a diameter of 48 inches. The length of the columns is 20 feet and the depth of the shaft is 60 feet.

The piers connection to the superstructure is either integral or bearing-isolated. In the integral connection, the columns are assumed to be rigidly connected to the superstructure. Figure 5.2-3 illustrates such an integral connection.

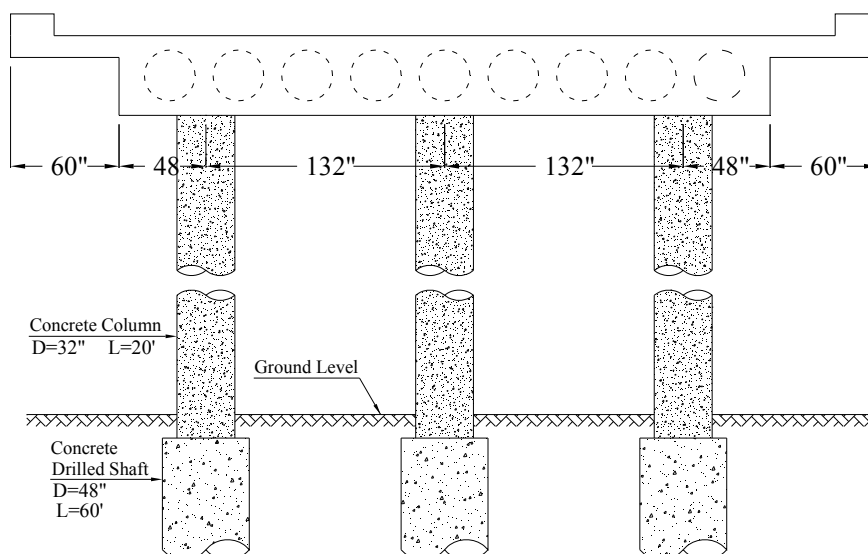


Figure 5.2-3. Integral Connection of Piers and Superstructure

In the bearing-isolated piers, the columns are connected to each other by means of a cap beam and the superstructure rests on the cap beam by means of a number of elastomeric bearings. Figure 5.2-4 shows a typical bearing-isolated superstructure to pier connection.

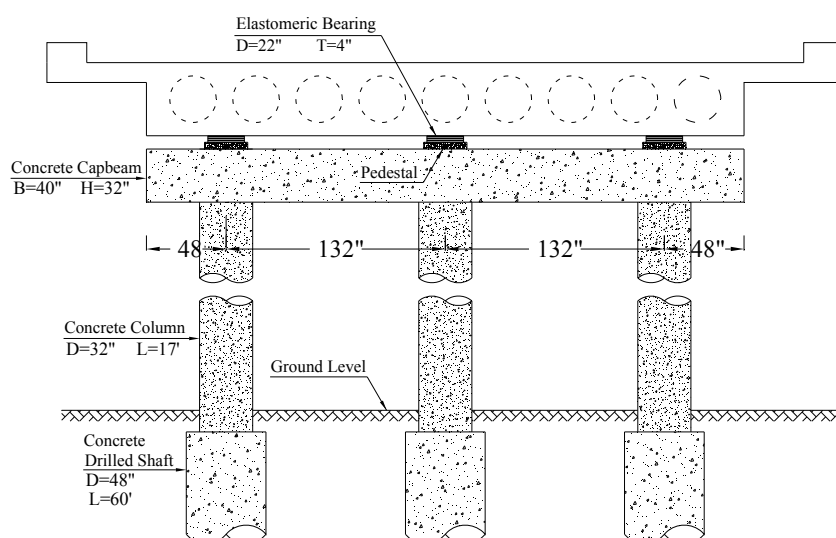


Figure 5.2-4. Bearing-Isolated Connection of Piers and Superstructure

5.3 *Finite Element Modeling*

In this section, the characteristics of the finite element models that are used to study the curve concrete integral bridges are explained. These characteristics include the material properties, the applied loads to the models, soil-structure interaction and the employed elements.

5.3.1 Material Properties

In the modeled bridges, different components are assumed to be reinforced concrete elements. The strength of the concrete in different parts varies based on the requirements of each part.

For all structural elements, the concrete material has a unit weight of 145 lb/ft³, a coefficient of thermal expansion of 6×10^{-6} /degrees F and a Poisson ratio of 0.2.

For voided slab superstructure, concrete columns and the stub abutment walls, the specified compressive strength of concrete is 5 ksi. The concrete in these parts has a modulus of elasticity of 4074 ksi and a shear modulus of elasticity of 1698 ksi.

For piles of piers and abutments, the modulus of elasticity of concrete material is equal to 3644 ksi and the shear modulus is 1518 ksi. For these piles the specified compressive strength of concrete is 4 ksi.

5.3.2 Loading

In this section, the applied loads to the modeled bridges are reviewed. These loads include the self weight of the bridge components, the weight of the wearing surface and

railing, the effects of live load including gravity, braking and centrifugal forces, the pressure of soil to the abutments, the thermal loads including expansion, contraction and temperature gradient through the thickness of superstructure and the effect of concrete shrinkage. Explanations for each of these loads are presented in the following subsections.

A) Dead Load (DC)

Assuming a unit weight of 145 lb/ft^3 , the dead load is applied to all of the components of the modeled bridges through calculating the volume of each element.

B) Wearing Surface Load (DW)

Considering a 4-inch thick overlay with a unit weight of 140 lb/ft^3 , the weight of wearing surface is applied to the bridges. In addition to the overlay, two curbs with a thickness of 12 inches are assumed to exist on the bridges. The weight of railings is considered to be 67 lb/ft. A schematic picture of the wearing surface components is shown in Figure 5.3-1.

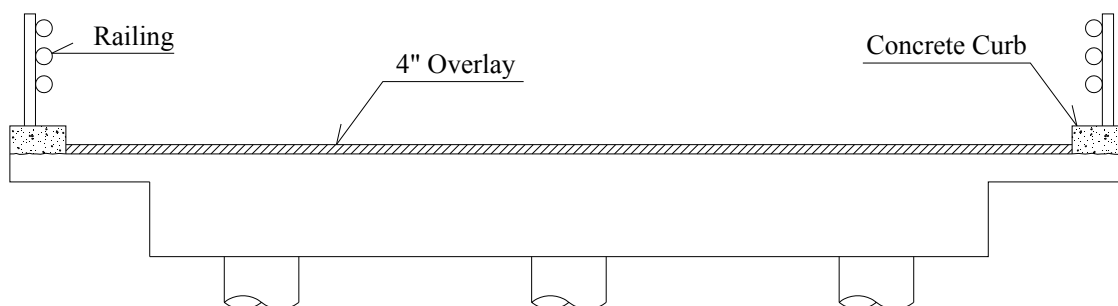


Figure 5.3-1. Wearing Surface of the Modeled Bridges

C) Earth Pressure (EH)

The pressure of the backfill soil is applied to the modeled bridges assuming a cohesionless soil with a unit weight of 125 lb/ft^3 and an angle of internal friction of 30 degrees. Therefore, the soil pressure is:

$$p_{soil} = k_o \gamma h = 3.617 * 10E - 5 * h$$

in which h is the depth of the soil layer in inches and p_{soil} is the soil pressure in ksi.

Elaborate explanations on how the soil pressure is applied to the structure are presented in Section 5.3.3 (Soil-Structure Interaction).

D) Live Load (LL)

Live load is applied to the models based on the AASHTO LRFD Bridge Design Specifications 2010. According to the specifications four different loads should be considered for such continuous superstructures:

- Design truck plus the lane load
- Design tandem plus the lane load
- For negative moments and piers reaction: 90 percent of dual design trucks plus the lane load
- And for the negative moments and piers reaction: dual tandem plus the lane load

An impact factor of 1.33 is applied to all live loads except the lane loads. In addition, a multiple lane presence factor is applied which is derived from Table 4.3-1.

The live loads are applied in the most critical place in each lane so that the maximum effects are concluded. Figure 5.3-2 shows the positioning of the live load on modeled bridge decks.

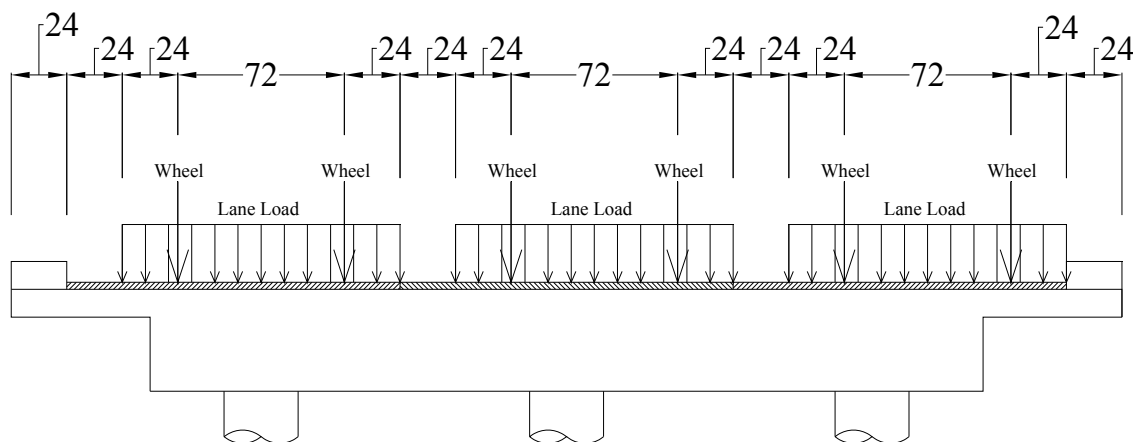


Figure 5.3-2. Positioning of the Live Load (distances in inch)

E) Braking Force (BR)

As per AASHTO LRFD Bridge Design Specifications, the braking force for each lane is the maximum of 25 percent of the design truck weight or 5 percent of the design truck plus lane load weight. This force is calculated for different bridge lengths and applied for different positions of the live load.

It should be noted that as there are three lanes on the modeled bridges and the simultaneous braking of the live load of all lanes is considered, a multilane presence factor, based on Table 4.3-1, is applied to these braking forces. Also, it is noteworthy that the braking force of each lane for bridges shorter than 450 feet is a constant load equal to 15.3 kips:

$$F_{BR} = 72 \text{ kip} * 0.25 * 0.85 = 15.3 \text{ kip/lane}$$

And for longer bridges, it increases with the bridge length as follows:

$$F_{BR} = 0.05(72 \text{ kip} + 0.64 * L) * 0.85 = (3.06 + 0.0272 * L) \text{ kip/lane}$$

F) Centrifugal Force (CE)

When a bridge has horizontal curvature, an important lateral load which is applied to the bridge superstructure is the centrifugal force of moving loads. Based on AASHTO LRFD Bridge Design Specification 2010, this radial force is the product of the weight of design truck or tandem and a C factor defined as:

$$C = f \frac{v^2}{Rg} \quad \text{Eq. 5.1}$$

Where f is equal to $4/3$ for all limit states other than fatigue, v is the design speed, R is the radius of curvature of the design lane and g is the gravitational acceleration equal to 32.2 ft/s^2 . If the parameters in this equation are in a consistent set of units, the C factor will be unitless. A multilane presence factor equal to 0.85 should also be included for three lanes of live load. Table 5.3-1 shows the assumed speed and the resulted centrifugal force for each radius. Note that the assumed design speeds are about 5 mph more than the speed given by Eq. 1.4.

Radius of Curvature (ft)	Geometrical Design Speed (mph)	Structural Design Speed (mph)	C Factor	Centrifugal Force (kips per lane)
200	25.1	30	0.401	24.53
600	43.5	50	0.371	22.70
1000	56.1	60	0.324	19.82

Table 5.3-1. C Factor for Different Radii

G) Uniform Temperature Changes

Seasonal temperature changes are applied to the modeled bridges based on the contour maps that are given in AASHTO as the more rigorous method of determining the temperature changes for each region. For a bridge superstructure which is just made of concrete, a maximum design temperature of 110°F and a minimum design temperature of -30°F can be the worst possible cases. A construction temperature of 60°F results in an increase of $+50^\circ\text{F}$ and a decrease of -90°F which the bridge should tolerate. These

two temperature changes are applied to the modeled bridges as the uniform temperature loading.

H) Temperature Gradient

The temperature gradient loading is applied to the modeled bridge based on the provisions of AASSTO Specifications. Assuming a solar radiation zone “1” for the location of the modeled bridges, a positive temperature gradient of 40 °F is suggested through the thickness of the superstructure. For the negative temperature gradient, a -0.3 factor should be multiplied to the positive gradient which results in a negative gradient of -12 °F. These two temperature gradients are also applied to the models.

I) Shrinkage

Concrete shrinkage is a time-dependent volume decrease of the concrete due to loss of moisture. This phenomenon happens for all concrete elements regardless of presence of external force on the element. To account for this effect in the models, first the strain due to concrete shrinkage is calculated and then the equivalent temperature decrease which causes the same amount of strain is found. In this way, the effect of concrete shrinkage is simulated.

To calculate the strain in concrete due to shrinkage, the method presented by AASHTO LRFD 2010 is used. In the code, the shrinkage strain is obtained using the following equation:

$$\varepsilon_{sh} = k_s k_{hs} k_f k_{td} 0.48 \times 10^{-3} \quad \text{Eq. 5.2}$$

For the definition of each of the parameters of Eq. 5.2, the reader is referred to Section 4.3.2J).

Assuming a relative humidity of 70 percent for the location of the bridge under consideration, a V/S ratio equal to 0.613 inch, an f'_c of 5 ksi for superstructure concrete and a time of infinity for calculation of the time development factor, the following values are obtained:

$$k_s = 1.45 - 0.13 \left(\frac{V}{S} \right) = 1.45 - 0.13 \times 6.44 = 0.613 < 1.0 \rightarrow k_s = 1.0$$

$$k_{hs} = 2 - 0.014 H = 2 - 0.014 \times 70 = 1.02$$

$$k_f = \frac{5}{1 + f'_{ci}} = \frac{5}{1 + 0.80 \times 5} = 1.00$$

$$k_{td} = \frac{t}{61 - 4f'_{ci} + t} = \frac{\infty}{61 - 4 \times 4 + \infty} = 1.0$$

Having the above factors evaluated, the shrinkage strain can be calculated as:

$$\varepsilon_{sh} = 1.0 \times 1.02 \times 1.0 \times 1.0 \times 0.48 \times 10^{-3} = 490 \times 10^{-6}$$

Now the equivalent temperature decrease can be evaluated using the following equation:

$$\alpha \Delta T_{equiv} = -\varepsilon_{sh}$$

Hence:

$$6 \times 10^{-6} \Delta T_{equiv} = -490 \times 10^{-6}$$

$$\Delta T_{equiv} = -81.7 ^\circ F$$

Since in the uniform temperature loading a decrease of -90°F was considered for bridge contraction and the equivalent temperature decrease of shrinkage is -81.7°F , the effects of the concrete shrinkage can be assumed to be % 90.8 of the effects resulted from bridge contraction.

5.3.3 Soil-Structure Interaction

The procedure employed to analyze the soil-structure interaction for studied concrete integral bridges, is similar to what used for steel bridges in Chapter 4. Again, as the abutment walls separate from the soil under specific loading conditions, but the piles are surrounded by soil, the soil response is studied in two different subsections for the walls and piles.

A) Soil-Abutment Interaction

The load-displacement curves of the soil behind the abutment wall of the studied concrete bridges are derived from the response curves of Figure 4.3-5, presented Clough and Duncan. For an abutment wall height of 7'-10", a backfill soil with a unit weight of 125 lb/ft^3 , an internal friction angle of 30 degrees and for springs of one square foot tributary area located at different depths, the force-displacement curves of Figure 5.3-3 are obtained which are used in the finite element models.

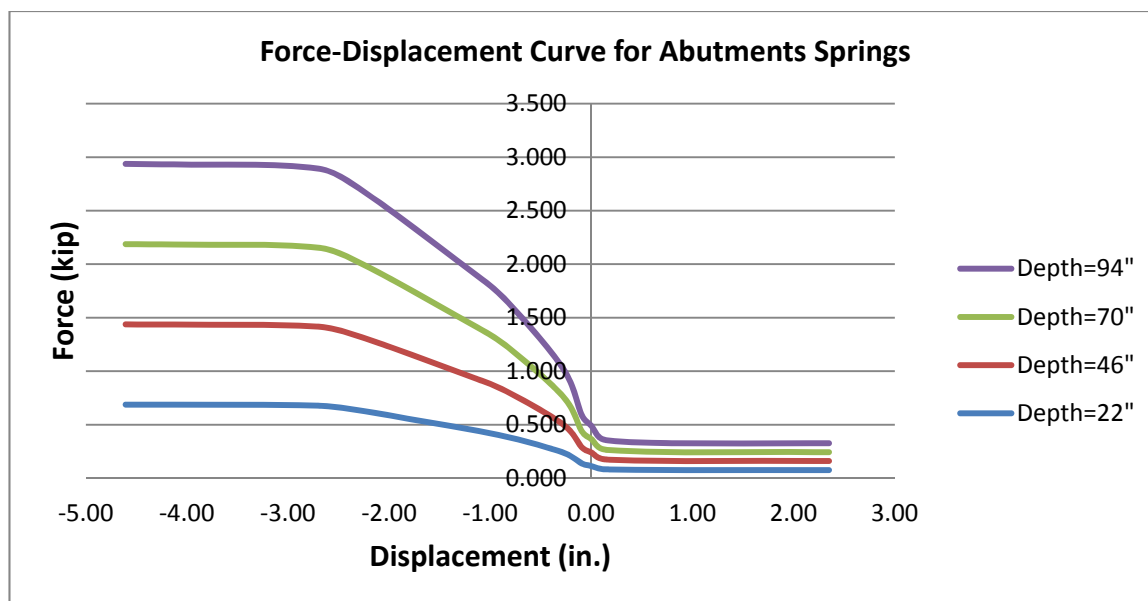


Figure 5.3-3. Force-Displacement Curves of the Abutment Backfill Springs

As the backfill of the bridge abutments are generally composed of granular soils, the response curve for abutment springs is only presented for cohesionless soils. Therefore, cohesive soil behavior for abutment backfill is ignored.

B) Soil-Pile Interaction

The response of the soil interacting with shafts of piers or abutments is modeled using the same technique that was used in steel bridges. The recommendations of American Petroleum Institute are adopted as the model for the soil behavior (American Petroleum Institute, 2005). The following subsections describe the resulted load-deflection curves.

B1) Lateral Load-Deflection in Soft Clay

The response of soft clay under lateral loading is generally a nonlinear behavior. API proposes a p - y curve for short term static loading which may be generated from Table 4.3-7. In that table, p is actual lateral pressure, y is the actual lateral deflection, y_c

is equal to $2.5\varepsilon_c \cdot D$, the ε_c is the strain which occurs at one half of the maximum stress on laboratory unconsolidated undrained compression tests of undisturbed soil samples, D is the pile diameter and p_u is the lateral bearing capacity of soft clay.

The lateral bearing capacity of soft clay has been found to be between $8c$ and $12c$ except at shallow depths which failure mode changes due to lack of enough overburden pressure. In the present study, this capacity is assumed to be equal to $9c$ for deep elements of the pile and for shallower positions, i.e. at depth smaller than reduced resistance zone (X_R), it is linearly increased between $3c$ and $9c$:

$$p_u = 3c + \gamma X + J \frac{cX}{D} \quad \text{for } X < X_R$$

$$p_u = 9c \quad \text{for } X \geq X_R$$

Eq. 5.3

c : Undrained shear strength for undisturbed clay samples

γ : Effective unit weight of soil

J : A dimensionless empirical constant with values ranging from 0.25 to 0.5

X : Depth below soil surface

X_R : Depth below soil surface to bottom of reduced resistance zone. For constant soil strength with depth:

$$X_R = \frac{6D}{\frac{\gamma D}{c} + J}$$

Based on the above equations, with assumed undrained shear strength of 2 ksf, ε_c of 0.01, J value of 0.4 and 5 feet spacing for the springs of the concrete piles of abutments with a diameter of 40 inches, the force-displacement curves are obtained which are

plotted in Figure 5.3-4. As can be observed, the behavior for the springs deeper than 33 feet, is independent of the depth of the soil. This constant response is applicable to springs down to the end of the piles which are 50 feet deep.

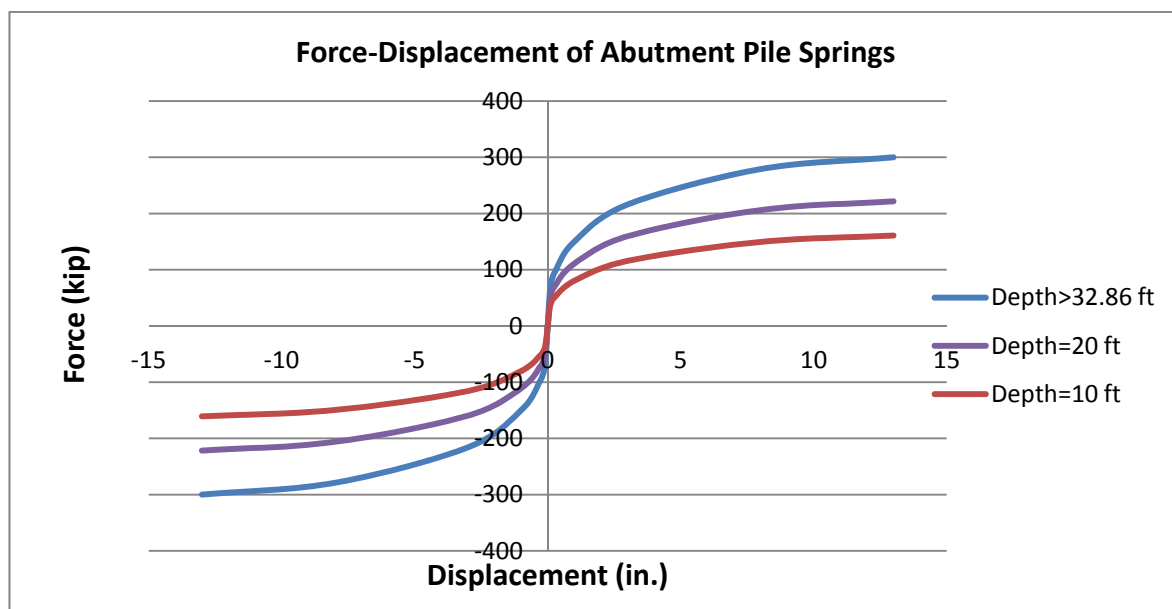


Figure 5.3-4. Force-Displacement Curves of the Springs of Piles of Abutments in Soft Clay

For the response of the soil neighboring the pile of piers which have a diameter of 48 inches, assuming the same constants and soil properties as for abutment piles, the curves of Figure 5.3-5 are derived. As can be seen, from the depth of 36.9 feet to the end of the piles, which is the depth of 65 feet, the reaction of the soil does not change.

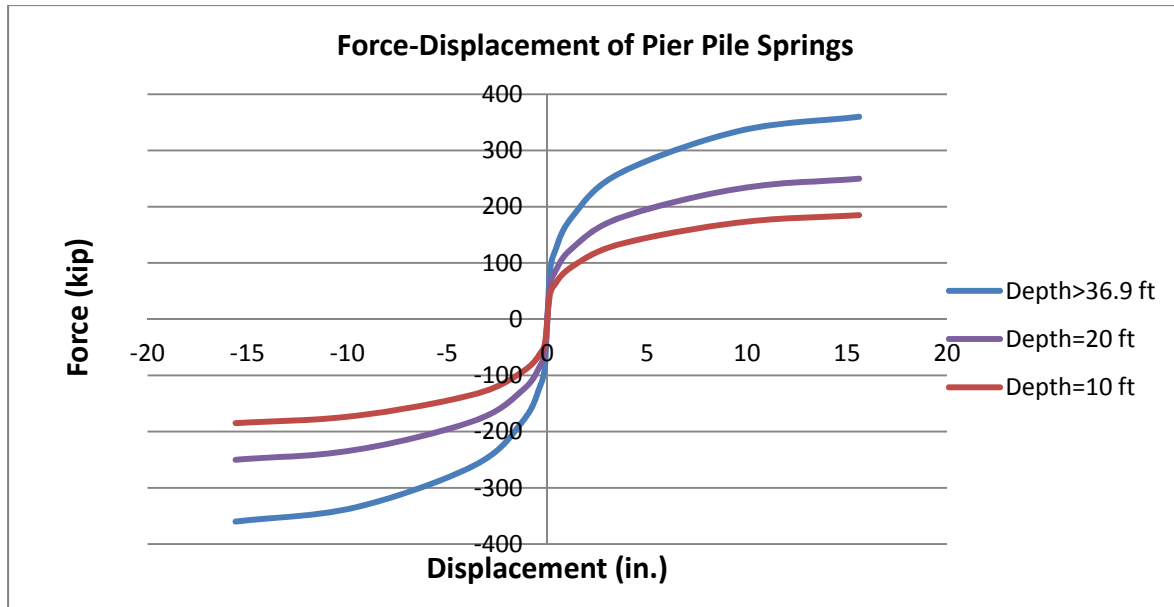


Figure 5.3-5. Force-Displacement Curves of the Springs of Piles of Piers in Soft Clay

B2) Lateral Load-Deflection in Sand

API recommends a hyperbolic tangent equation for the lateral force-displacement curve of the piles in sand as follows:

$$F_{spring} = C_0 \cdot p_u \cdot \Delta z \cdot \tanh\left(\frac{k z y}{\alpha p_u}\right) \quad \text{Eq. 5.4}$$

Where:

F_{spring} : Lateral soil resistance in a length of Δz of pile (force)

C_0 : An empirical correction factor, $C_0 = 3 - 0.8 \left(\frac{z}{D}\right) \geq 0.9$

p_u : Estimated ultimate lateral soil resistance (force/unit length)

Δz : Length of the pile section

k : Initial modulus of subgrade reaction from Figure 4.3-9

z : Soil depth from the top of the soil layer

y : Displacement in the horizontal direction

The ultimate soil lateral resistance can be obtained based on the given equations as the minimum of:

$$p_{us} = (C_1 z + C_2 D) \cdot \gamma' \quad \text{Eq. 5.5}$$

And

$$p_{ud} = C_3 \cdot \gamma' \cdot D \cdot z \quad \text{Eq. 5.6}$$

Where:

p_{us} : Ultimate sand lateral resistance at shallow depths (force/unit length)

p_{ud} : Ultimate sand lateral resistance at deep depths (force/unit length)

D : Pile Diameter

γ' : Effective soil density

φ : Angle of internal friction

$$C_1 = K_o \frac{\tan \varphi \tan \beta}{\tan(\beta - \varphi) \cos \alpha} + \frac{\tan^2 \beta \tan \alpha}{\tan(\beta - \varphi)} + K_o \tan \beta (\tan \varphi \sin \beta - \tan \alpha)$$

$$C_2 = \frac{\tan \beta}{\tan(\beta - \varphi)} - \tan^2 \left(45 - \frac{\varphi}{2} \right)$$

$$C_3 = K_o \tan \varphi \tan^4 \beta + K_a (\tan^8 \beta - 1)$$

$$\alpha = \varphi / 2$$

$$\beta = 45 + \frac{\varphi}{2}$$

K_a : Active earth pressure coefficient

K_o : At-rest earth pressure coefficient

The values of constants C_1 , C_2 and C_3 can be found from Figure 4.3-10. This figure may also be used to check the values obtained from the relevant equations.

Using the above equations and considering a diameter of 48 inches for the shafts of piers, a soil unit net weight of 125 /ft^3 , an angle of internal friction of 30 degrees and five feet spacing for the springs, a k value of 45 lb/in^3 is obtained from Figure 4.3-9 which results in the force-displacement curves of Figure 5.3-6 for the pile springs. As shown in the Figure 5.3-6, the force-displacement curves strongly depend on the depth of the springs.

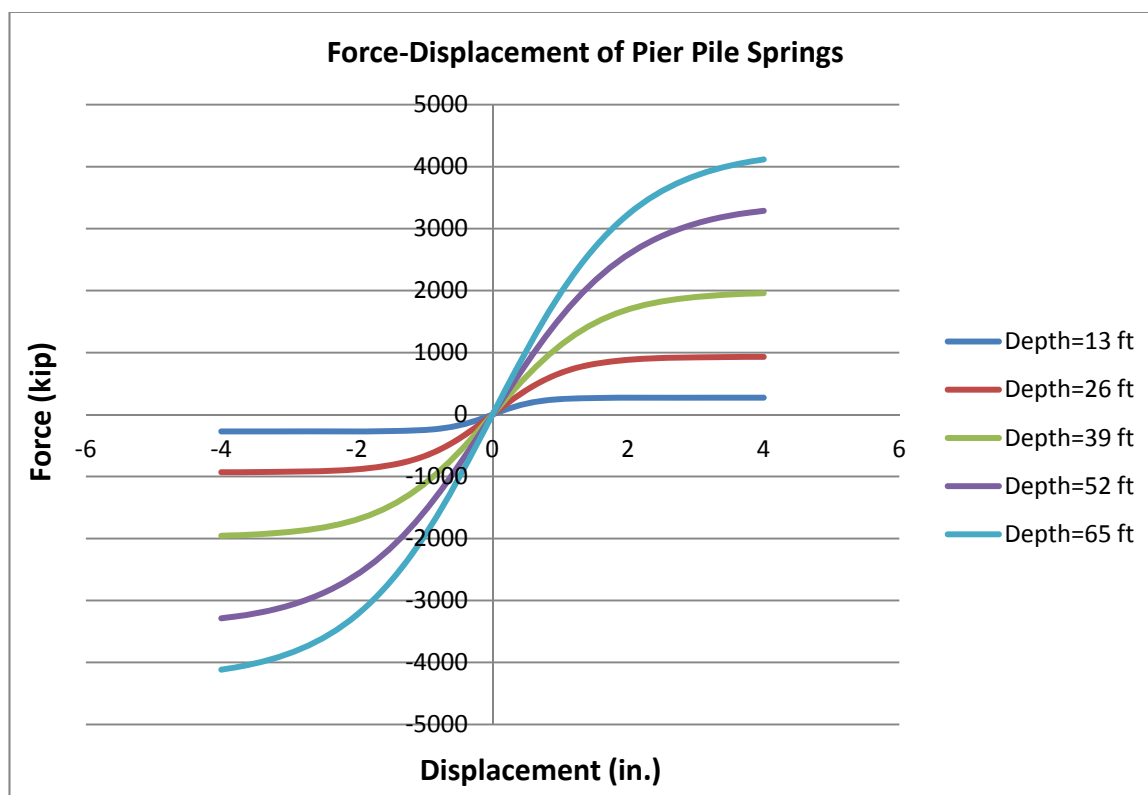


Figure 5.3-6. Force-Displacement Curves of the Springs of Piles of Piers in Sand

The response of the springs of the piles of the abutments can be plotted by employing the same values as used for the pier piles in the related equations and considering a

diameter of 40 inches for the piles. Figure 5.3-7 shows the force-displacement curves for these springs.

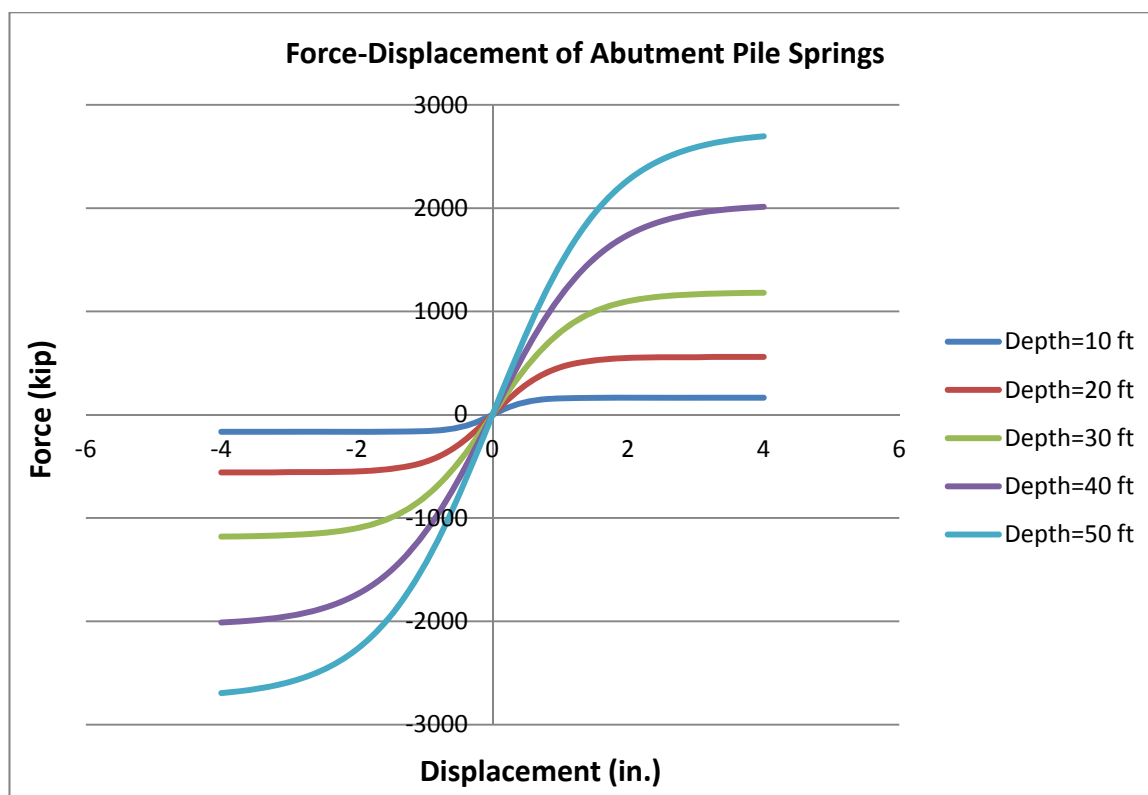


Figure 5.3-7. Force-Displacement Curves of the Springs of Piles of Abutments in Sand

5.3.4 Elements

The bridges studies in this chapter consist of voided slab superstructures, flexible integral abutments interacting with the backfill soil and the surrounding soil of the piles and some piers comprising concrete columns and piles. The piles of the piers are also in contact with the supporting soil. As can be observed, the bridge behavior is controlled by several structural elements that need different elements to be used for better modeling. An explanation of these finite elements is brought in the following subsections.

A) Beam Element

To model the pier columns and also the piles of the piers and abutments, two-node frame elements are used. For description of the beam elements refer to the Section 4.3.5A).

B) Shell Element

The superstructure including the voided slab deck and the side cantilevers and also the stub abutments of the bridges are modeled using shell elements. A shell element is a three- or four-node formulation which combines membrane and plate behaviors. For more complete description of the shell elements refer to Section 4.3.5B).

C) Nonlinear Link Element

Nonlinear link elements are used to connect two joints together with specified nonlinear properties. As explained in Chapter 3, each link element may have three different types of behavior based on the required properties and the analysis type. These properties include: linear, nonlinear and frequency-dependent.

In the modeled bridges, these link elements are used to simulate the elastomeric bearings connecting the piers to the superstructure. In design of the elastomeric bearings, it is assumed that the area of the bearing should be chosen so that the pressure on the bearing is not less than a specified value, namely one third or one fourth of the maximum allowed pressure on the bearing. This assumption yields to the fact that these types of bearings shall be not in tension in any of the load combinations. On the other hand, as the maximum applied pressure on the neoprene is limited by the manufacturers (typically to 2 ksi), the stiffness of the link element in the six degrees of freedom can be determined as

follows. In the following equations, the gravity direction of the neoprene is assumed as direction 1 and the two shearing directions are assumed as 2 and 3. For a circular elastomeric bearing of 22-inch diameter and 4-inch thickness, assuming an elastic modulus of 85.3 ksi and a shear modulus of 0.142 ksi, the following stiffnesses can be calculated:

Axial stiffness:

$$k_1 = \frac{EA}{T} = \frac{85.3 \times \frac{\pi}{4} \times 22^2}{4} = 8106 \text{ k/in}$$

Shearing stiffness:

$$k_2 = k_3 = \frac{GA}{T} = \frac{0.142 \times \frac{\pi}{4} \times 22^2}{4} = 13.5 \text{ k/in}$$

Torsional stiffness:

$$k_{11} = \frac{GJ}{T} = \frac{0.142 \times \frac{\pi}{32} \times 22^4}{4} = 816 \text{ k.in/rad}$$

Bending stiffness:

$$k_{22} = k_{33} = \frac{EI}{T} = \frac{85.3 \times \frac{\pi}{64} \times 22^4}{4} = 245216 \text{ k.in/rad}$$

Where:

A is the cross sectional area, E is axial modulus of elasticity, T is the total thickness including rubber and steel plates, G is the shear modulus of elasticity, J is the torsional constant (equal to $\frac{\pi D^4}{32}$ for circular neoprenes) and I is the moment of inertia of the section of the elastomeric bearing.

Therefore, the calculated stiffness of the bearings are entered into the finite element model. A picture of the elastomeric bearing modeling of a pier of the modeled bridges is shown in Figure 5.3-8.

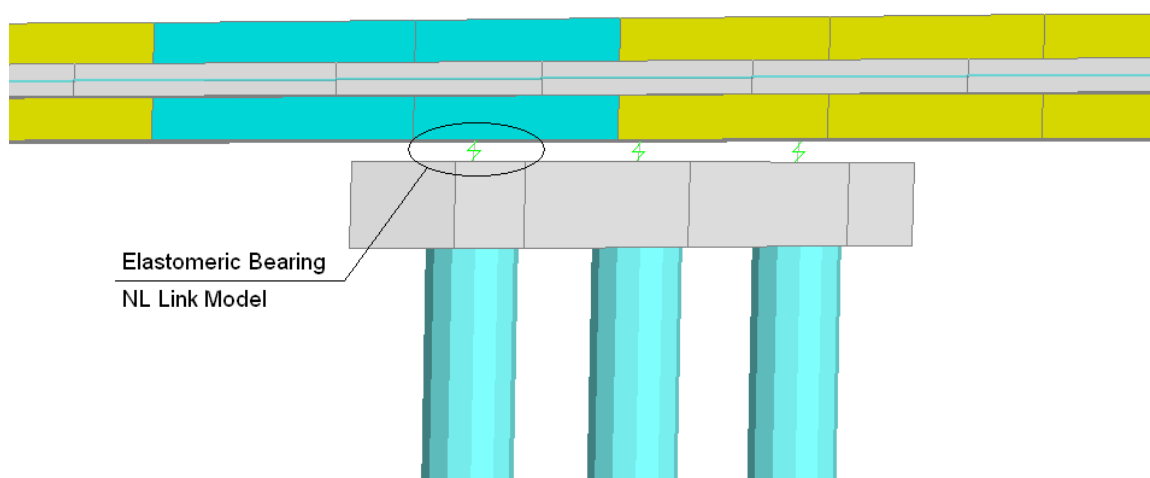


Figure 5.3-8. Modeling of the Elastomeric Bearings

D) Nonlinear Support Element

To model the effect of the soil support which acts on the abutment walls and the surface of the piles, nonlinear support elements are used. These elements are one-node grounded nonlinear springs.

As two different types of properties are supposed to be analyzed with these elements which are soil-abutment interaction and soil-pile interaction, two different sets of properties are defined for these elements.

The first set of assigned properties to nonlinear support elements is based on the force-displacement curves of Figure 5.3-3 which are assigned to the nonlinear springs of the abutment walls.

The second set of assigned properties to nonlinear springs is based on the force-displacement curves of Figure 5.3-4 and Figure 5.3-5 which are considered for the springs that are supposed to model the behavior of the surrounding soil of the shafts of abutments and piers. As the shafts are embedded in the soil, the springs have the same nonlinear response in tension and compression.

5.3.5 Finite Element Models

Based on the information provided in the previous sections, a comprehensive finite element analysis study is conducted. In the analyses, the movements and internal forces of curved integral abutment bridges are evaluated and compared to the responses of straight bridges.

In order to perform such analyses, several finite element models of curved bridges with radius of curvature equal to 200, 600 and 1000 feet are made. For each of these radii, the bridge is modeled in different lengths, namely 130, 215, 300, 470 and 640 feet. On the other hand, the equivalent straight bridge of each curved model is simulated with exact same characteristics as the curved bridge except the curvature. The length of the end spans and intermediate spans of the studied bridges are 65 and 85 feet, respectively. As shown before, the width of all the bridges is 40 feet. Figure 5.3-9 illustrates a typical finite element model that is made in this study.

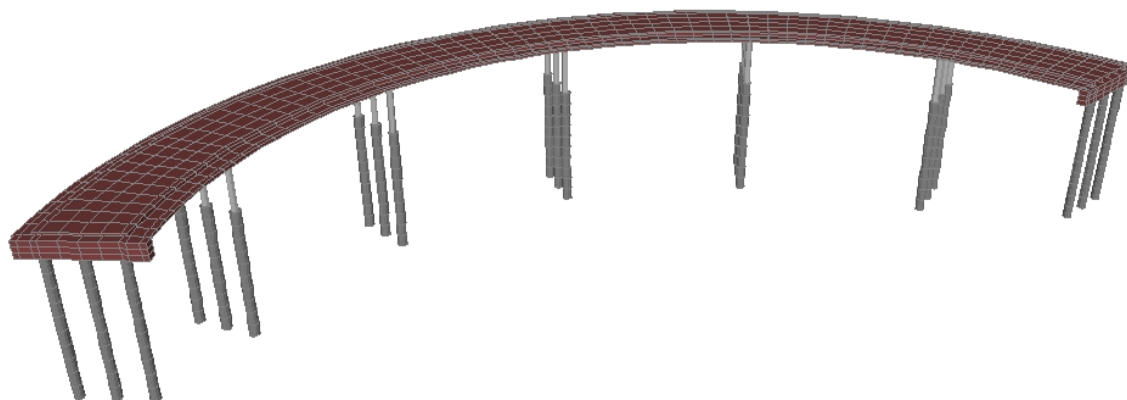


Figure 5.3-9. A Typical Finite Element Model of the Studied Bridges

5.4 Results of FE Analysis

In this section, the results of the previously explained finite element analyses are presented. To comprehend the behavior of curved concrete integral bridges, different problems are discussed. First, the internal forces of the abutment piles are studied and compared to counterpart straight bridges. The results are presented for a variety of load cases that were discussed in Section 5.3.2. Integral bridges can have bearing-isolated rigid piers or flexible integral piers. The responses in these two types of structures are compared. The other part of this section focuses on the integral piers. When the piers are integrally connected to superstructure, they should be flexible to accommodate the movements. And flexibility requires slender columns to be incorporated in the structure. The superiority of adopting integral bridge systems when slender columns are needed is then discussed.

5.4.1 Effect of Length and curvature on Load Responses

In this section, the consequences of variation in the bridge length and curvature on the load effects are presented. In the design of integral abutment bridges, the most critical response is the internal forces in abutment piles. In most cases, the pile forces determine the maximum possible bridge length. Other responses like the bending moments in the superstructure, the moments in the abutment concrete wall can be designed by choosing larger sections or stronger material. The axial forces in the piles can also be designed choosing enough long piles. Therefore, the study is narrowed down to the flexural forces of the abutment piles which are discussed in the following sections.

A) Bending Moment of Abutment Piles

Abutments of the modeled bridges are comprised of the stub wall and the piles. The height of the stub wall is just 50 inches and it is a continuous element compared to discrete supporting piles. Therefore, from a structural design point of view, the piles are more critical for design. This statement is more clarified noting the fact that the summation of the bending moments of the stub wall and the piles along the line of their intersection are equal. For the wall, this moment is distributed along the horizontal length of the wall which is 40 feet, but for the piles, the moment is divided among the piles, in this case among three piles. Hence, to study the variation of the internal forces of the abutments, those of the abutment piles are investigated.

AI) Contraction

The flexural moments of the abutment piles of the modeled bridges are evaluated using the finite element program for both curved and straight bridges under bridge contraction loading. These moments are plotted versus the length of the bridges in Figure 5.4-1. It is observed that for straight bridges the moment blows up as the length increases. In curved bridges the rate of increase in the moments reduces as the curvature increases. In highly curved bridges, the moments have a drastic decrease as the length of the bridge gets larger. For a radius of 200 feet, the moment in a bridge of 640 feet is smaller than that of a bridge with 130 feet length.

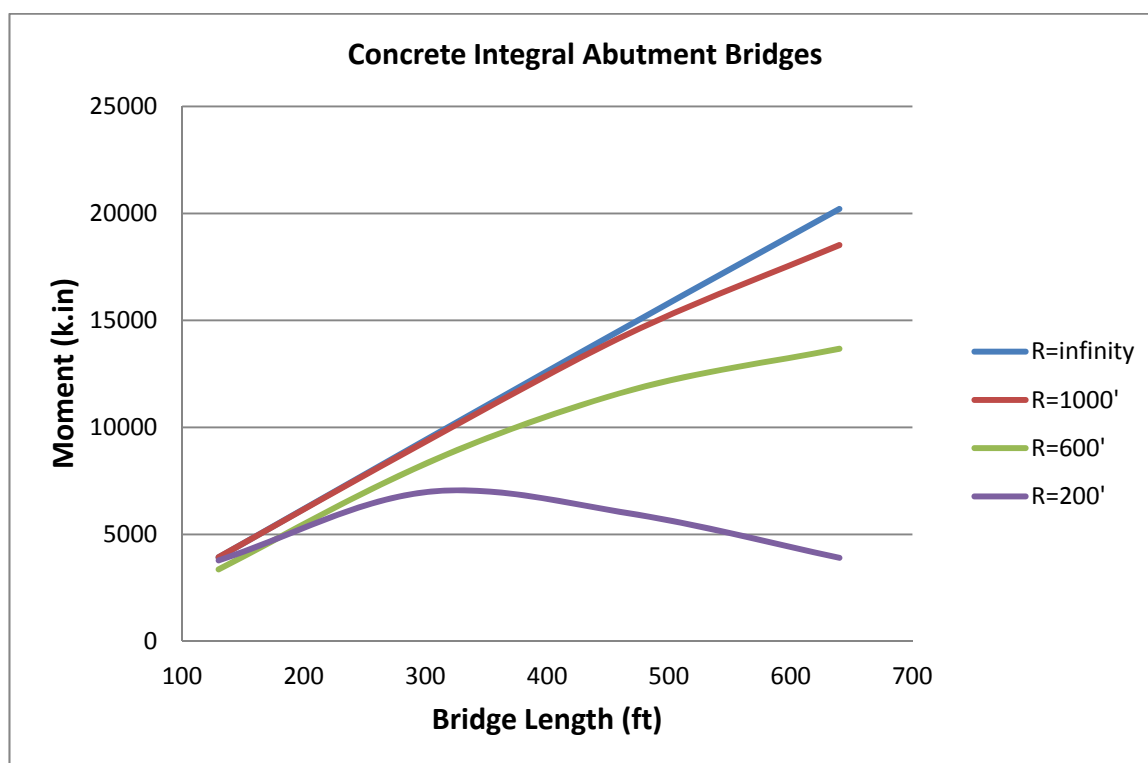


Figure 5.4-1. Maximum Moment of Abutment Piles Due to Contraction

A2) *Expansion*

The bending moment of abutment piles due to straight bridge expansion increases strictly as the length of the bridge increases. In curved bridges, the moment increases up

to a specific length at which a maximum moment occurs. The length corresponding to the maximum moment depends on the curvature, ranging from 300 feet for a radius of 200 feet to 500 feet for a radius of 1000 feet. For longer bridges the moments start to reduce.

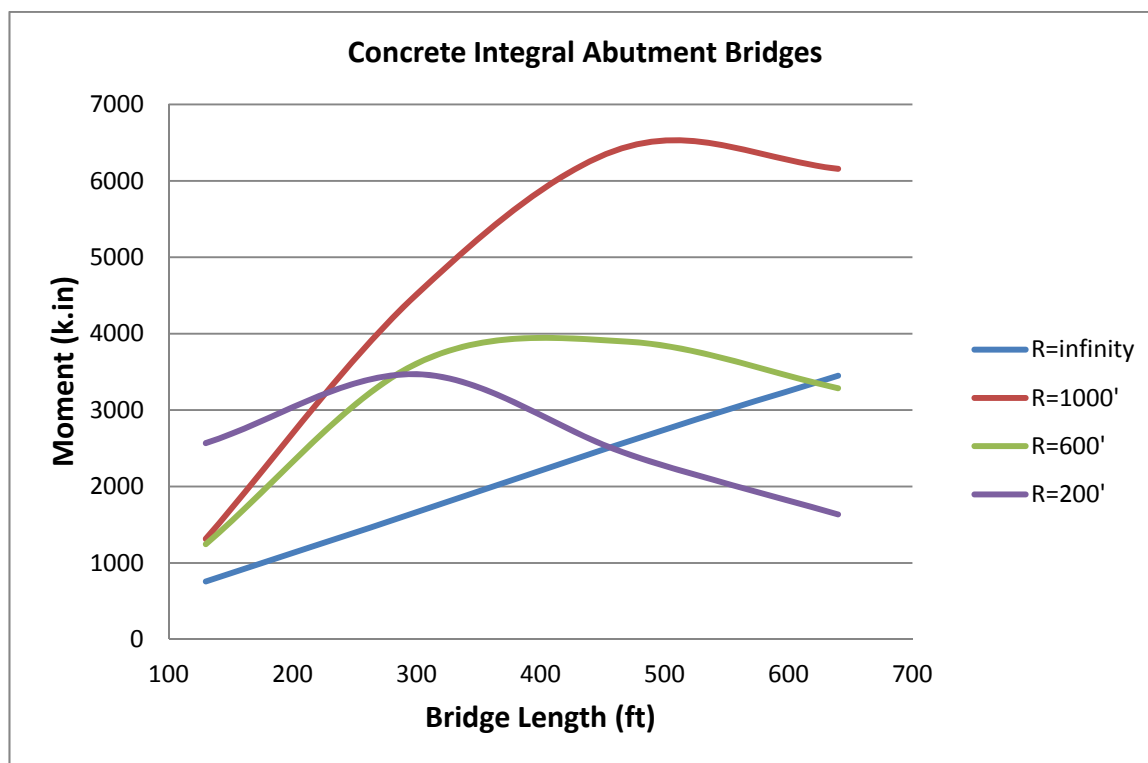


Figure 5.4-2. Maximum Moment of Abutment Piles Due to Expansion

A3) *Live Load*

For each radius, the pile moments due to live load have an increase as the length of the bridge increases from 130 feet (two-span bridge) to 300 feet (four-span bridge). For longer bridges, it is almost constant. The response for straight bridges and curved bridges with the radius of 1000 feet are very close. For a radius of 600 feet, the moments are larger than the other bridges.

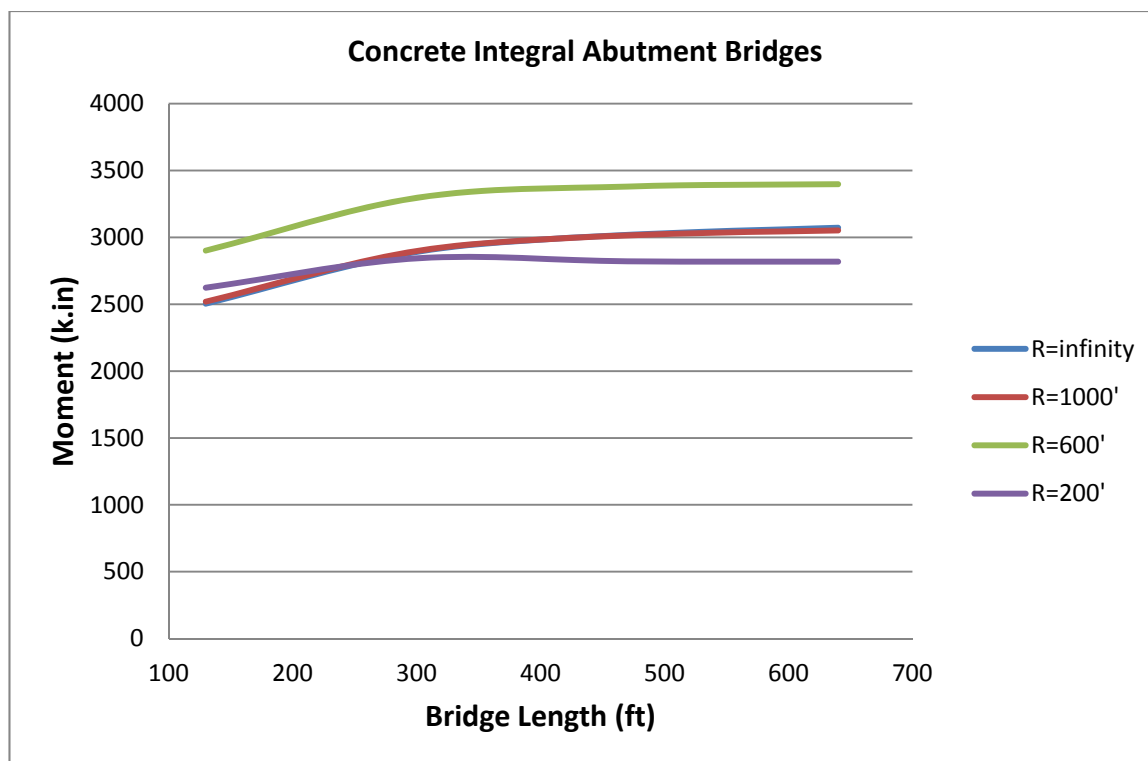


Figure 5.4-3. Maximum Moment of Abutment Piles Due to Live Load

A4) Dead Load

The bending moment in the abutment piles due to dead load of the bridge has a decreasing trend as the length of the bridge increases up to a specific length. In longer bridges, the moments are approximately constant for each bridge curvature. The moments in straight bridges and curved bridges with a radius of 1000 feet are very close. For long bridges, the dead load moments reduce as the radius of the bridge decreases.

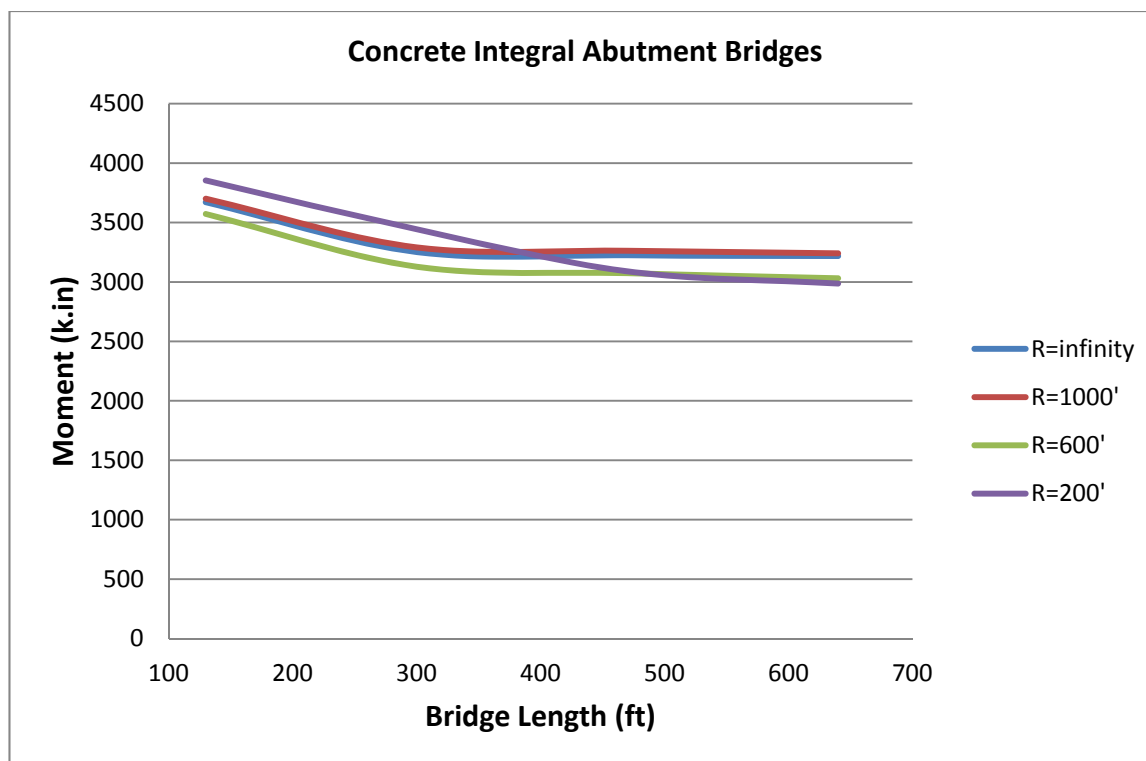


Figure 5.4-4. Maximum Moment of Abutment Piles Due to Dead Load

A5) Concrete Shrinkage

As the studied bridges are composed of only concrete elements, the responses due to concrete shortening is similar to those of bridge contraction. As can be observed, in straight bridges, the moments due to shrinkage are strictly increasing. As the radius reduces, the rate of increase decreases in a manner that for the tight radius of 200 feet, the moments have a maximum at the length equal to 300 feet and for longer bridges, the moments decrease rapidly. For larger radii, the moments have a concave curve which shows a response between that of straight and highly curved bridges. For large bridge radius like 1000 feet, the moments are close to those of straight bridges.

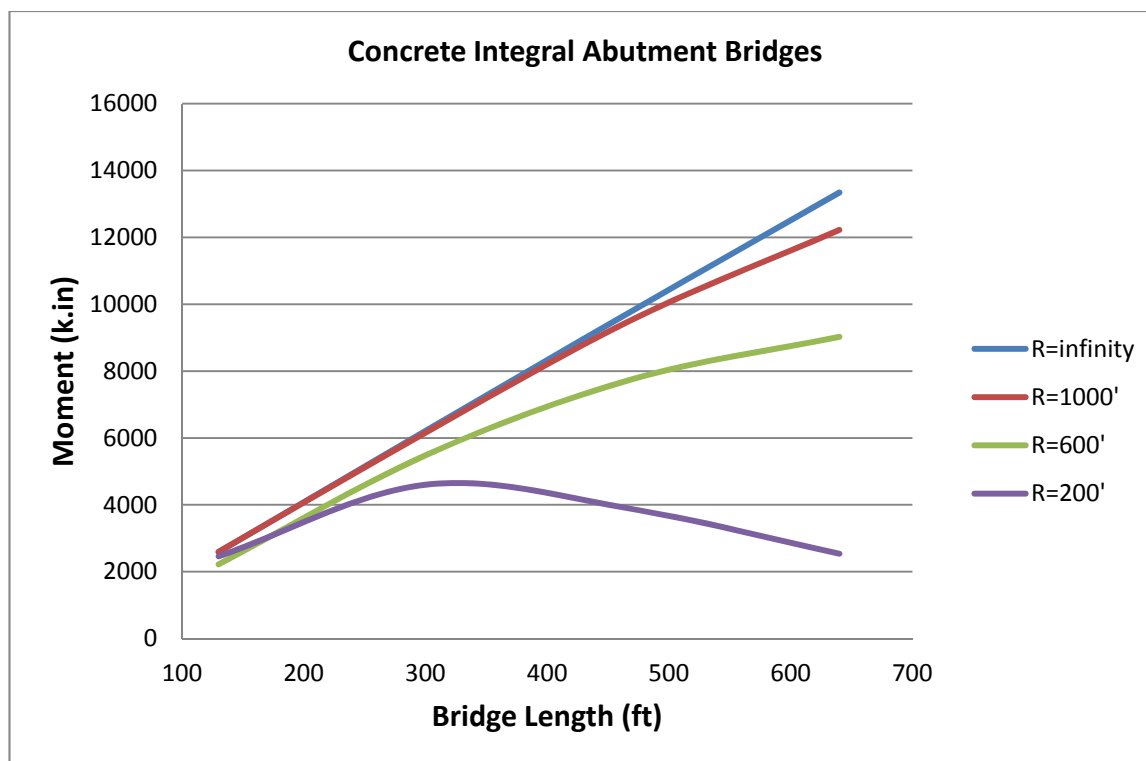


Figure 5.4-5. Maximum Moment of Abutment Piles Due to Concrete Shrinkage

A6) *Horizontal Earth Pressure (EH)*

The abutment pile moments are approximately constant for straight bridges. In this case, there is a slight increase in moments for longer bridges as depicted in Figure 5.4-6. For radius equal to 600 and 1000 feet, the response is similar to straight bridges with a larger increase as the length increases. For highly curved bridges, $R=200$ feet, the response is totally different. The moments increase rapidly as the radius decreases from 600 feet to 200 feet. The reason is illustrated in Figure 5.4-7 through Figure 5.4-9. In a straight bridge, the earth forces are in the same line and opposite to each other. Therefore, they balance each other and only cause local bending in the piles. In a tightly curved bridge depending on the length-to-radius ratio, the earth pressures are not counteracting like in straight bridges. For small Length/Radius ratios the major components of earth

pressure balance each other. But for large Length/Radius ratios, the earth pressure is mainly resisted by the internal forces in the structure. In some cases, as shown in Figure 5.4-7, the earth pressure may be almost perpendicular to each other. In such situations, large lateral displacements occur due to earth pressure which results in large bending moments in the abutment piles.

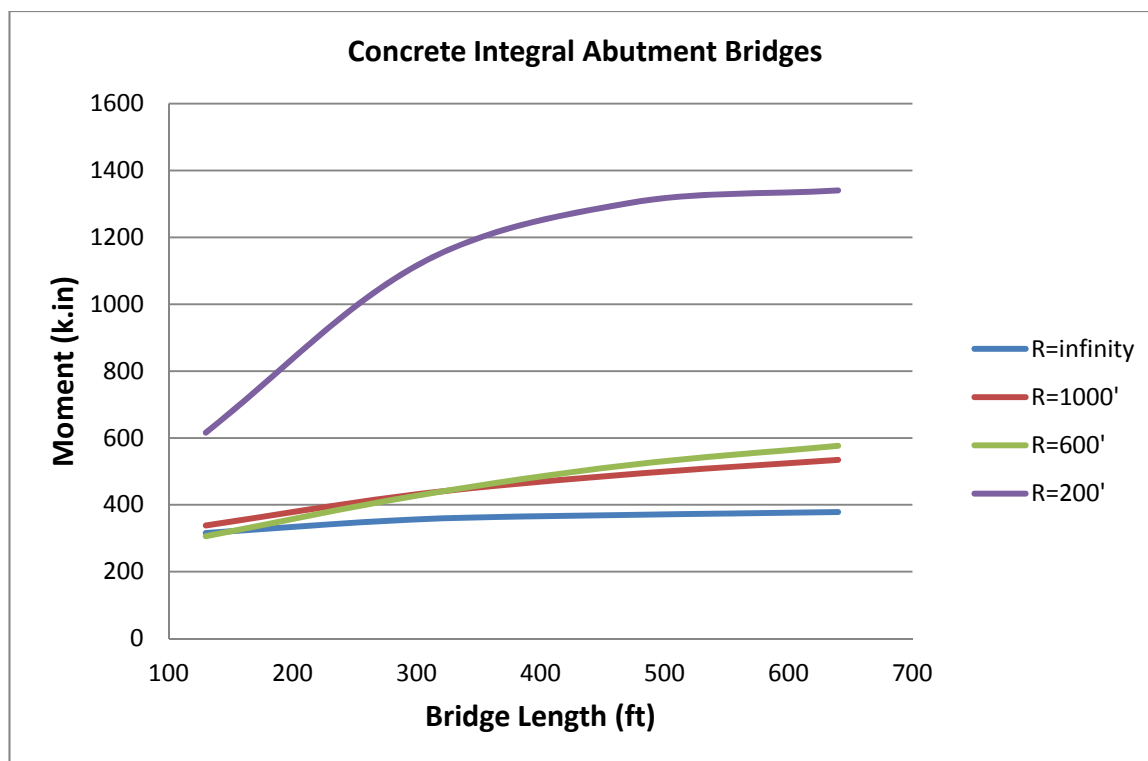


Figure 5.4-6. Maximum Moment of Abutment Piles Due to Horizontal Earth Pressure

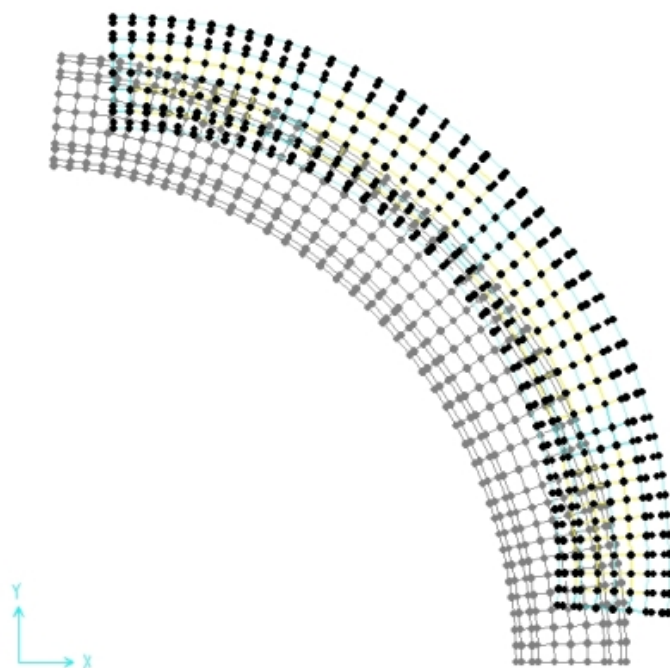


Figure 5.4-7. Plan View of Deformed Shape of the Bridge with R=200' under EH

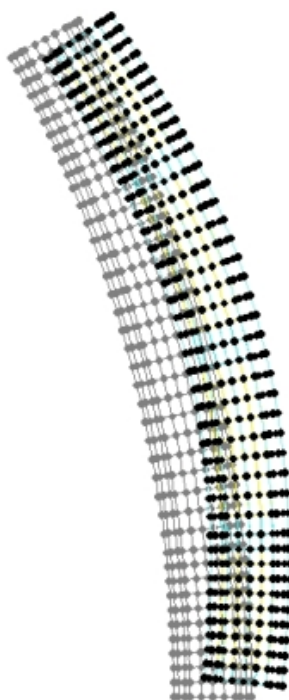


Figure 5.4-8. Plan View of Deformed Shape of the Bridge with R=600' under EH

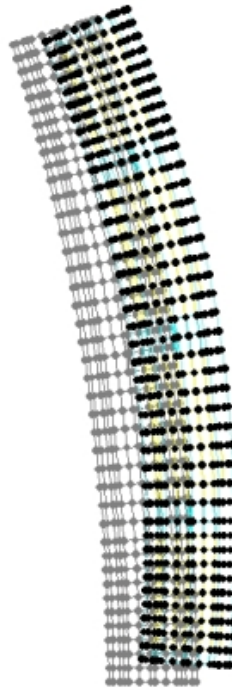


Figure 5.4-9. Plan View of Deformed Shape of the Bridge with R=1000' under EH

A7) *Centrifugal Force*

Figure 5.4-10 describes the pile moments due to centrifugal forces. It shows that the centrifugal moments are larger for short bridges. Up to a length of 400 feet, the moments are decreasing and for longer bridges, the moments are constant.

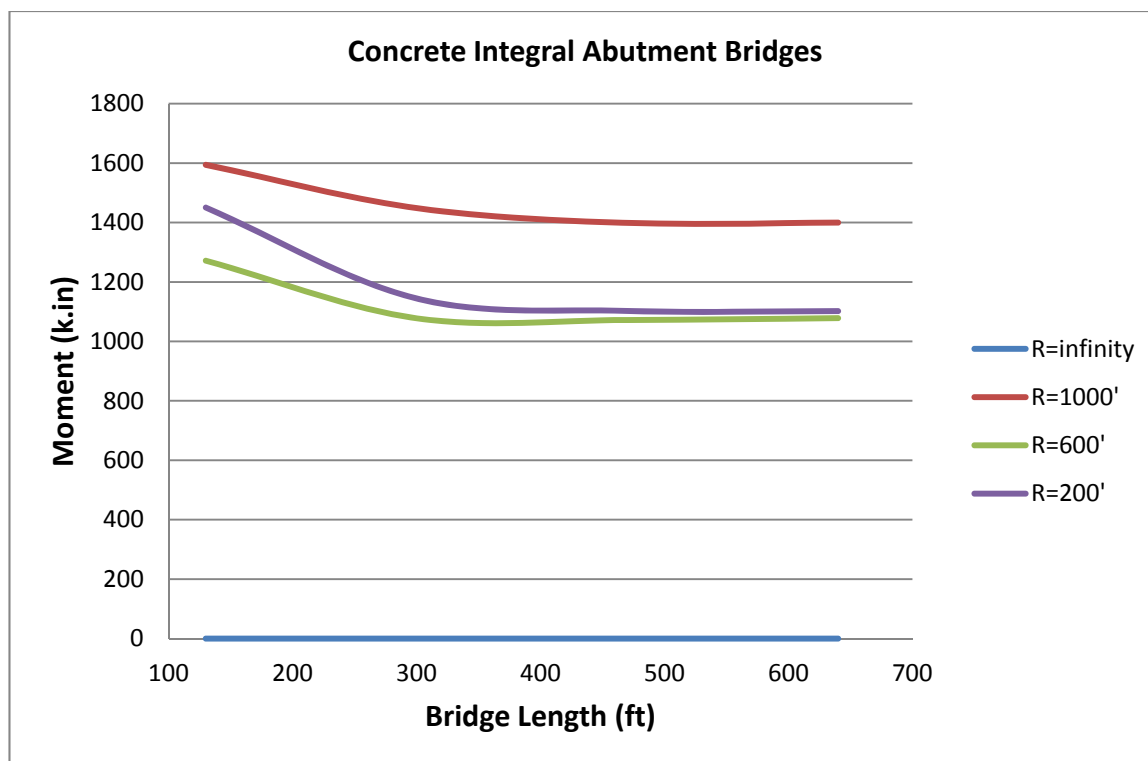


Figure 5.4-10. Maximum Moment of Abutment Piles Due to Centrifugal Force

A8) Weight of Wearing Surface

The changes in moments due the weight of wearing surface are similar to those of dead load. In general, there is a decreasing trend in the moments as the length increases. The response of bridges with the radius equal to 1000 feet is very close to that of straight bridges.

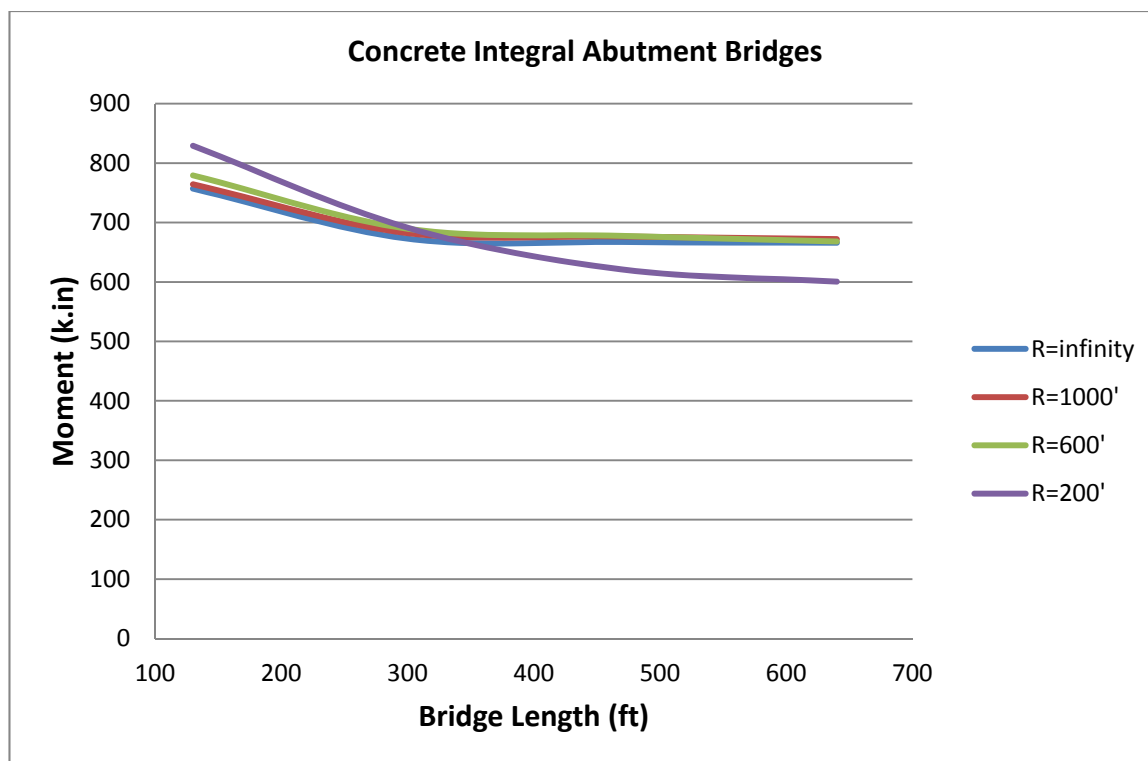


Figure 5.4-11. Maximum Moment of Abutment Piles Due to Weight of Wearing Surface

A9) *Braking Force*

The pile moments because of braking force are shown in Figure 5.4-12. It is observed that the moments increase as the radius of the bridge decreases. This is mainly attributed to the balance of braking force by the backfill pressure. In straight bridges or those with a large radius, the braking force is resisted by the passive pressure of the abutment backfill. But, in highly curved bridges, a large component of the braking force is not balanced by the earth pressure and creates a large bending moment in abutment piles and piers. The other fact is the increase in the slope of the curves for bridges longer than 450 feet. This is because of the change in the magnitude of braking force in the design code for bridges beyond this length.

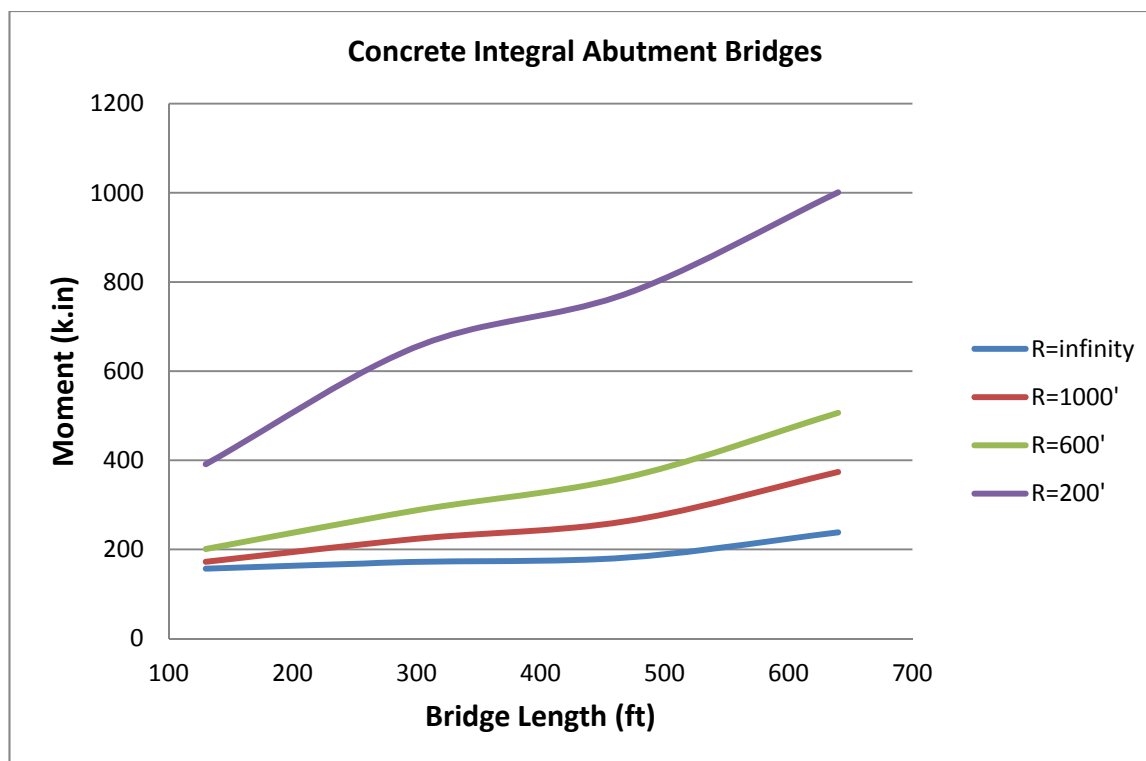


Figure 5.4-12. Maximum Moment of Abutment Piles Due to Braking Force

A10) Positive Temperature Gradient

It is shown in Figure 5.4-13 that the bending moments due to positive temperature gradient is approximately constant as the length of the bridge changes. Also, it is observed that these moments reduce as the radius of the bridge decreases. The difference in the moments between straight bridges and those with radius equal to 200 feet is less than 20 percent. So, as an estimate, it can be assumed that the moments due to temperature gradient are independent of bridge length and radius.

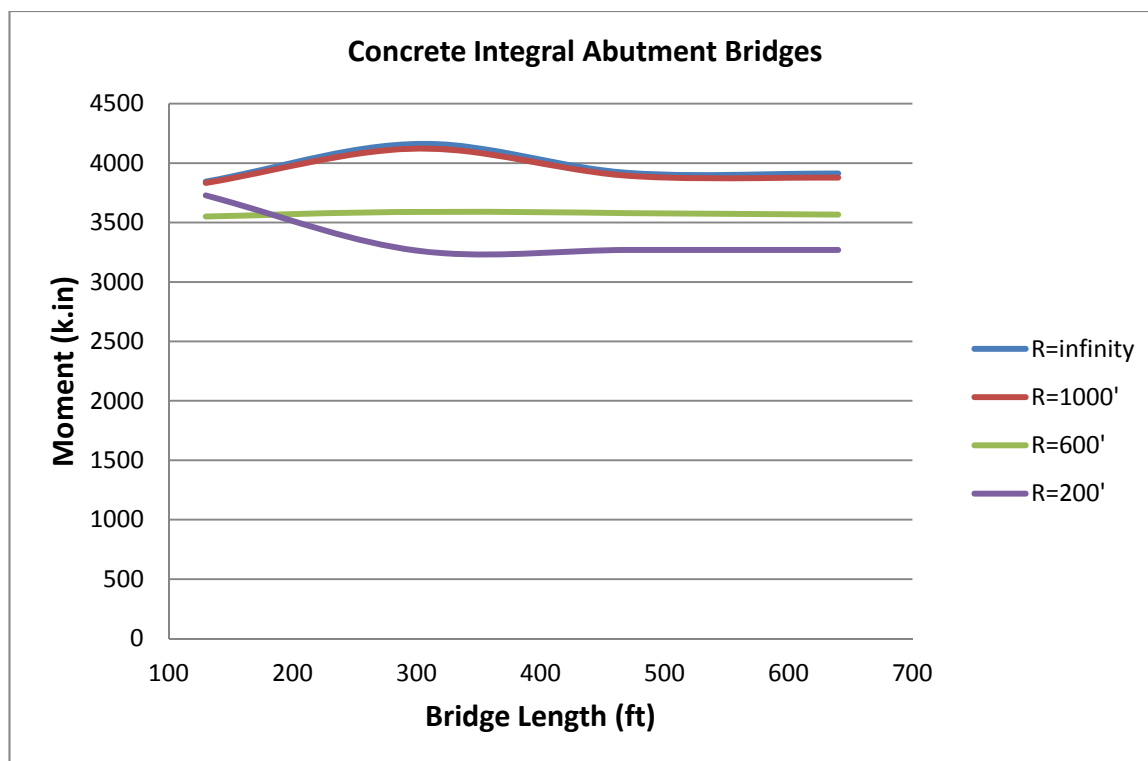


Figure 5.4-13. Maximum Moment of Abutment Piles Due to Positive Temperature Gradient

A11) Negative Temperature Gradient

As negative temperature gradient is equal to minus 30 percent of the positive one, the results pattern is similar to that of positive gradient. For description of the results, the reader is referred to the previous section.

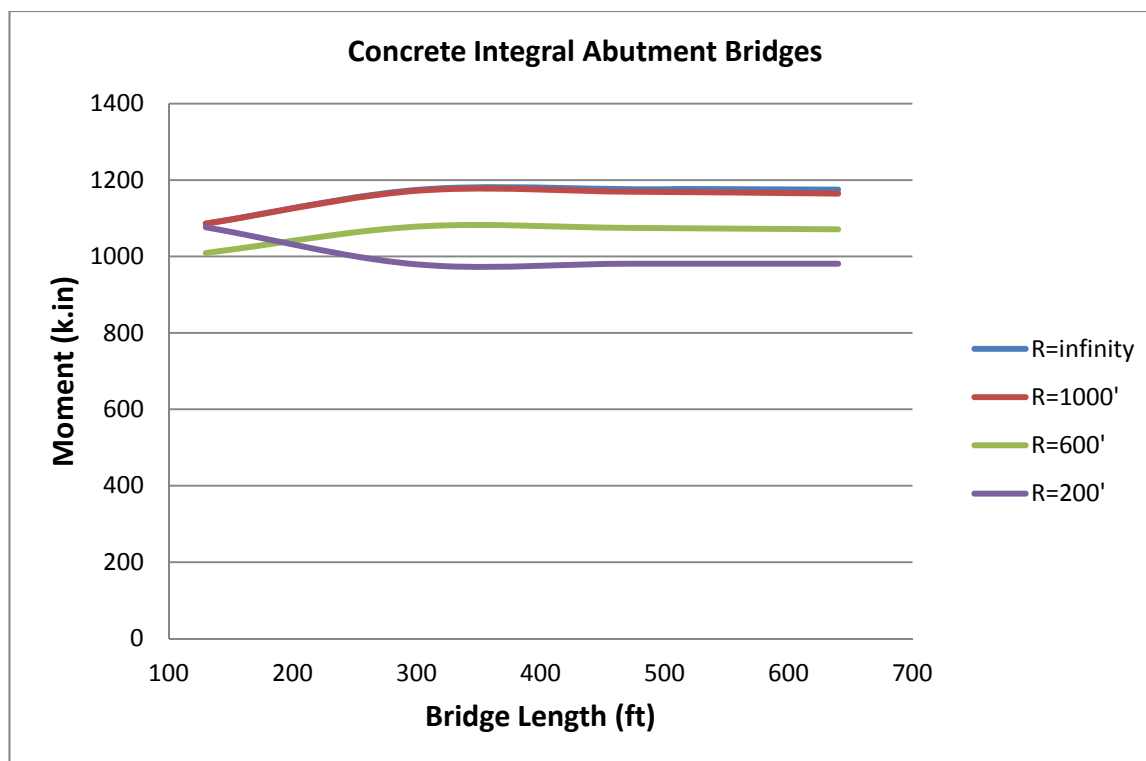


Figure 5.4-14. Maximum Moment of Abutment Piles Due to Negative Temperature Gradient

A12) Combination of the Loads

The final plot for load effects, and the most important one, is illustrated in Figure 5.4-15. The envelopes of the maximum bending moments in different load combinations are shown in this picture. The significant observation is that in curved bridges, the envelope moments are not strictly increasing. In highly curved bridges with radius equal to 200 feet, the moments are almost constant for bridges longer than 300 feet. In bridges with larger radius, the moments are between those of R=200 and straight bridges. The bridges with R=1000 feet have moments very close to straight bridges, so that these moment can be estimate ignoring the effect of curvature.

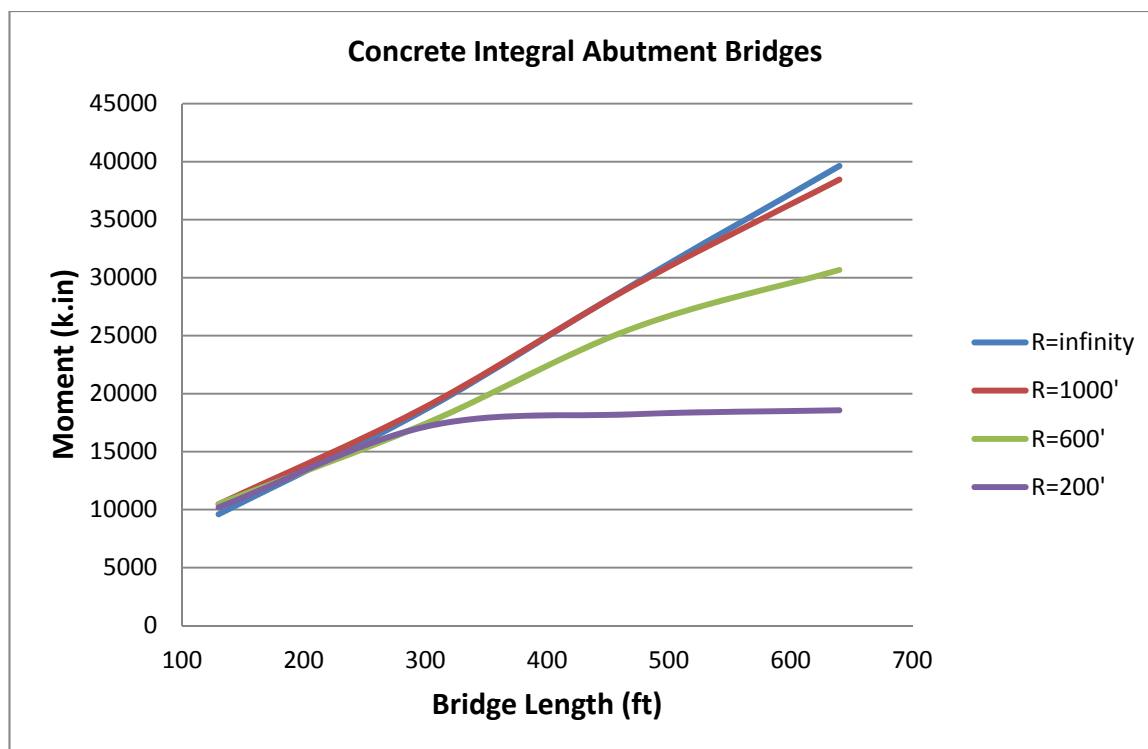


Figure 5.4-15. Envelope of Moment of Abutment Piles in Different Load Combinations

B) Shear Forces of Abutment Piles

In the case of steel bridges, it was observed that the graphs of shear forces of abutment piles (depicted in Appendix A) were similar to those of piles bending moments. Therefore, for the studied concrete bridges, for brevity, the discussion on the shear forces is disregarded.

5.4.2 Pile Orientation

In this section, the effect of pile orientation in concrete integral bridges is investigated. In the studied bridges, the abutments are supported by circular drilled shafts. As the section of the shafts is symmetric, the resulted moments from any horizontal direction of displacement are the same from structural design point of view. But in a concrete bridge,

the shafts can be asymmetric, like rectangular shafts, or the rebars in a symmetric shaft can be asymmetric. Then, different orientations of the shafts result in different internal forces. Therefore, there should be a criterion to determine the optimum orientation of the shafts.

To study this problem, the circular piles of the studied concrete bridges are replaced by rectangular shafts. The shafts have a 40-inch by 20-inch cross section. Two sets of finite element models are made with strong-axis and weak-axis bending orientations for the piles. The bridges are analyzed with these two shaft orientations to find the internal forces of the shafts including the axial force and bending moments. The results for the bridge with the length of 130 feet are shown in Table 5.4-1:

Orientation	Axial Force (kip)	M22 (weak axis moment) (k.in)	M33 (strong axis moment) (k.in)
Weak-Axis Bending	105	863	9381
Strong-Axis Bending	105	1143	8492

Table 5.4-1. Internal Forces of Shafts with Different Orientations

The shafts are designed by the program PCACOL to calculate the required rebar area in each of them. The results show that for the strong-axis orientation of the shafts, 8.22 square inches of Grade 60 rebar is required. This area of rebar is equal to 1.025 percent of the gross cross sectional area of the shaft. Figure 5.4-16 and Figure 5.4-17 depict the design details in the program format. The shaft with weak-axis orientation is also

designed for the resulted internal forces. The needed area of Grade 60 rebar for the weak-axis bending is 16.56 square inches. It is equivalent to 2.07 percent of the gross cross sectional area of the shaft. The details of the design process are shown in Figure 5.4-18 and Figure 5.4-19.

Therefore, it is concluded that the strong-axis bending of the drilled shafts results in more economical designs in the case of straight bridges. A similar conclusion was made for the orientation of steel piles in the previous chapter.

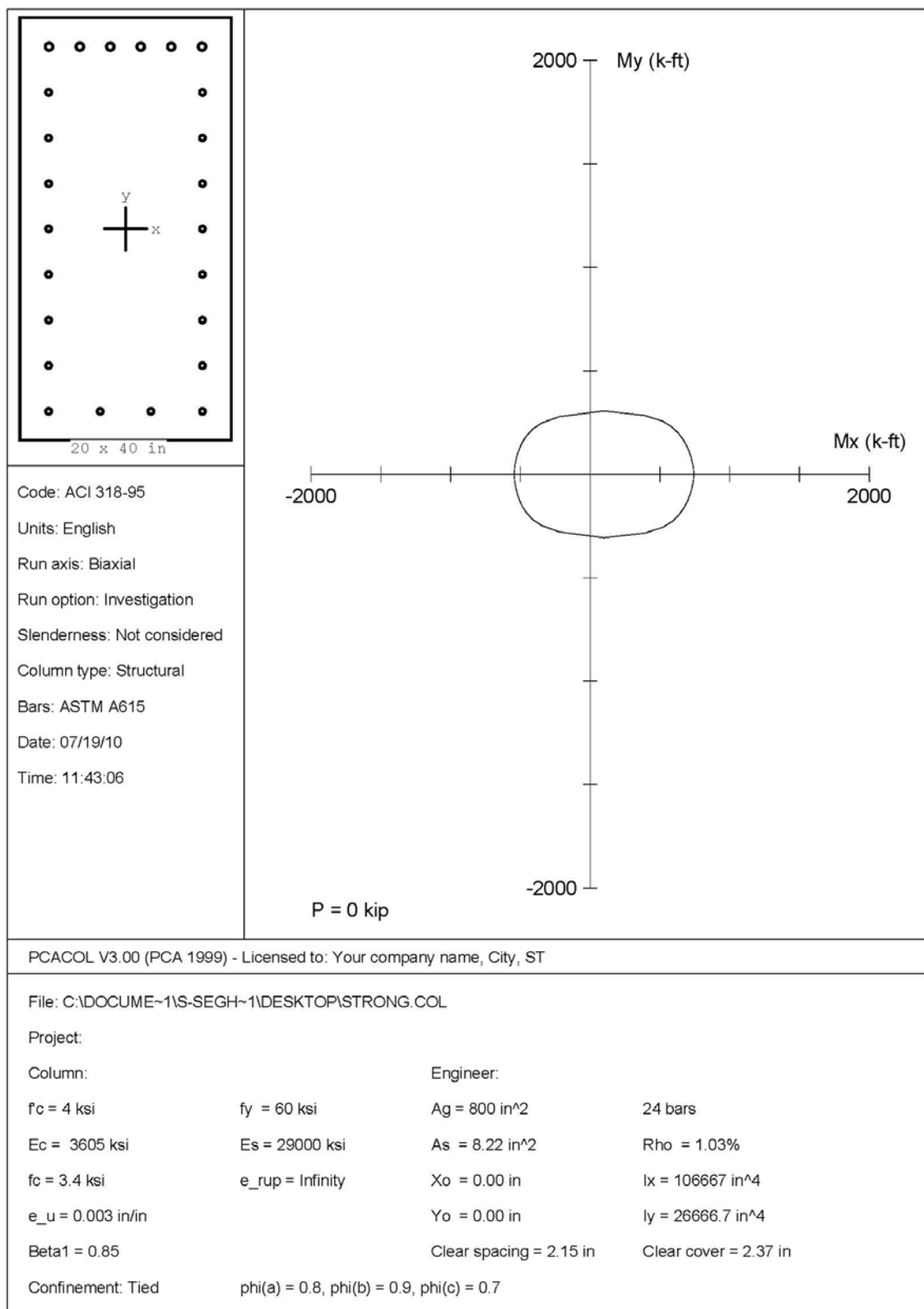


Figure 5.4-16. PCACOL Design Sheet for Strong-Axis Orientation (1 of 2)

07/19/10 PCACOL V3.00 - PORTLAND CEMENT ASSOCIATION -
 11:42:55 Licensed to: Your company name, City, ST

Page 2
 STRONG

General Information:

```
=====
File Name: C:\DOCUME~1\S-SEGH~1\DESKTOP\STRONG.COL
Project:
Column:                               Engineer:
Code:   ACI 318-95                     Units: English

Run Option: Investigation               Slenderness: Not considered
Run Axis:   Biaxial                     Column Type: Structural
```

Material Properties:

```
=====
f'c   = 4 ksi                        fy   = 60 ksi
Ec    = 3605 ksi                     Es   = 29000 ksi
fc    = 3.4 ksi                      Rupture strain = Infinity
Ultimate strain = 0.003 in/in
Beta1 = 0.85
```

Section:

```
=====
Rectangular: Width = 20 in           Depth = 40 in

Gross section area, Ag = 800 in^2
Ix = 106667 in^4                     Iy = 26666.7 in^4
Xo = 0 in                            Yo = 0 in
```

Reinforcement:

```
=====
Rebar Database: ASTM A615
Size Diam (in) Area (in^2)   Size Diam (in) Area (in^2)   Size Diam (in) Area (in^2)
-----
# 3      0.38      0.11   # 4      0.50      0.20   # 5      0.63      0.31
# 6      0.75      0.44   # 7      0.88      0.60   # 8      1.00      0.79
# 9      1.13      1.00   # 10     1.27      1.27   # 11     1.41      1.56
# 14     1.69      2.25   # 18     2.26      4.00
```

Confinement: Tied; #3 ties with #10 bars, #4 with larger bars.
 phi(a) = 0.8, phi(b) = 0.9, phi(c) = 0.7

Layout: Rectangular

Pattern: Sides Different (Cover to transverse reinforcement)

Total steel area, As = 8.22 in^2 at 1.03%

	Top	Bottom	Left	Right
Bars	6 # 6	4 # 5	7 # 5	7 # 5
Cover(in)	2	2	2	2

Factored Loads and Moments with Corresponding Capacities: (see user's manual for notation)

```
=====
No.      Pu      Mux      Muy      fMnx      fMny      fMn/Mu
      kip      k-ft      k-ft      k-ft      k-ft
-----
1      105.0    782.0    72.0    801.3    72.8    1.025
```

*** Program completed as requested! ***

Figure 5.4-17. PCACOL Design Sheet for Strong-Axis Orientation (2 of 2)

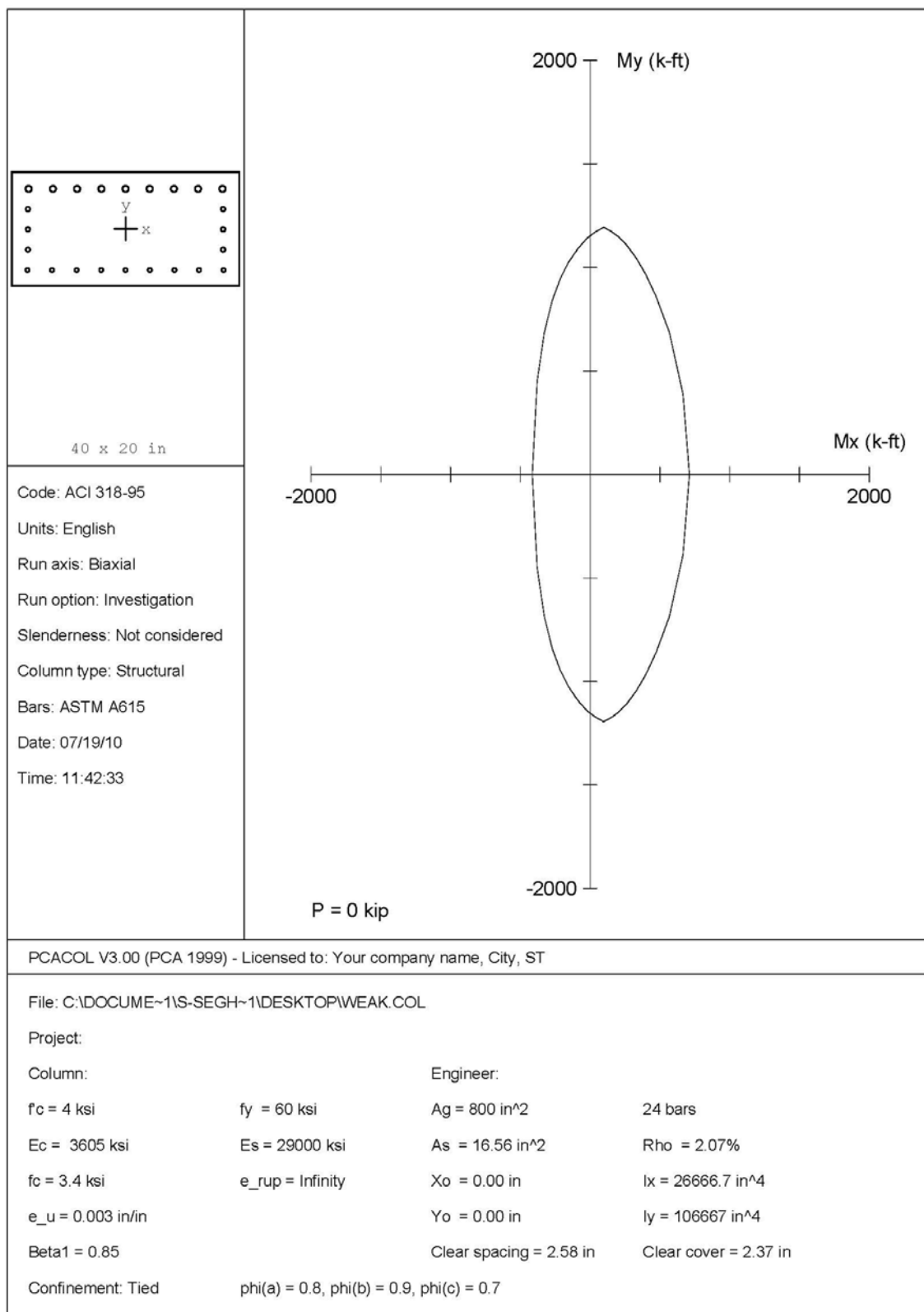


Figure 5.4-18. PCACOL Design Sheet for Weak-Axis Orientation (1 of 2)

07/19/10 PCACOL V3.00 - PORTLAND CEMENT ASSOCIATION -
 11:41:53 Licensed to: Your company name, City, ST

Page 2
 WEAK

General Information:

```
=====
File Name: C:\DOCUME~1\S-SEGH~1\DESKTOP\WEAK.COL
Project:
Column:                               Engineer:
Code:   ACI 318-95                     Units: English

Run Option: Investigation               Slenderness: Not considered
Run Axis:   Biaxial                     Column Type: Structural
```

Material Properties:

```
=====
f'c   = 4 ksi                        fy   = 60 ksi
Ec    = 3605 ksi                     Es   = 29000 ksi
fc    = 3.4 ksi                      Rupture strain = Infinity
Ultimate strain = 0.003 in/in
Beta1 = 0.85
```

Section:

```
=====
Rectangular: Width = 40 in           Depth = 20 in

Gross section area, Ag = 800 in^2
Ix = 26666.7 in^4                    Iy = 106667 in^4
Xo = 0 in                           Yo = 0 in
```

Reinforcement:

```
=====
Rebar Database: ASTM A615
Size Diam (in) Area (in^2)   Size Diam (in) Area (in^2)   Size Diam (in) Area (in^2)
-----
# 3      0.38      0.11   # 4      0.50      0.20   # 5      0.63      0.31
# 6      0.75      0.44   # 7      0.88      0.60   # 8      1.00      0.79
# 9      1.13      1.00   # 10     1.27      1.27   # 11     1.41      1.56
# 14     1.69      2.25   # 18     2.26      4.00
```

Confinement: Tied; #3 ties with #10 bars, #4 with larger bars.
 phi(a) = 0.8, phi(b) = 0.9, phi(c) = 0.7

```
Layout: Rectangular
Pattern: Sides Different (Cover to transverse reinforcement)
Total steel area, As = 16.56 in^2 at 2.07%

      Top      Bottom      Left      Right
Bars   -----
      9 # 9     9 # 6      3 # 7      3 # 7
Cover(in) 2      2        2        2
```

Factored Loads and Moments with Corresponding Capacities: (see user's manual for notation)

```
=====
No.      Pu      Mux      Muy      fMnx      fMny      fMn/Mu
      kip      k-ft      k-ft      k-ft      k-ft
-----
1      105.0    708.0    95.0     710.0     94.9     1.003
```

*** Program completed as requested! ***

Figure 5.4-19. PCACOL Design Sheet for Weak-Axis Orientation (2 of 2)

5.4.3 Bearing-Isolated Pier vs. Flexible Integral Pier

As described in the Section 5.2.3, there can be two different types of piers in the studied concrete integral bridges. In one of the pier types, the columns of the pier are integrally connected to the superstructure. As both columns and superstructure are concrete elements, just extending the rebars of the columns into the superstructure with the required development length provides the integrity of the piers and superstructure. In the second type of piers, the pier columns and a cap beam form a frame which the superstructure seats on it by means of elastomeric bearings. Therefore, a large amount of the movements of the superstructure can be accommodated by bearings instead of the pier structure. Figure 5.2-3 and Figure 5.2-4 describe these two types of piers graphically.

The concrete integral abutment bridges are analyzed with these two types of piers. As the stiffnesses of these two piers are not the same, the internal forces of the structures are different. The point of interest in the design of integral abutment bridges is the abutment piles. The envelope of flexural moment of abutment piles in different load combinations are derived from the finite element models and plotted versus different bridge lengths in Figure 5.4-20. As can be observed, in straight bridges, the difference between the pile moments with different pier types is ignorable. In curved bridges, the pile moments in the bridges with integral piers are greater than those of bridges with isolated piers. As the radius of curvature of the bridges is reduced, the difference between the moments is more profound. The largest change in the moments is for bridges with the radius equal to 200 feet which a 15 percent reduction is observed when the piers are bearing-isolated.

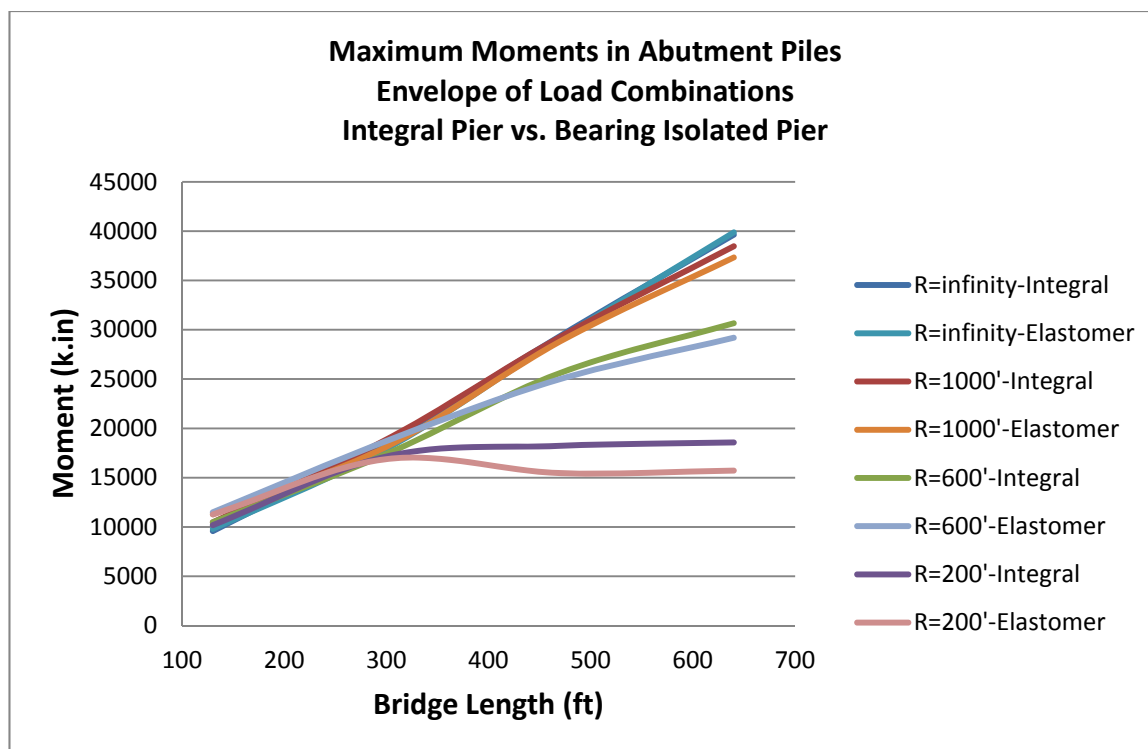


Figure 5.4-20. Envelope of Moment of Abutment Piles in Different Load Combinations in Bridges with Integral Piers vs. Bridges with Elastomeric Isolated Piers

5.4.4 Mitigation of Moment Magnification

In design of frames, the second order $P\Delta$ effects should be taken into account. The studied concrete integral abutment bridges which have integral piers are 3D frames. Such bridges have an enhanced $P\Delta$ behavior compared to jointed bridges. In this section, the difference between the behavior of these two types of bridges and the superiority of integral abutment designs are explained.

To design the columns of the piers of a jointed bridge, the flexural moments of the columns M_u should be determined from a second order elastic analysis or an approximate procedure as follows (American Institute of Steel Construction, American Institute of Steel Construction, & Manual of steel construction, 2005):

$$M_u = B_1 M_{nt} + B_2 M_{lt} \quad \text{Eq. 5.7}$$

in which

M_{nt} : required flexural strength assuming no lateral translation

M_{lt} : required flexural strength as a result of lateral translation only

$$B_1 = \frac{C_m}{1 - \frac{P_u}{P_{e1}}} \geq 1 \quad \text{Eq. 5.8}$$

where

$$P_{e1} = \frac{\pi^2 EI}{(K_{braced} L)^2} \quad \text{Eq. 5.9}$$

and

K_{braced} : effective length factor in the plane of bending determined for the braced frame

P_u : required axial compressive strength

C_m : a coefficient based on elastic first order analysis assuming no lateral translation equal to:

$$C_m = 0.6 - 0.4 \frac{M_1}{M_2} \quad \text{for members with no transverse loading}$$

$$C_m = 0.85 \quad \text{for end restrained members with transverse loading}$$

$$C_m = 1.0 \quad \text{for end unrestrained members with transverse loading}$$

$\frac{M_1}{M_2}$: smaller-to-larger end moments ratio (negative for single curvature)

And

$$B_2 = \frac{1}{1 - \sum P_u \left(\frac{\Delta_{oh}}{\sum HL} \right)} \quad \text{Eq. 5.10}$$

or

$$B_2 = \frac{1}{1 - \left(\frac{\sum P_u}{\sum P_{e2}} \right)} \quad \text{Eq. 5.11}$$

In which

$\sum P_u$: required axial strength of all columns in a story

Δ_{oh} : lateral inter-story deflection

$\sum H$: sum of all story horizontal shear producing Δ_{oh}

L : column height

$$P_{e2} = \frac{\pi^2 EI}{(K_{unbraced} L)^2} \quad \text{Eq. 5.12}$$

$K_{unbraced}$: effective length factor in the plane of bending determined for the unbraced frame.

The above formulations consider two buckling states for the columns. One is the situation in which a column is loaded axially but it cannot sway laterally, because it is attached to other columns through the top and bottom rigid diaphragms (floors) (Figure 5.4-21). The other state is when the columns are loaded axially and simultaneously can sway. But the lateral translation occurs for all columns altogether and in the same direction (Figure 5.4-22). Actually, these equations are derived from AISC manual of steel construction which is mainly developed for building design. In buildings, the main lateral loads are wind or seismic forces which have a unique direction for all the columns of a story at a given time.

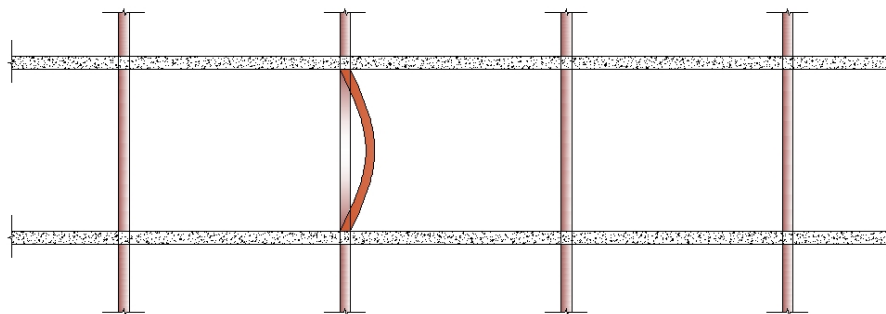


Figure 5.4-21. $P\Delta$ Effect in Non-Sway Mode

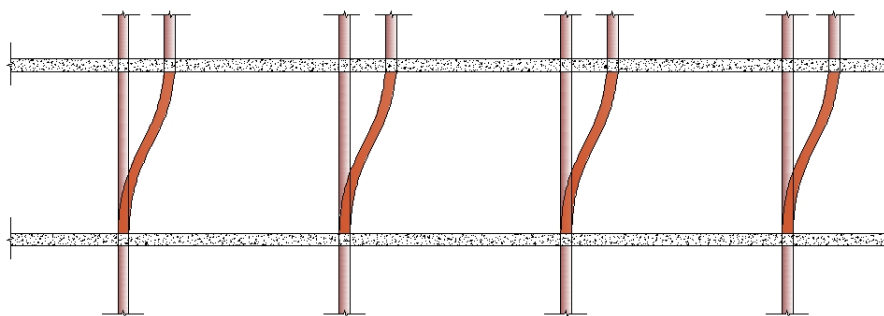


Figure 5.4-22. $P\Delta$ Effect in Sway Mode

In bridges in addition to the above two situations, one more state can happen. Consider a three-span bridge jointed at the abutments. When the bridge is under uniform thermal loads, for example contraction, the top of the columns move toward the center of the bridge (or more exactly toward the point of zero movement). The critical case takes place when the axial force of one of the columns is maximized due to presence of live load. Figure 5.4-23 shows a bridge in such a state. Under such circumstances, the moment in the loaded columns (left columns in the picture) tends to magnify. But, as the Δ and moments increase in this column, the other column tends to restore to its undeformed

shape. Therefore, the assumption in the building structures which a floor moves in a unique direction due to a loading case is not valid for bridge under the described conditions. In building structures, the terms such as $\sum P_u$ or $\sum P_{e2}$ are based on the assumptions that are valid only for that type of structure.

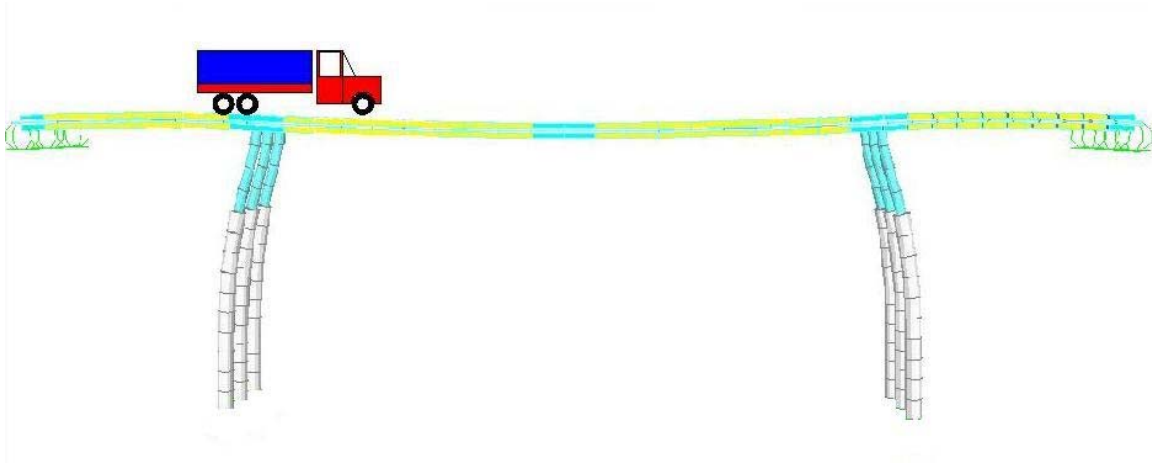


Figure 5.4-23. $P\Delta$ Effect in a Jointed Abutment Bridge with Flexible Piers

For bridge design, more critical conditions in which an axially loaded column can have a side sway while other columns do not have the same direction of side sway should be considered. In this case, the other columns, not only do not help the column that has the maximum axial load, but also they may act like springs that intensify the $P\Delta$ effect for the critical column. Therefore, the following magnification factor may be recommended for a column in such a situation.

$$B_{Jointed} = \frac{1}{1 - \frac{P_u}{P_{e,j}}} \geq 1 \quad \text{Eq. 5.13}$$

where

$$P_{e,j} = \frac{\pi^2 EI}{(K_{unbraced} L)^2} \quad \text{Eq. 5.14}$$

In integral abutment bridges, as the two ends of the bridge are connected to the abutments, for movement in any direction at least one of the abutments is a help for the intermediate columns. Figure 5.4-24 illustrates an integral abutment bridge under such a situation. As can be observed, the stiffness of the left abutment piles mitigates the moment magnification of the axially loaded columns. For this case, the following equation for the magnification factor can be recommended, in which the resisting elements are the left abutment and left pier.

$$B_{Integral} = \frac{1}{1 - \left(\frac{\sum P_{u,Resisting}}{\sum P_{e,Resisting}} \right)} \quad \text{Eq. 5.15}$$

In which

$$P_{e,Resisting} = \frac{\pi^2 EI}{(K_{unbraced} L)^2} \quad \text{Eq. 5.16}$$

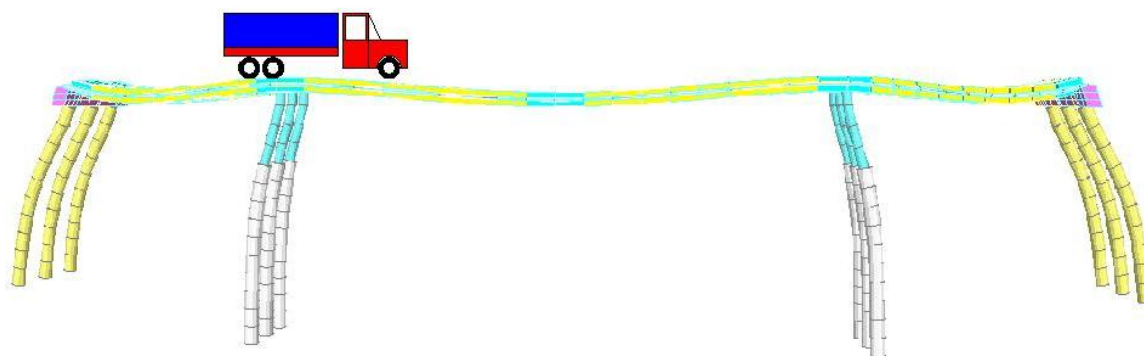


Figure 5.4-24. $P\Delta$ Effect in an Integral Abutment Bridge with Flexible Piers

Chapter 6

Concluding Remarks and Future Research

The concluding remarks of the present study are divided into three sections. First, the findings of the close-up analysis of the integral abutment connections are summarized. Then, the conclusions of the investigations on steel I-girder bridges are explained. After that, the results of the studies on concrete bridges are recapitulated. At the end, some recommendations for future research are presented.

6.1 Connections of Integral Abutments

An important part of the current study was to investigate the behavior of abutment connections in steel integral bridges. Each integral abutment has two connection zones: one is the superstructure-to-abutment wall connection and the other is the pile-to-abutment wall connection. The state of stresses in each of these two connections has been scrutinized.

For the girder-to-abutment wall connection, it was observed that the girder stresses in the vicinity of the wall face are mainly concentrated in the lower part of the girder web.

This means that the maximum stresses are not found in the bottom flange of the girder. This is attributed to the mechanism of stress transfer between the steel girder and the neighboring concrete wall. The effect of adding a stiffener to the girder web at the section of the wall face has also been studied. The results show that the stiffener is effective in spreading the stresses over the face of the concrete wall below the bottom flange. This had a minor effect on the stresses of the girder itself. Another idea that was studied was to add shear studs to the bottom flange of the girder for the length embedded in the wall. It was observed that shear studs did not change the maximum stresses of the girder, but were effective in reducing the concrete wall stresses by about 40 percent.

The second zone which has been studied is the pile-to-abutment wall connection. For this zone the significant observation is the high stresses in the steel pile, so that the pile section is almost fully plastic. The stresses in the concrete abutment wall are also high, even higher than the characteristic strength, which can be interpreted as the confinement effects. The effect of stiffener on the stresses in the pile and concrete wall was also examined. It was concluded that the pile stiffener reduces the maximum stresses on the face of the wall. This stiffener is not as effective as the stiffener for the girder-to-wall connection because of different load transfer configurations.

6.2 *Steel I-girder IA Bridges*

Several integral steel I-girder bridges were studied in this dissertation. The baseline model for the analyses was the I-480 Bridge in Omaha, NE, which is a four-span composite steel I-girder bridge with a radius of 538 feet. Several other models were generated based on this bridge for various bridge lengths and radii. The bridges were

analyzed using finite element models. Full 3D finite element analysis was conducted including the modeling of girder flanges and web plates, concrete deck slab, shear studs, cross frames, stiffener plates, different bearing connections, pier caps, non-prismatic columns, pile caps, pier H-piles, abutment walls, abutment piles and even parapets. Based on the need, different elements such as solid, shell, plate and beam elements are employed. The soil-structure interaction has been modeled as well. A wide variety of loads and load effects have been applied to the models including dead load, live load, centrifugal force, braking force, earth pressure, uniform temperature changes, temperature gradient, wind load and concrete shrinkage.

6.2.1 Effects of Bridge length and curvature on load responses

Based on the results of the analysis for different loads, a weight factor is defined for each load. The larger weight factor for a specific load means the larger internal forces due to that load. Therefore, a larger weight factor indicates the importance of the loading from a structural design point of view. The sorting of the loads based on their weight factors is as follows: contraction, expansion, live load, wind load, dead load, concrete shrinkage, horizontal earth pressure, centrifugal force, weight of wearing surface, braking force, positive temperature gradient and finally negative temperature gradient.

The results of the study show that the internal forces in the abutments of curved bridges due to contraction loading, which is the most critical loading for design purposes, are always smaller than those of straight bridges. As the radius of curvature of the bridge reduces, the internal forces reduce as well. Besides, the increase in the length of straight

or large-radius bridges increases the internal forces of the abutment piles. But for smaller radii, the abutment piles' internal forces start to decrease as the bridge is longer than a specific length.

For bridge expansion, the results show that in straight bridges the internal forces increase as the length of the bridge increases. But, in the case of curved bridges, there is an increase in the responses for shorter bridges and then the curves reach a maximum point. For longer bridges beyond the maximum point, the internal forces are decreasing. Therefore, it can be concluded that the internal forces due to expansion for bridges longer than a specific length are smaller than those of straight bridges. That specific length depends mainly on bridge curvature.

For live load effects, it is observed that the abutment pile stresses generally have the same level of intensity. The internal forces are mainly independent of radius of curvature. For short bridges, as the length increases, there is a slight increase in the internal forces due to live load. But beyond a specific length, the internal forces are constant. The increase in the shear forces and flexural moments is attributed to the loading pattern of the live load which is applicable to the multi-span bridges. The abutment pile's internal forces due to other gravity loads such as dead load of structure or weight of wearing surface are decreasing versus length of the bridge. The response curves do not have a large slope.

The results of the study for the effects of concrete shrinkage in composite steel bridges were complex and could not be interpreted easily. A general conclusion is that in straight bridges, the internal forces of the abutment piles increase as the length of the bridge increases. But in curved bridges, these forces remain constant for bridge lengths larger

than a specific value. The other important observation is that concrete shrinkage is not a secondary effect in composite integral abutment bridges. Its effects are more significant than some commonly understandable loads such as earth pressure and centrifugal force.

The abutment forces due to horizontal earth pressure are highly dependent on the radius of the curvature of the bridge. It is shown that for smaller radii, as the acting earth pressure on the abutments do not balance each other, larger lateral displacement is created in the whole structure. Therefore, the internal forces in the abutment piles that are integrally connected to the superstructure have large values.

In the studied steel bridges, the values of the shear forces and bending moments due to centrifugal force are shown to be almost independent of the radius of curvature. Even the length of the bridge has a minimal effect on the responses due to centrifugal force. The reason for this is the fact that the centrifugal force is approximately constant for different radii.

Other loads including braking force and temperature gradient show minor influence on the response of composite integral abutment bridges. The effects are so small that the obtained weight factors for both positive and negative temperature gradients are less than 0.5 (compared to 31 for contraction).

6.2.2 Bridge Movement

Since the internal forces in the abutment piles are mainly a result of the time-dependent movements of bridge abutments, a major goal in this dissertation was to study the displacements of curved integral abutment bridges. To perform such a complicated task, first the factors affecting the bridge end displacements were studied. It was

discovered that the bridge end displacement in this type of bridges is not just a function of seasonal temperature changes. Other loads like horizontal earth pressure can cause considerable movements in highly curved bridges. And even if the values of a curved bridge shortening or elongation due to some effects like temperature changes are known, the magnitude and direction of the bridge end displacements are unknown. The other fact is that the rotation of the abutments should be considered as a source of displacement at the pavement level. Knowing these facts, a comprehensive finite element study on the displacements of curved composite steel integral bridges was conducted. Using the results of the analyses, a relation was developed between the bridge end displacements and the shortening due to contraction and shrinkage. The effects of bridge end rotation and also the effects of other loads on curved bridge end displacements were incorporated into the solution by means of modification factors.

In the case of curved bridges, a major unknown in bridge movement is the direction of displacement. One of the factors that affects the direction of displacement is the bridge width. The effect of bridge width was investigated. For straight bridges, closed-form solutions were obtained for the effect of bridge width on the direction of displacement due to contraction and shrinkage. For curved bridges, the effect of bridge width was explored through several finite element analyses. It was observed that the effect of width can be extracted from the direction of displacement by means of two factors for inner and outer bridge corners. In this way, an equation was found using available curve fitting methods for the direction of end displacement of curved integral bridge.

Therefore, the magnitude and direction of bridge end displacements for composite steel I-girder integral bridges were found.

6.2.3 Pile Orientation

Orientation of the abutment piles is an important problem in design of integral bridges. In most of the references of integral abutment bridges, it is clearly stated that the piles should be oriented for weak-axis bending so that the stresses are kept low. In the present study, a closed-form solution for straight bridges was presented that showed lower levels of stress resulted from strong-axis bending of the piles. To verify the solution, the stresses were examined in several finite element models of the studied bridges. The results show that the strong-axis bending of the piles yields lower levels of stress.

In the case of curved bridges, as the direction of the movement of the abutments is not necessarily perpendicular to abutment line, the optimum orientation for the piles is not strong or weak axis. The results of the finite element models are used to find the average direction of maximum displacement of the pile heads. These directions were plotted versus L/R ratios. Based on the findings of the optimum orientation for straight bridges, it was concluded that the piles should be oriented so that the strong-axis of the piles is perpendicular to the direction of the maximum displacement. This method of optimization was verified by the finite element analysis which showed lower stresses in 30 out of 32 cases compared to strong- or weak- axis bending.

6.2.4 Effect of Bearing Type

To study the effect of bearing type on the response of curved integral abutment bridges, different bearing types were surveyed. All the existing bearings were categorized based on the provided degrees of freedom for the connecting members. The effects of plain and reinforced elastomeric bearings, fixed pot or disc bearings, guided pot or disc

bearings and sliding bearings were studied. The findings of the finite element studies show that using fixed bearings over piers reduces the abutment pile moments compared to the pile moments of bridges with sliding bearing over the piers. But, the reduction in most cases was less than 20 percent. The bridges that had elastomeric bearings had pile moments between those with sliding and fixed bearing. The maximum pile moments of bridges with guided bearings were very close to the moments of bridges with fixed bearings.

The flexural moments in the piers were studied in two perpendicular directions: longitudinal and transverse. The longitudinal moments of the piers were maximized if the bearings were fixed. If the bearings were of sliding or guided types, the longitudinal moments were very close to zero. One of the reasons for not having an exact zero moment was the applied loads to the piers themselves, such as the wind load. In the case of elastomeric bearings, the longitudinal moments of the piers were between those of the bridges with sliding bearings and fixed bearings.

The transverse moments of the piers were maximized when the bearings of the piers were fixed or guided. The values of these moments were much greater than those of bridges with sliding bearings, namely about 2.5 times. It should be noted that even with sliding bearings the transverse moments of the piers were not close to zero. That is because of the nature of the studied piers: massive columns framed by means of another gigantic element: the cap beam. In other words, if two massive hammerhead columns are framed together, large values of internal forces should be expected. The transverse moments of piers with elastomeric bearing were larger than those of piers with sliding bearings but still much smaller than those with fixed or guided bearings.

As guided bearings were proved to produce large bending moments in the piers of curved integral abutment bridges, bridge designers should not look for finding an optimum orientation for this type of bearings. It is recommended that elastomeric or sliding bearings be used in the piers of curved integral abutment bridges.

6.3 Concrete IA Bridges

A broad study has been conducted on curved integral abutment concrete bridges. The superstructure of the bridges was composed of a continuous voided slab integrally connected to the abutment walls. The abutment walls were supported on drilled shafts. The pier columns were either integral with the superstructure or isolated by means of elastomeric bearings and a cap beam. The piers were also supported on drilled shafts. Different lengths and radii were considered for analysis. The effects of different loads including dead load, live load, centrifugal and braking force, earth pressure, temperature and shrinkage loads have been investigated on the bridges.

6.3.1 Effects of Bridge Length and Curvature on Load Responses

The findings on the effects of variation in radius and length on bridge behavior showed that in straight bridges, the internal forces of the abutment piles due to contraction loading increase as the length of the bridge increases. As the radius decreases, the increases in the internal forces tend to lessen. For highly curved bridges, like those with a radius of 200 feet, the bending moments increase up to length of 300 feet and beyond that length the moments become constant.

For the pile bending moments due to expansion, it was observed that shorter curved bridges have larger bending moments in the abutment piles compared to straight ones. But, as the length gets larger, the moments start to decrease after reaching a peak. Therefore, it can be concluded that the bending moments due to expansion in very long curved bridges are smaller than that of equivalent straight bridges.

For the pile moments due to gravity loads, two different behaviors were observed. For the bending moment due to live load, there was an increase up to the length of 300 feet and beyond that length, the live load moments were almost constant for each radius of curvature. The reason for the increase in the moments from the two-span bridge with the length of 130 feet to the four-span bridge with the length of 300 feet is the number of spans and possibility of patterned loading for the four-span bridge. The other gravity loads such as dead load or weight of wearing surface showed a decreasing trend for the pile moments versus the length of the bridge. For these gravity loads, the responses of the bridge with the radius equal to 1000 feet were very close to those of straight bridges.

The shape of abutment pile bending moment curves due to shrinkage in concrete integral bridges was very similar to those due to contraction. The only difference was the magnitude of the moments. The reason for that is the fact that after completion of the construction of the bridge, all the elements continue shrinking which causes the same effects as the contraction. The only difference can be the different ages of the elements which causes different strain rates.

For the bending moments of piles due to horizontal earth pressure, there was a huge difference between the results for highly curved bridges and other bridges. In straight bridges and the bridges with large radius of curvature, the earth pressures applied to the

two abutments either balance each other or their major components are balanced. But in highly curved bridges, these forces do not counteract and consequently cause horizontal displacement of the whole bridge. Therefore, the resulted bending moments in the abutment piles are noticeably larger compared to other bridges.

The bending moments due to positive and negative temperature gradient are approximately equal for different bridge length or bridge radius. The moments in bridges with the radius of 1000 feet are almost the same as those of straight bridges. The other important observation is the relatively large magnitude of these moments in the piles of concrete bridge. That is because of larger size and stiffness of the concrete piles of these bridges compared to those of steel bridges.

The final conclusion for the effects of loads on the studied concrete bridges can be made by looking at the envelope of load combinations. It is observed that in straight bridges the combination of bending moments increase strictly as the length of the bridge increases. In the case of curved bridges, the increase in the combination of bending moments is not as strict as that of straight bridges. For small radii of curvature, they have an increase up to the length of 300 feet and beyond that length a plateau is observed. The fact that the envelope of piles bending moments is almost constant in highly curved bridges is probably the most significant conclusion of this part of the study.

6.3.2 Pile Orientation

In the studied concrete integral bridges, the abutments are supported on circular drilled shaft. Therefore, if the rebars are symmetric in the shafts, all horizontal directions would be the same for pile movement. But since the drilled shafts can be noncircular or the

rebars in circular shafts can be asymmetric, the shafts of the abutments have been changed to rectangular ones to study the effect of the shafts orientation. It was discovered that even for rectangular concrete shafts, the strong-axis bending would result in more economic designs. Therefore, the result of pile orientation study is the same for the studied steel and concrete bridges.

6.3.3 Bearing-Isolated Piers versus Integral Piers

Two different types of pier-to-superstructure connections were studied for the integral concrete bridges: integral and bearing-isolated. In the integral one, the pier columns are integrally connected to the superstructure, while in the other type of bridges, the columns are framed into a cap beam and the superstructure seats on the cap beam by means of elastomeric bearings. The results of the finite element study reveals that the bridges with integral piers have larger moments in the abutment piles compared to those with bearing-isolated piers. But the increase in the moments in all cases is less than 15 percent (in most of them about 5 percent). Therefore, there should not be a major concern about designing integral piers in this type of bridges.

6.3.4 Mitigation of Moment Magnification Factor

In the current design codes, two modes of buckling are assumed for the columns of a multi-bay structure. One is buckling of a single column without any lateral sway. The other is buckling of a column in a story that all the columns sway laterally at the same time. Based on these two modes of buckling, two different moment magnification factors are defined. In the present study, it is shown that these two modes are not the only modes of buckling for columns of bridges. Due to bridge expansion and contraction, another

mode of buckling can happen that is much more critical than the other two. In this mode, the relative lateral translation of the column ends happens due to changes of the bridge length while the moments are magnified by vertical loads, such as live load. It is shown that this phenomenon is more critical in the case of jointed bridges. In integral abutment bridges, at least one of the abutments is helping the loaded column to mitigate its moment magnification. The moment magnification factor for the new mode of buckling is also recommended.

6.4 Recommendations for Future Research

In this dissertation, the behavior and responses of curved integral abutment bridges were studied. The effects of several parameters were considered. But, there is still a need to continue the research on this topic and develop a comprehensive design guide for this type of bridges. One of the main problems that should be continued is to study the bridge movement in other types of integral bridges. In this dissertation, a method for finding the displacements of curved steel bridges was proposed. The displacements of other types of bridges such as prestressed concrete girder bridges should also be studied. The effect of different span length and number of spans should be investigated as well. The other problem is to continue the study on pile orientation for other types of bridges and other span lengths or ratios.

As some curved bridges are skewed at the ends, skewness is another topic that should be incorporated into the effects of curvature. In the case of skew bridges, in several previous reports, the only limitation that is set on the bridge geometry is a skew angle less than 20 degrees. But, what is forgotten is that the skew angle is not the only factor

causing the rotation of the bridge. The other factor is the length-to-width ratio. When a bridge has large length-to-width ratios, a small skew angle can cause a huge rotation in the bridge structure. While for small ratios, the bridge may be able to tolerate larger skew angles.

References

Al-Omaishi, N., Tadros, M. K., & Seguirant, S. J. (2009). Elasticity modulus, shrinkage, and creep of high-strength concrete as adopted by AASHTO. *PCI Journal*, 54(3), 44-63.

American Association of State Highway and Transportation Officials. (1980). *Guide specifications for horizontally curved highway bridges - 1980*. Washington, D.C: A.A.S.H.T.O.

American Association of State Highway and Transportation Officials. (1993). *Guide specifications for horizontally curved highway bridges*. Washington, D.C: American Association of State Highway and Transportation Officials.

American Association of State Highway and Transportation Officials. (2007). *AASHTO LRFD bridge design specifications, customary U.S. units* (4th ed.). Washington, DC: American Association of State Highway and Transportation Officials.

American Association of State Highway and Transportation Officials. (2010). *AASHTO LRFD bridge design specifications* (5th ed.). Washington, D.C: American Association of State Highway and Transportation Officials.

American Association of State Highway and Transportation Officials. Subcommittee on Bridges and Structures. (2003). *AASHTO guide specifications for horizontally curved steel girder highway bridges, 2003 : With design examples for I-girder and box-girder bridges*. Washington, DC: American Association of State Highway and Transportation Officials.

American Institute of Steel Construction, American Institute of Steel Construction, & Manual of steel construction. (2005). *Steel construction manual. uniform title: Steel construction* (13th ed.). Chicago, Ill.: American Institute of Steel Construction.

American Iron and Steel Institute, Tennessee, Dept. of Transportation, Structures Division, & National Steel Bridge Alliance. (1996). *Integral abutments for steel bridges. vol. 2, chapter 5, highway structures design handbook* Printed by National Steel Bridge Alliance.

American Petroleum Institute. (2005). *Recommended practice for planning, designing, and constructing fixed offshore platforms : Working stress design* (21st ed.). Washington, D.C: American Petroleum Institute.

Arockiasamy, M., & Sivakumar, M. (2005). Time-dependent behavior of continuous composite integral abutment bridges. *Practice Periodical on Structural Design and Construction*, 10(3), 161-170.

Arsoy, S., Barker, R. M., Duncan, J. M., Virginia Polytechnic and State University, Charles E. Via Dept. of Civil and Environmental Engineering, Virginia Transportation Research Council, et al. (1999). *The behavior of integral abutment*

bridges : Final contract report (FHWA/VTRC 00-CR3 ed.). Richmond, Va.:

Virginia Dept. of Transportation.

- Barros, M. H. F. M., Martins, R. A. F., & Ferreira, C. C. (2001). Tension stiffening model with increasing damage for reinforced concrete. *Engineering Computations* (Swansea, Wales), 18(5-6), 759-785.
- Bell, B. J., & Linzell, D. G. (2007). Erection procedure effects on deformations and stresses in a large-radius, horizontally curved, I-girder bridge. *Journal of Bridge Engineering*, 12(4), 467-476.
- Boresi, A. P., & Schmidt, R. J. (2003). *Advanced mechanics of materials* (6th ed.). New York: John Wiley & Sons.
- Burke, M. P. (2009). *Integral and semi-integral bridges*. Chichester, U.K. ; Ames, Iowa: Wiley-Blackwell.
- Clough, G. W., Duncan, J. M., University of California, B., & Dept. of Civil Engineering. (1971). *Finite element analyses of retaining wall behavior*. Berkeley, Calif: Dept. of Civil Engineering, University of California.
- Davidson, J. S., Keller, M. A., & Yoo, C. H. (1996). Cross-frame spacing and parametric effects in horizontally curved I-girder bridges. *Journal of Structural Engineering* New York, N.Y., 122(9), 1089-1096.
- Davidson, J. S., & Yoo, C. H. (1996). Local buckling of curved I-girder flanges. *Journal of Structural Engineering* New York, N.Y., 122(8), 936-947.

- Davidson, J. S. (1996). *Nominal bending and shear strength of horizontally curved steel I-girder bridges*
- DeSantiago, E., Mohammadi, J., & Albaijat, H. M. O. (2005). Analysis of horizontally curved bridges using simple finite-element models. *Practice Periodical on Structural Design and Construction*, 10(1), 18-21.
- Fennema, J. L., Laman, J. A., & Linzell, D. G. (2005). Predicted and measured response of an integral abutment bridge. *Journal of Bridge Engineering*, (6)
- Fiechtl, A. L. (1987). *Approximate analysis of horizontally curved girder bridges*. Austin, TX: Center for Transportation Research , University of Texas at Austin.
- Hall, D. H., Grubb, M. A., Yoo, C. H., United States, Federal Highway Administration, National Cooperative Highway Research Program, et al. (1999). *Improved design specifications for horizontally curved steel girder highway bridges*. Washington, D.C: National Academy Press.
- Hall, D. H., National Research Council (U.S.), Transportation Research Board, National Cooperative Highway Research Program, & Bridge Software Development International, Ltd. (1998). *Recommended specifications for steel curved-girder bridges*. Coopersburg, PA: Bridge Software Development International.
- Huo, X. S., Al-Omaishi, N., & Tadros, M. K. (2001). Creep, shrinkage, and modulus of elasticity of high-performance concrete. *ACI Materials Journal*, 98(6), 440-449.

- Kalayci, E. (2010). *Analysis of curved integral abutment bridges*, Master of Science Thesis, University of Massachusetts Amherst,
<http://scholarworks.umass.edu/theses/389/>
- Kulicki, J. M., National Cooperative Highway Research Program., American Association of State Highway and Transportation Officials., & United States. Federal Highway Administration. (2006). *Development of LRFD specifications for horizontally curved steel girder bridges*. Washington, D.C.: Transportation Research Board.
- Kulicki, J. M., National Cooperative Highway Research Program, & Modjeski and Masters. (2005a). *AASHTO-LRFD design example : Horizontally curved steel box girder bridge*. Harrisburg, Pa: Modjeski and Masters, Inc.
- Kulicki, J. M., National Cooperative Highway Research Program, & Modjeski and Masters. (2005b). *AASHTO-LRFD design example: Horizontally curved steel I-girder bridge*. Harrisburg, Pa: Modjeski and Masters, Inc.
- Linzell, D., Hall, D., & White, D. (2004). Historical perspective on horizontally curved I girder bridge design in the united states. *Journal of Bridge Engineering*, 9(3), 218-229.
- Linzell, D., Leon, R. T., & Zureick, A. H. (2004). Experimental and analytical studies of a horizontally curved steel I-girder bridge during erection. *Journal of Bridge Engineering*, 9(6), 521-530.

- Nevling, D., Linzell, D., & Laman, J. (2006). Examination of level of analysis accuracy for curved I-girder bridges through comparisons to field data. *Journal of Bridge Engineering*, 11(2), 160-168.
- Ozbolt, J., & Bazant, Z. (1996). Numerical smeared fracture analysis: Nonlocal microcrack interaction approach. *International Journal for Numerical Methods in Engineering*, 39(4), [d]635-661.
- Pugasap, K., Kim, W., & Laman, J. A. (2009). Long-term response prediction of integral abutment bridges. *Journal of Bridge Engineering*, 14(2), 129-139.
- Tadros, M. K., National Research Council (É.-U.), Transportation Research Board, National Cooperative Highway Research Program, États-Unis, & Federal Highway Administration. (2003). *Prestress losses in pretensioned high-strength concrete bridge girders*. Washington, D.C: Transportation Research Board.
- Tamboli, A. R. (2010). *Handbook of structural steel connection design and details* (2nd ed.). New York: McGraw-Hill.
- Thanasattayawibul, N. (2006). Curved Integral Abutment Bridges. Doctor of Philosophy Dissertation, University of Maryland, College Park.
- United States, Environmental Data Service, & National Climatic Center. (1900s). Climatography of the united states. [Climatography of the United States Preceding Title: Climatography of the United States]

- Visser, S. S. (1954). *Climatic atlas of the united states* Cambridge, Harvard University Press.
- Wang, C., Salmon, C. G., & Pincheira, J. A. (2007). *Reinforced concrete design* (7th ed.). Hoboken, NJ: John Wiley & Sons.
- White, D. *Development of design equation for curved steel I girder. (2001)*
<http://hdl.handle.net/1853/19352>; Materials specified: Item Resolution URL
 Instruction: Put this Resolution URL in a web browser to view this item.
- Yakel, A. J. (2009). *Flexural strength and ductility of high performance steel girders*. PhD Dissertation, University of Nebraska-Lincoln
- Zureick, A., & Naqib, R. (1999). Horizontally curved steel I-girders state-of-the-art analysis methods. *Journal of Bridge Engineering*, 4(1), 38-47.
- Zureick, A., Naquib, R., Yadlosky, J. M., United States, Federal Highway Administration, & HDR Engineering. (1994). *Curved steel bridge research project. interim report I, synthesis* (FHWA-RD-93-129 ed.). McLean, Va; Springfield, Va: Federal Highway Administration; Available through the National Technical Information Service.
- Maruri, R., & Petro, S. (2005). Integral Abutments and Jointless Bridges (IAJB) 2004 Survey Summary. The 2005 FHWA Conference (Integral Abutments and Jointless Bridges). Baltimore, Maryland.
- Akiyama, H. (2008). Fundamentally Structural Characteristics of Integral Bridges.

Kanazawa University, Graduate School of Natural Science & Technology.

American Association of State Highway and Transportation Officials. (2004). A Policy on Geometric Design of Highways and Streets, 5th Edition. American Association of State Highway and Transportation Officials, 2004.

Barker, R. M., Duncan, J. M., Rojiani, K. B., Ooi, P. S., Tan, C. K., & Kim, S. G. (1991). National Cooperative Highway Research Program (NCHRP) Manuals for the Design of Bridge Foundations. Washington: Transportation Research Board.

Bogard, D., & Matlock, H. (1980). Simplified Calculation of p-y Curves for Laterally Loaded Piles. Unpublished Report, Ertec Inc.

Bonczar, C., Civjan, S., Brena, S., & DeJong, J. (2005). Behavior of Integral Abutment Bridges: Field Data and Computer Modeling. Boston: EOT Office of Transportation Planning.

Brena, S. F., Bonczar, C. H., Civjan, S. A., DeJong, J. T., & Crovo, D. S. (2007). Evaluation of seasonal and Yearly Behavior of an Integral Abutment Bridge. *Journal of Bridge Engineering*, 12 (3), 296-305.

Chavel, B. W., & Earls, C. J. (2006). Construction of a Horizontally Curved Steel I-Girder Bridges. Part I: Erection Sequence. *Journal of Bridge Engineering*, 11 (1), 81-90.

Collin, P., Veljkovic, M., & Petursson, H. (2006). International Workshop on the Bridges with Integral Abutments. Lulea University of Technology.

Galambos, T. V., Hajjar, J. F., Huang, W.-H., Pulver, B. E., Leon, R. T., & Rudie, B. J. (2000). Comparison of measured and computed stresses in a steel curved girder bridge. *Journal of Bridge Engineering*, 5 (3), 191-199.

Greimann, L. F., Wolde-Tinsae, Amde, A. M., & Yang, P. S. (1985). Effects of Predrilling and Layered Soils on Piles. *Journal of Geotechnical Engineering*, 111(1), 18-31

Greimann, L. F., Wolde-Tinsae, Amde, A. M., & Yang, P. S. (1986). Nonlinear Analysis of Integral Abutment Bridges. *Journal of Structural Engineering*, 112 (10), 2263-2280.

Howell, T. D., & Earls, C. J. (2007). Curved Steel I-Girder Bridge Response during Construction Loading: Effects of Web Plumbness. *Journal of Bridge Engineering*, 12 (4), 485-493.

Iles, D. (2006). Integral Bridges in UK. International Workshop on IAB's – Lulea University of Technology.

Jayakumaran, S., Bergmann, M., Ashraf, S., & Norrish, C. (2005). Case Study: A Jointless Structure to Replace the Belt Parkway Bridge Over Ocean Parkway”,. FHWA Conference.

Kim, W. S., Laman, J. L., & Linzell, D. G. (2007). Live Load Radial Moment Distribution for Horizontally Curved Bridges. *Journal of Bridge Engineering*, 12 (6), 727-736.

Linzell, D. G. (1999). Studies of a full-scale horizontally curved steel I-girder bridge system under self-weight. PhD Dissertation, Georgia Institute of Technology, School of Civil and Environmental Engineering.

McElwain, B. A., & Laman, J. A. (2000). Experimental Verification of Horizontally Curved I-Girder Bridge Behavior. *Journal of Bridge Engineering*, 5 (4), 284-292.

Ministry of Transportation - Province of Ontario. (1999). Performance of Integral Abutment Bridges.

Moorthy, S., & Roeder, C. W. (1992). Temperature-Dependent Bridge Movements. *Journal of Structural Engineering* , 118 (4), 1090-1105.

Roeder, C. W., & Moorthy, S. (1990). Thermal Movements in Bridges. *Transportation Research Record* , 1290 , 135-143. Washington, D.C.: Transportation Research Board, National research Council.

Samaan, M., Sennah, K., & Kennedy, J. B. (2002). Positioning of bearings for curved continuous spread-box girder bridges. *Canadian Journal of Civil Engineering* , 29 (5), 641-652. 179

Ting, J. M., & Faraji, S. (1998). Streamlined Analysis and Design of Integral Abutment Bridges. University of Massachusetts Lowell, Department of Civil and Environmental Engineering. Amherst: University of Massachusetts Transportation Center.

Womack, K., Halling, M., & Bott, S. (2001). Static and dynamic testing of a curved steel girder bridge in Salt Lake City, Utah. Utah Department of Transportation.

Zhang, H., Huang, D., & Wang, T.-L. (2005). Lateral load distribution in curved steel I-girder bridges. *Journal of Bridge Engineering*, 10 (3), 281-290.

VTrans. 2009. Integral Abutment Bridge Design Guidelines. Montpelier, Vermont : VTrans, 2009.

ABAQUS Analysis User's Manual, version 6.9-1 (2006), Hibbit, Karlsson & Sorenson, Inc., Pawtucket, Rhode Island. ABAQUS Theory Manual, version 6.6-1 (2006), Hibbit, Karlsson & Sorenson, Inc., Pawtucket, Rhode Island.

Carreira D. J., & Chu K. (1985). Stress-Strain Relationship for Plain Concrete in Compression. *ACI Journal*, November-December 1985, 797-804.

National Steel Bridge Alliance, American Iron and Steel Institute. 1996. Integral Abutments for Steel Bridges. s.l.: Tennessee Department of Transportation, 1996.

White, D. W., Zureick, A. H., Phoawanich, N., and Jung, S. (2001). "Development of Unified Equations for Design of Curved and Straight Steel Bridge I Girders," *Final Report, Prepared for American Iron and Steel Institute Transportation and Infrastructure Committee, Professional Service Industries, Inc., and Federal Highway Administration*, School of Civil and Environmental Engineering, Georgia Institute of Technology, Atlanta, GA.

White, D. W. (2008). "Unified Flexural Resistance Equations for Stability Design of Steel I-Section Members: Overview." *Journal of Structural Engineering*, 134(9), ASCE, 1405-1424.

White, D. W., and Barker, M. G. (2008). "Shear Resistance of Transversely Stiffened Steel I-Girders." *Journal of Structural Engineering*, 134(9), ASCE, 1425-1436.

White, D. W., Barker, M. G., and Azizinamini, A. (2008). "Shear Strength and Moment-Shear Interaction in Transversely Stiffened Steel I-Girders." *Journal of Structural Engineering*, 134(9), ASCE, 1437-1449.

White, D. W., and Duk Kim, Y. (2008). "Unified Flexural Resistance Equations for Stability Design of Steel I-Section Members: Moment Gradient Tests." *Journal of Structural Engineering*, 134(9), ASCE, 1471-1486. 226

White, D. W., and Jung, S. (2008). "Unified Flexural Resistance Equations for Stability Design of Steel I-Section Members: Uniform Bending Tests." *Journal of Structural Engineering*, 134(9), ASCE, 1450-1470.

Marchon, P. H. A. (2007). *Nonlinear Finite Element Analysis of Composite Bridges At Ultimate Load*, Master of Science Thesis, University of Nebraska-Lincoln

Appendix A

Effect of Bridge Length and Curvature on Shear Force of Abutment Piles

In Appendix 1, the developed shear force in the abutment piles of the studied steel integral bridges is investigated in more details. First, the shear force of piles due to each load or load effect is plotted and discussed. Then, the envelope of the shear forces in different load combinations which is a design parameter is studied. Similar to the section 4.4.1A), the loads are presented based on their normalized weight factor.

A1 Contraction

Figure A-1. shows the abutment piles shear forces under contraction loading for different bridge length and radii of curvature. One can see that the shear forces decrease as the radius of curvature decreases. The other observation is that in a straight bridge the shear force increases as the bridge gets longer. But in a curved bridge when the length increases the shear forces increases up to a certain length and after that it starts to reduce.

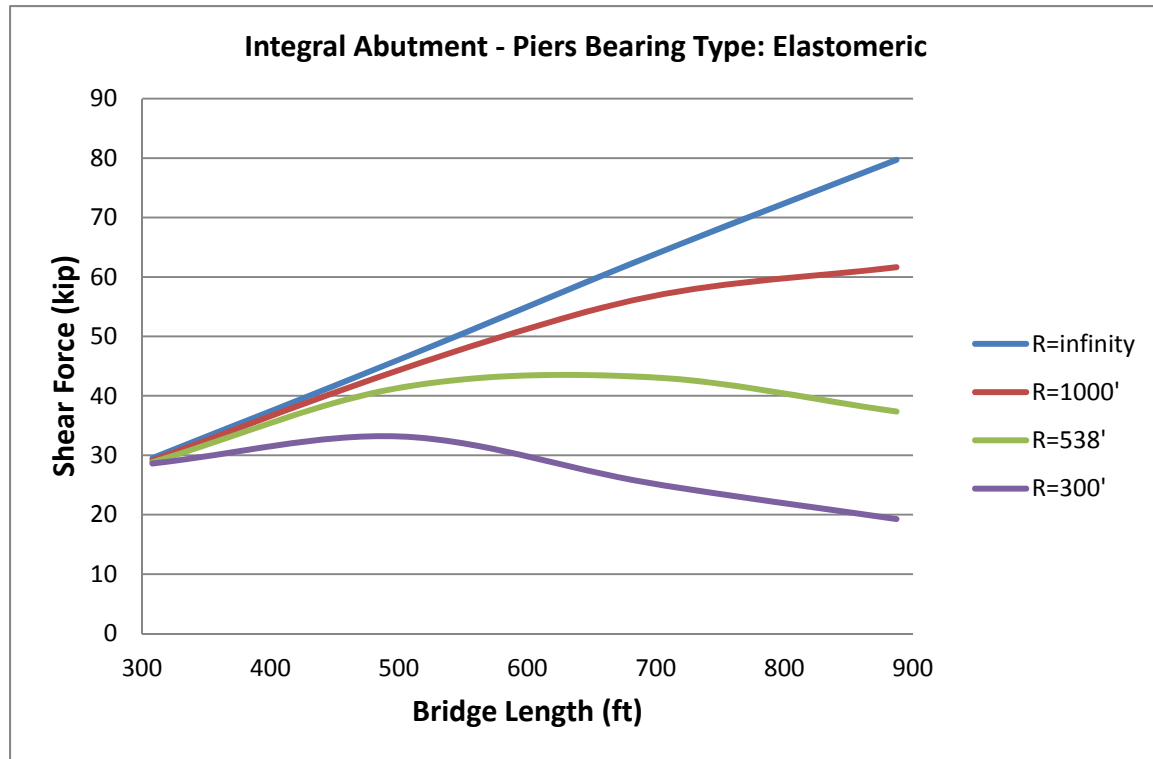


Figure A-1. Maximum Shear Force in Abutment Piles Due to Contraction

The piles shear forces are normalized in Figure A-2. by dividing the shear force of the curved bridges by that of the straight bridge of the same length. It can be seen that the shear forces of curved bridges can reduce about 75 percent when the bridge has a small radius of curvature.

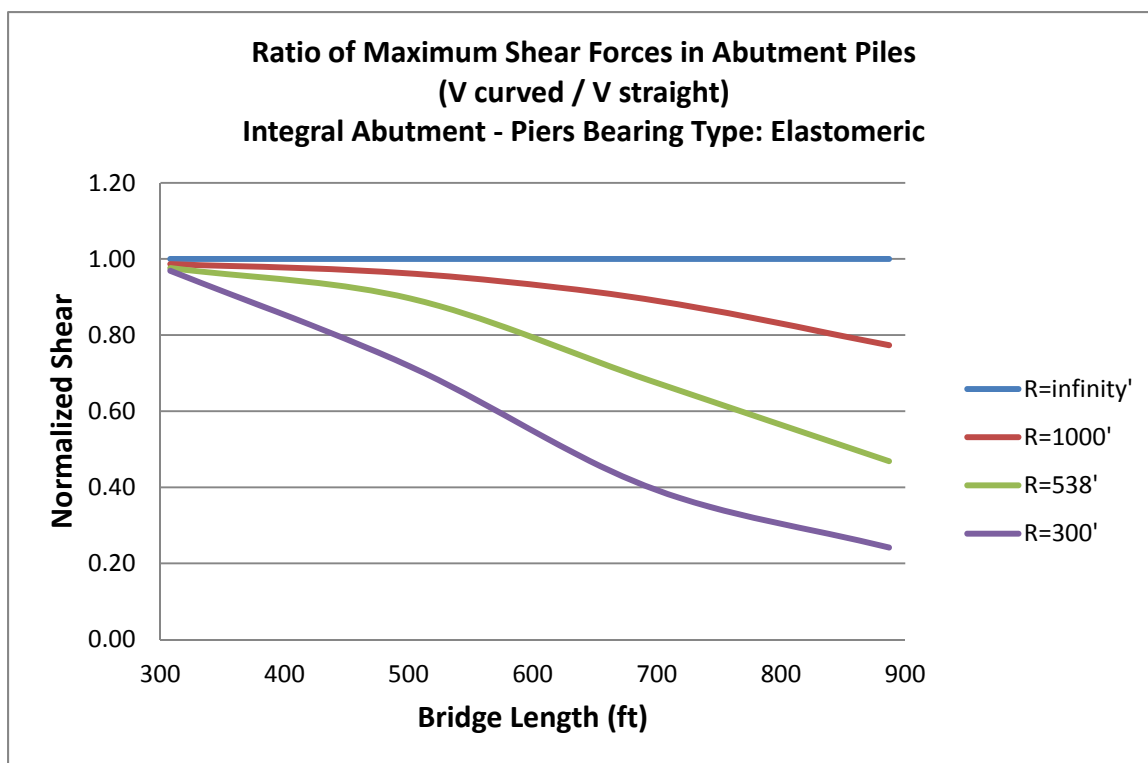


Figure A-2. Normalized Shear Force in Abutment Piles Due to Contraction

A2 Expansion

In the list of normalized weight factors, expansion has the second rank. This shows that expansion can create large internal forces in the abutment piles. The values of shear forces in the piles of studied steel bridges are plotted in Figure A-3. It is shown that for shorter bridges, curvature causes creation of larger shear forces in the piles. But, the shear force for all curved bridges has a concave shape. This means it starts reducing after a specific length.

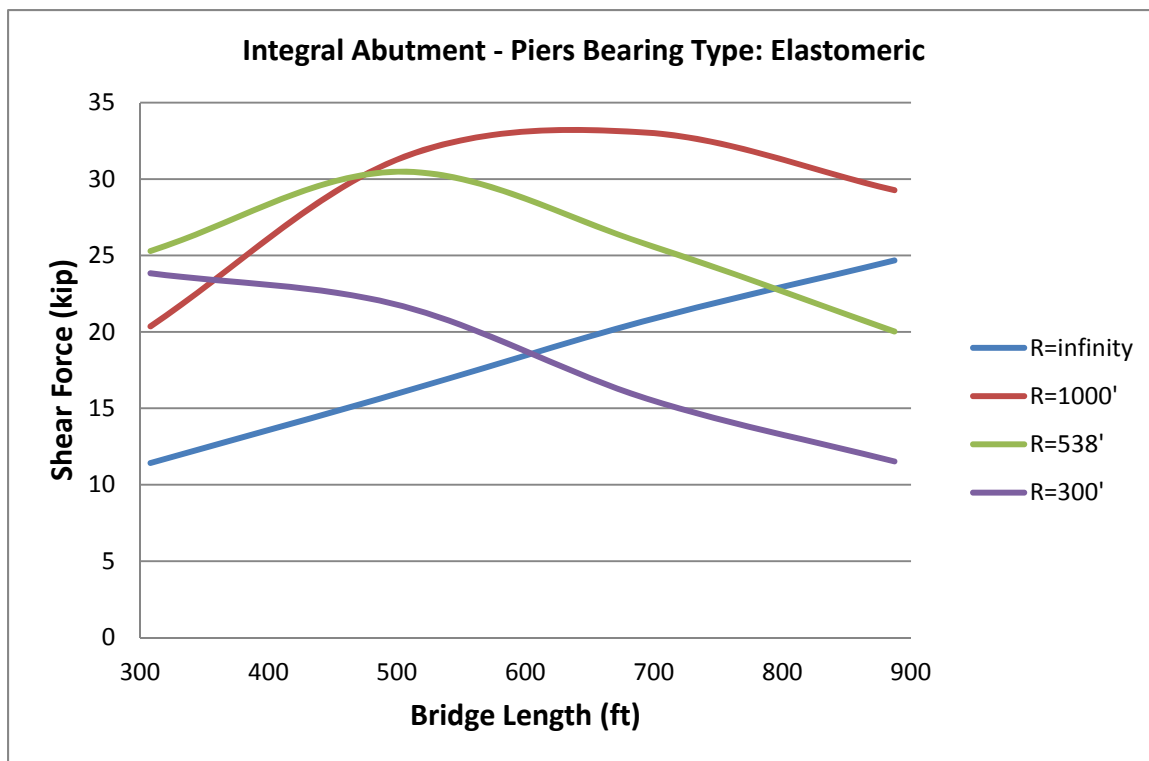


Figure A-3. Maximum Shear Force in Abutment Piles Due to Expansion

The shear forces are Normalized in Figure A-4. This picture shows that the shear force of piles of curved bridges are about two times of that of equivalent straight bridges. But for highly curved bridges it can be half of the shear force of straight bridge for long bridges of length about 900 feet.

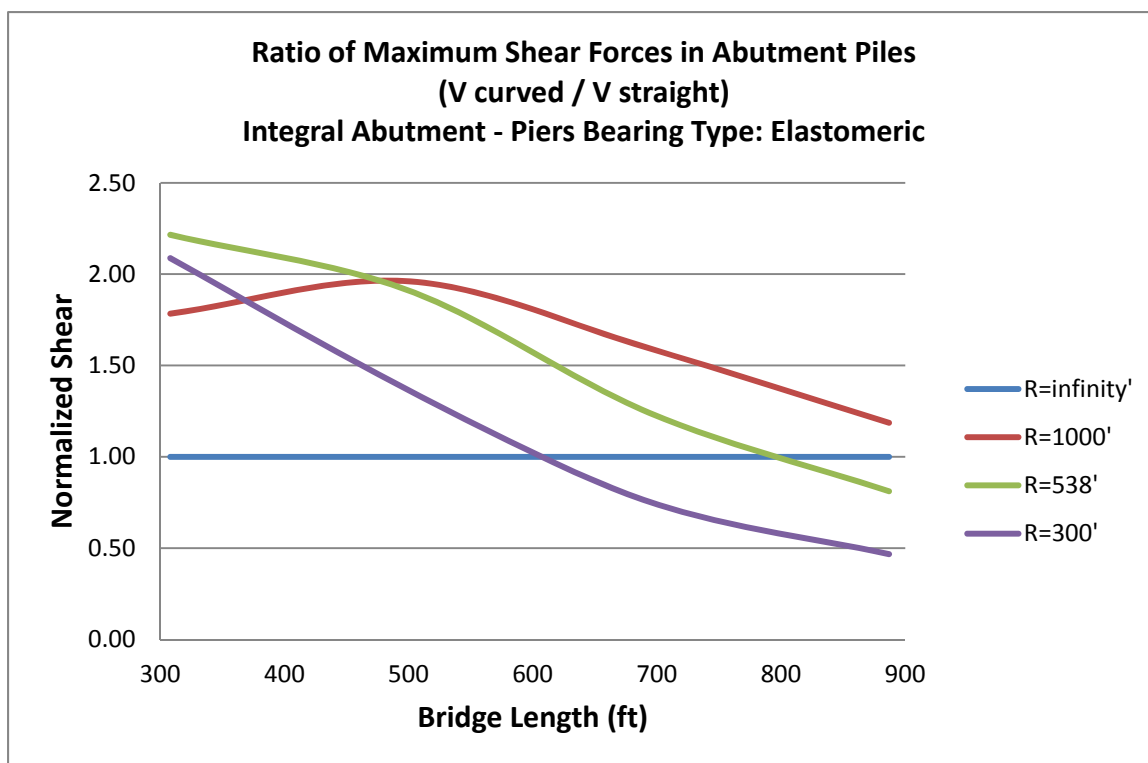


Figure A-4. Normalized Shear Force in Abutment Piles Due to Expansion

A3 Live Load

Among gravity loads, live load has the biggest weight factor which is because of its larger load factor. Figure A-5. shows the shear force in abutment piles as a result of application of live load to the models. This graph demonstrates that the shear forces do not change drastically as the length of the bridge increases.

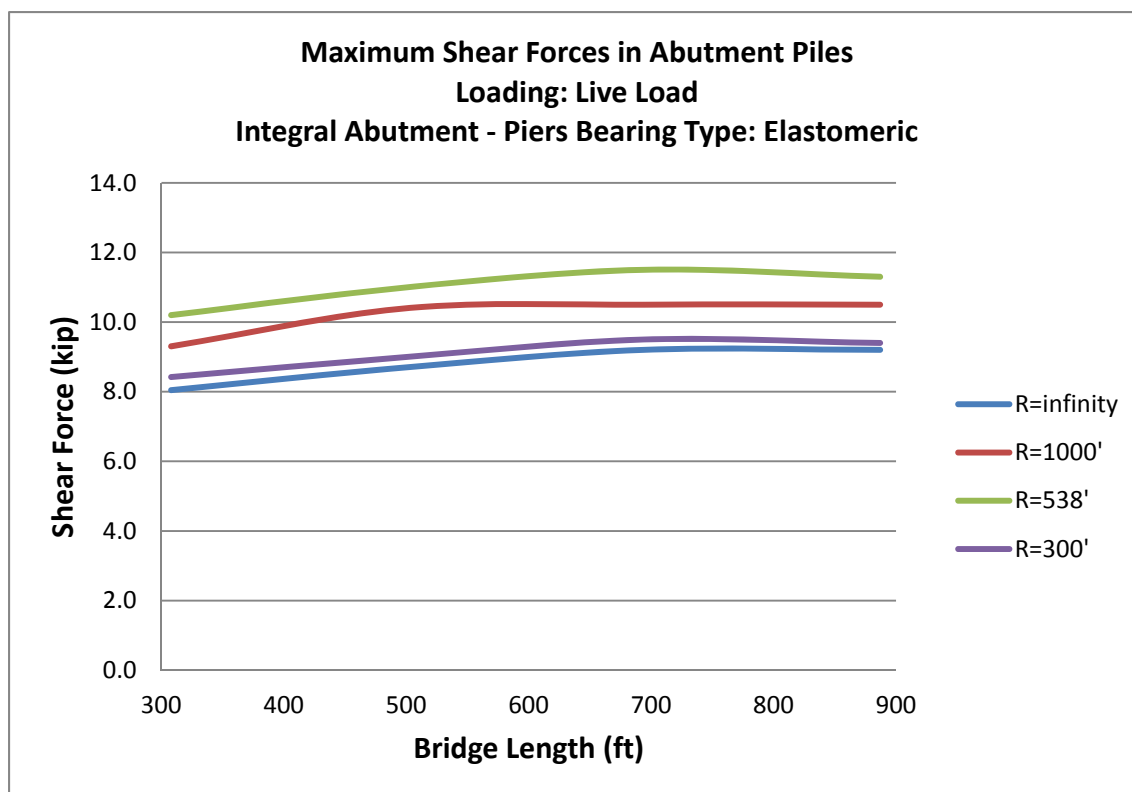


Figure A-5. Maximum Shear Force in Abutment Piles Due to Live Load

The ratios of variation of shear forces are shown in Figure A-6. From this graph, it can be observed that the shear force does not change drastically when the length or the curvature of the bridge changes. All the variations are within plus/minus 26 percent even if the length or radius changes three times.

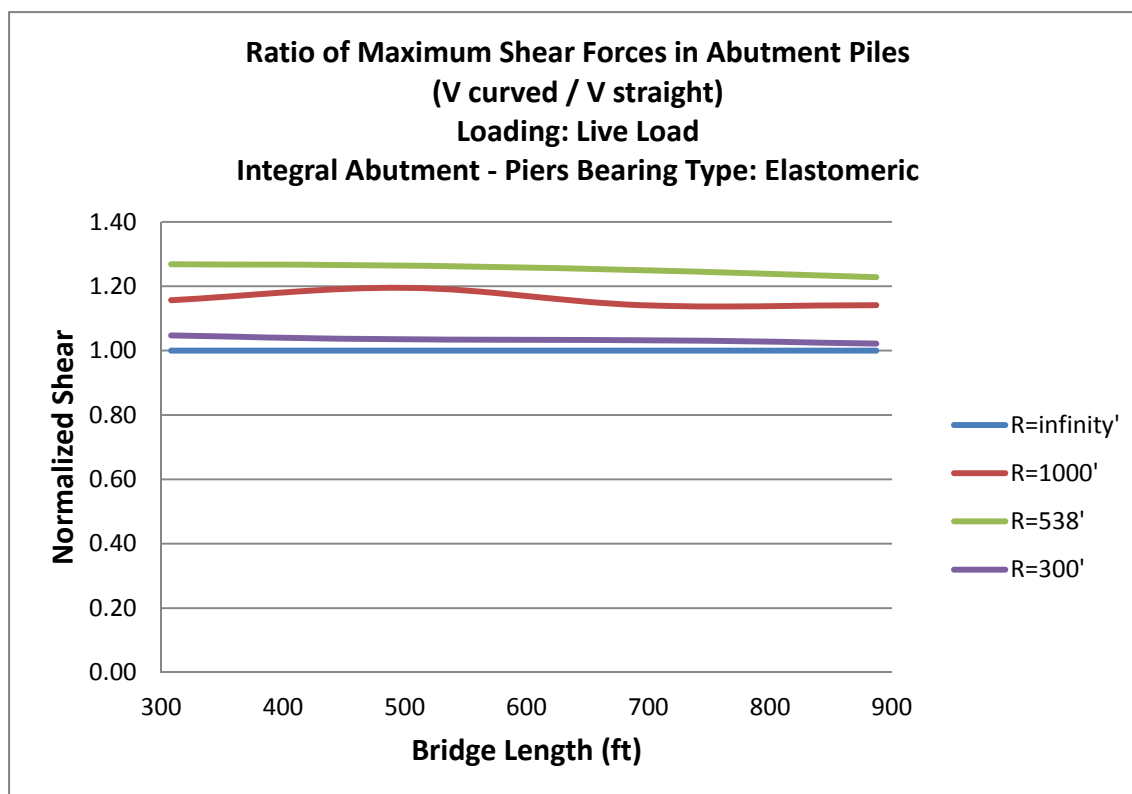


Figure A-6. Normalized Shear Force in Abutment Piles Due to Live Load

A4 Wind Load

The shear forces of the abutment piles are given in Figure A-7. This plot shows that up to a length of about 600 feet, the shear forces in bridges with different radius of curvature are almost the same as that of the straight bridge of equal length. However, as the length of the bridge goes beyond 600 feet, the effect of bridge curvature is more profound and larger differences are observed.

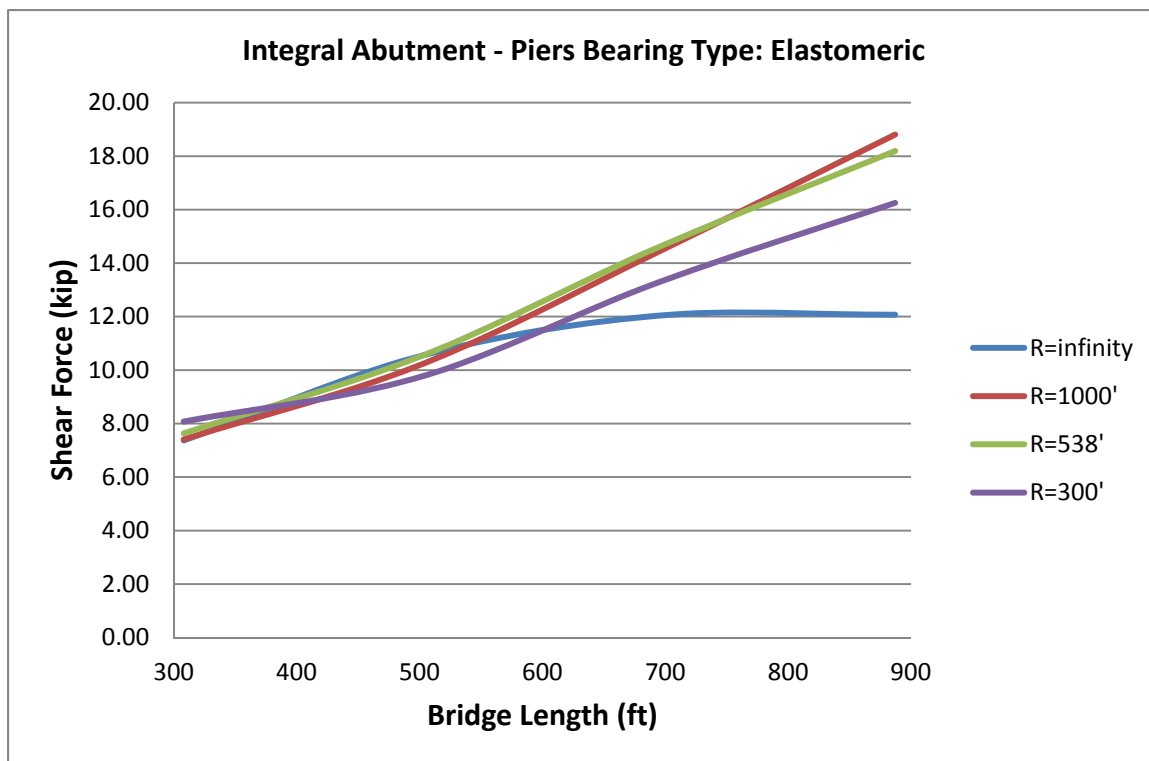


Figure A-7. Maximum Shear Force in Abutment Piles Due to Wind Load

Figure A-8. discusses the ratios of the shear forces due to wind load. It is seen that for a bridge of about 900 feet length, the shear force in a curved bridge can be about 50 percent larger than that of a straight bridge.

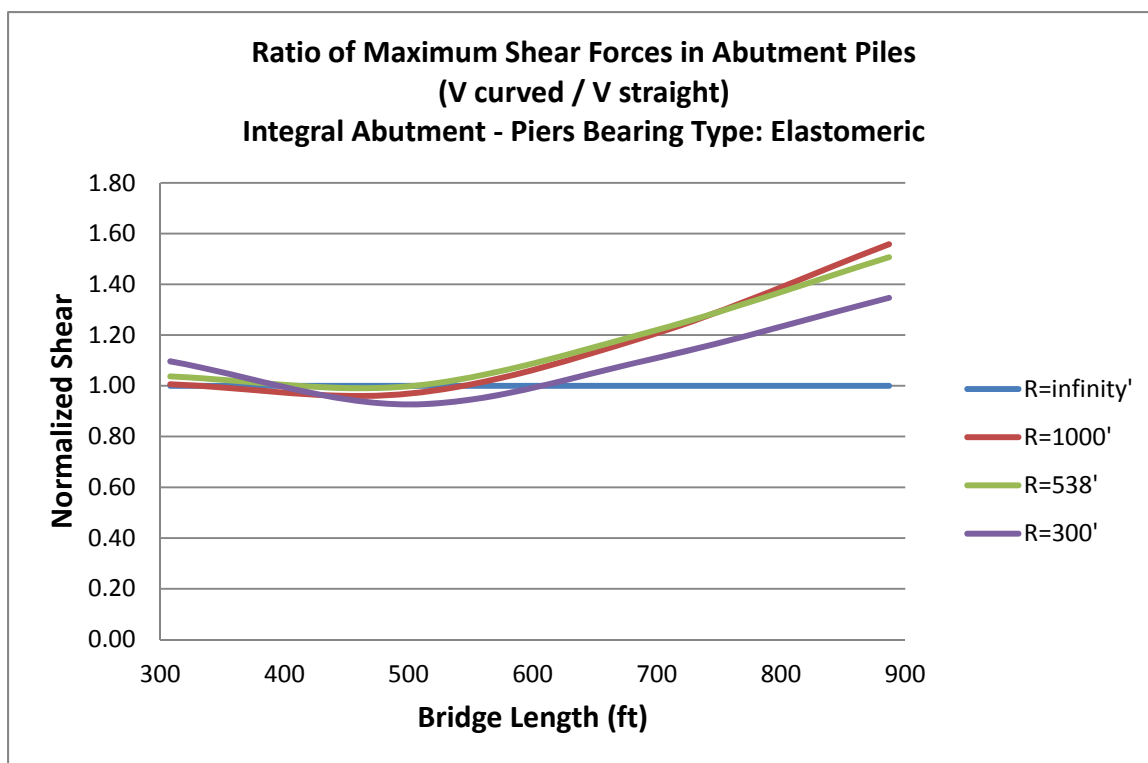


Figure A-8. Normalized Shear Force in Abutment Piles Due to Wind Load

A5 Dead Load

The shear response of the piles of integral steel bridges subjected to dead load is depicted in Figure A-9. Like live load, dead load has a decreasing trend as the length of the bridge increases. The other remark is that, although the straight bridge shows lower shear force for shorter bridges, as the length increases the curves of non-straight bridges fall below that of straight ones.

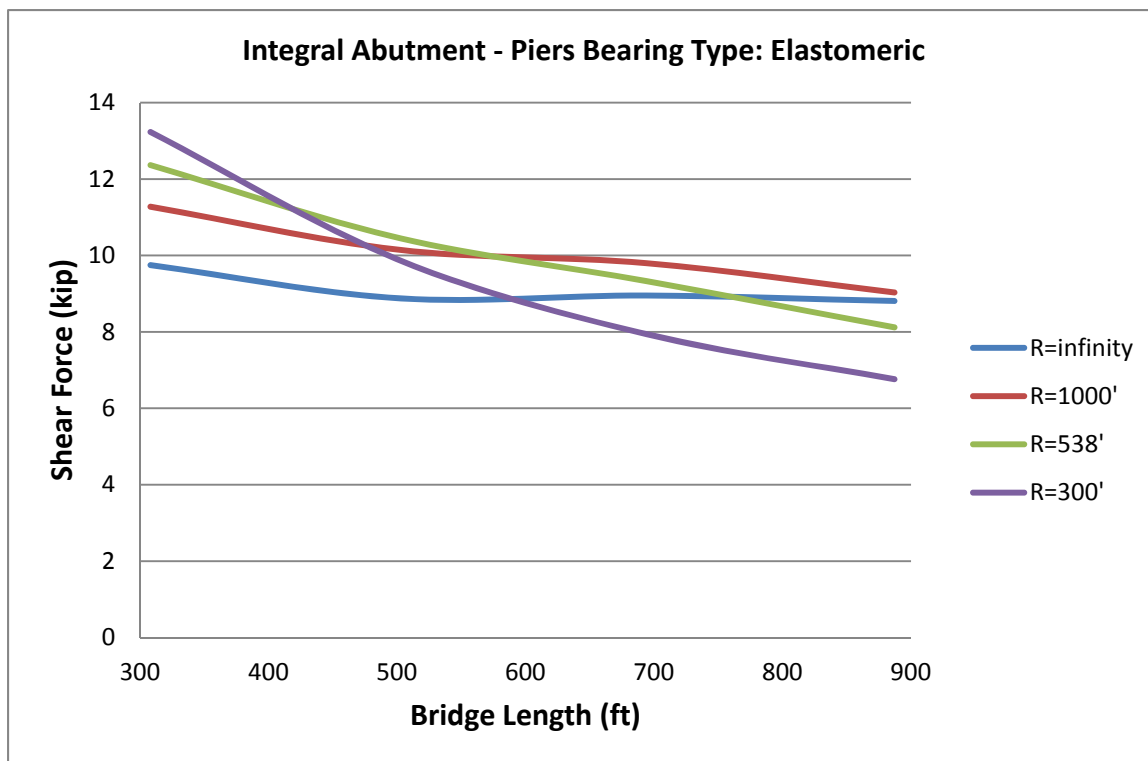


Figure A-9. Maximum Shear Force in Abutment Piles Due to Dead Load

Figure A-10. illustrates the normalized shear force of the abutment piles. It shows that the greatest drop in shear force per length increment is for the highest curvature, i.e. $R=300$ feet. When the bridge has lower curvature, the response is closer to that of straight bridge, which seems reasonable.

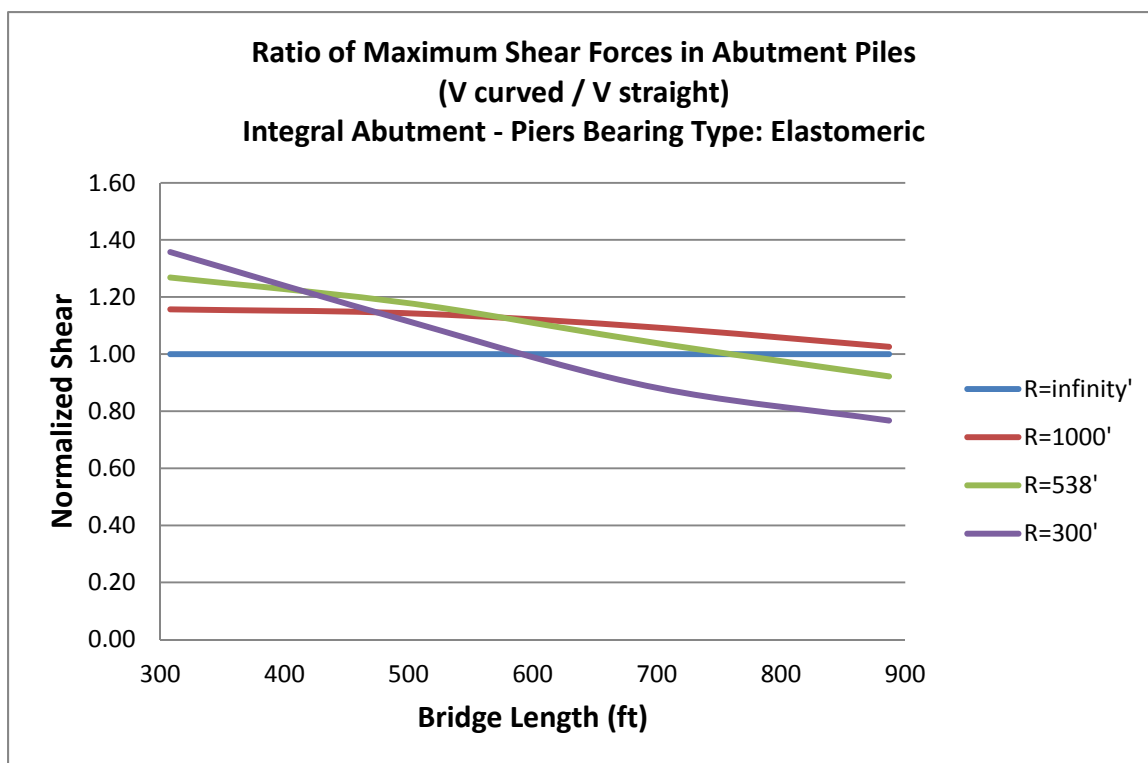


Figure A-10. Normalized Shear Force in Abutment Piles Due to Dead Load

A6 Concrete Shrinkage

Figure A-11. shows the shear force of piles when the bridge is subject to the effects of concrete shrinkage. The response of straight bridges and curved bridges with large radius is a convex curve, while that of highly curved bridges is concave. As such, shear forces increase for larger radii of curvature (including infinity) and finally decrease for smaller radii (after the maximum point). The other point is that the shear force of curved bridges longer than about 700 feet is less than the force of a straight bridge of the same length.

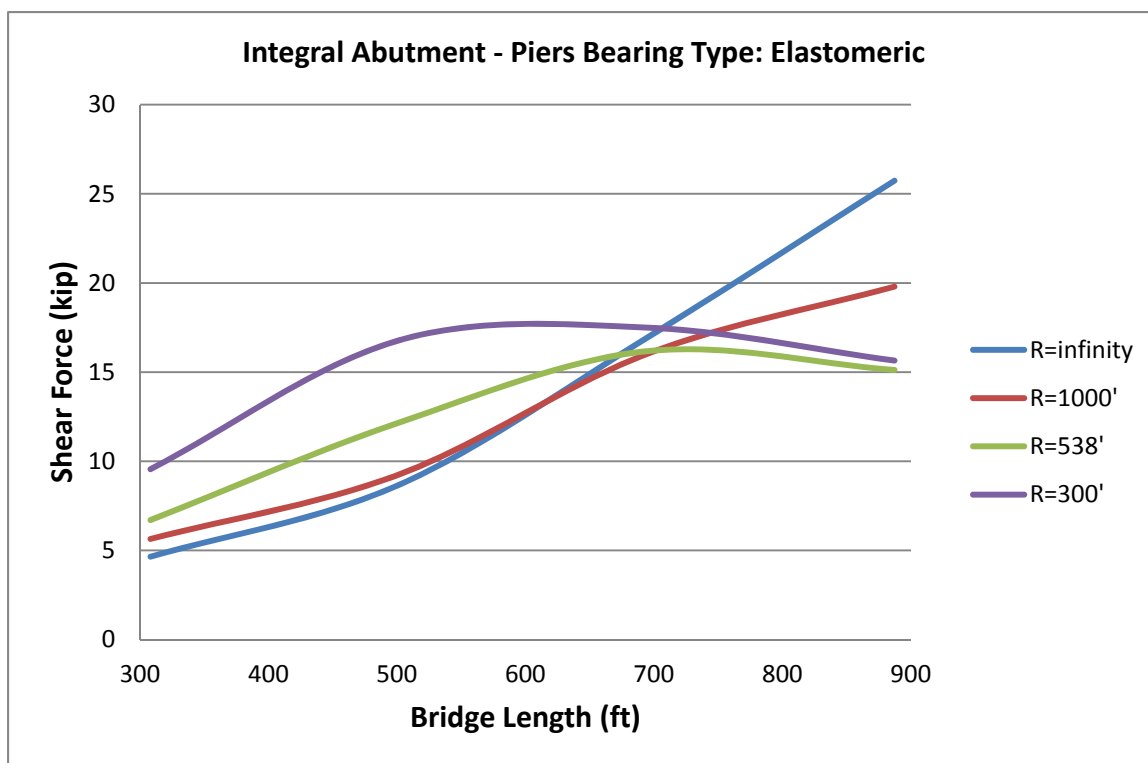


Figure A-11. Maximum Shear Force in Abutment Piles Due to Concrete Shrinkage

Normalized shear forces of the abutment piles are plotted versus length in Figure A-12. This picture shows the shear force from another perspective. In shorter bridges, the shear forces of piles of highly curve bridges due to shrinkage are about two times larger than that of straight bridges. As the length goes up to about 900 feet, the shear force drops down to about 60 percent of the shear of the equivalent straight bridge. Also, a pivot point with approximate length of 700 feet is observable.

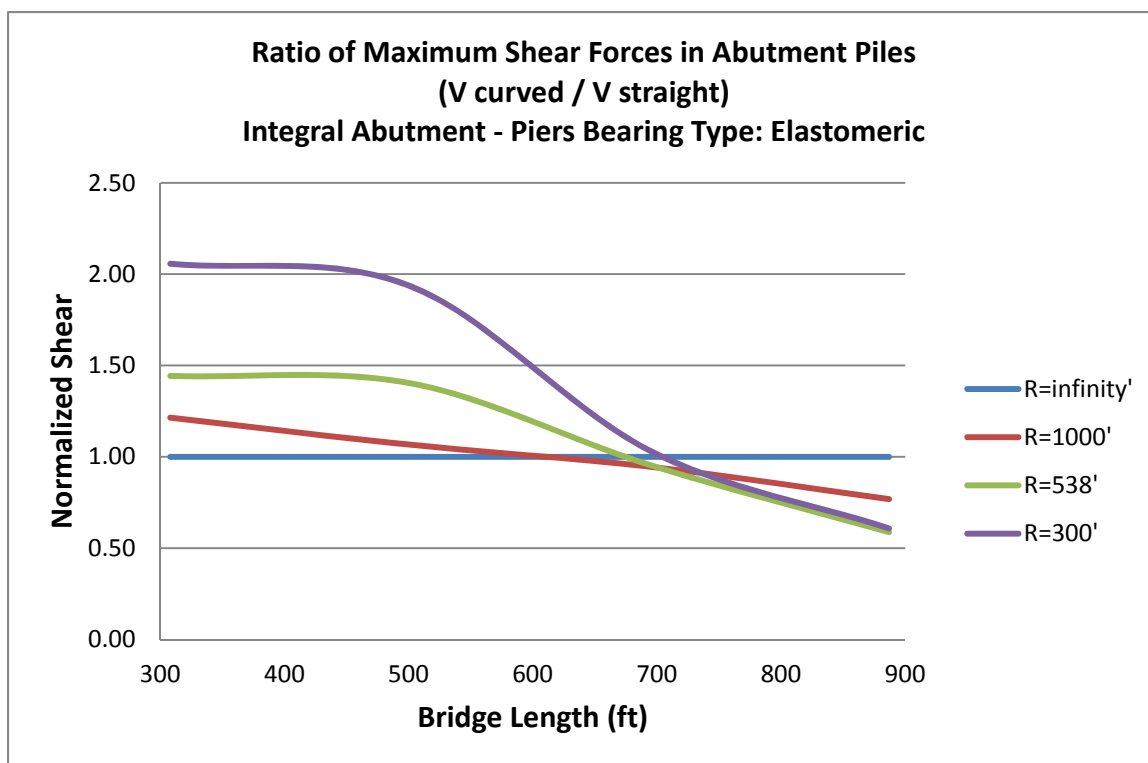


Figure A-12. Normalized Shear Force in Abutment Piles Due to Concrete Shrinkage

A7 Horizontal Earth Pressure

Figure A-13. shows the shear forces of the abutment piles when horizontal earth pressure is applied to the bridge. The shear force in straight bridges does not depend on the length of the bridge which is reasonable. But, in the case of curved bridges, it changes as the length changes. For small radii of curvature like 300 feet, it has the largest values which tend to be constant for longer bridges. For larger radii like 1000 feet, it shows increasing trend as the length increases.

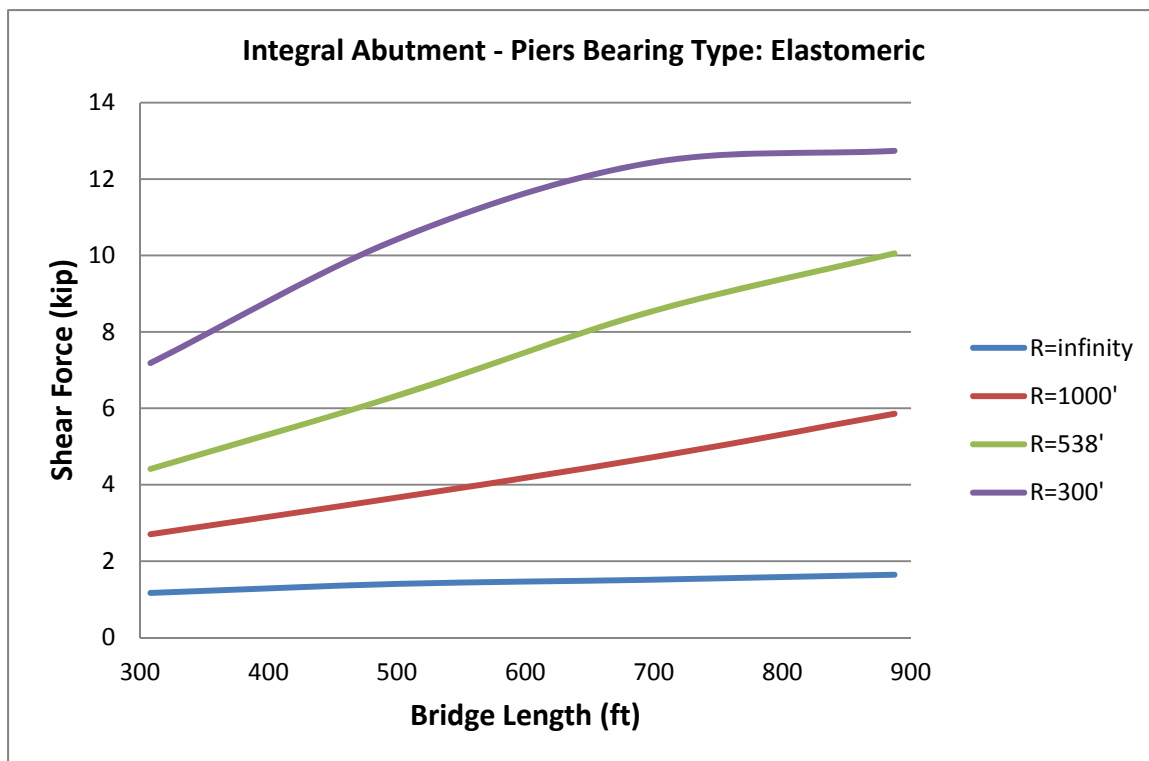


Figure A-13. Maximum Shear Force in Abutment Piles Due to Earth Pressure

Figure A-14. illustrates the normalized shear forces of piles versus bridge length. As can be seen, the values of shear forces in highly curved bridges can be several times larger than those of straight bridges of the same length. The smaller the radius of curvature of the bridge is, the larger the shear force can be. The highest ratio is for the length of about 700 feet for a bridge with radius equal to 300 feet.

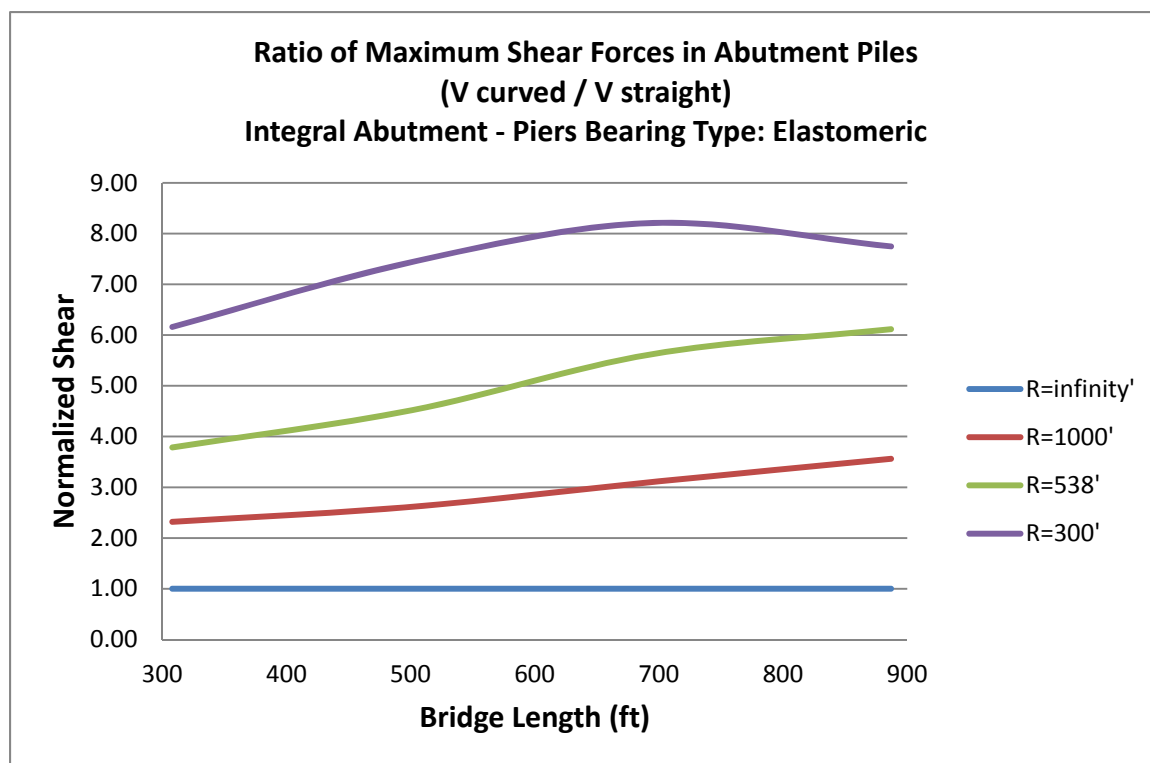


Figure A-14. Normalized Shear Force in Abutment Piles Due to Earth Pressure

A8 Centrifugal Force

The shear forces of piles created by centrifugal force of the live load are plotted versus length in Figure A-15. As can be observed, the piles shear force is approximately unchanged upon variation of bridge length or radius. As there is no centrifugal force in straight bridges, a normalized shear force is not defined for this load in the same way as the other loads.

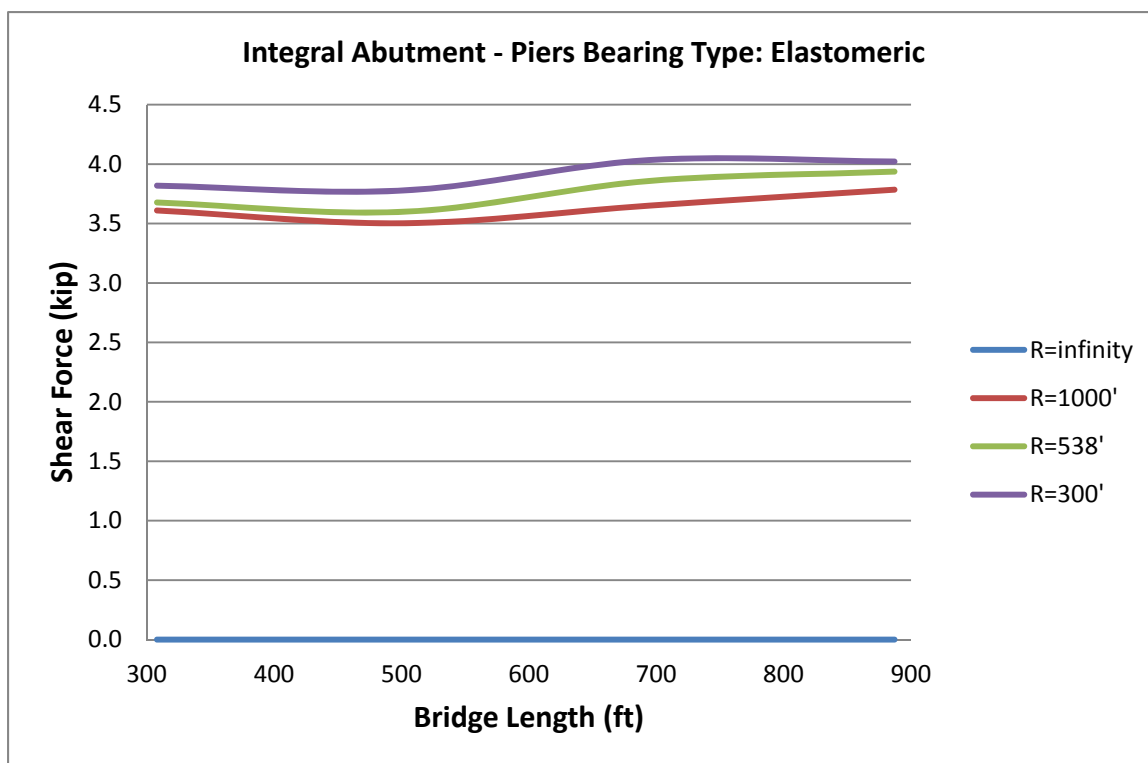


Figure A-15. Maximum Shear Force in Abutment Piles Due to Centrifugal Force

A9 Weight of Wearing Surface

Figure A-16. represents the shear force of abutment piles for different bridge length and curvature. As can be seen, the general trend is similar to the other gravity loads. The shear force reduces as the length of the bridge increases and the slope of reduction is larger for smaller radii of curvature. As expected, the shear force for straight bridges is almost the same for different bridge lengths. This is attributed to the fact that this shear force in a straight bridge is mainly a function of the end span length which has been the same for all studied bridge.

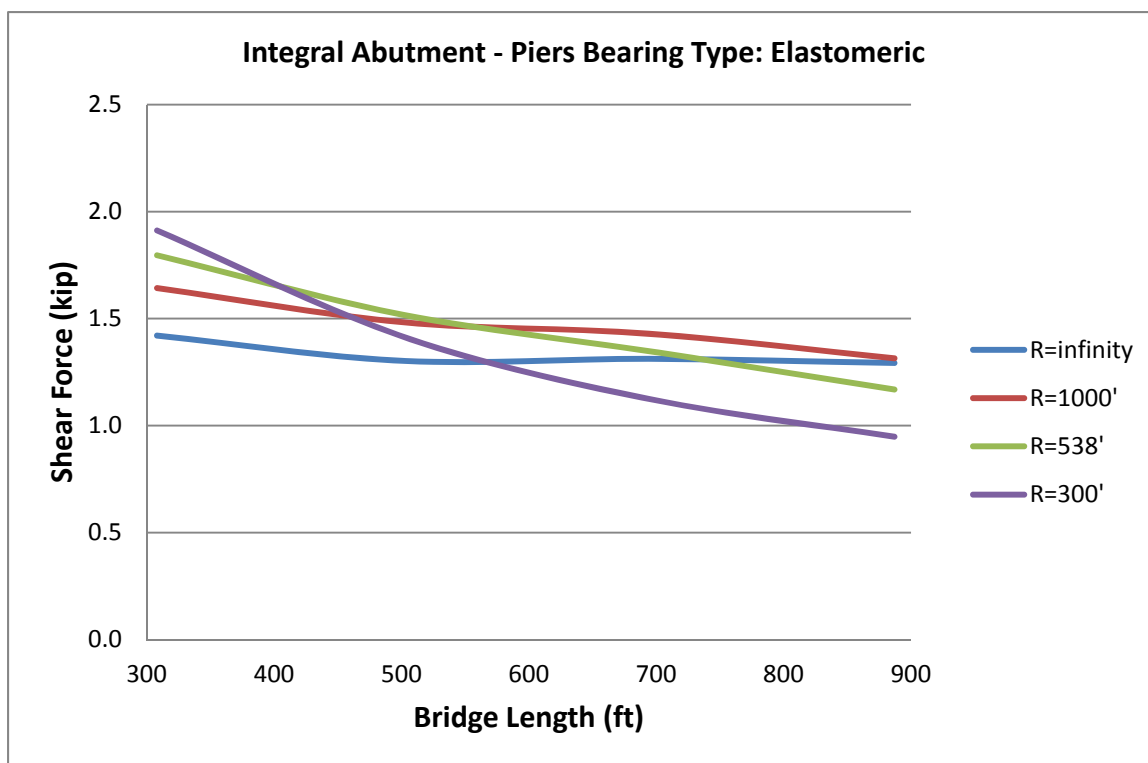


Figure A-16. Maximum Shear Force in Abutment Piles Due to Weight of Wearing Surface

By dividing the shear force of the curved bridges by that of the straight bridge of the same length, the shear forces are normalized which are graphed in Figure A-17. As one can observe, the normalized shear graph is very similar to that of dead load. This is because these two loadings are of the same nature. Again, it is seen that the rate of changes is maximum for smallest radius of curvature.

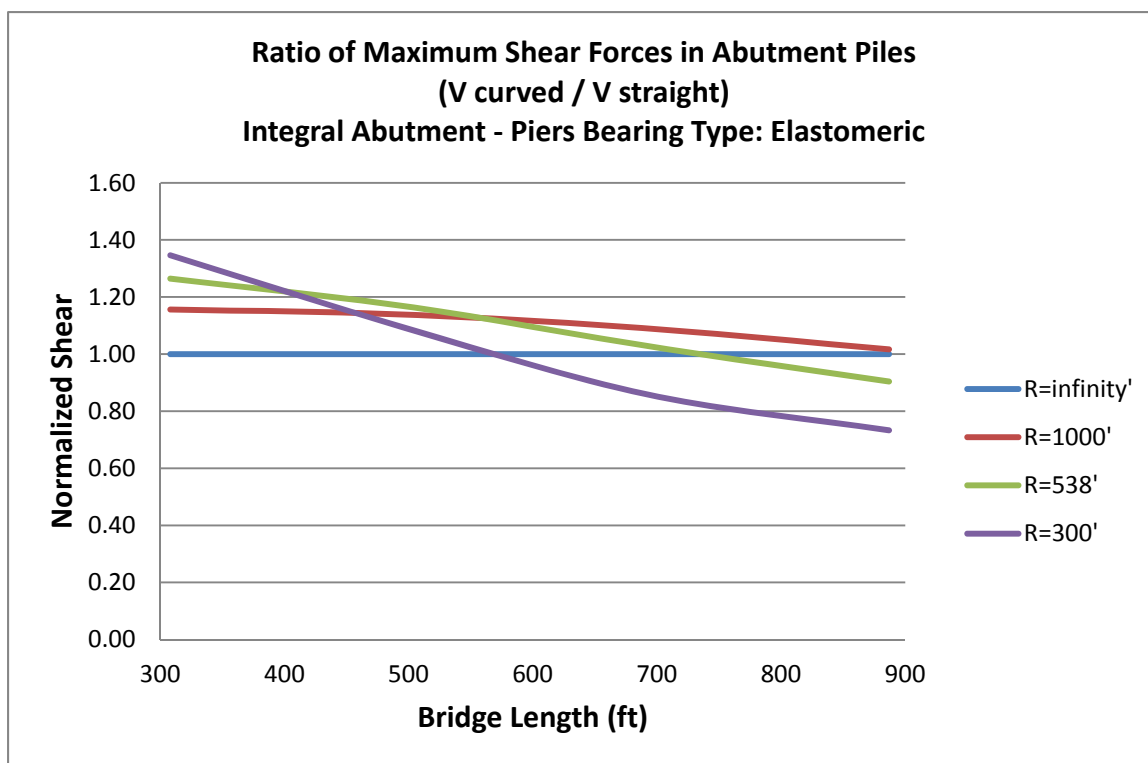


Figure A-17. Normalized Shear Force in Abutment Piles Due to Weight of Wearing Surface

A10 Braking Force

The shear force caused by braking load of the live loads is illustrated in Figure A-18. Braking force has one of the smallest weight factors among various loads. That can be ascertained by looking the shear values developed in the piles by this loading. The shear forces are tiny. The change in the rate of forces which starts for lengths larger than 450 feet, is because of the change in definition of the load in that range of lengths. The normalized shear forces are also shown in Figure A-19.

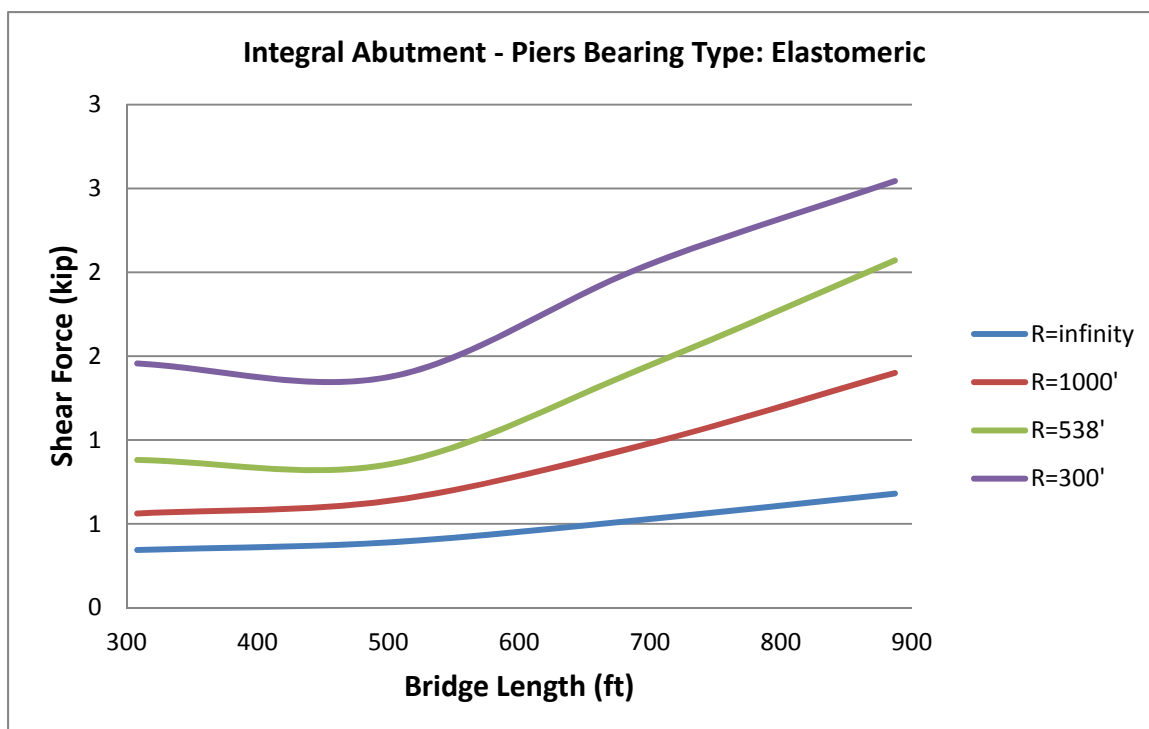


Figure A-18. Maximum Shear Force in Abutment Piles Due to Braking Force

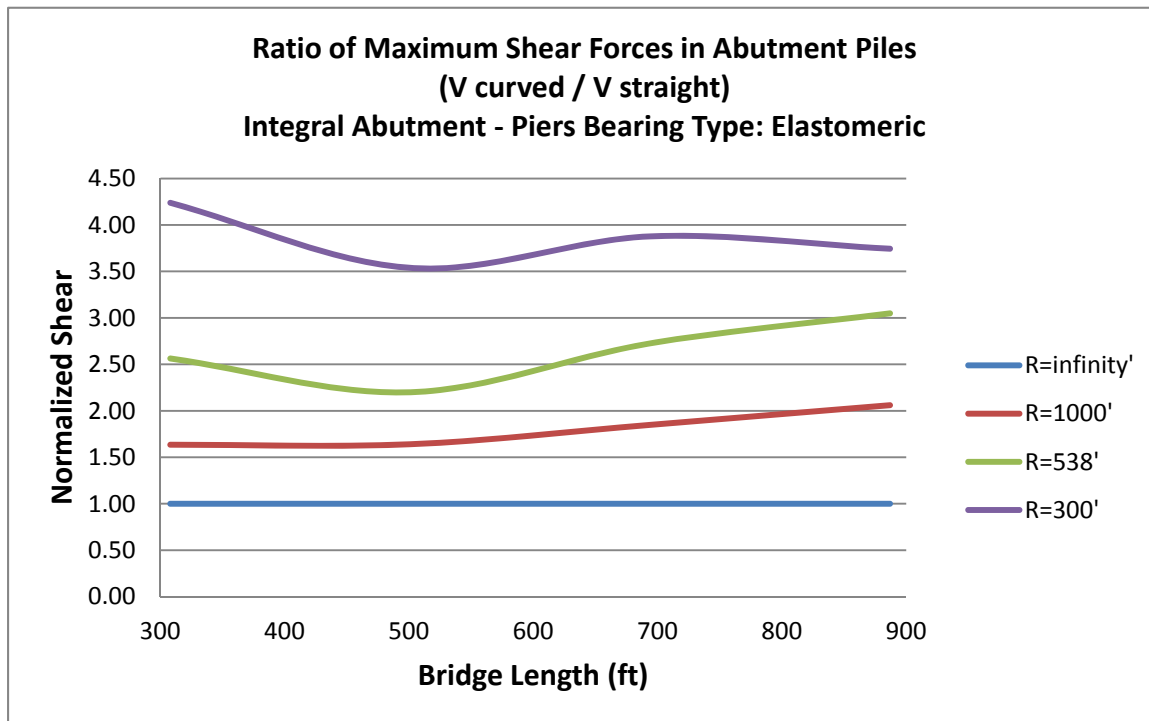


Figure A-19. Normalized Shear Force in Abutment Piles Due to Braking Force

A11 Positive Temperature Gradient

The shear forces due to positive temperature gradient are shown in Figure A-20. As can be seen, the shear forces are ignorable compared to the shear forces developed by other load effects. The change of these forces is out of order. But it can be seen that the shear force of curved bridges has been less than straight bridges in all cases. Figure A-21. shows the normalized shear forces.

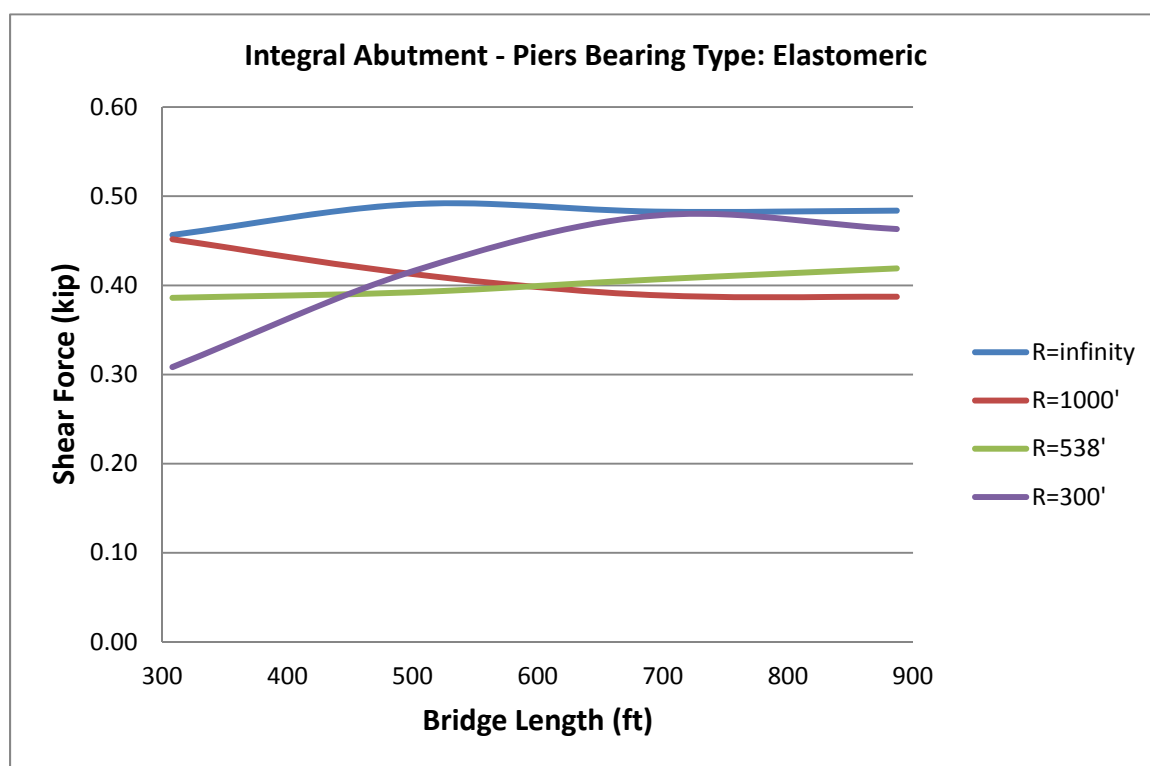


Figure A-20. Maximum Shear Force in Abutment Piles Due to Positive Temperature Gradient

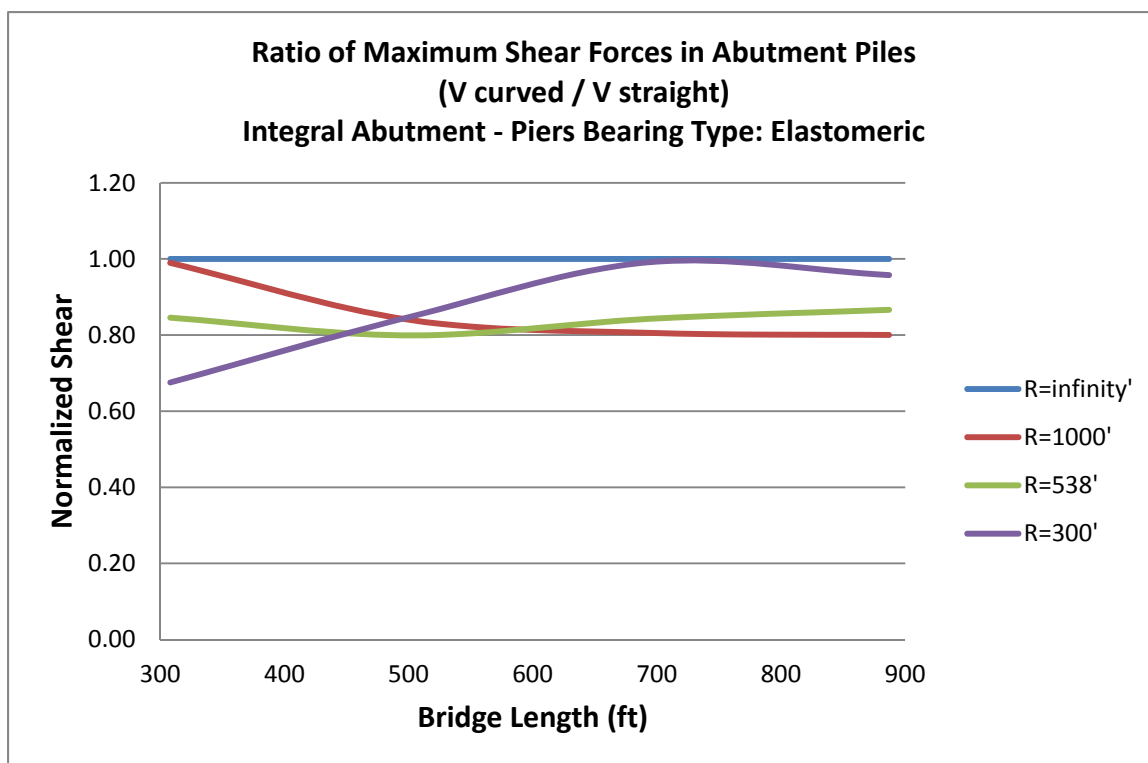


Figure A-21. Normalized Shear Force in Abutment Piles Due to Positive Temperature Gradient

A12 Negative Temperature Gradient

Having the smallest weight factor among all loads proves trifling nature of negative temperature gradient in design procedure of studied bridges. The shear forces are all less than 0.2 kips. Therefore, the regime of their changes is not discussed. The normalized shear force is shown in Figure A-23. It shows that this tiny shear force in curved bridges can be in some conditions smaller and in some other cases greater than that of straight counterpart which is not of great importance.

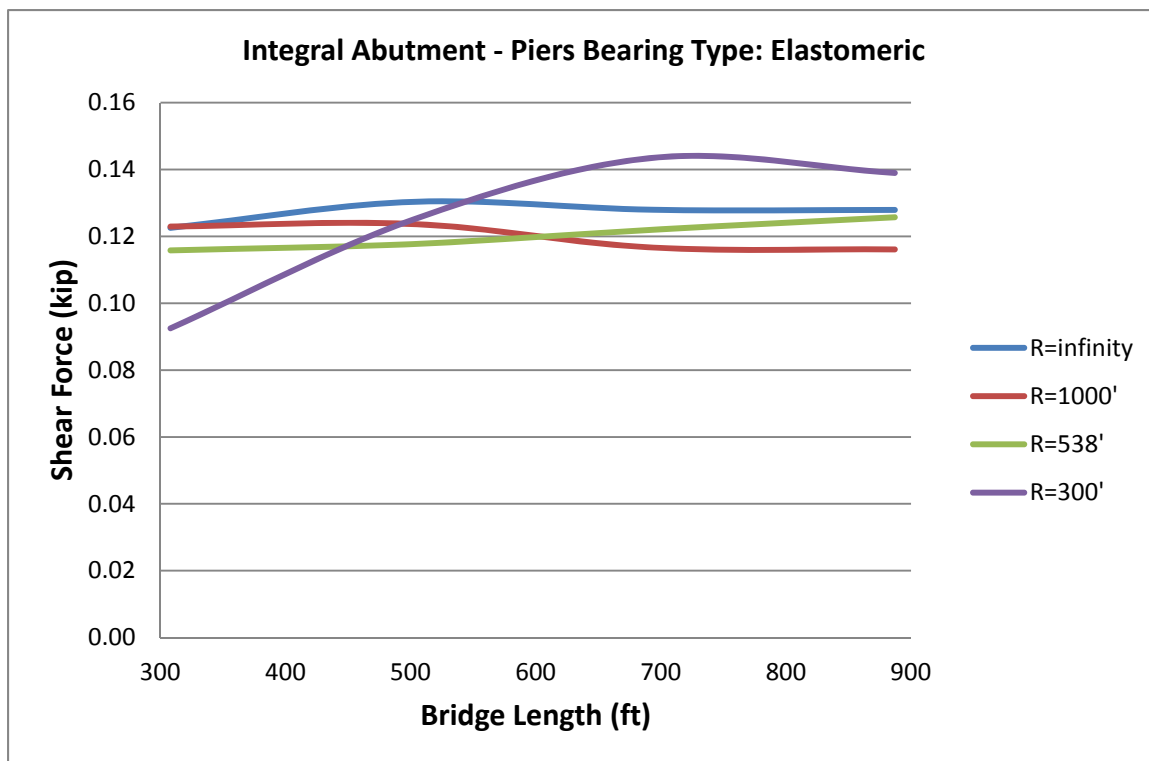


Figure A-22. Maximum Shear Force in Abutment Piles Due to Negative Temperature Gradient

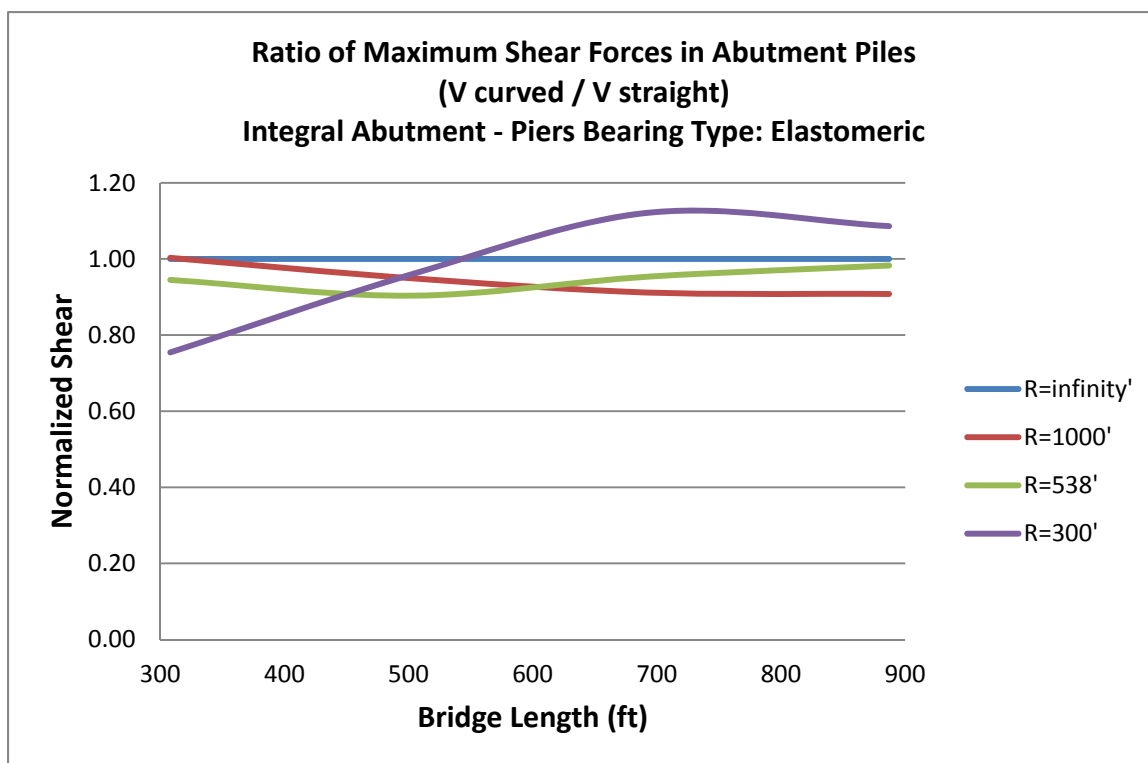


Figure A-23. Normalized Shear Force in Abutment Piles Due to Negative Temperature Gradient

A13 Combination of the Loads

After discussing the effect of bridge length and curvature on the shear force of abutment piles of studied bridges, in this section the envelope of shear force in different load combinations of AASHTO code is studied in more details. As can be observed from Figure A-24, the shear forces of piles in straight bridges increase as the length of the bridge increases. But, in curved bridge variations is a function of curvature. In bridges with large radius of curvature, the trend is somehow similar to straight bridges, but with a more moderate rate of change. In highly curved bridge, the slope of changes reduces so that the shear forces can decrease as the length increases.

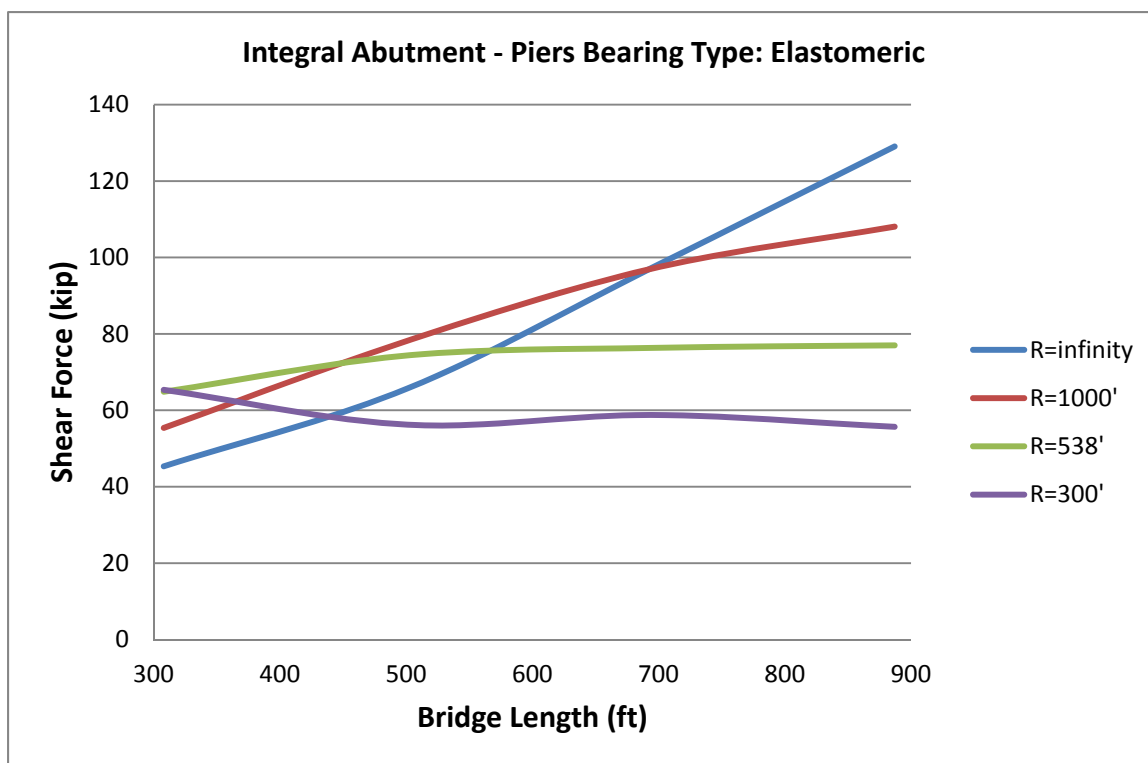


Figure A-24. Envelope of Maximum Shear Force in Abutment Piles in Different Load Combinations

Figure A-25. shows the normalized factored shear force envelope in the abutment piles. it can be observed that the design shear force in a curved bridge of small length ($L=300'$) is larger than that of the equivalent straight bridge. It also shows that depending on the bridge curvature, the shear force of curved bridge is equal to that of the straight. For bridge longer than that specific length, the shear force starts to be smaller than that of the straight bridge so that at the length of about 900 feet, the shear force of the pile can be as small as 45 percent of the shear force of straight bridge. This shows that piles of long curved bridge are more designable compared to straight bridge with equal length from shear design point of view.

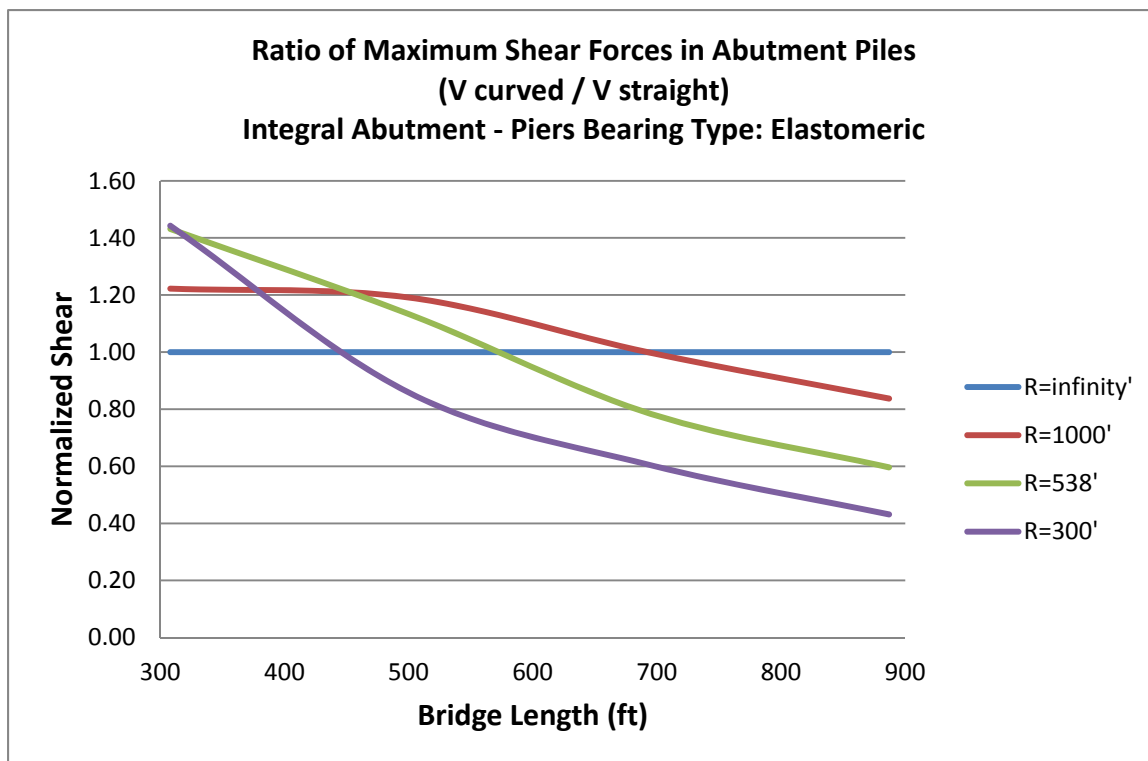


Figure A-25. Envelope of Normalized Shear Force in Abutment Piles in Different Load Combinations

Appendix B

MATLAB Moment-curvature Program

In this appendix, the MATLAB program developed to analyze the moment capacity of the composite steel section at the face of integral abutment is presented:

```
disp('Units: kips, inch');
format long;
disp('Is it the first time you are running the program (after loading MATLAB)?');
first=input('y for "yes" or n for "no" (Default= no): ','s');
if isempty(first)
    first='n';
end
if first=='y'
    B=zeros(100,1);
    D=zeros(100,1);
    material=zeros(100,1);
end
% color('green');
n_sec = input('Number of section changes? (Default=5)');
if isempty(n_sec)
    n_sec = 5;
```

```

end
sum_D=zeros(n_sec,1);
for i=1:n_sec
    disp('%%');    disp('%%');    disp('  Width B(i,1)was:');
    disp(B(i,1));
    disp('Press "Enter" if there is no changes in the section width. ');
    Btemp= input('Width of the section? ');
    if isempty(Btemp)
        aaaa=1;
    else
        B(i,1) = Btemp;
    end
    disp('%%');    disp('%%');    disp('  Depth(i,1)was:');
    disp(D(i,1));
    disp('Press "Enter" if there is no changes in the section depth. ');
    Dtemp= input('Depth of the section? ');
    if isempty(Dtemp)
        aaaa=1;
    else
        D(i,1) = Dtemp;
    end
    disp('%%');    disp('%%');
    disp('Material of the section:');
    disp('    Enter 1 for GR50 Steel');
    disp('    2 for GR60 Steel');
    disp('    3 for GR100 Steel');
    disp('    4 for NSC');
    disp('    5 for HSC');
    disp('    6 for UHPC');
    % material(i,1)= input('Select a Material (1 to 6):');
    disp('    Material(i,1)was:');

```

```

if material(i,1)== 1;
    disp(' 1: GR50 Steel');
elseif material(i,1)==2;
    disp(' 2: GR60 Steel');
elseif material(i,1)==3;
    disp(' 3: GR100 Steel');
elseif material(i,1)==4;
    disp(' 4: NSC');
elseif material(i,1)==5;
    disp(' 5: HSC');
elseif material(i,1)==6;
    disp(' 6: UHPC');
end
disp(material(i,1));
disp('Press "Enter" if there is no changes in the section material. ');
mattemp= input('Material of the section? ');
if isempty(mattemp)
    aaaa=1;
else
    material(i,1) = mattemp;
end
end
% forming the total height
h=0;
for i=1:n_sec
    h=h+D(i,1);
end
disp('%%'); disp('%%');
disp('Total Height=');
disp(h);
% forming the partial depths

```

```

sum_D(1,1)=D(1,1);
for i=2:n_sec
    sum_D(i,1)=sum_D(i-1,1)+D(i,1);
end
disp('%%'); disp('%%');
n = input('Number of increments in the section (for Default n=1000 Press "Enter")?');
if isempty(n)
    n = 1000;
end
% setting breadth and material for each increment
b=zeros(n+1,1);
d=zeros(n+1,1);
mat=zeros(n+1,1);
for j=1:n_sec-1
    for i=1:n+1
        d(i,1)=(i-1)/n*h;
        if d(i,1)<=sum_D(1,1)
            b(i,1)=B(1,1);
            mat(i,1)=material(1,1);
        elseif d(i,1)>sum_D(j,1)
            b(i,1)=B(j+1,1);
            mat(i,1)=material(j+1,1);
        else
            b(i,1)=b(i,1)+0;
        end
    end
end
end
% k represents the current location of N.A.
k=round(n/2);
% integer
% incofe is the increments of strain

```

```

incofe=0.00022;
% n_inc is the number of increments of strain to be considered (ie max strain)
n_e_inc=100;
strain=zeros(n+1,1);
stress=zeros(n+1,1);
f=zeros(n+1,1);
m=zeros(n+1,1);
curvature=zeros(n_e_inc+1,1);
M=zeros(n_e_inc+1,1);
M(1,1)=0;
curvature(1,1)=0;
%E=20;
%a=2;
%Fy=2;
%ey=Fy/E;
dy=h/n;
% an approximate method for calculating the convergence limit
dummy_force=zeros(n_sec,1);
for i=1:n_sec
    if material(i,1)== 1;
        ff=50;
    elseif material(i,1)==2;
        ff=60;
    elseif material(i,1)==3;
        ff=100;
    elseif material(i,1)==4;
        ff=4;
    elseif material(i,1)==5;
        ff=15;
    elseif material(i,1)==6;
        ff=18.4;

```

```

end
dummy_force(i,1)=B(i,1)*D(i,1)*ff;
end
dum_force=0.003*sum(dummy_force(:,1));
disp('%%'); disp('%%');
disp('3/1000 of yield axial force of the section is:');
disp(dum_force);
CL= input('Convergence Force Limit (for Default=0.003*Yield force Press "Enter")?');
NoConv=0;
if isempty(CL)
    CL = dum_force;
end
disp('%%'); disp('%%');
disp('RUNNING ...');
pause(0.1);
rup_flag=0;
if NoConv==0
    for j=2:n_e_inc+1
        if (rup_flag==0 && NoConv==0)
            etop=(j-1)*incofe;
            for i=1:n+1
                strain(i,1)=-etop+(i-1)/k*etop;
                if mat(i,1)== 1;
                    StressGR50;
                elseif mat(i,1)==2;
                    StressGR60;
                elseif mat(i,1)==3;
                    StressGR100;
                elseif mat(i,1)==4;
                    StressNSC;
                elseif mat(i,1)==5;

```



```

        StressHSC;
elseif mat(i,1)==6;
    StressUHPC;
end
end
for i=1:n
    f(i,1)=(stress(i,1)+stress(i+1,1))/2*(b(i,1)+b(i+1,1))/2*dy;
end
F=sum(f(:,1));
while (abs(F)>CL && NoConv==0)
    if (F>0 && k<n-1)
        k=k+1;
        for i=1:n+1
            strain(i,1)=-etop+(i-1)/k*etop;
            if mat(i,1)== 1;
                StressGR50;
            elseif mat(i,1)==2;
                StressGR60;
            elseif mat(i,1)==3;
                StressGR100;
            elseif mat(i,1)==4;
                StressNSC;
            elseif mat(i,1)==5;
                StressHSC;
            elseif mat(i,1)==6;
                StressUHPC;
            end
        end
    end
    for i=1:n
        f(i,1)=(stress(i,1)+stress(i+1,1))/2*(b(i,1)+b(i+1,1))/2*dy;
    end
end

```

```

elseif (F<0 && k>1)
    k=k-1;
    for i=1:n+1
        strain(i,1)=-etop+(i-1)/k*etop;
        if mat(i,1)== 1;
            StressGR50;
        elseif mat(i,1)==2;
            StressGR60;
        elseif mat(i,1)==3;
            StressGR100;
        elseif mat(i,1)==4;
            StressNSC;
        elseif mat(i,1)==5;
            StressHSC;
        elseif mat(i,1)==6;
            StressUHPC;
        end
    end
    end
    for i=1:n
        f(i,1)=(stress(i,1)+stress(i+1,1))/2*(b(i,1)+b(i+1,1))/2*dy;
    end
    else
        NoConv=1;
        disp('There is no convergence!');
    end
    F=sum(f(:,1));
end;
for i=1:n
    m(i,1)=f(i,1)*(i-0.5)*dy;
end
M(j,1)=sum(m(:,1));

```

```

curvature(j,1)=etop/(k*dy);
for i=1:n+1
    if rup_flag==0
        if mat(i,1)== 1;
            StrainGR50;
        elseif mat(i,1)==2;
            StrainGR60;
        elseif mat(i,1)==3;
            StrainGR100;
        elseif mat(i,1)==4;
            StrainNSC;
        elseif mat(i,1)==5;
            StrainHSC;
        elseif mat(i,1)==6;
            StrainUHPC;
        end
    end
end
elseif rup_flag==1
    M(j,1)=M(j-1,1);
    curvature(j,1)=curvature(j-1,1);
end
disp(curvature(j,1));
disp(M(j,1));
%   plot(curvature(j,1),M(j,1));
end
else
    disp('There is no convergence!');
end
disp('Total Height=');
disp(h);

```

```
disp('Maximum Curvature=');
disp(curvature(j,1));
disp('Maximum Moment=');
disp(M(j,1));
disp('Top Strain=');
disp(strain(1,1));
disp('Bottom Strain=');
disp(strain(n+1,1));
plot(curvature,M);
% plot stress
z=zeros(n+1,1);
for i=1:n+1
    z(i,1)=h-d(i,1);
end
plot(stress,z);
```